

---

# X-ray Emission of Simulated Galaxies - From Stars to Cosmic Filaments

Stephan Vladutescu-Zopp

---



München 2024



---

# **X-ray Emission of Simulated Galaxies - From Stars to Cosmic Filaments**

**Stephan Vladutescu-Zopp**

---

Dissertation  
an der Fakultät für Physik  
der Ludwig–Maximilians–Universität  
München

vorgelegt von  
Stephan Vladutescu-Zopp  
aus Rosenheim

München, den 14.11.2024

Erstgutachter: Prof. Dr. Klaus Dolag  
Zweitgutachter: Prof. Dr. Rolf Kudritzki  
Tag der mündlichen Prüfung: 08.01.2025

# Zusammenfassung

Viele der physikalischen Prozesse, die den Aufbau und die Entwicklung großräumiger Strukturen im Universum steuern, setzen Strahlung im Röntgenbereich frei. Von diesen Strukturen sind Galaxien besonders interessant, da in ihnen optimale Bedingungen für jene Prozesse herrschen. Zum Beispiel wird das interstellare Medium (ISM) von Supernova (SN) Explosionen, den Winden massereicher Sterne, sowie der intensiven Strahlung des zentralen supermassiven schwarzen Lochs (SMBH) aufgeheizt. Des Weiteren können Röntgendoppelsterne, die durch Akkretionsprozesse an kompakten Objekten (CO) ihre Leuchtkraft erlangen, als Punktquellen in den Sternfeldern von Galaxien beobachtet werden. Gleichzeitig wird großräumig verteiltes Gas im Gravitationspotential des zugrundeliegenden Halos dunkler Materie aufgeheizt. Dieses Reservoir an heißem Gas reguliert, zum Beispiel, die Sternentstehungsrate im Inneren des Halos. Alle hier genannten Phänomene können im Röntgenstrahlenbereich beobachtet werden und bilden einen wichtigen Eckpfeiler für unser Verständnis von Strukturbildung im Universum.

Zu den aufgezeigten Beobachtungen können moderne kosmologische hydrodynamische Simulationen eine ergänzende Funktion einnehmen, da sie morphologische und hydrodynamische Eigenschaften von Galaxien und deren Umgebung im Kiloparsec-Bereich auflösen können. Der Fortschritt in der numerischen Astrophysik ermöglicht es, realistische Umgebungsbedingungen für Galaxienentwicklung zu schaffen, sodass detaillierte Analysen mit dem Informationsgehalt des gesamten Phasenraums durchgeführt werden können. In dieser Arbeit stellen wir eine Analyse der Röntgeneigenschaften von simulierten Galaxien aus der modernen kosmologischen Simulationsreihe *Magneticum Pathfinder* vor. Dabei nutzen wir ein virtuelles Röntgenobservatorium genannt PHOX, welches die intrinsischen Eigenschaften der Simulation nutzt, um realistische Pseudobeobachtungen im Röntgenbereich zu produzieren. Das Novum in unserer Analyse basiert auf der Entwicklung eines numerischen Modells, das die stellare Komponente kosmologischer Simulationen nutzt, um realistische Abbilder von Röntgendoppelsternpopulationen zu generieren.

Teil I beginnt mit einer allgemeinen Einleitung über fundamentale Prinzipien der Galaxienentwicklung sowie physikalischer Prozesse, die die Kühlung von astrophysikalischen Gasen beschreiben. Im Nachhinein geben wir einen Überblick über Beobachtungen der verschiedenen Größenskalen von Galaxien im Röntgenbereich, die vom ISM bis zum zirkumgalaktischen Medium (CGM) reichen. Wir schließen Teil I mit einer detaillierten Beschreibung der Entstehung und Entwicklung von Röntgendoppelsternen sowie der relevanten Akkretionsprozesse.

In Teil II präsentieren wir zunächst die numerische Implementierung physikalischer Modelle in *Magneticum* anhand der Sternentstehung und Energierückkopplung des SMBH und beschreiben die Konvertierung von Simulationsdaten zu Pseudobeobachtungen im Röntgenbereich.

Darauffolgend beschreiben wir unser neues Modell zur Darstellung von Röntgendoppelsternen mithilfe der Eigenschaften der kosmologischen Simulation. Wir führen verschiedene Prüfungen unseres Modells durch, um die korrekte Darstellung empirischer Relationen und räumlicher Verteilung von Röntgendoppelsternen in simulierten Galaxien zu gewährleisten. Des Weiteren zeigen wir, dass unser Modell korrekte Röntgenspektren von Galaxien erzeugt und dass der Beitrag von Röntgendoppelsternen den Ergebnissen von Beobachtungen entspricht. Darauf aufbauend untersuchen wir die Flächenverteilung der Leuchtkraft im Röntgenbereich von simulierten Galaxien, wobei unser Modell wichtige Einblicke in mögliche Kontaminationsquellen im CGM gibt. Wir zeigen, dass etwa 10% der Leuchtkraftverteilung nahe des Virialradius einer Galaxie auf Röntgendoppelsterne zurückgeführt werden kann. Zusätzlich ist die Normalisierung der Leuchtkraftverteilung in Galaxien mit hohen Sternentstehungsraten größer als in solchen mit niedrigen Raten. Die maximale räumliche Ausdehnung der Leuchtkraftverteilung ist außerdem abhängig vom Massenanteil und der mittleren Temperatur des heißen Gases der Galaxie sowie von der Gesamtmasse an Sternen. Unter näherer Betrachtung der Gaskomponente stellen wir quantitativ steilere Leuchtkraftverteilungen in simulierten als in realen Galaxien fest, wobei die Steigung mit der Gesamtleuchtkraft im Röntgenbereich und dem Massenanteil an heißem Gas positiv korreliert. Interessanterweise weist die momentane Akkretionsrate des zentralen SMBH Korrelationen mit denselben Parametern auf, was auf die regulierenden Eigenschaften des SMBH im Zusammenhang mit Galaxienentwicklung hindeutet. Trotz der steileren Leuchtkraftverteilung ist die Gesamtleuchtkraft der simulierten Galaxien als Funktion der Virialmasse im Einklang mit beobachteten Relationen.

In Teil III fokussieren wir unsere Analyse auf filamentartige Netzwerke der Materie, welche großräumige Strukturen miteinander verbindet. Das dünne Plasma innerhalb dieser Filamente zeigt lediglich schwache Abstrahlung im Röntgenbereich und wird von Galaxien und Galaxienhaufen überstrahlt. Daher präsentieren wir eine vorläufige Studie zu den Fähigkeiten von zukünftigen Röntgenteleskopen, die sich der Mikrokalorimetrie bedienen, um mit hoher spektraler Auflösung die schwache Emission der Filamente zu erschließen. Abschließend fassen wir unsere Ergebnisse in Teil IV zusammen und zeigen Perspektiven für zukünftige Studien mit unserem Modell auf. Diese beinhalten unter anderem Synergien zwischen räumlich hochauflösenden Röntgen- und Infrarotteleskopen, welche die Beschreibung von Röntgendoppelsternen in simulierten und realen Galaxien verbessern werden. Außerdem kann der genaue Beitrag von Galaxien und Röntgendoppelsternen zum kosmischen Röntgenhintergrund abgeschätzt werden.

# Abstract

Many of the physical processes governing the assembly and evolution of structures in the universe release radiation in the X-ray regime. Galaxies, in particular, exhibit the necessary conditions for these processes. For instance, the interstellar medium (ISM) is heated and ionized by shockwaves of Supernova (SN) remnants, by the intense winds of massive stars, and by the intense radiation and energy deposition of an actively accreting Super Massive Black Hole (SMBH) in the galactic center. Point-like X-ray Binary (XRB) sources observed in the stellar field of galaxies are associated with binary stars containing a compact object (CO) where gravitational and orbital interaction funnel material onto the CO via a viscously heated accretion disc. Lastly, the gas surrounding each galaxy from the primordial assembly is heated by the gravitational potential well of the galaxy's dark matter halo and acts as a recycling agent for star formation processes in the inner halo. Therefore, X-ray observations of galaxies are an important cornerstone for our understanding of structure formation and processes governing the cooling and heating of astrophysical plasmas.

Observations are complemented by cosmological hydrodynamical simulations which are able to resolve morphological features and hydrodynamic properties of the gas within galaxies down to kiloparsec scales and provide realistic environments for their evolution. The tremendous progress in the field of computational astrophysics provides a controlled physical representation of galaxy evolution which can be analyzed in depth using the full phase-space information of such simulations. In this work, we present an analysis of X-ray properties of simulated galaxies from the state-of-the-art hydrodynamical cosmological simulation suite *Magneticum Pathfinder* and also connect them to the large-scale environment. We make use of the virtual X-ray photon observatory PHOX which converts the intrinsically tracked properties of the simulation to produce a realistic X-ray mock observation. The novelty in our analysis lies in the development of a new numerical model that produces realistic XRB sources for X-ray mock observations of the stellar component in the simulation.

In Part I of the thesis, we begin with a general introduction to the main principles of galaxy formation and the main physical processes governing the cooling of astrophysical gas. We follow up with an overview of X-ray observations on various scales ranging from their ISM to the circum-galactic medium (CGM) and describe the formation and evolution of XRB sources in much greater detail also touching on the main aspects regarding accretion physics.

In the following Part II, we start by presenting implementation details of the physical models included in *Magneticum*, i.e. star formation and SMBH feedback, and describe the process of converting the simulation output into realistic X-ray mock observations. We continue with

an in-depth description of our new model which produces realistic XRB populations from the stellar component of the simulation. We perform various tests to confirm that the modeled XRB populations follow empirically derived X-ray scaling relations and the appropriate stellar age distribution within the simulated galaxy. Furthermore, we show that the inclusion of this new approach for XRB sources produces galaxy X-ray spectra that are in perfect agreement with observations. Our model predicts the correct relative contribution of XRB towards the X-ray spectrum. As a follow-up, we then investigate the surface brightness (SB) of simulated galaxies in *Magneticum* including our XRB model to gain insights into possible contaminants when targeting the faint X-ray emission from the CGM. We find that XRB can contribute up to 10% of the signal received close to the virial radius of a galaxy indicating the presence of a diffuse stellar component. Furthermore, we find that the SB of Star-Forming Galaxies (SFG) has a higher normalization than for Quiescent Galaxies (QG). The extent of the SB in SFG declines with stellar mass, hot gas fraction, and hot gas temperature. Focusing on the gas component in simulated galaxies, we found quantitatively steeper fitted  $\beta$ -profiles in simulated galaxies compared to observations. The slope is correlated with the hot gas fraction and X-ray luminosity of the gas. Interestingly, the current accretion rate of the central SMBH is also correlated with the aforementioned quantities highlighting its regulatory role in galaxy evolution. Despite the steeper profile shapes the total gas X-ray luminosity within the virial radius as a function of halo mass is in good agreement with observed scaling relations.

In Part III we focus on the large-scale cosmic web in which galaxies are embedded. We show a preliminary study on the faint emission and galaxy contamination of the thin plasma in the filamentary bridges between galaxy clusters. Specifically, we test the capabilities of future X-ray telescopes employing microcalorimeter technology to achieve much higher spectral resolution. We conclude this thesis in Part IV by summarizing our findings and giving future perspectives on additional studies. This includes possible synergies between high-resolution X-ray and infrared observations to improve the description of XRB populations in simulated and real galaxies. Another application would be the estimate of the contribution of galaxies in general and XRBs in particular towards the cosmic X-ray background.

# Contents

<b>Zusammenfassung</b>	<b>v</b>
<b>Abstract</b>	<b>vii</b>
<b>List of Acronyms</b>	<b>x</b>
<b>I Introduction</b>	<b>1</b>
<b>1 Galaxy evolution in a nutshell</b>	<b>3</b>
1.1 Galaxies in cosmology . . . . .	3
1.2 Assembly of galaxies . . . . .	7
1.3 Cooling of astrophysical gas . . . . .	11
<b>2 X-ray observations of galaxies</b>	<b>15</b>
2.1 Hot gas within and around Galaxies . . . . .	18
2.2 Active galactic nuclei . . . . .	23
2.3 Stellar X-ray sources . . . . .	27
<b>3 X-ray Binaries</b>	<b>31</b>
3.1 Classification . . . . .	31
3.2 Formation and Evolution . . . . .	34
3.3 X-ray Spectral Energy Distribution . . . . .	40
3.4 Scaling relations . . . . .	47
<b>II X-ray binaries in simulated galaxies</b>	<b>51</b>
<b>4 Magneticum Pathfinder Simulations</b>	<b>53</b>
4.1 A brief history on cosmological simulations . . . . .	53
4.2 Magneticum . . . . .	55

<b>5</b>	<b>Let the Simulations Shine in X-ray</b>	<b>61</b>
5.1	PHOX X-ray photon simulator . . . . .	61
5.2	General code updates . . . . .	66
<b>6</b>	<b>Seeding X-ray binaries in the simulations (Paper 1)</b>	<b>69</b>
6.1	Modeling of XRB populations within SSPs . . . . .	71
6.2	XRB emission model . . . . .	74
6.3	Simulated data set . . . . .	76
6.4	Validation of the modeling . . . . .	78
6.5	Relative emission of hot gas and XRBs . . . . .	91
6.6	Discussion . . . . .	98
6.7	Summary and conclusions . . . . .	102
<b>7</b>	<b>The X-ray atmospheres of simulated galaxies (Paper 2)</b>	<b>105</b>
7.1	Simulated data set . . . . .	107
7.2	Galaxy X-ray surface brightness . . . . .	111
7.3	Discussion . . . . .	127
7.4	Summary . . . . .	133
7.5	Appendix . . . . .	135
<b>III</b>	<b>Inter-Galactic X-ray emission from cosmic filaments in simulations</b>	<b>141</b>
<b>8</b>	<b>Emissivity of low-density gas in cosmic filaments: a case study</b>	<b>143</b>
8.1	Data Set . . . . .	146
8.2	Intrinsic filament emission . . . . .	151
8.3	Outlook . . . . .	155
<b>IV</b>	<b>Conclusions &amp; Future Perspectives</b>	<b>157</b>
<b>9</b>	<b>Conclusion</b>	<b>159</b>
<b>10</b>	<b>Outlook</b>	<b>161</b>
10.1	Extensions of the XRB model . . . . .	161
10.2	Redshift evolution of XRB emission . . . . .	162
10.3	Age dating of XRB populations . . . . .	162
10.4	The X-ray bright Future of astronomy . . . . .	163
	<b>Bibliography</b>	<b>165</b>
	<b>Acknowledgements</b>	<b>197</b>

# List of Acronyms

**AGN** Active Galactic Nucleus

**APEC** Astrophysical Plasma Emission Code

**BH** Black Hole

**CO** compact object

**CDM** Cold Dark Matter

**CGM** circum-galactic medium

**CIE** Collisional Ionization Equilibrium

**CMB** Cosmic Microwave Background

**CXB** Cosmic X-ray Background

**DM** Dark Matter

**eROSITA** extended ROentgen Survey with an Imaging Telescope Array

**eRASS** eROSITA All-Sky Survey

**eFEDS** eROSITA Final Equatorial Depth Survey

**HMXB** High-Mass X-ray Binary

**ICM** Intra Cluster Medium

**IGM** Inter Galactic Medium

**IMF** Initial Mass Function

**ISM** interstellar medium

**LEM** Line Emission Mapper

**LMXB** Low-Mass X-ray Binary

**LOS** line of sight

**LSS** Large Scale Structure

**MEKAL** Mewe-Gronenschild-Kaastra-Liedahl

**MW** Milky Way

**PIE** Photo-Ionization Equilibrium

**QG** Quiescent Galaxy

**RASS** ROSAT all-sky survey

**RLO** Roche-Lobe Overflow

**SBP** Surface Brightness Profile

**SDSS** Sloan Digital Sky Survey

**SFG** Star-Forming Galaxy

**SFR** Star-Formation Rate

**SMBH** Super Massive Black Hole

**SN** Supernova

**SPH** Smoothed-Particle Hydrodynamics

**SSP** Simple Stellar Population

**WHIM** Warm-Hot Intergalactic Medium

**XLF** X-ray luminosity function

**XRB** X-ray Binary

**XSPEC** X-ray Spectral Fitting Package

**ZAMS** Zero Age Main Sequence

# **Part I**

## **Introduction**



# 1 | Galaxy evolution in a nutshell

## 1.1 Galaxies in cosmology

In the standard cosmological picture, galaxies represent the transition point of hierarchical structure formation from the birth of the first stars towards the assembly of galaxy clusters as the largest gravitationally bound and virialized structures in the universe. Galaxies are themselves gravitationally bound objects consisting of stars, gas and dust, and vast amounts of a so-called dark matter component. They have been instrumental in unveiling key aspects of the evolution and buildup of our universe as well as astrophysical processes governing this evolution. For instance, distance measurements to nearby galaxies using Cepheid variable stars revealed that they have recession velocities increasing with distance which is due to an inherent expansion of the universe following Einstein's theory of general relativity (Hubble, 1929; Lemaître, 1931, 1933). The associated redshift of a galaxy,  $z$ , is a cosmological quantity which is the relative shift of the observed wavelength  $\lambda_{\text{obs}}$  of a photon compared to its restframe wavelength  $\lambda_{\text{rest}}$  which arises from the apparent expansion of space in which photons are traveling

$$z = \frac{\lambda_{\text{obs}} - \lambda_{\text{rest}}}{\lambda_{\text{rest}}}. \quad (1.1)$$

In fact, distance measurements of galaxies at higher redshift using Supernovae (SNe) of type Ia not only confirmed this view but revealed an accelerated expansion of space due to an unknown energy component (dark energy) acting as a negative pressure counteracting gravity at large scales (Riess et al., 1998; Perlmutter et al., 1999).

The distribution of galaxies in 3D space is fundamentally connected to cosmology. It is highly sensitive to the energy content of the universe and is specifically targeted in recent observational campaigns such as the Sloan Digital Sky Survey (SDSS) or EUCLID (see Fig. 1.1 Kollmeier et al., 2019). The apparent shape of this Large Scale Structure (LSS) is often called the cosmic web due to its characteristic appearance. It emerges from the initial density fluctuations in the almost homogeneous and isotropic early universe by exciting acoustic waves in the primordial plasma where baryons and photons were coupled together through Thomson scattering (see e.g. Weinberg, 1972). These fluctuations can still be appreciated today as tiny deviations ( $\delta T \sim 10^{-5}$ ) on top of a relic thermal radiation coming from the epoch of decoupling between matter and radiation at  $z \sim 1100$  (see Fig. 1.2). This radiation otherwise appears as a perfect black body spectrum with its peak in the microwave band and a temperature of  $T \approx 2.73 \text{ K}$  today, for which it is thus called the Cosmic Microwave Background (CMB) (see Penzias & Wilson, 1965, for initial

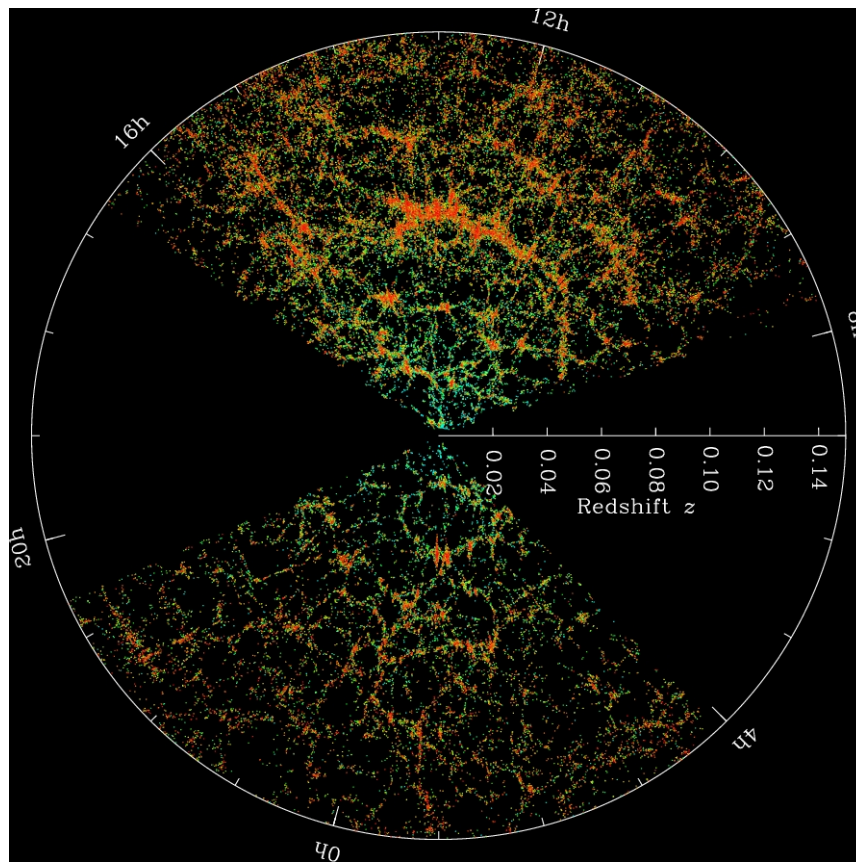


Figure 1.1: The position and distribution of galaxies as determined by SDSS out to a redshift of  $z \approx 0.14$ . The dark wedges in the figure coincide with the galactic plane of the Milky Way where no reliable measurements of galaxy positions can be made. Each point corresponds to a single galaxy with the color indicating the galaxy number density at its location with red being higher density. Credits: <https://www.sdss4.org>

discovery). The apparent homogeneity in the radiation field means that different regions of the sky were in causal contact and could equilibrate temperature differences. A possible explanation for the initial density fluctuations is given by a period of rapid expansion before decoupling such that initial quantum fluctuations in the density field were frozen and expanded in size in the so-called inflationary period.

The collapse of fluctuations into large-scale structures that can be observed today is fueled by the presence of a non-baryonic matter component that only seems to interact gravitationally, namely Dark Matter (DM) (Weinberg, 1972). The term was coined from observations of clusters of galaxies which seemed to require vast amounts of an unseen matter component to explain the observed velocity dispersion of galaxies moving within the cluster potential (Zwicky, 1933). The necessity for a Cold Dark Matter (CDM) component became more obvious to explain various observations for which baryonic matter alone is not sufficient, i.e. in dynamical modeling of galaxies and their rotation curves (Rubin et al., 1980), gravitational lensing experiments (see e.g.

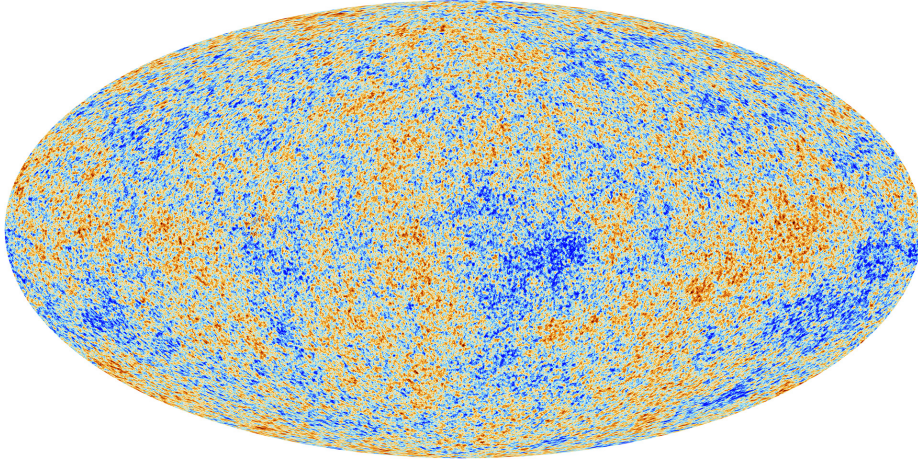


Figure 1.2: The intensity of the cosmic microwave background radiation as measured by the PLANCK satellite after correction for peculiar motions of the observer with respect to the CMB (Planck Collaboration et al., 2020). Colors indicate hotter (red) or colder (blue) regions in the CMB compared to a perfect black body spectrum with an average temperature of 2.73 K. *Credits: ESA and the Planck Collaboration.*

Massey et al., 2010) or for X-ray emitting gas atmospheres of galaxies and clusters of galaxies (see e.g. Sarazin, 1988; Fabbiano, 1989). Cold in this context means that DM had non-relativistic velocities at the moment of decoupling. Up to today, the true nature of dark matter is still debated (Arbey & Mahmoudi, 2021).

Through cross-correlation of the angular distribution of temperature fluctuations in the CMB, it is possible to derive a power spectrum of fluctuations on different length scales. Peaks in the power spectrum result from contraction and rarefaction of the acoustic waves in the primordial plasma before decoupling and provide an independent measurement of the energy content of the early universe due to the relative height and position of the peaks (see Fig. 1.3 Komatsu et al., 2011; Planck Collaboration et al., 2020). From both, the spatial distribution of galaxies and the CMB, we arrive at the current best description of the universe through flat  $\Lambda$ CDM, where  $\Lambda$  stands for a cosmological constant associated with accelerated expansion and flat meaning a geometrically flat Euclidean space. In this framework, smaller overdensities collapse first and build larger structures through merging leading to a "bottom-up" hierarchical structure formation.

The standard equation describing the dynamic evolution with redshift of a flat  $\Lambda$ CDM universe can be derived from the Friedmann-Lemaître-Robertson-Walker (FLRW) metric in general relativity assuming no intrinsic curvature and depends on the energy content of the universe

$$H(z) = H_0 \sqrt{\Omega_{m,0}(1+z)^3 + \Omega_{r,0}(1+z)^4 + \Omega_{\Lambda,0}}, \quad (1.2)$$

where  $\Omega_0 = \rho_0/\rho_{\text{crit},0}$  is the density of each component at  $z = 0$  for the critical density  $\rho_{\text{crit},0} = \frac{3H_0^2}{8\pi G} \simeq 1.878 \cdot 10^{-29} h^2 \text{ g cm}^{-3}$ , with  $\Omega_{m,0}, \Omega_{r,0}$  and  $\Omega_{\Lambda,0}$  being the matter, radiation and dark energy densities, respectively, and

$$H_0 = h \cdot 100 \text{ km s}^{-1} \text{ Mpc}^{-1}$$

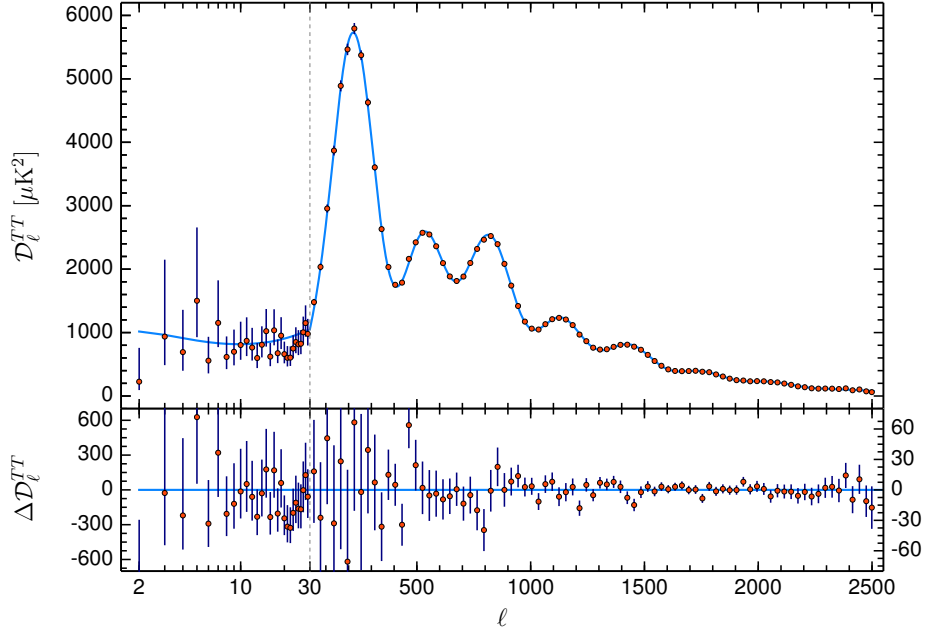


Figure 1.3: The temperature-temperature (TT) angular power spectrum as measured by the PLANCK satellite (Planck Collaboration et al., 2020). Red dots with errorbars are the data measured by PLANCK, and the blue line is the best-fit model assuming a flat  $\Lambda$ CDM cosmology with cosmological constant  $\Omega_\Lambda = 0.6889 \pm 0.0056$  matter density  $\Omega_m = 0.3111 \pm 0.0056$ , baryon density  $\Omega_b h^2 = 0.02242 \pm 0.00014$  and dark matter density  $\Omega_{\text{dm}} h^2 = 0.11933 \pm 0.00091$ . The lower panel shows the relative error between data and the best-fit model.

the Hubble parameter quantifying the current expansion rate of the universe with the numerical value  $h \approx 0.672$  (Planck Collaboration et al., 2020). Here,  $\Omega_m$  contains both DM ( $\Omega_{\text{dm}}$ ) and baryonic matter ( $\Omega_b$ ). Their ratio is the cosmic baryon fraction  $f_b = \frac{\Omega_b}{\Omega_m}$ .

The comoving distance between two observers at rest in an expanding space is always the same and is given by

$$\mathcal{D}_C = c \int_0^z \frac{dz'}{H(z')}, \quad (1.3)$$

where  $c$  is the speed of light. The energy flux  $F$  of radiation coming from a source with intrinsic luminosity  $L$  can be related through the luminosity distance

$$F = \frac{L}{4\pi \mathcal{D}_L^2}, \quad (1.4)$$

which for a flat  $\Lambda$ CDM universe yields

$$\mathcal{D}_L = (1+z)\mathcal{D}_C. \quad (1.5)$$

For an extended source of physical size  $b$ , we measure an angular size  $\theta$  by defining the angular diameter distance

$$\theta = \frac{b}{\mathcal{D}_A}, \quad (1.6)$$

where  $\mathcal{D}_A$  is related to the other distance measurements through

$$\mathcal{D}_A = (1+z)^{-1} \mathcal{D}_C = (1+z)^{-2} \mathcal{D}_L, \quad (1.7)$$

assuming a spatially flat spacetime. For the current model of  $\Lambda$ CDM,  $\mathcal{D}_A$  peaks at a redshift  $z \simeq 1.5$  and declines for higher redshifts. This means that objects appear to increase in angular size at higher redshift.

## 1.2 Assembly of galaxies

– This section is based on the textbook by [Cimatti et al. \(2020\)](#) if not noted otherwise

Initially, small perturbations in the DM density field evolve linearly, where their growth is coupled to the expansion rate. If the perturbation reaches a sufficient density contrast, it enters the non-linear regime where DM particles will collapse into a virialized halo. Since DM is considered collisionless, the collapse is governed by two relaxation processes: (i) *violent relaxation* where orbital energy is redistributed in a time-varying gravitational potential ([Lynden-Bell, 1967](#)), (ii) *phase mixing* where orbits tend to spread in phase space ([Binney & Tremaine, 2008](#)). At the time of virialization, the halo will have achieved equipartition in kinetic and potential energy, such that  $E_{\text{kin}} = -\frac{E_{\text{pot}}}{2}$ . Assuming a homogeneous sphere, one arrives at the virial mass  $M_\Delta$  enclosed in a radius  $r_\Delta$  around the overdensity

$$M_\Delta = \frac{4\pi}{3} \Delta_c \rho_{\text{crit}} r_\Delta^3, \quad (1.8)$$

with reference overdensity<sup>1</sup>  $\Delta_c \simeq 101 - 178$  between  $z = 0$  and  $z \gtrsim 5$  for a flat  $\Lambda$ CDM cosmology and critical density  $\rho_{\text{crit}}$ . In reality, dark matter halos are not homogeneous spheres but have density profiles broadly following a Navarro-Frenk-White (NFW) profile ([Navarro et al., 1996](#)) with embedded additional subhalos<sup>2</sup> and can have ellipsoidal shapes.

Simultaneously, the ambient primordial gas undergoes gravitational collapse within the growing DM halos, provided that the internal pressure of the accreting gas does not prevent further collapse. Because the infalling gas is collisional, it is expected to be shock heated to virial temperature  $T_{\text{vir}}$  during infall either at the halo center or through impact with gas already present

<sup>1</sup>The exact redshift dependence of the virial reference density is  $\Delta_c(z) = 18\pi^2 + 82y - 39y^2$  where  $y = \Omega_m(z) - 1$  ([Kravtsov & Borgani, 2012](#)). Typically, if the redshift-dependent virial parameters are being referenced, one writes  $M_{\text{vir}}, R_{\text{vir}}$ . If  $\Delta_c$  is chosen constant, the exact number is used as subscript, i.e.  $R_{200}, M_{200}$ .

<sup>2</sup>Smaller dark matter halos orbiting within larger halos.

within the halo (Birnboim & Dekel, 2003). Under the assumption of hydrostatic equilibrium<sup>3</sup> and isothermal conditions,  $T_{\text{vir}}$  of a halo can be expressed as a function of the virial mass  $M_{\text{vir}}$

$$T_{\text{vir}} \simeq 6 \cdot 10^5 \left( \frac{M_{\text{vir}}}{10^{12} M_{\odot}} \right)^{\frac{2}{3}} \left( \frac{h}{0.7} \right)^{\frac{2}{3}} \text{ K}. \quad (1.9)$$

Therefore, the accreted gas has to cool efficiently, to allow for continued collapse and eventual triggering of star formation. In particular, the cooling time  $t_{\text{cool}}$  and the dynamical time  $t_{\text{dyn}}$  have been identified play an important role in galaxy evolution (Binney, 1977; Rees & Ostriker, 1977; Silk, 1977; White & Rees, 1978). The radiative cooling time is dependent on the density and the cooling rate  $\Lambda$  of the gas

$$t_{\text{cool}} \approx \frac{3 (n_p + n_e) k_B T}{2 n_p n_e \Lambda(T, Z)}, \quad (1.10)$$

where  $T$  is the temperature,  $k_B$  is the Boltzmann constant,  $n_p$ ,  $n_e$  are the proton and electron number densities of the plasma, respectively, and  $Z$  is the metallicity with respect to solar abundance. We will give a more detailed description of the cooling rate in Sec. 1.3. The dynamical time is equivalent to the free-fall time of the gas

$$t_{\text{dyn}} \equiv \sqrt{\frac{1}{G\rho}}. \quad (1.11)$$

Taking both timescales into account two accretion regimes can be differentiated: (i) *cold accretion* occurs when  $t_{\text{cool}} < t_{\text{dyn}}$  where shocked gas cools rapidly decreasing thermal pressure and leading to clumping or the formation of thin filaments; (ii) *hot accretion* when  $t_{\text{cool}} > t_{\text{dyn}}$ , shocked gas is maintained longer in the halo potential by thermal pressure and is accreted gradually (see also review by Faucher-Giguère & Oh, 2023).

Realistically, the collapsing gas is already subjected to cooling processes before infall and the gas within a halo is not isothermal. As a result, the ratio of  $t_{\text{cool}}/t_{\text{dyn}}$  is a function of radius such that the outer halo gas is virialized first since  $t_{\text{cool}}/t_{\text{dyn}} > 1$ , while the inner halo gas may rapidly cool ( $t_{\text{cool}}/t_{\text{dyn}} < 1$ ) and reach virialization much later (Stern et al., 2020).

### 1.2.1 Star formation and Quenching

In the inner halo, the gas density is high and the temperature is low ( $T < 10^4$  K) such that most atoms are no longer ionized which forms the basis of the interstellar medium (ISM). From the gravitational collapse of the halo, angular momentum is imparted onto the baryonic component through tidal torques (Peebles, 1969; Mo et al., 2010). Through dissipative collapse, the gas loses energy through radiative processes while conserving angular momentum which facilitates the formation of a disc (Fall & Efstathiou, 1980). Within the atomic gas disc, gravitational instabilities and the development of spiral structures lead to the fragmentation of the ISM into cold clouds with much higher density compared to the ambient ISM.

<sup>3</sup>Force balance between the internal pressure gradient of the gas and gravity.

Fueled by these high densities, molecules start forming in cold clouds. Those molecules then enable further efficient cooling through collisional excitation and radiative de-excitation of their rotational and vibrational modes. Eventually, temperatures fall below  $T \lesssim 30$  K in the now molecular cold clouds whose further collapse can be described by the Bonner-Ebert solution (Ebert, 1955; Bonnor, 1956) and happen on the free-fall timescale  $\propto t_{\text{dyn}}$  (Eq. (1.11)). Magnetic fields within the contracting cloud transfer angular momentum from the core to the outskirts through magnetic braking, ultimately leading to the cloud's total collapse to form a star. The exact fragmentation of the molecular cloud typically leads to the formation of entire clusters of stars where most stars have multiple companion stars (see e.g. Moe & Di Stefano, 2017; Offner et al., 2023, for a census on multiplicity in stars).

The number distribution  $dN$  of newly formed stars in a given mass range  $dm$  can be described by an Initial Mass Function (IMF)  $\phi(m)$  (Salpeter, 1955; Chabrier, 2003) with typical power-law shapes

$$dN = \phi(m)dm = \phi_0 m^{-2.35} dm, \quad (1.12)$$

as given e.g. for a Salpeter IMF, with  $m$  in units of solar masses  $M_\odot$ . Stars evolve along the main sequence of the Hertzsprung-Russell-Diagram (HRD) given their effective temperature and luminosity where their time on the main sequence is determined by the nuclear-burning timescale of hydrogen fusion (see Eq. (3.1), and Sec. 3.2.1). Massive stars and stars near the end of their life have favorable conditions in their cores to facilitate the production of chemical elements heavier than helium (often referred to as "metals") and part of their mass is returned to the ISM through stellar winds, SN explosions or at the planetary nebulae phase.

Due to the vast amount of energy released by SNe, galactic winds can be launched which transport enriched gas back to the surrounding circum-galactic medium (CGM)<sup>4</sup> (Tumlinson et al., 2017; Faucher-Giguère & Oh, 2023). Therefore, the effective change of gas mass within the ISM is governed by the mass exchange between the CGM and ISM while accounting for the Star-Formation Rate (SFR)

$$\frac{dM_{\text{gas}}}{dt} = \dot{M}_{\text{acc}} - \dot{M}_{\text{out}} + \dot{M}_{\text{ret}} - \text{SFR}, \quad (1.13)$$

where  $\dot{M}_{\text{acc}}$  is the gas accretion from the CGM,  $\dot{M}_{\text{out}}$  is the outflow from the ISM,  $\dot{M}_{\text{ret}}$  is the mass returned to the ISM through stellar evolution and SFR are of the order  $\text{SFR} \approx 0.1 - 10 M_\odot \text{ yr}^{-1}$  in normal Star-Forming Galaxies (SFG).

In this self-regulated system of star-formation, some fundamental properties of SFG arise such as the star-forming main sequence of galaxies which relates the galaxy stellar mass to its SFR<sup>5</sup> (Elbaz et al., 2007; Pearson et al., 2018) or galaxy stellar mass metallicity relations which show that more massive galaxies have higher total metallicities as a consequence of the metal enrichment from stellar evolution (Zahid et al., 2017). From Eq. (1.13), it is evident that SFR is sensitive to the availability of cold gas in the ISM while it is being depleted on rather short

<sup>4</sup>The virialized gas from which the ISM formed initially

<sup>5</sup> $\text{SFR} \propto \left( \frac{M_*}{10^{11} M_\odot} \right)^\alpha$ , with  $\alpha \approx 0.6 - 1$  depending on sample selection and redshift.

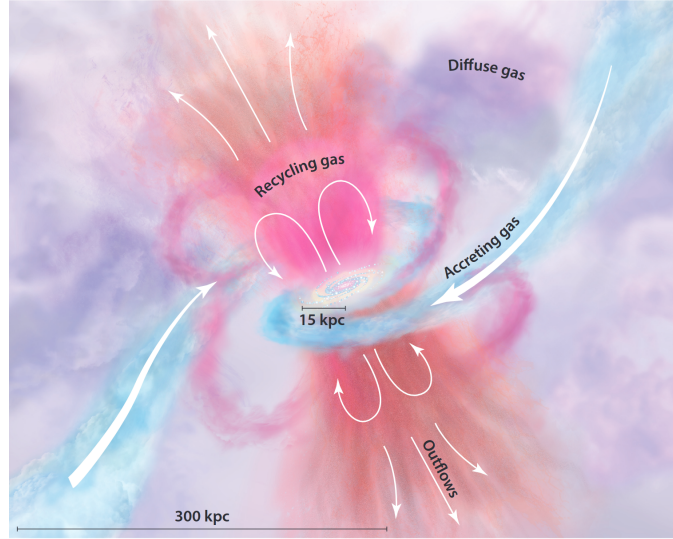


Figure 1.4: Illustration of a galaxy’s CGM. The galaxy at the center of the image is fed by filamentary accretion from the intergalactic medium (blue) and galactic outflows emerge perpendicular from the disc (pink, orange). Previously ejected gas is recycled and the diffuse gas (purple) is likely a mixture of all components. Figure is directly taken from (Tumlinson et al., 2017).

timescales

$$t_{\text{depl}} = \frac{M_{\text{gas}}}{\text{SFR}} \lesssim 1 \text{ Gyr}. \quad (1.14)$$

Thus, present-day SFG must have had continued accretion from their surrounding CGM to sustain star formation for a long time. The mass exchange between the ISM and CGM is a complex interplay between accretion flows of cooling gas from the hot halo onto the central galaxy and the hot outflows of the central galaxy induced by stellar feedback and feedback from an active Super Massive Black Hole (SMBH) at the center of the galaxy. Observations have shown that the CGM indeed can host a cold component at temperatures lower than  $T_{\text{vir}}$  which makes the CGM multiphase (Tumlinson et al., 2017). This cold gas can form either through precipitation (Donahue & Voit, 2022) or buoyant cold clouds which were lifted from the ISM through galactic winds (Faucher-Giguère & Oh, 2023). In Fig. 1.4 we show an impression of the gas structures around a Milky Way (MW) analog star-forming disc galaxy. It is derived from observational as well as theoretical results and reflects the current understanding of galaxy formation (Tumlinson et al., 2017). Nevertheless, if star formation can not be sustained, the galaxy will fall below the main sequence and be considered a Quiescent Galaxy (QG).

The sustainability of star-formation is also a function of halo mass because above a certain critical mass  $M_h \gtrsim 10^{12} M_{\odot}$  the virialized hot gas atmosphere becomes more efficient in assimilating accretion streams with  $T < T_{\text{vir}}$  from outside the halo through turbulent mixing and thermal conduction processes. If a gas-rich satellite galaxy is being accreted its cold gas is disrupted by the hot atmosphere of the larger halo through tidal and ram-pressure stripping before finally

merging with the halo. Similarly, satellite galaxies can be quenched from their orbits within the hot atmosphere of their central galaxy. Again through tidal interactions and ram-pressure stripping, the CGM of the satellite is incorporated into the atmosphere of the central galaxy effectively starving the satellite on longer timescales. (see chapter 10.6 in [Cimatti et al., 2020](#))

For a halo to maintain the hot gas atmosphere, a mechanism to stop it from cooling is needed, especially in the center where higher densities would amplify cooling. In large halos, an efficient way to stop central cooling is feedback from an actively accreting SMBH (or Active Galactic Nucleus (AGN)) at the center of a galaxy. Cooling gas flowing towards the center of the halo triggers accretion onto the SMBH which in turn releases energy to its surroundings, reheating the gas. In smaller halos with a QG at the center, Type Ia SNe from the old stellar populations may already be sufficient to maintain the hot gas atmosphere (see e.g. [Voit et al., 2015a](#)). Additionally, negative feedback from excessive star formation bursts or galaxy mergers affects the central gas of a galaxy and may remove large fractions of the available cold gas. During the merger of two gas-rich disk galaxies, compression and tidal interaction of the gas results in intense star formation in the center and enhanced accretion onto the central SMBH. The sudden amplification of energy feedback may completely disrupt the star-forming gas and eject it from the central galaxy through strong galactic winds.

## 1.3 Cooling of astrophysical gas

An efficient mechanism by which an astrophysical gas can be cooled is through radiative processes. Emitted photons carry away energy that reduces the internal energy of a thermal gas. In the context of galaxy evolution, gas surrounding galaxies can be considered optically thin such that radiation can escape from the system and is not reabsorbed by the same gas. A critical temperature for radiative cooling is given by the ionization limit of hydrogen ( $T \approx 10^4$  K). Above this critical temperature, most radiative processes occur through the interaction of partly or fully ionized atoms with free electrons in the gas:

### (i) *Thermal Bremsstrahlung (free-free)*

Free electrons deflect off of charged ions. The velocity change caused by the deflection produces radiation whose energy depends on the ion charge and the impact parameter of the electron. In the statistical limit, the spectrum of many encounters becomes continuous, and, assuming thermally distributed electrons, can be described as

$$\varepsilon_{\text{ff}}(E, T, Z) \approx 5.44 \cdot 10^{-41} g_{\text{ff}} Z_i^2 \left( \frac{n_e n_i}{\text{cm}^{-6}} \right) \left( \frac{T}{10^4 \text{ K}} \right)^{-\frac{1}{2}} \exp \left\{ - \left( \frac{E}{k_B T} \right) \right\} \text{ erg s}^{-1} \text{ cm}^{-3} \text{ sr}^{-1} \text{ Hz}^{-1}, \quad (1.15)$$

where  $n_e$  and  $n_i$  are electron and ion density, respectively,  $Z_i$  is the ion charge,  $k_B$  is the Boltzmann constant, and  $g_{\text{ff}} \approx 1$  is the dimensionless Gaunt factor which has a weak dependence on temperature  $T$  and photon energy  $E$ .

**(ii) Radiative recombination (free-bound)**

In this process, a free electron is captured by a charged ion. The recombination of the electron and the ion forms a less ionized or fully neutral atom which releases photons with energy according to the quantum energy levels of the specific ion. The specific line emission of this process can be thermally broadened due to the thermal motion of the atoms. Additionally, line emission can broaden from a turbulent velocity dispersion in the gas.

**(iii) Radiative de-excitation (bound-bound)**

Electrons bound to a neutral atom or ion emit photons at specific energies when they transition from a higher to a lower energy level.

The expression of these radiative cooling processes is set by the physical conditions affecting the gas where two main regimes can be identified. In the collisional ionization regime, atoms are ionized by collisions with free electrons while in the photoionization regime, atoms are ionized from radiation of an external source such as the UV or X-ray background (Dopita & Sutherland, 2003; Wiersma et al., 2009; Khabibullin & Churazov, 2019). In equilibrium, the rate of ionization is perfectly balanced by recombination and several numerical codes try to solve either Collisional Ionization Equilibrium (CIE), for instance Mewe-Gronenschild-Kaastra-Liedahl (MEKAL) (Kaastra & Mewe, 1993) or Astrophysical Plasma Emission Code (APEC) (Smith et al., 2001), or Photo-Ionization Equilibrium (PIE), e.g. CLOUDY (Ferland et al., 1998, 2013, 2017; Chatzikos et al., 2023).

By combining the various radiative processes and integrating over the whole frequency range, one arrives at the radiative cooling function  $\Lambda(T, Z)$ . In Fig. 1.5 we show  $\Lambda(T, Z)$  as a function of temperature and total gas metallicity as determined by Sutherland & Dopita (1993) for a gas in CIE. In the temperature range between  $4.5 \leq \log T [\text{K}] \leq 7$ , the cooling function strongly depends on metallicity due to line emission from the excitation of various metal species. Above  $\log T [\text{K}] \geq 7.5$ , bremsstrahlung radiation is the most dominant process and very few emission lines contribute to the cooling function. In both cases, a large fraction of the energy is released in the form of far UV or X-ray radiation. The exact composition of the cooling function assuming solar metal abundance and CIE is shown in Fig. 1.6.

Below the critical temperature ( $T < 10^4$  K) gas no longer cools efficiently through radiation because electrons can no longer excite transition in hydrogen or helium. While high metallicities can still contribute to radiative cooling due to low excitation energy in some ions (see e.g. Smith et al., 2008), cooling mainly occurs through molecules. In systems where both hot and cold gas are present, the UV and X-ray radiation of the hot component is absorbed by the cold component again through radiative excitation (Morrison & McCammon, 1983; Wilms et al., 2000). The same is true for cold material between the source and the observer such that for very high column densities in the line of sight, only the most energetic photons can reach an observer. The extinction caused by an absorbing agent in the line of sight to a source is of the form

$$I'(E) = I(E) \exp(-\sigma(E) N_H), \quad (1.16)$$

where  $I(E)$  is the intensity of the source,  $\sigma(E)$  is the absorption cross-section per hydrogen atom, and  $N_H$  is the equivalent column density of neutral hydrogen which acts as a proxy for the

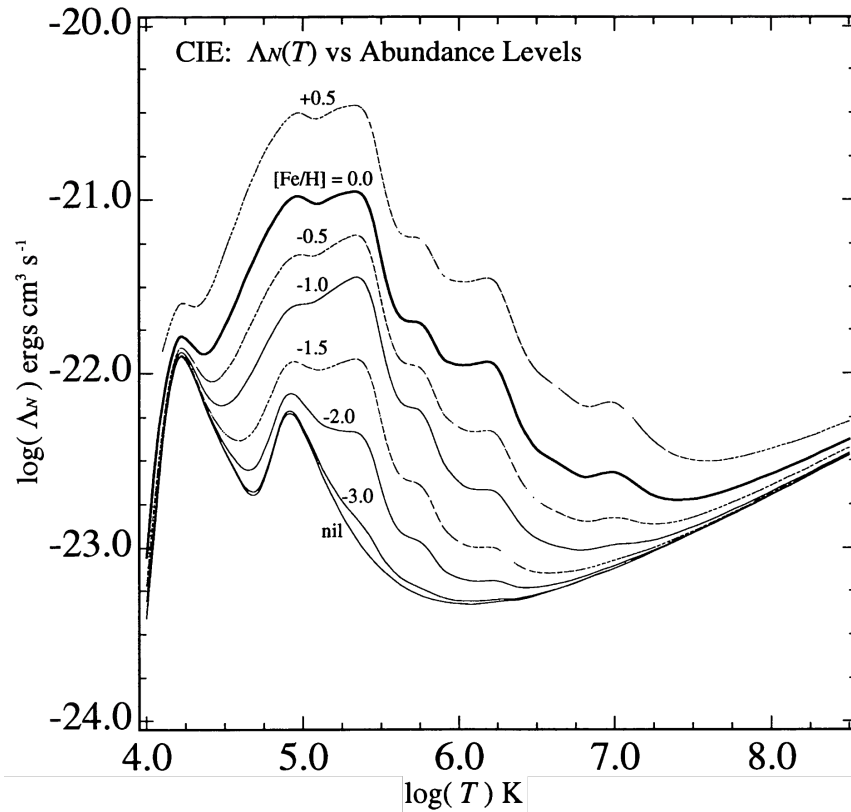


Figure 1.5: The cooling function  $\Lambda$  as a function of temperature for a plasma in Collisional Ionization Equilibrium (CIE). Additionally, the metallicity dependence as traced by the iron abundance  $[\text{Fe}/\text{H}]$  is shown. For temperatures between  $4.5 \leq \log T/\text{K} \leq 7$ , the cooling function strongly depends on metallicity, mainly due to emission lines from recombination. For temperatures higher than  $\log T/\text{K} \geq 7.5$  metallicity is not important and the shape of the cooling function is mostly determined by thermal bremsstrahlung radiation. Adapted from Fig.8 in [Sutherland & Dopita \(1993\)](#).

amount of cold material in the line of sight (see e.g. [Wilms et al., 2000](#)). Absorption is especially problematic for observations in the far UV and soft X-ray wavelength regimes since the cold gas effectively reduces the number of available photons even to the point of non-detection.

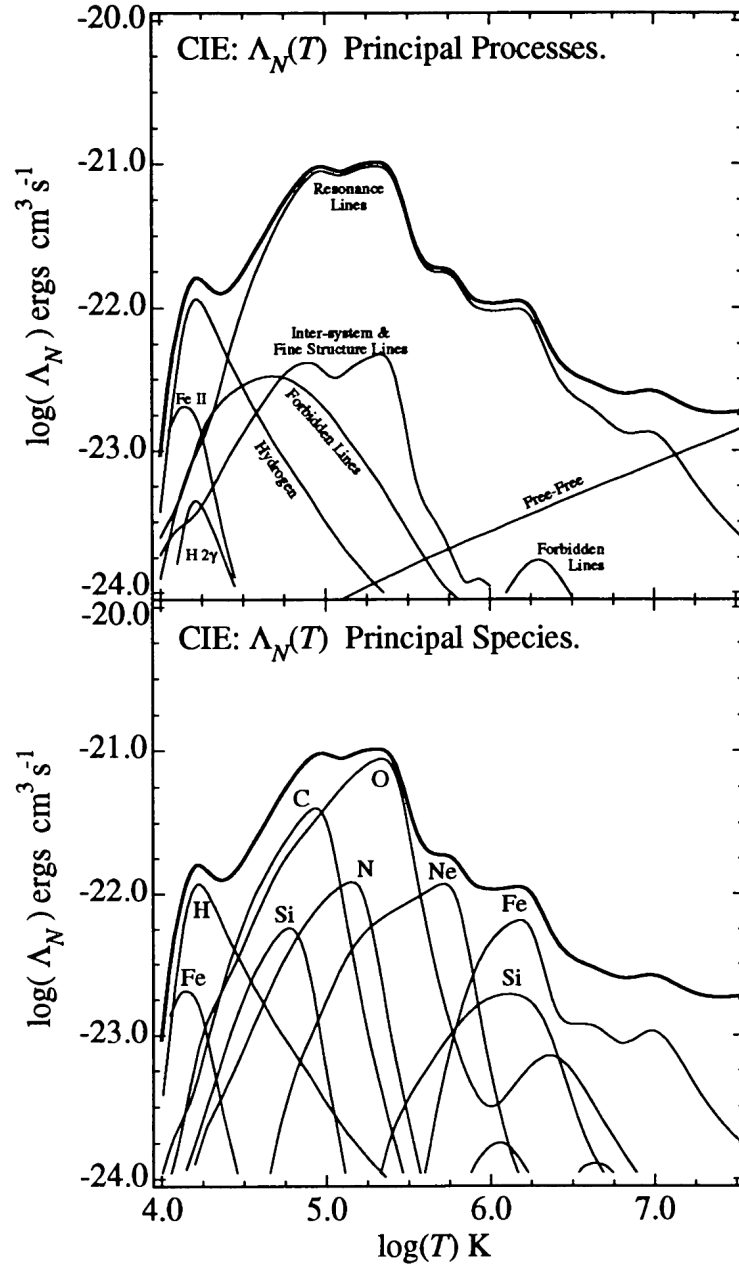


Figure 1.6: Composition of the cooling function  $\Lambda(T, Z)$  as a function of temperature at solar abundance  $Z = Z_{\odot}$ . The top panel shows the most important processes responsible for cooling, the lower panel shows the most important metal species contributing to the cooling function both assuming Collisional Ionization Equilibrium (CIE). For the temperature regime shown here, the most dominant cooling process occurs from resonant lines (free-bound or bound-bound). Adapted from Fig. 18 in (Sutherland & Dopita, 1993).

## 2 | X-ray observations of galaxies

Many of the physical processes in galaxy formation result in the emission of highly energetic photons facilitating the cooling of astrophysical plasmas, as described by the cooling function (see Sec.1.3). The hot gas in and around galaxies has temperatures and densities such that thermal Bremsstrahlung and recombination are the most dominant factors describing the cooling function. In figure 2.1 we show the X-ray spectral energy distribution (SED) of thermal plasma in CIE at 0.3 solar abundance for two temperatures close to the virial temperature of a MW-like galaxy ( $M_{\text{vir}} \simeq 10^{12} M_{\odot}$ ), namely  $k_b T = 0.3 \text{ keV}$  and  $k_B T = 0.9 \text{ keV}$ . The main features of the spectrum are the exponential decline at high energies and emission lines at the transition levels of different ion species. The shape of the continuum is characterized by the temperature, according to Eq.(1.15), and the prominence of emission lines by the ionization balance which is temperature dependent. Characteristic for these temperatures is the forest of lines at  $\sim 1 \text{ keV}$  photon energies produced by the Fe-L shell transitions and the OvII and OvIII lines at 0.574 keV and 0.654 keV, respectively (see e.g. [Smith et al., 2001](#)). The normalization of the spectrum is given by the emission measure

$$E.M. = \int n_e n_H dV, \quad (2.1)$$

where  $n_e$  and  $n_H$  are the electron and hydrogen density, respectively, integrated over the occupied volume  $dV$ . Since the emissivity of these hot plasmas is also dependent on their density, the radial distribution of the emission can be used to construct density and temperature profiles (see e.g. [Sarazin, 1988](#)). Those profiles can then give insight into the state of the plasma at different distances from the galaxy center and reveal substructures either from shocks or mergers within the galactic environments. Therefore, X-ray observations are a useful tool for giving insights into various aspects of structure formation.

Although observational X-ray astronomy is relatively young compared to other fields, significant progress has been made at the turn of the millennium. Starting with the first extrasolar discovery of the brightest X-ray source in the sky, *Scorpius X-1* (Sco X-1) ([Giacconi et al., 1962](#)), subsequent observational campaigns have revealed more X-ray sources with dedicated surveys. The first X-ray sky survey was conducted between 1970 and 1973 by the *SAS-A Uhuru* satellite ([Giacconi et al., 1971](#)) which identified 338 sources in the sky ([Forman et al., 1978](#)) in the energy range of 2-20 keV. By the end of the 1970s, another X-ray experiment installed on the HEAO-1 observatory ([Rothschild et al., 1979](#)), resulted in the identification of 842 X-ray sources in the energy range of 0.25-25 keV ([Wood et al., 1984](#)). Its successor, the *Einstein* (HEAO-2) observatory

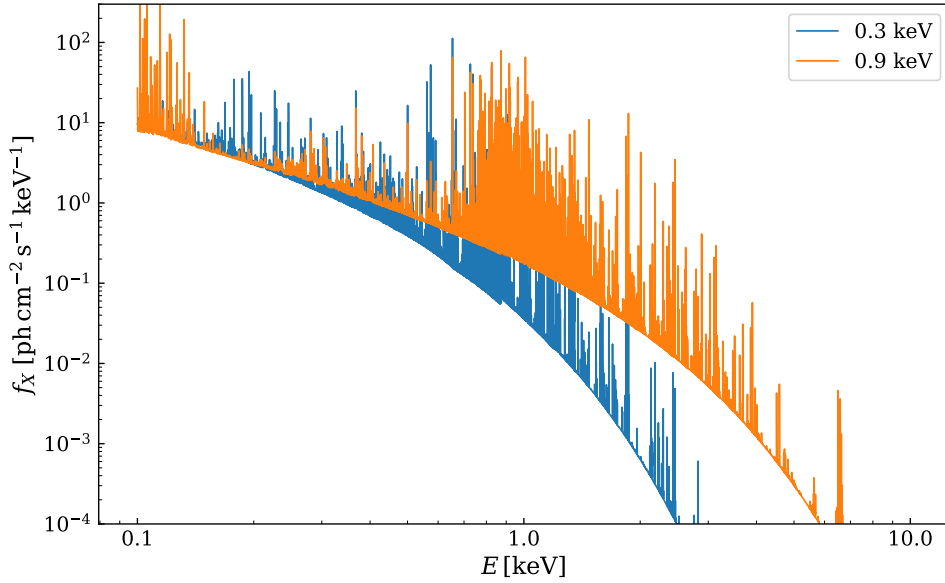


Figure 2.1: Spectra of two X-ray emitting plasmas in CIE at 0.3 solar metallicity for temperatures  $k_B T = 0.3$  keV (blue) and  $k_B T = 0.9$  keV (orange). Spectrum normalization is set to one.

(Giacconi et al., 1979), surveyed a third of the sky between 1979 and 1981 and led to the discovery of more than 4000 X-ray sources (Harris, 1990) and a diffuse X-ray background in the 0.5-3.5 keV energy range. A major step in advancing X-ray astronomy came with the ROSAT X-ray observatory which operated between 1990 and 1999 (Truemper, 1982). The ROSAT mission achieved much higher sensitivities compared to previous surveys and revealed more than  $10^5$  sources within its first six months of operation. For the first time, a detailed scan of the X-ray sky in the soft energy regime from 0.1-2.4 keV was available after the completion of the ROSAT all-sky survey (RASS) which allowed population studies on X-ray properties of galaxies.

The launch of the *Chandra* X-ray observatory on 23rd of July 1999 from NASA changed the X-ray landscape forever and the telescope is still operational to this date although at lower efficiency (Weisskopf et al., 2000). Its unprecedented spatial resolution of  $\sim 0.45''$  and an energy range of 0.1-10 keV compensate for its narrow field of view and allow for detailed studies of extragalactic sources. Particularly with its deep field observations, *Chandra* provided a profound understanding of the X-ray morphology and redshift evolution of X-ray properties in distant galaxies (Aird et al., 2017). It also provided direct evidence for the presence of compact X-ray sources in external galaxies (Grimm et al., 2003; Gilfanov, 2004; Remillard & McClintock, 2006) and solidified our understanding of the Cosmic X-ray Background (CXB) as being made up of X-ray bright point sources at high redshift (Hickox & Markevitch, 2006; Gilli et al., 2007; Georgakakis et al., 2008). Other X-ray telescopes that were pivotal in the study of compact X-ray sources are, e.g. XMM-Newton (Jansen et al., 2001) and NuSTAR (Harrison et al., 2013), which together provided coverage across a vast energy range of 0.5 – 80 keV deepening our understanding of accretion physics.

---

In the past 4 years, results from the extended ROentgen Survey with an Imaging Telescope Array (eROSITA) consortium revolutionized the field of X-ray astronomy and made it viable as a cosmological probe by providing a large sample of X-ray-detected galaxy clusters ( $> 10^5$ ). eROSITA is a wide-field focusing X-ray telescope array with a large effective area and field of view in the soft X-ray band (0.3-2.4 keV) and thus the nominal successor of ROSAT (Predehl et al., 2021). It is part of the Spectrum-Roentgen-Gamma (SRG) orbital observatory (Sunyaev et al., 2021) and has an angular resolution sufficient to reliably distinguish between AGN and galaxy clusters. Its observing strategy focused on completing several scans of the entire sky over 4 years, the eROSITA All-Sky Surveys (eRASSs) (see Merloni et al., 2024, for most recent data release). eROSITA performed a benchmark at 1.5 times the depth of the full 4-year all-sky program on a large area of the sky ( $140 \text{ deg}^2$ ). The so-called eROSITA Final Equatorial Depth Survey (eFEDS) field confirmed the capability of eROSITA to detect various classes of X-ray sources (Brunner et al., 2022) which were subsequently identified using other multi-wavelength surveys coinciding with the same field (see e.g. Liu et al., 2022a,b; Salvato et al., 2022; Vulic et al., 2022; Comparat et al., 2022).

Following the completion of the first scan of the sky, the eROSITA collaboration released the resulting image in galactic coordinates ( $l, b$ , center of the MW in the center of the image, see Fig. 2.2). Next to the most prominent X-ray sources in the sky, it also revealed many new extra-galactic sources and new insights for the MW. In particular, the North Polar spur shows enhanced X-ray emission compared to the background with intricate structure and associated radio emission and roughly situated perpendicular to the plane of the MW. It roughly coincides spatially with the Fermi bubbles detected in gamma rays (Su et al., 2010). A symmetric structure can be seen south of the galactic plane strengthening the hypothesis of a central engine. However, the structure's exact origin is still debated because of conflicting evidence concerning temperature and density contrasts between the ambient medium and the exact energetics involved. The coincidence with the Fermi bubbles suggests that past activity of the central SMBH, Sgr A\*, is responsible for the structures due to mechanical outflows from accretion events (Kataoka et al., 2021). However, the data permits different lines of interpretations, as pointed out by Churazov et al. (2024) who suggest outflows from star-forming regions near the center of the MW as a possible source. Such features have yet to be observed in other galaxies.

In the following sections, we will give an overview of X-ray observables in galaxies and focus specifically on properties connected to galaxy formation and evolution. In particular, we will introduce the main X-ray-emitting components of galaxies, namely the hot gas in the ISM and CGM, accreting SMBH, and the stellar component (e.g. young stars and active binaries), accompanied by important observational results. In part II, we will introduce a new model for X-ray post-processing cosmological hydrodynamical simulations including X-ray Binary (XRB) sources. Therefore, we give a more in-depth introduction to accretion-fueled XRB systems and their underlying physics in Chap. 3. Furthermore, we will highlight some connections to background and foreground contamination when observing galaxies in X-ray and which other processes need to be considered.

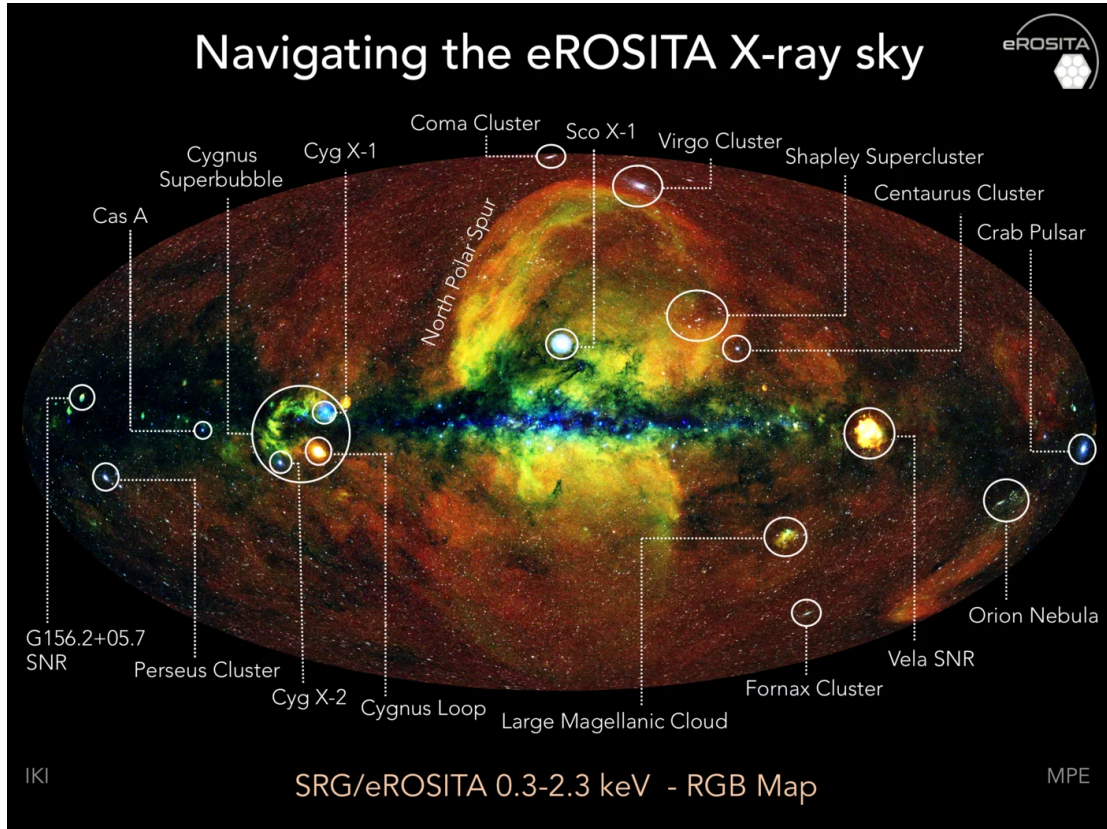


Figure 2.2: False color image of the eROSITA first all-sky survey with labels indicating famous X-ray sources in the sky. Color composition according to photon energies registered in each pixel (red: 0.3-0.6 keV, green: 0.6-1 keV, blue: 1-2.3 keV). Figure taken from the press release of the first eROSITA all-sky survey (<https://www.mpe.mpg.de/7461950/erass1-presskit>, last access: 15.09.2024). Credit: Jeremy Sanders, Hermann Brunner, Andrea Merloni, and the eSASS team (MPE); Eugene Churazov, Marat Gilfanov (on behalf of IKI)

## 2.1 Hot gas within and around Galaxies

Typically, the X-ray spectrum of galaxies is comprised of multiple components which can be classified into two main contributions (see e.g. [Persic & Rephaeli, 2003](#); [Lehmer et al., 2016](#)). One is directly associated with hot gas in the halo and is typically modeled assuming a single or two-temperature plasma model as described in Sec. 1.3 and 2.1. A power law with a photon index of  $\Gamma \sim 2$  typically describes the second component and mostly includes accretion-powered compact stellar sources or unresolved stellar sources which will be described in Sec. 2.3. If the spatial resolution of the instrument used for observations is high, point sources like accreting binaries can be extracted separately and masked for the remaining analysis. It is also common to exclude or mask the very central part of galaxies if they show spectral features of an AGN, i.e. when the galaxy center is bright in multiple energy bands or exceeds certain threshold luminosities in radio and X-ray.

### 2.1.1 The hot interstellar medium

Unambiguous detection of hot gas within a few effective radii of a galaxy has been achieved in multiple independent studies (see e.g. [Fabbiano, 2019](#), for a review). The first detections of a hot ISM in the form of outflows and galactic winds were performed using the *Einstein* observatory ([Fabbiano, 1989](#)). Subsequent studies with *Chandra* allowed for a much more detailed investigation of the hot ISM because contaminating point sources could be identified easily and removed both spatially and spectrally from the hot ISM emission.

While one expects to find very little virialized hot gas in the center of a SFG, the presence of a hot ISM is the result of shocks induced by stellar feedback. From the Rankine-Hugoniot jump conditions, the temperature increase of a medium is dependent on the shock velocity  $v_{\text{sh}}$  such that

$$T \simeq 1.4 \cdot 10^5 \left( \frac{\mu}{0.62} \right) \left( \frac{v_{\text{sh}}}{100 \text{ km s}^{-1}} \right)^2 \text{ K}, \quad (2.2)$$

where  $\mu$  is the mean atomic weight at solar metallicity. Stellar winds from massive stars reach velocities of  $\sim 10^3 \text{ km s}^{-1}$  (see e.g. [Kudritzki & Puls, 2000](#)) and supernova remnants (SNR) plow through the ISM with several  $100 \text{ km s}^{-1}$  such that part of the ISM can be collisionally ionized from those shocks. Thus, the X-ray luminosity of the ISM,  $L_X^{\text{ism}}$ , is correlated with SFR in SFG ([Ranalli et al., 2003](#); [O'Sullivan et al., 2003](#); [Strickland et al., 2004](#); [Mineo et al., 2012b, 2014b](#); [Lehmer et al., 2022](#)). Massive stars are short-lived (see Eq. (3.1)), thus, feedback from those massive stars can only be active following a recent star-formation event. Tracers of star-formation<sup>1</sup> probe SFR on timescales of  $\leq 100 \text{ Myr}$  therefore probing directly the short-term effects of massive stars on their environment. For higher SFR, more short-lived massive stars are being formed and release energy into the ISM through SNe type II. The amount of energy released from SN type II needed to maintain the central hot gas can be estimated from scaling relations and is of the order of  $\epsilon_{\text{SNII}} \sim 5\%$  ([Strickland & Stevens, 2000](#); [Strickland et al., 2004](#); [Mineo et al., 2012b](#)). Though higher efficiencies  $\epsilon_{\text{SNII}} \geq 30\%$  have been observed in individual star-burst galaxies such as M82 ([Strickland & Heckman, 2009](#)). Typical scaling relations between SFR and hot gas luminosity are

$$L_{X,\text{sf}}^{\text{ism}} \simeq 10^{39} \left( \frac{\text{SFR}}{\text{M}_{\odot} \text{ yr}^{-1}} \right) \text{ erg s}^{-1}, \quad (2.3)$$

which we show in the left panel of Fig. 2.3. However [Mineo et al. \(2012b\)](#) point out that the exact scaling is uncertain within a factor of a few because of differences in data reduction and model assumptions especially regarding intrinsic absorption from the cold ISM. [Lehmer et al. \(2022\)](#) also found that the  $L_X^{\text{ism}} - \text{SFR}$  relation is sensitive to the gas phase metallicity with higher luminosities in metal-rich galaxies. This is somewhat expected because of the metallicity dependence of the cooling function (see Fig. 1.5).

The hot ISM of QG was also discovered with the *Einstein* observatory, although it was unclear if these atmospheres were caused by the poor spatial resolution of Low-Mass X-ray Binaries (LMXBs) (see Ch. 3). Later investigations using ROSAT data found a linear increase of

<sup>1</sup>For example  $H\alpha$  or UV brightness

$L_X^{\text{ism}}$  with stellar mass<sup>2</sup> although the contribution from LMXBs was still only estimated empirically (Diehl & Statler, 2007). Since QG are characterized by an old stellar population, most of the mass input to the ISM is through late stellar evolution. In particular, this includes mass lost from the red giant, asymptotic giant branch, and planetary nebula phases of low-mass stars (Pellegrini, 2012). Additional mass is provided from the evolution of binary star systems which explode as type Ia SNe and provide a heating mechanism of the ambient ISM. Another important source of energy in keeping the ISM from cooling comes from the activity of the central SMBH (Ciotti & Ostriker, 2012). The exact timescales involved in balancing the precipitating cold gas in the outer hot halo and heating of the central halo of a QG are set by type Ia SNe and the SMBH (Voit et al., 2015b). It was therefore found using *Chandra* data of nearby QG that  $L_X^{\text{ism}}$  indeed scales with the stellar mass of its host galaxy

$$L_{X,\text{qu}}^{\text{ism}} \approx 10^{39} \left( \frac{L_K}{10^{11} L_\odot} \right)^{2.6} \text{ erg s}^{-1} \quad (2.4)$$

although on a steeper relation than previously found and large intrinsic scatter (Boroson et al., 2011). We show the corresponding scaling relation of the QG ISM in the right panel of Fig. 2.3 where typical scaling relations of LMXB (cyan) and other binaries (green) are also shown.

In this study, the contribution from point sources and nuclear emission could be properly accounted for thanks to the spatial resolution of *Chandra*. It was found, that  $L_X^{\text{ism}}$  in massive QG was correlated to the temperature of the hot ISM. This dependence is consistent with expectations for a virialized halo<sup>3</sup> such that  $L_X^{\text{ism}} \propto T_X^{4.5}$ , and depends on the dynamical state of the QG (Kim & Fabbiano, 2013, 2015; Forbes et al., 2017; Babyk et al., 2018).

### 2.1.2 The circum-galactic medium

From the assembly history of halos, all galaxies are expected to have an extended gaseous halo with temperatures close to the virial temperature. This so-called CGM hosts a large fraction of the baryon budget of each galaxy and it is thought that most of the baryonic matter resides in the warm-hot phase ( $\sim 10^6$  K) (Péroux & Howk, 2020, see e.g. review of). A successful technique to study the CGM has been through absorption spectroscopy, where the spectrum of background quasars are absorbed by the CGM of a galaxy in the quasar sightline. Absorption signatures have been found in the UV for gas at temperatures  $10^{5-6}$  K with constraints on total mass contained in that phase being consistent with theoretical predictions (Werk et al., 2014; Faerman et al., 2017; Tumlinson et al., 2017). X-ray absorption has been used to constrain properties of the MW CGM (Mathur et al., 2021). However, there are few detections for X-ray line absorption in the CGM of external galaxies (Nicastro et al., 2023) and some theoretical studies using simulations of galaxies (Bogdán et al., 2023). The presence of the hot CGM ( $T \geq 10^6$  K) has also been claimed using signal stacking from the thermal Sunyaev-Zel'dovich effect<sup>4</sup> effect (Planck Collaboration et al.,

<sup>2</sup>Because the total stellar mass depends on assumptions such as metallicity and IMF, these scaling relations are derived for total luminosity in the B or K optical band which trace the stellar mass.

<sup>3</sup>This only accounts for the X-ray emission and mass within five effective radii. For a gas in virial equilibrium,  $M \propto T_{\text{vir}}^{1.5}$ . Given an empirical relation of  $L_X \propto M (< 5r_w)^3$  results in  $L_X \propto T_{\text{vir}}^{4.5}$ .

<sup>4</sup>Scattering of CMB photons off free electrons in a plasma

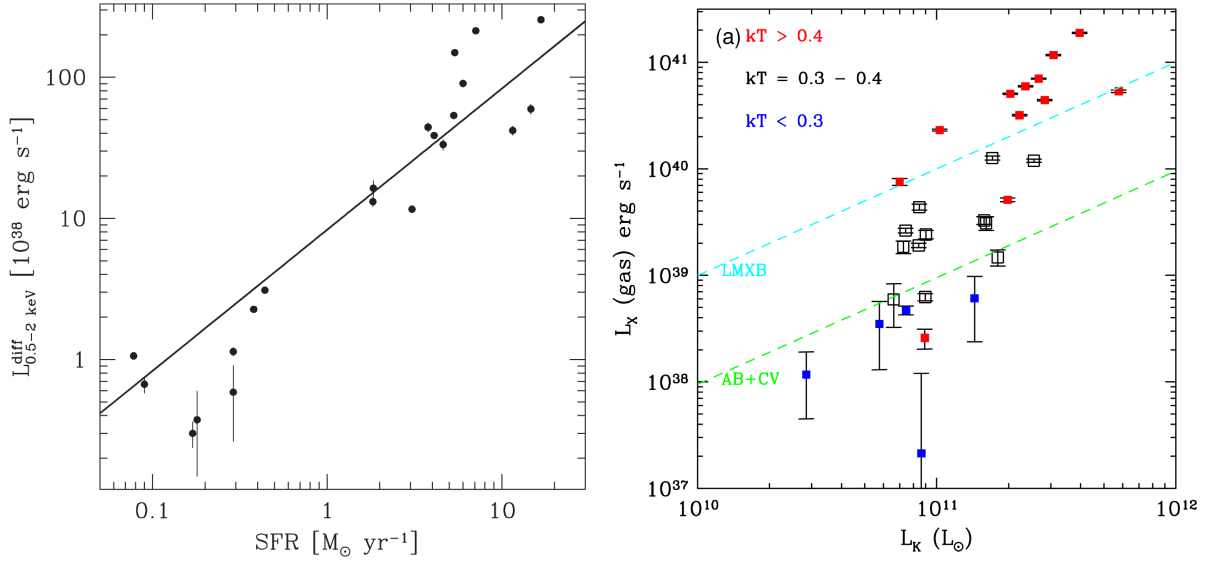


Figure 2.3: Typical X-ray scaling relations of the ISM in SFG (left) and QG (right). In SFG, the X-ray luminosity of the ISM is linearly dependent on the SFR (black line). In QG, it is dependent on the stellar mass, indicated here by the luminosity in the K-band,  $L_K$ . In the right panel, data points are color-coded according to the temperature of the hot ISM. The colored dashed lines indicate scaling relations for LMXB (cyan) as well as active binaries (AB) and cataclysmic variables (CV) (green). The left figure is directly taken from Mineo et al. (2012b), the right figure is directly taken from Boroson et al. (2011).

2013; Greco et al., 2015). Their measurements imply a self-similar relation down to galaxy-scale halos which is in tension with X-ray emission limits and the soft X-ray background (Tumlinson et al., 2017).

The difficulty in detecting the hot halo gas in X-ray is due to the decline in volume emissivity of a plasma with its density squared (see Eq. (1.15)). Thus, the emissivity of halo gas in a declining density profile drops significantly after a few effective radii, or  $r > 0.1 R_{\text{vir}}$ . As a result, there are only a few direct X-ray measurements of the CGM limited to nearby massive galaxies. In particular, the massive SFG, NGC 1961 ( $M_* \sim 4 \cdot 10^{11}$ ), has been the target of *Chandra* (Anderson & Bregman, 2011) and XMM-Newton observations (Bogdán et al., 2013). The first study was able to detect the hot CGM within a radius of 50 kpc and the second study was able to detect direct emission from the CGM of NGC 1961 at a radius of  $0.15R_{200} (\approx 140 \text{ kpc})$ . However, NGC 1961 is also a highly star-forming galaxy such that the conditions for detecting the CGM are particularly favorable. A systematic investigation of X-ray Surface Brightness Profiles (SBPs) in QG using deep *Chandra* observations showed that they follow  $\beta$ -profiles (Cavaliere & Fusco-Femiano, 1978), however, the direct emission could only be constrained within five effective radii ( $< 0.1 R_{\text{vir}}$ ) (Babyk et al., 2018). Using *Suzaku* and XMM-Newton data, the hot CGM of the galaxy NGC 3221 could be constrained out to a radius of 200 kpc (Das et al., 2019, 2020). A recent investigation of inclined star-forming disc galaxies in the Virgo cluster yielded only weak constraints on CGM outflows in direct emission (Hou et al., 2024). In the cluster environment,

the CGM of SFG is likely to dissipate within the cluster atmosphere due to ram-pressure stripping and tidal interaction, so its emission is much fainter.

A more promising approach to enhance the signal of low surface brightness components uses the stacking technique. In this approach, individual images of observational targets are centered either on their X-ray peak or optical center. The angular size of the image is then transformed into physical coordinates given the redshift of the observation. The flux of each image is then combined to construct an average image, where weights are dependent on instrument specifications and geometrical considerations (see e.g. [Comparat et al., 2022](#)). This technique can then be used on collections of objects grouped by their intrinsic properties, i.e. stacks within galaxy stellar or halo mass bins. The advantage of this technique is the enhancement of signal-to-noise in low surface brightness regimes. The disadvantage is that error estimation in average quantities is sensitive toward extreme outliers in the sample. The latter can be mitigated by resampling the stacks using a bootstrapping approach ([Andrae et al., 2010](#); [McIntosh, 2016](#)).

A comprehensive study by [Anderson et al. \(2015\)](#) used 250000 galaxies extracted from RASS and cross-matched with SDSS galaxies from [Blanton et al. \(2005\)](#) such that all galaxies in the sample are the brightest in their dark matter halo. They extracted counts from the stacked images for different mass bins out to radii of 3 Mpc for the most massive galaxies to determine the CGM luminosity for a radial range of  $0.15 - 1 R_{500}$ . They found a relation with halo mass assuming a self-similar evolution and find

$$L_X^{\text{cgm}} \approx 1.4 \cdot 10^{44} \left( \frac{M_{500}}{1.4 \cdot 10^{14} M_\odot} \right)^{1.84}, \quad (2.5)$$

$$(2.6)$$

which is steeper than expected from self-similarity  $M^{1.33}$  and holds only down to  $M_{500} \sim 5 \cdot 10^{12} M_\odot$  where the relation flattens. Below this mass threshold, their data is background-dominated and completeness limited due to the shallow depth of the ROSAT survey. The slope is in agreement with previous studies and consistent with scaling relations of groups and clusters although the normalization is lower due to biases ([Anderson et al., 2015](#)). They performed the same stacking analysis on stellar mass bins and found a similar dependence with  $L_X \propto M_*^\alpha$ , where  $\alpha \simeq 3$ . is sensitive to the chosen energy range and if satellite galaxies are included in the stellar mass estimates. They benchmarked their scaling relations against cosmological simulations of galaxy formation and found that their results are consistent with non-gravitational heating in the form of AGN feedback.

Using eROSITA data from the eFEDS field and galaxy data from the GAMA survey ([Liske et al., 2015](#)), [Comparat et al. \(2022\)](#) found significant emission above the background out to radii of 300 kpc corresponding to the virial radius of the MW. The normalization of their SBPs depends on stellar mass for both QG and SFG but the profile slopes remained consistent across stellar mass bins. In general, they find surprisingly flat profiles at large radii and their stellar mass scaling relations do not agree well with measurements from [Anderson et al. \(2015\)](#). It was later found to be caused by contamination from satellite galaxies ([Zhang et al., 2024b](#)). The same study was thus repeated using X-ray data from eRASS:4 and two optical galaxy catalogs consisting of  $\sim 380000$  spectroscopically confirmed SDSS galaxies and 2.4 million photometric

galaxies from DESI. These detailed galaxy catalogs could significantly improve the handling of the contaminating signal from satellite galaxies (Zhang et al., 2024b,c). They further cleaned the sample by accounting for unresolved AGN and XRBs in the galaxy center being affected by the telescope response. We show their results in Fig 2.4.

In the left panel of Fig. 2.4 three different average surface brightness profiles are shown for galaxies in stellar mass bins corresponding to the MW (green), M31 (orange), and two times M31 (purple). The dotted lines correspond to the point-spread function (PSF) of eROSITA. The dash-dotted vertical lines indicate the virial radius of the respective stellar mass bin. In the right panel, the total (green) and CGM (purple) x-ray luminosity is shown as a function of the halo mass  $M_{500c}$ . The red dashed line is the best-fit relation of the CGM luminosity from Zhang et al. (2024c) which is compared to previous works and predictions from various cosmological simulations. Zhang et al. (2024b) found steeper profiles at large radii compared to Comparat et al. (2022) and confirmed the stellar mass trend of the profile normalization. They recomputed stellar mass and halo mass scaling relations of the CGM luminosity in Zhang et al. (2024c) and found a slight break in the relation at  $M_{500} \sim 10^{12.8} M_{\odot}$ . For halos with higher mass, their derived slope is steeper than expected for self-similarity and consistent with results from the group and cluster regime (Lovisari et al., 2021) which implies the necessity for non-gravitational heating (Fabian, 2012; Eckert et al., 2021; Oppenheimer et al., 2021). For halos with lower mass, the relation is consistent but slightly shallower than self-similarity which allows for the implication of non-gravitational processes being sub-dominant. In fact, the CGM of halos in the lower mass regime and redshift  $z < 0.5$  are expected to reach virialization (Faucher-Giguère & Oh, 2023; Zhang et al., 2024c).

## 2.2 Active galactic nuclei

An AGN is an accretion-powered SMBH at the center of a galaxy and occurs in approximately 1-10% of observed galaxies indicating a complex co-evolution between the AGN and its host. Their large bolometric luminosity ( $L_{\text{bol}} \geq 10^{43} \text{ erg s}^{-1}$ ) across all wavelengths is produced by an optically thick accretion disc which emits thermally due to heating resulting from viscous dissipation (Shakura & Sunyaev, 1973). We will describe accretion disc physics in more detail in Ch. 3. As a consequence, AGN are also bright X-ray sources and it has been found that the CXB is comprised of more or less obscured point sources at different redshifts (Gilli et al., 2007; Ueda et al., 2014; Cappelluti et al., 2017). The classification of AGN saw the rise of innumerable naming conventions depending on various features in their spectra which Padovani et al. (2017) tried to summarize. Here we will focus on AGN as actively accreting SMBH emitting X-ray radiation. The spectral components of the X-ray emission from an AGN are for one direct emission from the hottest part of the accretion disc, producing a soft excess. Most of the X-ray emission, however, is produced by Compton up-scattered optical and UV photons from the accretion disc in the hot electron coronae about the SMBH. This process produces X-ray photons following a power-law distribution with photon index  $\Gamma \approx 1.8 - 2.0$  and exponential cutoff at  $E \sim 200 \text{ keV}$  (Remillard & McClintock, 2006; Done et al., 2007).

Other components observed in AGN X-ray spectra are a reflection spectrum from high energy

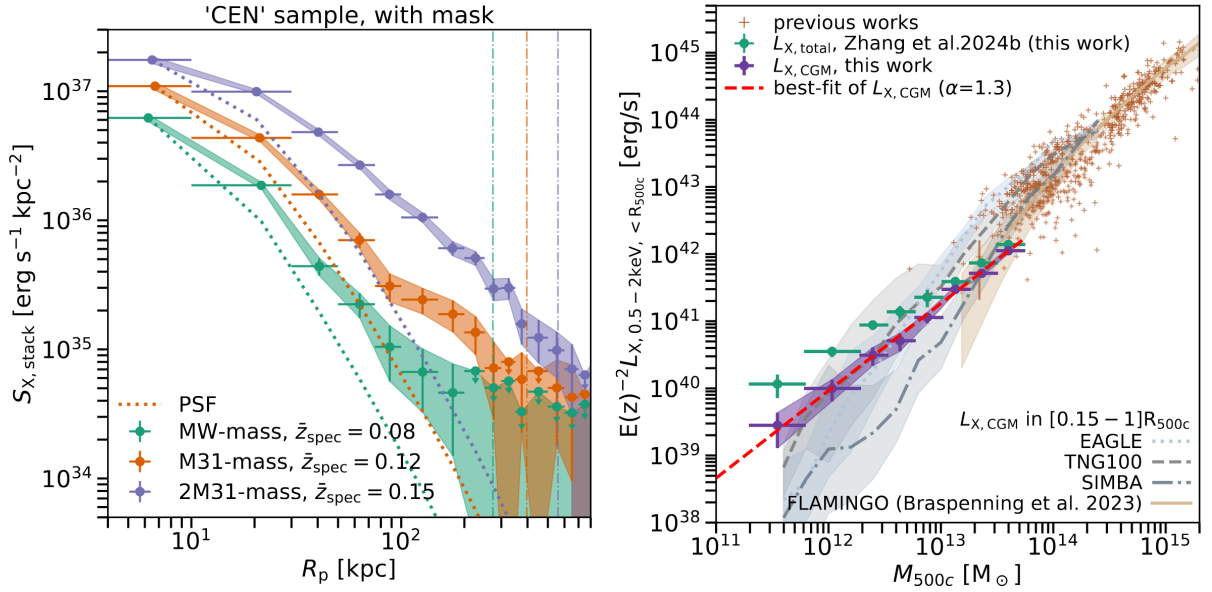


Figure 2.4: *Left*: Mean surface brightness profiles of stacked central galaxies in the  $\log \frac{M_*}{M_\odot} = 10.5 - 11.0$  (MW, green),  $\log \frac{M_*}{M_\odot} = 11.0 - 11.25$  (M31, orange), and  $\log \frac{M_*}{M_\odot} = 11.25 - 11.5$  (2M31, purple) stellar mass range after applying corrections for unresolved point sources and background subtraction. The dotted line shows the profile of a point source affected by the instrumental response. The vertical dash-dotted lines indicate the virial radius of the respective mass bin. Figure is directly taken from Zhang et al. (2024b). *Right*: The total (green) and CGM (purple) X-ray luminosity of stacked central galaxies as a function of their halo mass  $M_{500c}$  directly taken from Zhang et al. (2024c). The total luminosity includes the emission from hot gas, AGN and XRBs while the CGM luminosity only includes hot gas. The red dashed line is their best-fit single power-law relation, although they discuss evidence of a slope transition at  $M_{500c} \sim 10^{12.8} M_\odot$ .

photons being reflected off of the accretion disc and resulting fluorescent lines<sup>5</sup>, and a scattered soft component (Petrucci et al., 2001; Ricci et al., 2011; Merloni et al., 2014). The appearance of the latter components depends on the assumed accretion geometry and obscuration fraction. Obscuration in AGN generally refers to the density of absorbing material close to or in the line of sight to the AGN and has been systematically studied (Merloni et al., 2014; Ueda et al., 2014; Buchner et al., 2014). Interestingly, Buchner et al. (2017) found an additional absorption component associated with the host galaxy of an AGN which scales with the stellar mass of the host,  $N_H^{\text{gal}} \simeq 10^{21.7} \cdot \left( \frac{M_*}{10^{9.5} M_\odot} \right)^{\frac{1}{3}} \text{cm}^{-2}$ , where  $N_H^{\text{gal}}$  is the absorbing hydrogen column density and  $M_*$  is the host galaxy stellar mass. This relation appears to be consistent with the highest column densities of the MW, the Magellanic clouds, and local star-forming dwarf galaxies (see Buchner et al., 2017; Lehmer et al., 2022) and therefore also crucial in understanding the hot ISM and

<sup>5</sup>most prominently the Fe-K $\alpha$  line at 6.4 keV

X-ray emission coming from other galaxies. For a review on obscuration in AGN, we refer the reader to [Hickox & Alexander \(2018\)](#). We show an idealized spectrum for an obscured AGN in Fig. 2.5 where individual components discussed above are highlighted.

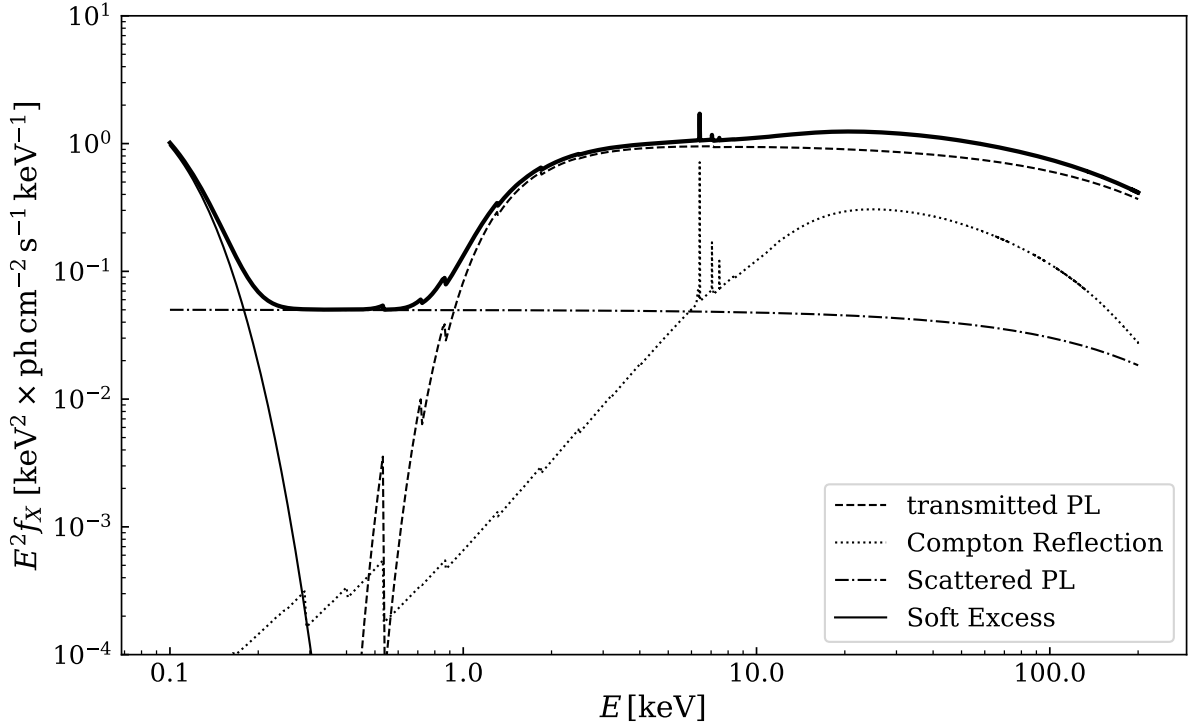


Figure 2.5: Idealized X-ray spectrum of an AGN. The dashed line is the transmitted power-law (PL) component with photon index  $\Gamma = 2$  produced by Comptonized photons which are obscured by a warm absorber with  $N_H = 10^{22} \text{ cm}^{-2}$ . The dash-dotted line is a scattered PL component with the same slope as the transmitted PL. The dotted line is the Compton reflected component with the resulting fluorescent Fe-K $\alpha$  line ( $E_{K\alpha} = 6.4 \text{ keV}$ ) modeled after [Magdziarz & Zdziarski \(1995\)](#), `pexmon` in XSPEC). The thin solid line corresponds to a black-body emitter at  $kT_{bb} = 15 \text{ eV}$  accounting for soft-excess emission ([Done et al., 2012](#)). The solid thick black line is the sum of all individual components.

Because of their brightness, compiling the luminosity and redshift distribution of AGN from large sky surveys is straightforward. The resulting X-ray luminosity functions (XLFs) of AGN are well studied ([Hopkins et al., 2007](#); [Hasinger, 2008](#); [Aird et al., 2010, 2015](#); [Hirschmann et al., 2014](#); [Buchner et al., 2015](#)) and are an essential tool not only for understanding the background in X-ray observations ([Georgakakis et al., 2008](#)) but also for the growth and co-evolution between SMBHs and its host galaxy ([Kormendy & Ho, 2013](#); [McConnell & Ma, 2013](#)). In Fig. 2.6 we show the best model of AGN XLF from [Aird et al. \(2015\)](#) accounting for unobscured ( $20 \leq \log \frac{N_H}{\text{cm}^{-2}} \leq 22$ , *blue*), obscured ( $22 \leq \log \frac{N_H}{\text{cm}^{-2}} \leq 24$ , *red*) and Compton thick ( $\log \frac{N_H}{\text{cm}^{-2}} \geq 24$ ) AGN at different redshifts. It is well known that the growth of the central SMBH

plays an important role in galaxy evolution through feedback and displacement of enriched gas (e.g. [Fabian, 2012](#)). Furthermore, the XLFs of AGN can be an important benchmark for numerical simulations to adjust their feedback prescriptions ([Di Matteo et al., 2008, 2012](#); [Booth & Schaye, 2011](#); [Hirschmann et al., 2014](#); [Sijacki et al., 2015](#); [Steinborn et al., 2015, 2016](#); [Koulouridis et al., 2018](#)). Since AGN are associated with their host galaxies, their spatial distribution can be used to construct one- or two-point correlation functions to study their clustering and potentially reveal properties of the underlying cosmology. In [Comparat et al. \(2019\)](#) they constructed a mock AGN catalog in preparation for eRASS by sampling from the XLFs and using lightcones from numerical simulations to estimate this clustering.

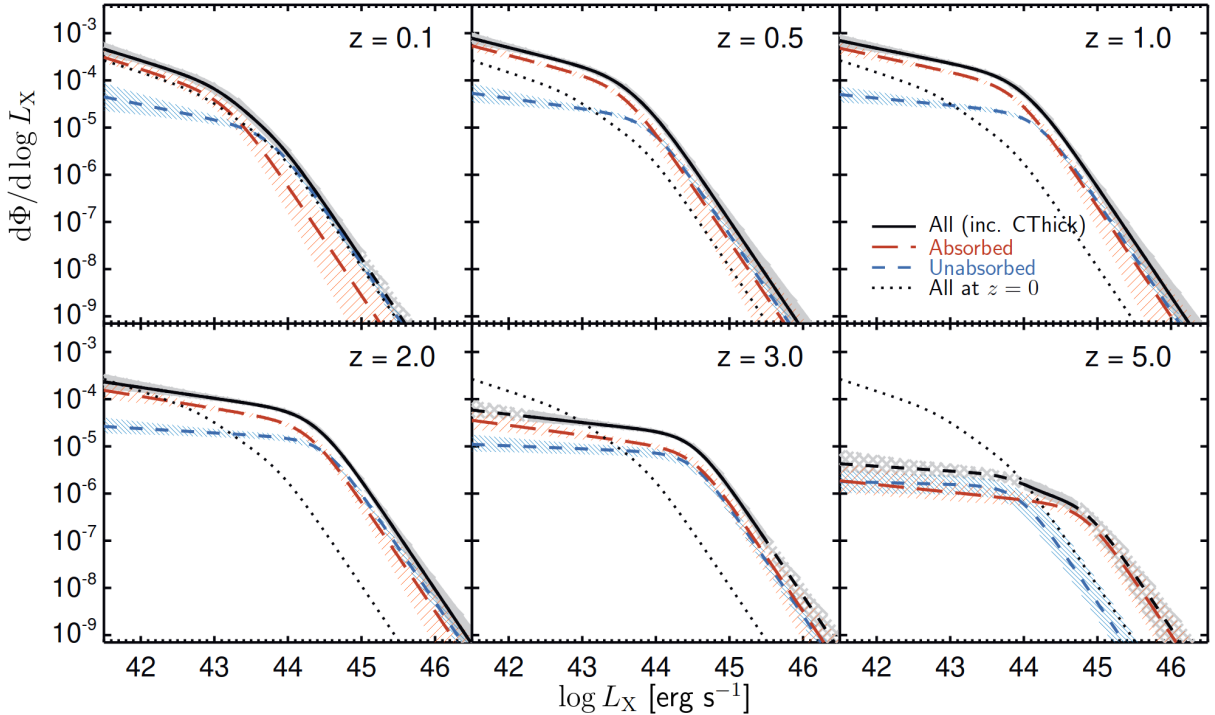


Figure 2.6: Best fit model for the XLF of AGN at various redshifts. The blue dashed line shows the XLF of unobscured sources, the red dashed line shows obscured sources, and the black solid line includes both the red and blue lines additionally including Compton-thick AGN. Figure directly taken from [Aird et al. \(2015\)](#).

While AGN can reach X-ray luminosities of up to  $L_X^{\text{agn}} \leq 10^{46} \text{ erg s}^{-1}$ , the flux of low-luminosity AGN can be comparable to the combined emission of XRBs and the hot ISM. For this reason, there are numerous ways to observationally identify an X-ray AGN in a galaxy (see [Xue et al., 2011](#); [Lehmer et al., 2016](#)).

1. If the intrinsic X-ray luminosity of a galaxy exceeds  $L_X^{0.5-7 \text{ keV}} \geq 3 \cdot 10^{42} \text{ erg s}^{-1}$ , the source is likely to be an AGN.
2. If the X-ray to R-band optical flux ratio exceeds  $\log \left( \frac{f_X}{f_R} \right) > -1$ , the source is classified as

an AGN.

3. If the source shows optical spectroscopic features typical for AGN, i.e. broad-line regions or high-excitation emission lines, it is considered an AGN.
4. If the intrinsic X-ray luminosity of the source exceeds the scaling relation between monochromatic radio luminosity,  $L_{1.4\text{GHz}}$ , and X-ray luminosity of normal star-forming galaxies by at least a factor of  $\geq 3$  (Alexander et al., 2005).

The last point is an empirical scaling which takes into account the X-ray emission from the hot ISM and XRBs in star-forming galaxies and correlates it with the radio emission produced by SN remnants and star-forming regions. Enhanced radio emission can also be associated with an AGN as a result of relativistic jets launched by the accretion disc and embedded magnetic fields in which accelerated electrons produce synchrotron radiation. These jets impart large amounts of mechanical energy into the surrounding matter which can lead to galactic outflows and transport of material into the CGM and Inter Galactic Medium (IGM). In galaxy cluster environments, jets can carve cavities in the cluster atmospheres which can be seen as depressions in X-ray surface brightness and can be associated with past activity of the central SMBH (e.g. Fabian et al., 2005).

## 2.3 Stellar X-ray sources

### 2.3.1 Young stellar objects

With the *Chandra* observatory, X-ray emission from star-forming regions in the MW could directly be associated with very young stars (T Tauri stars) (Preibisch & Feigelson, 2005). In T Tauri stars, the X-ray emission results from the interaction of strong magnetic fields close to the stellar surface with the accretion flow from the protostellar disc (Preibisch et al., 2005; Günther et al., 2007). Individual T Tauri stars can reach X-ray luminosities up to  $L \leq 1 \cdot 10^{32} \text{ erg s}^{-1}$ , such that several active star-forming regions can contribute to the diffuse X-ray emission in galaxies. The exact contribution of young stellar objects towards the total X-ray luminosity of a galaxy is not exactly known because their emission can not be easily separated from the hot ISM (Mineo et al., 2012b). They have, however, significantly harder spectra than the hot ISM and can therefore be approximated by plasma emission with  $k_B T \sim 3 \text{ keV}$  in spectral modeling (Winston et al., 2007; Mineo et al., 2012b).

### 2.3.2 Massive stars

With increasing mass, the luminosity of a star significantly increases such that its energy input to the surroundings becomes increasingly important. The most massive stars of spectral types O and B are crucial for understanding properties of the ISM because they launch strong line-driven winds with high mass loss rates of  $\dot{M}_W \simeq 10^{-9} - 10^{-5} M_\odot \text{ yr}^{-1}$  which heat and enrich their environments (see e.g. Kudritzki & Puls, 2000). With the launch of the *Einstein* X-ray probe, O and B stars have also been known to be strong X-ray emitters. With the capabilities of *Chandra*

and XMM-Newton, it was possible to catalog several hundreds of massive stars that are also X-ray bright (see e.g. [Nebot Gómez-Morán & Oskinova, 2018](#)). While a small fraction of X-ray emission originates from the high surface temperatures of O/B stars, the majority of X-ray flux is due to shock heating within the wind (see e.g. [Martínez-Núñez et al., 2017](#); [Rauw, 2022](#)). The emission can be modeled by a collisional plasma (see Eq. (1.15)) with a temperature of  $k_B T \sim 2$  keV and the ratio of X-ray to bolometric luminosity for a single O/B star is  $\frac{L_X^{\text{OB}}}{L_{\text{bol}}} \simeq 10^{-6}$  such that  $L_X^{\text{OB}} \leq 10^{34} \text{ erg s}^{-1}$  ([Nebot Gómez-Morán & Oskinova, 2018](#)). The dependence of the X-ray luminosity on wind parameters such as the terminal wind velocity or the clumping factor is not well understood and only weak relations have been found. However, a wind model with cold clumps embedded in the larger wind geometry is favored to explain the observed X-ray and UV line profiles in the stellar wind of O/B stars ([Martínez-Núñez et al., 2017](#)).

From stellar evolution, O and B types will eventually end in a powerful supernova explosion which injects energy ( $E \sim 10^{51} \text{ erg}$ ) and metals into the local ISM. The resulting supernova remnant is X-ray bright in the initial phases of its evolution due to the shock propagating through the local ISM. The remnants of these explosions are compact objects, either stellar mass Black Holes (BHs) or neutron stars ([Schneider et al., 2021](#), see e.g.). Since most massive stars have a lower mass binary companion ([Moe & Di Stefano, 2017](#); [Offner et al., 2023](#)), the further interaction of the compact remnants with their companion following a SN can lead to mass transfer resulting in X-ray Binaries (XRBs).

### 2.3.3 Active Binaries

Without a formal definition, active binary (AB) stars describe a collection of phenomena attributed to the orbital interaction of evolved, low-mass stars in a binary system producing X-ray emission. The main scenario involves a tidally locked evolved low-mass star and a low-mass main sequence star ( $< 1 M_{\odot}$ ) in a binary system with a low orbital period ( $P \leq 10 d$ ). Through accretion processes and tidal interactions, X-ray emission is produced with  $L_X \leq 10^{34} \text{ erg s}^{-1}$  (see e.g. [Szczygieł et al., 2008](#)). A more distinctive class of binaries are the cataclysmic variables (CVs) which are low-mass close binaries between a Roche-Lobe filling (see Ch. 3) post main-sequence star and a magnetized white dwarf (see [Warner, 1995](#)). They are the host systems for classical and dwarf novae. In classical nova outbursts, the optical brightness of a CV increases once by  $\gtrsim 10$  orders of magnitude because of material buildup at the surface boundary of the white dwarf leading to a thermonuclear runaway explosion disrupting the binary. In contrast, dwarf novae are characterized by a regular brightening of the system by  $\simeq 2 - 5$  orders of magnitude which is directly related to the accretion process ([Longair, 2011](#)). The latter is of particular importance as it allows for spectroscopic investigation in the optical and UV energy range which would be inaccessible in other types of binaries dominated by the emission of the companion star. As such, it is possible to directly measure properties of the accretion disk, i.e. temperature and structure, during outbursts using the UV H $\beta$  and H $\gamma$  emission lines ([Marsh & Horne, 1990](#); [Frank et al., 2002](#)).

Close to the white dwarf, magnetic fields funnel material from the accretion disc onto the magnetic poles as accretion columns. At the boundary layer between the columns and the

white dwarf's surface (see Fig. 3.5), the accreted material is reprocessed at  $T \approx 10^5$  K which releases extreme UV and soft X-ray radiation. Furthermore, hard X-ray emission is also observed in CVs coming from the same accretion column where the high-velocity infall can produce shocks and plasma of significantly higher temperature above the stellar surface (Frank et al., 2002). Individual CVs can thus episodically reach X-ray luminosities of  $L_X \leq 10^{35}$  erg s<sup>-1</sup>. Nevertheless, the abundance of these systems is a strong function of the host galaxy's stellar mass because they originate from long-lived main-sequence stars. Therefore, their cumulative X-ray luminosity may contribute substantially to the diffuse X-ray emission of a QG galaxy. Boroson et al. (2011) determined scaling relations between the combined X-ray luminosity of unresolved active binaries and the total stellar mass for elliptical galaxies

$$L_X^{\text{AB+CV}} \simeq 9.5 \cdot 10^{27} \left( \frac{L_K}{L_\odot} \right) \text{ erg s}^{-1}, \quad (2.7)$$

which is a factor of 10 lower than the contribution from LMXBs (see Ch. 3). However, since strongly emitting point sources like LMXB could be identified and removed from the diffuse component using *Chandra*, they concluded that the contribution of CVs and ABs needs to be accounted for to explain the residual emission in QG (Revnivtsev et al., 2009; Boroson et al., 2011).



## 3 | X-ray Binaries

X-ray Binaries (XRBs) are among the brightest hard X-ray sources in the sky (Lewin & van der Klis, 2006) and there are hundreds of known sources in the MW alone. They are stellar binary systems composed of a degenerate relativistic compact object, usually a neutron star or stellar BH, and a donor star. Their X-ray emission is powered by accretion due to mass exchange from the donor onto the compact object (Shakura & Sunyaev, 1973) and they reach luminosities close to the Eddington limit of the compact accretor ( $L_X \simeq 10^{38} \frac{m}{M_\odot} \text{ erg s}^{-1}$ ). They are an unavoidable intermediate step in the formation of a close binary pair consisting of neutron stars or stellar mass BHs (Tauris et al., 2017). The eventual merger of binary neutron stars or stellar BH mergers can then be detected as kilonovae or gravitational wave sources (Abbott et al., 2017a,b). Early X-ray observations already hinted at extra-galactic populations of XRBs due to X-ray scaling relations between tracers of star formation and stellar mass (see e.g. Fabbiano, 2006; Gilfanov et al., 2022) which also strengthened the picture of two distinct classes of XRB, one associated to young stellar populations and one to older populations. The sub-arcsecond resolution of *Chandra* (Weisskopf et al., 2000) enabled the study of these extra-galactic populations in much greater detail and solidified our current understanding of their properties and evolution.

In this chapter, we will briefly discuss the main aspects of XRBs formation and evolution, their classification, and give an overview of the most prominent accretion processes. We will then describe their spectral features and X-ray scaling relations obtained from extra-galactic XRB populations. The physics involved in the description of XRBs is vast and fueled by a detailed understanding of multiple fields of study, whose description is beyond the scope of this thesis. We will therefore limit our description to the basic concepts and mention some simplifications along the way. For a much broader description of the topic, we refer the reader to the comprehensive book by Tauris & van den Heuvel (2023).

### 3.1 Classification

Heuristically, XRBs can be categorized into two major classes depending on the mass of the donor star in the system. High-Mass X-ray Binaries (HMXBs), for which donors have masses of  $m_{\text{donor}} \gtrsim 8 M_\odot$ , or Low-Mass X-ray Binaries (LMXBs) which have donor masses of  $m_{\text{donor}} \lesssim 1 M_\odot$ . The accretor in these systems is typically a compact object, either a neutron star or a stellar mass BH, both remnants of the stellar evolution of a massive star. X-ray radiation in both classes is produced by mass transfer between the donor and the compact object, where in HMXB

the compact object (CO) accretes spherically from a Roche-Lobe filling stellar wind or from atmospheric expansion of the donor's radiative atmosphere. The Roche-Lobe is the equipotential surface enclosing the binary pair through the inner Lagrange point,  $L_1$ . We will more thoroughly introduce this concept in Sec. 3.2.2 In LMXB, the mass transfer onto the CO occurs through Roche-Lobe Overflow (RLO) of the low-mass donor either through orbital shrinkage of the binary or by nuclear evolution of the donor. We show a schematic illustration of the two kinds of accretion in Fig. 3.1 which also includes typical orbital periods  $P$  of the binary. There are however clear observational criteria distinguishing the two classes from the perspective of the MW.

- (i) *Optical luminosity.* Since HMXBs harbor a luminous massive star of spectral type O or B, the optical luminosity is dominated by the spectrum of the donor ( $L_{\text{opt}} \geq L_X$ ). Instead, in LMXBs, the stellar companion is faint and its spectrum can not be observed.
- (ii) *Spatial distribution.* A clear spatial distinction is observed between the two classes where HMXB are more concentrated towards the galactic plane and spiral arms but not the central bulge, similar to young stellar populations. Since the massive donor star of  $m > 8 M_{\odot}$  does not live much longer than 30 Myr, must have a similar age. In contrast, LMXB are more concentrated toward the central stellar bulge, roughly follow the stellar surface density, and have an enhanced concentration in globular clusters. This distribution is in line with the behavior of an old stellar population as expected of the long evolutionary time of the donor in LMXB.
- (iii) *X-ray variability.* In most HMXB, the accretor is an X-ray pulsar with spin periods between 0.1 and 1000 seconds and strong magnetic fields, where cyclotron lines in the X-ray spectrum confirm its presence (see e.g. [Staubert et al., 2019](#)). Regular X-ray pulsations are rarely seen in LMXB. Instead, they show thermonuclear X-ray flares implying a weakly magnetized neutron star as the accretor in these systems because strong magnetic fields would suppress the thermonuclear reaction ([Strohmayer & Bildsten, 2006](#)). Furthermore, LMXB show millisecond variation in their X-ray spectra in the form of quasi-periodic oscillations. These effects are not observed when the accretor is a BH.
- (iv) *Average spectrum.* The average spectra of HMXB is harder ( $k_B T \geq 10$  keV) compared to LMXB ( $k_B T \leq 10$  keV). This is believed to also follow from stronger magnetic fields in neutron stars of HMXB ([Tauris & van den Heuvel, 2023](#)).
- (v) *Orbital periods.* Both classes have distinct orbital periods, where LMXB have a wide range of 11 min to a hundred days, while HMXB have between 1.5 and a few hundred days. The lower limit of orbital periods in HMXB is longer than for LMXB because hydrogen-rich massive stars have much larger radii. The requirement to have an orbit outside the Roche radius forbids shorter periods. From similar arguments, the lowest periods in LMXB must be due to a hydrogen-poor star, either a white dwarf or helium star ([Tauris & van den Heuvel, 2023](#)).

While intermediate-mass X-ray binaries (IMXB), where the donor mass is  $2 M_{\odot} \leq m_{\text{donor}} \leq 6 M_{\odot}$ , should in principle exist, they are rarely detected due to selection bias towards LMXB and HMXB. For one, the intermediate-mass companion is not massive enough to launch substantial winds to power an X-ray source persistently. Second, if the intermediate-mass donor eventually initiates RLO, the ensuing super-Eddington mass transfer rates are unstable on sub-thermal timescales ( $\leq 10 \text{ Myr}$ ) and quickly deplete the donor atmosphere. Additionally, the accretor is either completely enshrouded by an optically thick absorber or the binary enters common envelope evolution, quenching any observable X-rays. The latter process is however required to explain some systems such as Cen X-3<sup>1</sup> or as progenitors to binaries consisting of a white dwarf and a pulsar (Tauris & van den Heuvel, 2006, 2023).

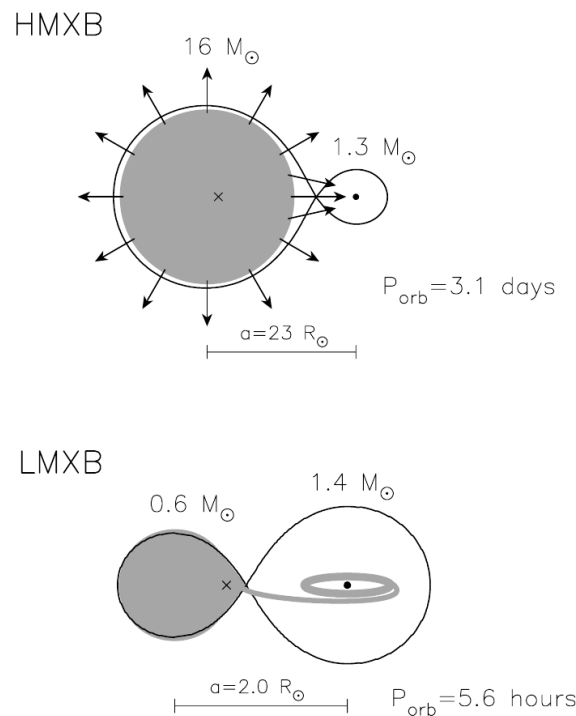


Figure 3.1: Schematic illustration of typical HMXB and LMXB orbital configurations with the corresponding accretion mechanism and typical orbital periods  $P_{\text{orb}}$ . The HMXB case shows spherical accretion from the stellar wind of its massive companion. The LMXB case shows the RLO accretion from its evolved main sequence low-mass companion. The figure is directly taken from Tauris & van den Heuvel (2006).

<sup>1</sup>The Centaurus X-3 system shows periods of extended "off" states. They are preceded by an increase in X-ray absorption resulting from an increasing accretion rate.

## 3.2 Formation and Evolution

### 3.2.1 Evolution of single stars

As outlined in the previous section, the more massive binary component will eventually expand because of stellar evolution. We will therefore interlude here with a brief description of the governing timescales in stellar evolution needed for the exemplary evolutionary paths of XRB in Sec. 3.2.3 and 3.2.4. Using basic assumptions about the structure and evolution of isolated stars, we can gain insights into the possible formation pathways and timescales on which a massive binary may evolve. In principle, a binary system is largely affected by the more rapid evolution of the primary, which means the more massive star. Its life on the stellar main sequence is determined by the nuclear fusion of hydrogen in its core and the stellar main sequence is often referred to as Zero Age Main Sequence (ZAMS) implying the start of hydrogen fusion. Other fusion reactions may occur in more massive stars with higher core temperatures, though they proceed on much shorter timescales due to nuclear reactions scaling with  $T^n$ , with  $n \geq 4$ . Therefore, the nuclear timescale governs the overall lifetime of the star and is set by the energy released by hydrogen fusion per unit mass,  $\eta_{\text{pp}} = 0.007c^2$ , a core mass of  $M_{\text{core}}$ , and the luminosity  $L_*$  of a star which gives

$$\tau_{\text{nuc}} = \frac{0.007M_{\text{core}}c^2}{L_*} \simeq 10^{10} \left( \frac{m_*}{M_{\odot}} \right)^{-2.5} \text{ yr}, \quad (3.1)$$

if one assumes conservative mass-luminosity relation of  $L_* \propto m_*^{3.5}$  for ZAMS stars of  $m_* \geq 1 M_{\odot}$ .

If radiative losses and the energy production are not in equilibrium, i.e. when the hydrogen fuel in the core is insufficient, a star will adjust the thermal equilibrium on timescales set by its current thermal energy  $E_{\text{th}}$  and luminosity

$$\tau_{\text{th}} = \frac{E_{\text{th}}}{L_*} = \frac{Gm_*^2}{2R_*L_*} \simeq 1.6 \cdot 10^7 \left( \frac{m_*}{M_{\odot}} \right)^{-2.2} \text{ yr}, \quad (3.2)$$

additionally assuming a mass-radius relation of  $R \propto m_*^{0.7}$ . The assumed relations between mass, radius, and luminosities are empirically motivated from measurements of stars in spectroscopic binaries (Torres et al., 2010; Eker et al., 2015). There are however indications of mass-dependent slope transitions in the mass-luminosity and mass-size relations (Baraffe et al., 1998; Eker et al., 2015).

If the hydrostatic equilibrium of a star is disturbed, e.g. by sudden mass-loss, a new equilibrium state will be reached on dynamical timescales which are set by a soundwave crossing the stellar radius with sound speed  $c_s = \sqrt{\frac{\gamma P}{\rho}}$

$$\tau_{\text{dyn}} = \frac{R}{c_s} \simeq 50 \sqrt{\frac{\bar{\rho}_{\odot}}{\bar{\rho}}} \text{ min} \simeq 50 \left( \frac{m_*}{M_{\odot}} \right)^{0.55} \text{ min}, \quad (3.3)$$

with  $\bar{\rho}_{\odot} = 1.4 \text{ g cm}^{-3}$  being the mean solar density.

The further evolution of a star after hydrogen is exhausted in its core largely depends on the mass of the star (Maeder & Meynet, 1989; Ekström et al., 2012). Generally, as the nuclear fusion of hydrogen ceases, the lack of radiation pressure leads to the contraction of the now helium-enriched core until helium fusion into carbon and oxygen ensues. In most cases, the envelope of the star will expand due to the steepening of temperature gradients and the decrease of the mean molecular weight towards the limb of the star (see e.g. Iben, 2013a,b; Tauris & van den Heuvel, 2023). While the most massive stars  $m_* \geq 12 M_\odot$  cycle through various fusion processes up to the production of iron and end in a SN type II (Woosley et al., 2002), the onset of other burning cycles in less massive stars is subject to electron degeneracy in the core. Further complications arise from the dependence on stellar rotation, metallicity, and mass-loss (Brott et al., 2011; Ekström et al., 2012; Eggenberger et al., 2021) such that in the most extreme cases, massive stars will have shed their entire hydrogen-rich envelope due to strong line-driven winds (Kudritzki & Puls, 2000) before the ignition of helium. The resulting fast-spinning naked helium stars (Wolf-Rayet stars) are indeed observed and constitute a small fraction of donor stars in HMXB and require separate evolutionary calculations (Kruckow et al., 2018). Crucially, it was shown that the cores of helium stars undergo further fusion processes as if they retained a hydrogen-rich envelope, which results in another period of expansion and a hydrogen deficient SN (type Ib/c) at the final collapse (see e.g. Woosley, 2019).

### 3.2.2 Roche-Lobe Equipotentials and Stability of mass-transfer in binaries

A crucial difference between the evolution of single stars and stars in a binary system is the amount of mass transferred between the two components. The complex interplay between mass transfer and stellar evolution is still an active topic of research today where numerical calculations rely on assumptions on the mass transfer rate (see e.g. review Marchant & Bodensteiner, 2024). The major driver of binary evolution is the effective gravitational potential shared by the orbiting binary pair and can be described as

$$\Phi = -\frac{Gm_1}{r_1} - \frac{Gm_2}{r_2} - \frac{\omega^2 r_3^2}{2}, \quad (3.4)$$

where  $G$  is Newton's constant,  $r_1, r_2$  are the distances of the stars from the barycenter with masses  $m_1, m_2$ , respectively,  $\omega$  is the orbital angular velocity, and  $r_3$  is the distance to the rotational axis. Assuming that the stars are sufficiently small with respect to their orbital separation and tidal forces have circularized the orbit, the orbital angular velocity is

$$\omega = \sqrt{\frac{Gm_{\text{tot}}}{a^3}}, \quad (3.5)$$

where  $a$  is the orbital separation of the binary and  $m_{\text{tot}} = m_1 + m_2$ . The resulting equipotential surfaces in a co-moving frame of reference are shown in Fig. 3.2.

Force balance between gravity and centrifugal force is reached at the Lagrange points  $L$ , where the equipotential surfaces crossing  $L_1$  define the Roche-Lobe. If the Roche-Lobe is filled by the more rapidly evolving initially more massive star (donor), the pressure imbalance at  $L_1$

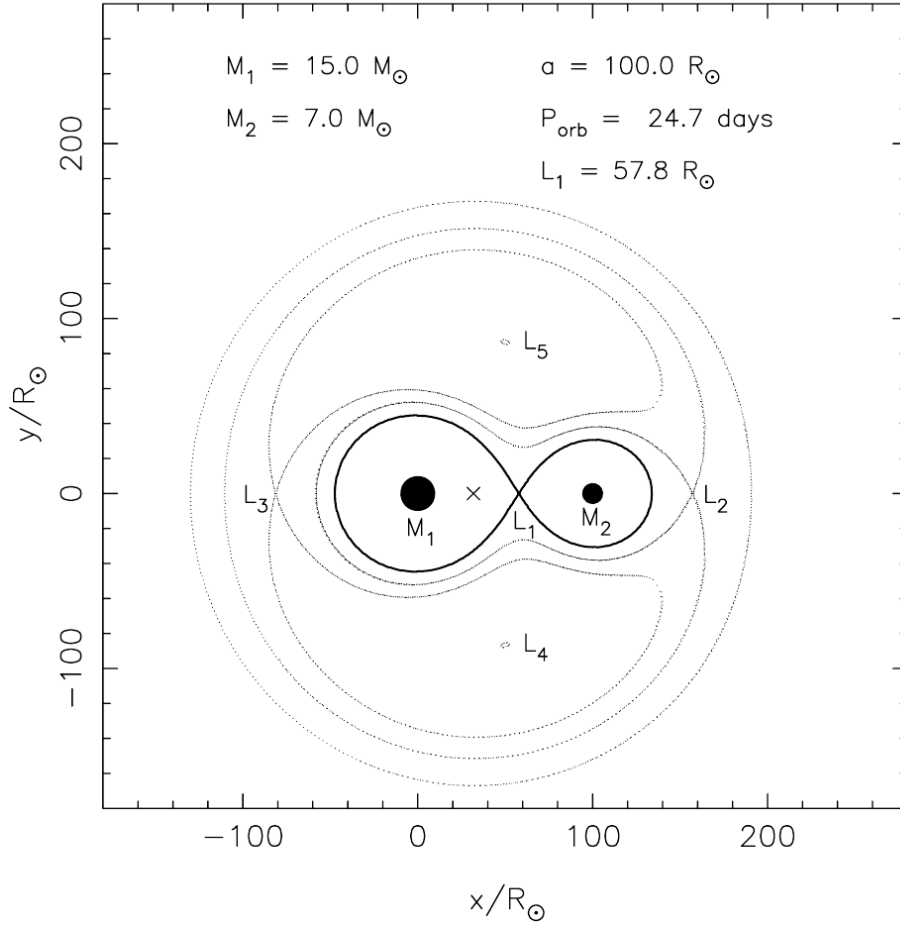


Figure 3.2: Cross section through the equatorial plane of a binary showing the equipotential surfaces of the effective potential  $\Phi$  (see Eq. (3.5)). The  $x$  and  $y$  coordinates are given in solar radii  $R_{\odot}$ . Binary parameters are given in the figure legend in solar units and  $P_{\text{orb}}$  is the orbital period about the center of mass marked with an  $x$ . The thick curve enclosing the binaries through  $L_1$  represents the Roche-Lobe at a distance of  $57.8 R_{\odot}$  from the primary star  $M_1$ .

will initiate mass transfer (Roche-Lobe Overflow (RLO)) onto the companion (accretor). In a spherical approximation, the Roche-Lobe radius,  $R_L$ , of the donor is approximately given by

$$\frac{R_L}{a} = \frac{0.49q^{\frac{2}{3}}}{0.6q^{\frac{2}{3}} + \ln(1 + q^{\frac{1}{3}})}, \quad (3.6)$$

where  $q = \frac{m_{\text{donor}}}{m_{\text{acc}}}$  is the mass ratio of the donor and accretor (Eggleton, 1983). The onset of RLO can be caused either by the expansion of the donor star or by orbital shrinkage due to angular momentum losses from the binary system and further evolution of the binary depends on the evolutionary stage of the donor at the time of RLO (Kippenhahn & Weigert, 1967). The mass transfer will continue on a thermal timescale until the mass ratio  $q$  is reversed or most of the

donor's hydrogen-rich envelope is lost when it will no longer fill its Roche-Lobe. Loss of angular momentum influences the orbital separation of the binary system and the orbital momentum balance equations can describe the rate of change in the orbital separation of the system

$$\frac{\dot{a}}{a} = 2 \frac{\dot{J}_{\text{orb}}}{J_{\text{orb}}} - 2 \frac{\dot{m}_{\text{donor}}}{m_{\text{donor}}} - 2 \frac{\dot{m}_{\text{acc}}}{m_{\text{acc}}} + 2 \frac{\dot{m}_{\text{donor}} + \dot{m}_{\text{acc}}}{m_{\text{tot}}}, \quad (3.7)$$

where

$$J_{\text{orb}} = \frac{m_{\text{donor}} m_{\text{acc}}}{m_{\text{tot}}} \omega a^2 \sqrt{1 - e^2}, \quad (3.8)$$

is the orbital angular momentum. For most real applications in XRB systems, a good approximation for the loss of angular momentum is given by the isotropic re-emission model with conservative mass transfer, such that

$$\frac{\dot{J}_{\text{orb}}}{J_{\text{orb}}} \approx \beta \frac{q^2}{1 + q} \frac{\dot{m}_{\text{donor}}}{m_{\text{donor}}}, \quad (3.9)$$

$$\dot{m}_{\text{donor}} = -(1 - \beta) \dot{m}_{\text{acc}}, \quad (3.10)$$

where  $\beta$  is the fraction of mass lost from the system near the accretor (see [Tauris & van den Heuvel, 2006, 2023](#), and references therein.). Other effects influencing the orbital angular momentum to a lesser degree are due to magnetic braking, gravitational wave emission, or spin-orbit coupling.

The stability of the mass transfer through  $L_1$  depends on the rate of change between  $R_L$  and  $a$  during mass loss. In the case considered here, the Roche-Lobe as well as the orbit will generally expand for a comparatively light donor ( $q \leq 1$ ) leading to stable mass transfer which is the case for most LMXB. Conversely, the Roche-Lobe and orbit will shrink for systems where  $q \geq 1$  which can lead to an unstable mass transfer depending on the state of the donor star (see also [Postnov & Yungelson, 2014](#)). Namely, in addition to the orbital changes and the change of  $R_L$ , the adjustment of the donor's radius when subjected to mass loss also needs to be considered. The two distinguishing cases are stars with a convective or radiative envelope. Stars with a radiative envelope will generally shrink on a dynamical timescale due to mass loss. In LMXB, this will always lead to a period of stable mass transfer if the mass ratio  $q$  is small. For large mass ratios, the stability of mass transfer depends on the exact orbital parameters and the state of the donor star. Stability can only be reached in these cases if the Roche-Lobe radius adjusts faster to mass loss than the donor.

In contrast, stars with a convective envelope will expand quickly because of a super-adiabatic temperature gradient. Together with a fast decline in orbital separation for high mass ratios ( $q \geq 1.5$ ), this will lead to an unstable situation.  $L_1$  will lie within the donor's envelope such that the accretor will quickly disperse the envelope.

### 3.2.3 Schematic evolution of HMXB

In Fig. 3.3 we show the schematic formation pathway of HMXB based on the arguments presented in the previous sections and we will largely follow the description of [Tauris & van den Heuvel](#)

(2023) (see also [Tauris & van den Heuvel, 2006](#); [Postnov & Yungelson, 2014](#); [Tauris et al., 2017](#)). From an initial binary pair with ZAMS masses of  $14.4 M_{\odot}$  and  $8.0 M_{\odot}$ , respectively, the more massive star will expand first and fill its Roche-Lobe upon reaching the end of hydrogen burning after  $\tau_{\text{nuc}}$ . The first mass transfer onto the lighter is considered to be stable (semi-conservative) and proceeds on thermal timescales of the donor ( $\tau_{\text{th}} \approx 5 \cdot 10^4 \text{ yr}$ ) until the naked helium core of the donor is exposed. As discussed previously, the helium core will continue its evolution and eventually explode as a type Ib/c SN leaving behind a neutron star<sup>2</sup>. The explosion will impart a velocity kick onto the neutron star and force it into a wide eccentric orbit. After mass transfer, the now more massive secondary continues its evolution on a nuclear timescale accompanied by a strong stellar wind. The stellar wind ejected by the secondary will fill the Roche-Lobe before the expanding stellar surface. The wind arrives isotropically through the Roche-Lobe at the neutron star where it is accreted, forming a wind-fed HMXB. During the second mass exchange, the binary will shrink rapidly eventually ending in a common envelope, dissipating most of the hydrogen envelope which leaves behind the helium core of the secondary. The secondary's helium core will expand due to shell burning initiating another RLO before ending in a second SN which produces an eccentric neutron star binary.

The formation scenario depicted here will give rise to a B-emission type HMXB (Be-HMXB) where the system shows emission features from the wind decretion disc of a fast-rotating Be-type companion star. They are the most common and long-lived type of HMXB. The resulting X-ray source will be transient in this case because the eccentric orbit only allows for sufficient accretion onto the neutron star in the periastron. If the companion of the compact object is a super-giant O-type star (sgHMXB), the X-ray source is powered by the isotropic wind of the O-star and modulated by the build-up of stellar wind material close to the neutron star which can temporarily lead to high absorption column densities occluding the X-ray source. In these systems, the donor star is believed to be close to filling its Roche-Lobe where direct RLO of the envelope is possible, producing much brighter X-ray sources due to super-Eddington mass transfer of the entire envelope. The X-ray properties of sgHMXB can be used to study properties such as the clumping factor and self-absorption of the stellar wind of O-type stars and the irradiation of the wind through the X-ray emission of the accretor may alter its properties further (see [Martínez-Núñez et al., 2017](#), for a review on sgHMXB). From observational facts, the supergiant donor star needs to be close to filling its Roche-Lobe ( $\geq 0.9 R_L$ ) in most HMXB such that the lifetime of these systems is the time needed to fill the Roche-Lobe which is  $\sim 1 - 2.5 \cdot 10^5 \text{ yr}$ . In some HMXB the donor star may initiate atmospheric RLO which leads to the formation of an accretion disc similar to LMXB resulting in much more luminous HMXB though only about 7% of the galactic HMXB population are RLO systems ([Tauris et al., 2017](#)).

The low abundance of RLO HMXB is a result of mass-transfer proceeding on thermal timescales of the donor's envelope ( $\tau_{\text{th}} \sim 10^4 \text{ yr}$ ) which would result in super-Eddington transfer rates of  $\sim 10^{-3} M_{\odot} \text{ yr}$  and correspondingly  $\sim 10^{40} \text{ erg s}^{-1}$  in luminosity ([Rappaport et al., 2005](#)). However, the high mass-transfer rates would eventually completely drown the X-ray source and

---

<sup>2</sup>In fact, the remnant of a helium core will be a neutron star in most cases even if the original star would have been massive enough to form a BH which is dependent on the evolutionary stage of the core at the time of envelope dissipation.

lead to the formation of a common envelope. Therefore, these systems are in a phase of beginning atmospheric RLO where the mass-transfer rates are still below the Eddington limit (Tauris et al., 2017; Tauris & van den Heuvel, 2023).

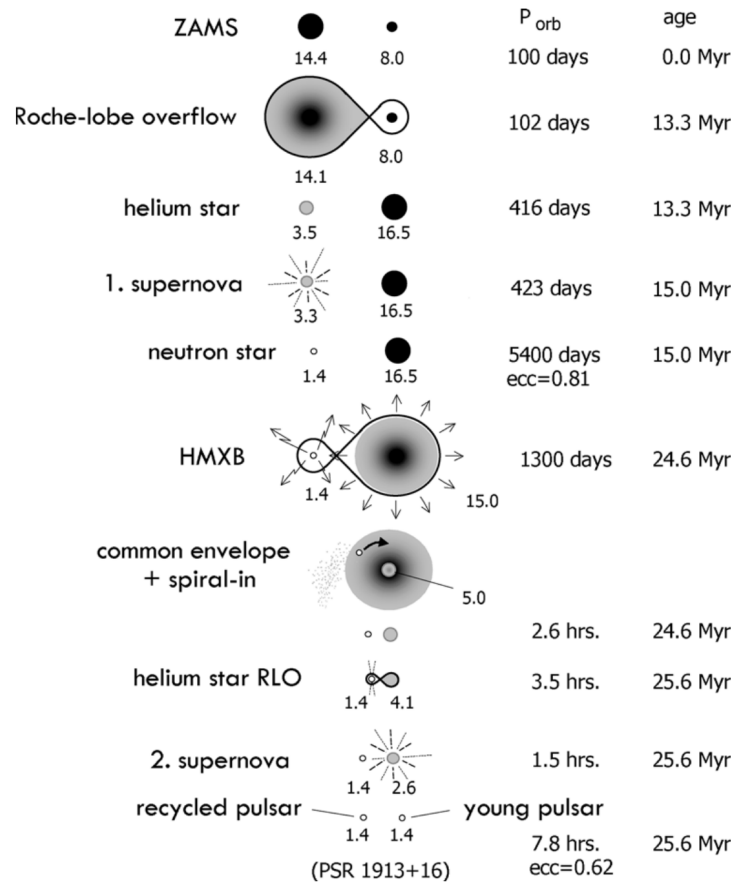


Figure 3.3: Schematic mechanism to form a Be-HMXB from two massive ZAMS stars. These systems undergo two SN explosions resulting in a close pair of two neutron stars. See Sec. 3.2.3 for a description. Directly taken from Tauris & van den Heuvel (2006).

### 3.2.4 Schematic evolution of LMXB

Similar to Sec. 3.2.3, we follow Tauris & van den Heuvel (2023) for the description of a possible formation pathway of LMXB as depicted in Fig. 3.4. Starting from a binary pair with a large mass ratio and orbital separation the more massive star evolves first on a nuclear timescale. During the evolution of the primary, mass and angular momentum loss from stellar winds will cause the binary orbit to widen. The more massive star will quickly expand filling its Roche-Lobe and quickly overshooting it, reaching the low-mass secondary in the process. This results in a common envelope leading to a spiral-in of the secondary due to angular momentum transfer to the primary's envelope which completely evaporates as a consequence. The remaining naked

helium core and the unscathed low-mass secondary will stay in a close orbit with a short orbital period where the helium star continues its evolution to eventually end in a SN type Ib/c and a neutron star remnant. Because the binary's binding energy is lower compared to the HMXB case, it may be completely disrupted by the kick velocity imparted on the newly formed neutron star. Therefore, to retain the binary, the SN kick must have a favorable direction and magnitude with respect to the orbital motion of the neutron star. A LMXB then develops either from the low-mass secondary filling its Roche-Lobe upon reaching the end of hydrogen burning ( $\tau_{\text{nuc}} \gtrsim 1$  Gyr) or if the binary orbit shrinks further for even less massive secondaries. Mass transfer onto the neutron star will proceed on a thermal timescale of the donor ( $\tau_{\text{th}} \gtrsim 100$  Myr) forming an accretion disc. The final step in the evolution of this particular binary will be a neutron star pulsar, spun up by the accretion stream, and a white dwarf remnant from the donor. With the ignition of the pulsar, the companion star will be evaporated by intense winds caused by irradiation of the accretion disc from pulsar radiation.

Another significant formation channel for LMXB is through tidal capture and multibody exchange in dense stellar environments such as globular clusters and the centers of galaxies. Indeed, several studies showed a direct association of bright X-ray sources with the position of globular clusters (Kim et al., 2009; Voss et al., 2009; Lehmer et al., 2014, 2020; Mineo et al., 2014a; Dage et al., 2019) and an increased abundance of LMXB in galaxies with high specific frequency of globular clusters (Gilfanov, 2004; Irwin, 2005; Boroson et al., 2011; Zhang et al., 2011; Lehmer et al., 2020). The direct association with globular clusters also yielded metallicity dependence as LMXB sources were found to be more abundant in metal-rich, red globular clusters than in metal-poor, blue globular clusters (Sivakoff et al., 2007; Kim et al., 2013; Cheng et al., 2018). Further studies confirmed that LMXBs follow the stellar surface density of a galaxy (Zhang et al., 2013) and that the dissolution of globular clusters may seed LMXB in the galactic field (Grindlay et al., 1984; Kremer et al., 2018).

### 3.3 X-ray Spectral Energy Distribution

This section will briefly review the classical accretion processes responsible for the X-ray emission in XRBs. We will highlight the connection of the different accretion geometries to observed spectral features and briefly touch on processes responsible for variability in XRBs. In this section, we will mostly follow the descriptions by Lewin et al. (1995); Frank et al. (2002); Tauris & van den Heuvel (2006); Done et al. (2007); Tauris et al. (2017) as well as Tauris & van den Heuvel (2023).

#### 3.3.1 Spherical accretion

A compact object moving relative to an isotropic ambient medium will accrete spherically from its environment by gravitationally focusing the medium in its wake. This is the case for isotropic accretion of the ISM by a SMBH or for BHs or neutron stars embedded in the wind of its supergiant companion, such that the gravitational capture radius is given by the Bondi-Hoyle-

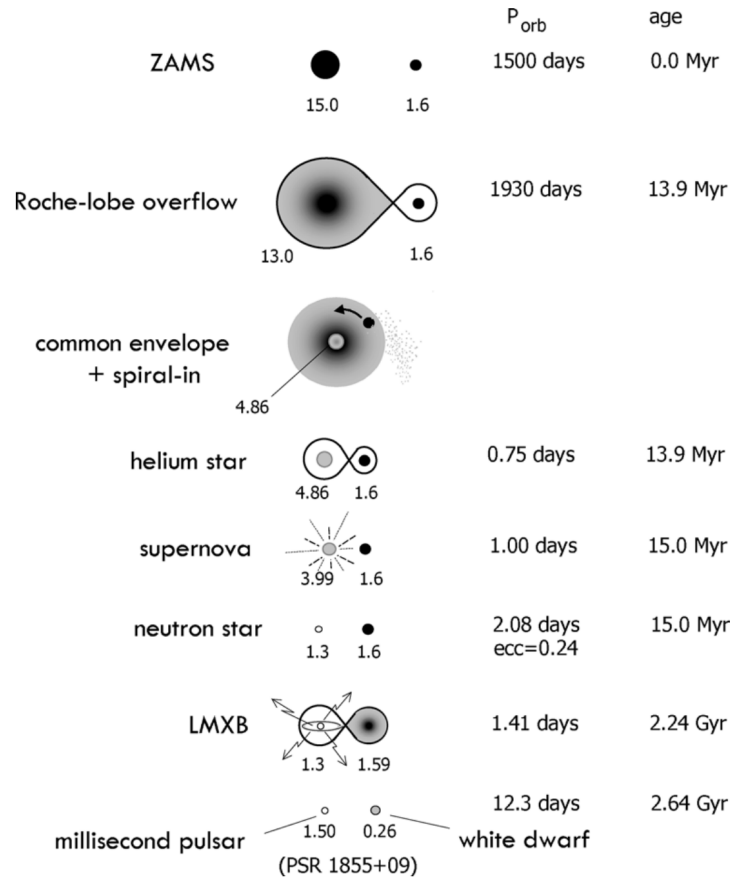


Figure 3.4: Schematic mechanism to form a typical LMXB from a binary with large initial mass ratio. The evolution of the binary culminates in a neutron star and white dwarf binary. See Sec. 3.2.4 for a description. Directly taken from [Tauris & van den Heuvel \(2006\)](#).

Lyttleton prescription ([Hoyle & Lyttleton, 1939](#); [Bondi & Hoyle, 1944](#); [Bondi, 1952](#))

$$R_g = \frac{2Gm_{\text{acc}}}{v_{\text{rel}}^2 + c_s^2}, \quad (3.11)$$

with the resulting accretion rate being

$$\dot{m}_{\text{acc}} = \frac{4\pi(Gm_{\text{acc}})^2\rho}{\left(v_{\text{rel}}^2 + c_s^2\right)^{\frac{3}{2}}}, \quad (3.12)$$

where  $G$  is Newton's gravitational constant,  $m_{\text{acc}}$  is the mass of the compact accretor,  $\rho$  is the ambient density which may be dependent on time and distance from the accretor,  $c_s = 11\sqrt{T/(10^4 \text{ K})} \text{ km s}^{-1}$  the local speed of sound, and  $v_{\text{rel}}$  is the relative velocity of the accretor with respect to the ambient medium. Focusing on the stellar wind fueling the X-ray emission of

HMXB, we consider a compact object moving through the stellar wind of its companion such that

$$v_{\text{rel}}^2 = v_{\text{wind}}^2 + v_K^2, \quad (3.13)$$

with  $v_K = \omega a \simeq 50 \text{ km s}^{-1}$  being the Keplerian velocity at orbital separation  $a$ . Stellar wind velocities are supersonic and exceed the local sound speed and orbital Keplerian speed with  $v_{\text{wind}} \gtrsim 1000 \text{ km s}^{-1}$  (Kudritzki & Puls, 2000) and typical mass-loss rates  $|\dot{M}_{\text{wind}}| \simeq 10^{-6} - 10^{-5} M_{\odot} \text{ yr}^{-1}$ . We note that the exact mass-loss rates depend on various factors such as clumping, metallicity, and absorption of the local medium (see e.g. Martínez-Núñez et al., 2017). Assuming mass conservation in an isotropic stellar wind, the wind density at orbital separation is given by the continuity equation

$$\rho(a) = \frac{|\dot{M}_{\text{wind}}|}{4\pi a^2 v_{\text{wind}}}, \quad (3.14)$$

and the accretion rate onto the compact object becomes

$$\dot{m}_{\text{acc}} = \frac{(Gm_{\text{acc}})^2 \dot{M}_{\text{wind}}}{a^2 v_{\text{wind}}^4} \simeq 10^{-4} \dot{M}_{\text{wind}}. \quad (3.15)$$

Thus, only a fraction of the stellar wind is being accreted by the compact object. Assuming direct conversion of the kinetic energy gained during infall into radiation, the resulting X-ray luminosity would be

$$L_X^{\text{acc}} = \frac{Gm_{\text{acc}}\dot{m}_{\text{acc}}}{r_{\text{acc}}} \simeq 10^{37} \text{ erg s}^{-1}, \quad (3.16)$$

where  $r_{\text{acc}}$  is the radius of the accretor and typical accretion rates are of the order  $\dot{m}_{\text{acc}} \simeq 10^{-9} M_{\odot} \text{ yr}^{-1}$ . As a consequence, the gravitational infall is eventually balanced by radiation pressure such that an upper limit on accretion rate and thus luminosity is reached. The so-called Eddington limit can be expressed as

$$L_{\text{edd}} = \frac{4\pi Gm_{\text{acc}}c}{\kappa}, \quad \dot{M}_{\text{edd}} = \frac{4\pi m_{\text{acc}}c}{\kappa\eta}, \quad (3.17)$$

where  $c$  is the speed of light,  $\kappa$  is a measure for the opacity, e.g. Thomson scattering, and  $\eta$  is an efficiency parameter. There are however further complications to the simple picture of spherical accretion. For instance, the wind velocities in the decoration discs of Be-stars are lower by an order of magnitude, much denser, and not isotropic compared to O-type stars, making the accretion rate onto a compact object highly dependent on orbital parameters. Furthermore, if the accretor is a fast-spinning, magnetized neutron star, which is the case in a majority of HMXB systems, the interaction between the magnetic field and the incoming material may inhibit the accretion flow, i.e. through magnetic or centrifugal gating (Bozzo et al., 2008; Martínez-Núñez et al., 2017). We also note that the material close to the accretor may still form temporary accretion discs.

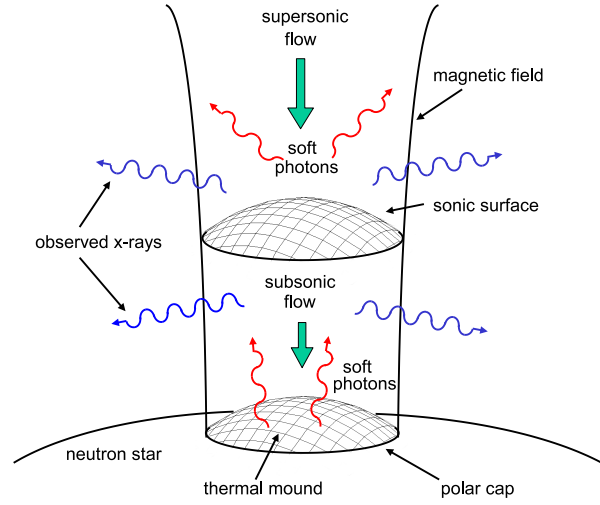


Figure 3.5: Schematic view of the accretion column of a neutron star producing X-rays. Figure taken from (Becker & Wolff, 2007).

The X-ray spectrum of wind-fed HMXB largely depends on the type of accretor. While BH accretors exhibit spectral state transitions due to the presence of a persistent accretion disc (see Sec. 3.3.2), neutron stars typically have strong magnetic fields that influence the production of X-ray emission. In the latter case, if not inhibited completely, the accreted material is funneled along the magnetic field lines onto the poles of the neutron star (see Fig. 3.5). At the magnetic poles, the accretion columns will produce X-ray emission in the form of a power-law with photon index  $\Gamma \sim 0 - 2$  with exponential cutoff at  $\sim 10$  keV (see e.g. Fornasini et al., 2023). Seed photons from the blackbody emission of neutron star's polar caps, or bremsstrahlung and cyclotron emission from the accretion columns/shocks will be Compton scattered to higher energies due to thermal electrons in the accretion flow (see Sec. 3.3.2 for a description on Compton scattering). However, no self-consistent physical model has been developed yet that can explain the variety of spectra observed in wind-fed HMXB across a broad range of accretion rates (Mushtukov & Tsygankov, 2022; Fornasini et al., 2023).

### 3.3.2 Accretion discs

If material is transported toward the compact object and retains a large fraction of its initial specific angular momentum,  $J$ , a ring will form roughly at the circularization radius

$$R_{\text{circ}} = \frac{J^2}{Gm_{\text{acc}}}. \quad (3.18)$$

The stream of material will collide with itself forming a hotspot and through viscous dissipation, the ring will spread into a disc. Accretion onto the compact object can only be accomplished by the gradual loss of angular momentum with each circular orbit closer to the accretor. Without a sink for angular momentum, such as a magnetic field, it needs to be transported outwards increasing the disc's size. The main agent for energy dissipation and angular momentum transfer is viscosity, however, the physical nature of viscosity in discs is not completely settled. A strong candidate is magneto-rotational instability where a disc permeating magnetic field is wound up by orbital shear (Balbus & Hawley, 1991). Nevertheless, some properties are independent of the viscosity in steady accretion discs.

Assuming that cooling is efficient in keeping the local sound speed of the disc super-sonic at all radii, one arrives at the thin disc approximation, where the disc is geometrically thin and optically thick, lying in the orbital plane with a small vertical extent

$$H \simeq \frac{c_s}{v_K} R \ll R, \quad (3.19)$$

and can be completely described by its surface density  $\Sigma$ . From mass and angular momentum conservation, the surface density obeys a nonlinear diffusion equation

$$\partial_t \Sigma = \frac{3}{R} \partial_R \left( \sqrt{R} \partial_R \left[ \nu \Sigma \sqrt{R} \right] \right), \quad (3.20)$$

where  $\nu$  is the viscosity. For a steady state accretion disc,  $\partial_t \Sigma = 0$ , which implies

$$\nu \Sigma = \frac{\dot{M}}{3\pi} \left[ 1 - \beta \sqrt{\frac{R_{\text{in}}}{R}} \right], \quad (3.21)$$

where  $\dot{M}$  is the mass transport through the disc, and  $\beta$  depends on the boundary conditions at the inner disc edge  $R_{\text{in}}$ . For a non-rotating star,  $\beta = 1$ , and  $R_{\text{in}} = R_{\text{acc}}$  is at the surface of the accretor which we will assume for the following. From viscous dissipation, one arrives at an expression for the disc surface temperature

$$T(R) = \left[ \frac{3Gm_{\text{acc}}\dot{M}}{8\pi R^3 \sigma_{\text{SB}}} \left( 1 - \sqrt{\frac{R_{\text{in}}}{R}} \right) \right]^{\frac{1}{4}}, \quad (3.22)$$

where  $\sigma_{\text{SB}}$  is the Stefan-Boltzmann constant. Assuming black-body radiation and accounting for the two-sided geometry of the disc, the total radiated luminosity is

$$L = \frac{1}{2} \frac{Gm_{\text{acc}}\dot{M}}{R_{\text{acc}}}, \quad (3.23)$$

which is exactly half the potential energy per unit time of an infalling mass element. The remaining energy is available at the accretor's boundary layer causing outflows which is therefore equally important to understand the total emission of the disc.

A useful parametrization for viscosity in the accretion disc is given by the  $\alpha$ -viscosity prescription (Shakura & Sunyaev, 1973)

$$\nu = \alpha c_s H, \quad (3.24)$$

assuming that random motions can not exceed the disc height and that supersonic motions are dissipated in shocks. This would require  $\alpha \lesssim 1$  which is supported by observations of dwarf novae in cataclysmic variables.

While the thin disc picture appears to be a reasonable approximation for most systems, a more complete picture of the accretion geometry is required for XRB (Done et al., 2007; Zdziarski et al., 2021). In fact, the standard picture of accretion discs in XRB systems is a truncated advection disc model, which includes a thin cold disc transitioning into a hot inner accretion flow at the truncation radius (see Fig. 3.6). The thin disc will flare at large radii due to the injection of turbulence from the Roche-Lobe accretion stream interacting with the disc. The energy released by the accretion disc produces regions of hot coronal plasma with thermal electrons on both sides of the disc at a plasma temperature of  $k_B T \simeq 100$  keV. Soft seed photons emitted by the accretion disc with energies  $E < 4k_B T$  will be Compton scattered to higher energies leading to cooling of the coronal plasma. Each scattering event provides an increase in energy equivalent to the Compton amplification factor,  $A$ ,

$$A = \frac{4k_B T - E}{m_e c^2}, \quad (3.25)$$

where  $k_B T$  is the temperature of the plasma,  $E$  is the photon energy, and  $m_e c^2 = 511$  keV is the rest mass of the electron. The average number of scattering events  $N$  is determined by the Thomson optical depth  $\tau$  of the plasma, such that  $N \propto \tau$  for an optically thin medium, and  $N \propto \tau^2$  for  $\tau \gg 1$ . A photon undergoing  $N$  scattering events will gain a total amount of energy equal to

$$y = A \times N = \frac{4k_B T}{m_e c^2} \max(\tau, \tau^2), \quad (3.26)$$

where  $y$  is the Compton optical depth or Compton  $y$ -parameter. Ultimately, the Compton scattering of soft seed photons leads to a power-law distribution in photon energies. The power-law slope,  $\Gamma$ , is connected to the optical thickness,  $\tau$ , through the following relation

$$\Gamma = \sqrt{\frac{9}{4} + \frac{3m_e c^2}{k_B T \left[ \left( \tau + \frac{3}{2} \right)^2 - \frac{9}{4} \right]}} - \frac{1}{2}, \quad (3.27)$$

which is a solution to the Kompaneets equation (see Longair, 2011, for a derivation). We note that the relations discussed for the truncated disc model only apply to BH accretors. In cases where the accretor is a neutron star, magnetic interactions and the solid surface of the neutron star need to be considered since they alter the accretion geometry considerably.

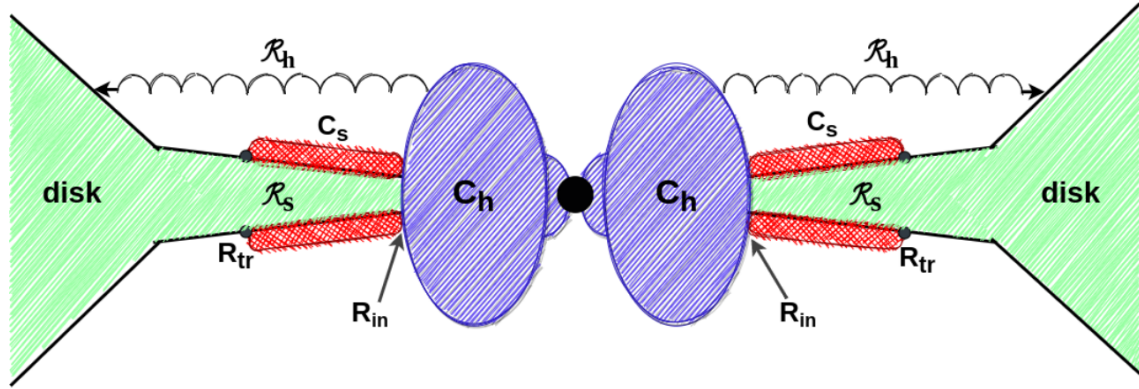


Figure 3.6: Schematic illustration of the accretion geometry of a truncated disc with truncation radius  $R_{in}$ . The disc is covered by a Comptonizing coronal plasma,  $C_s$ , from  $R_{in}$  to  $R_{tr}$ . Inside of  $R_{in}$ , a hot accretion flow with large scale height,  $C_h$ , covers the central object. Both comptonization regions,  $C_s$  and  $C_h$ , give rise to softer or harder power-law components, respectively. Emission from  $C_h$  is reflected from a flared disc beyond  $R_{tr}$ , denoted here as  $R_h$ . Part of the emission from  $C_s$  is reflected from the disc beneath, denoted here as  $R_s$ . Figure taken and description adapted from [Zdziarski et al. \(2021\)](#) who studied the accretion geometry around BH LMXB *Maxi J1820+070*.

### 3.3.3 Variability

The majority of XRB systems experience some form of variable behavior. For instance, most BH XRB appear to cycle through different spectral states where the hardness of the spectrum, the ratio of hard to soft X-ray photons, depends non-trivially on the total luminosity of the system. This hysteresis is attributed to the non-stationary behavior of the accretion flow ([Done et al., 2007](#)). Nonetheless, the truncated disc model is an elegant explanation for the different spectral states in those systems as various aspects of the accretion geometry are only expressed for certain accretion rates. We show this transitional behavior in Fig. 3.7 (see [Done et al., 2007](#)). At low luminosities, Compton cooling of electrons is inefficient which leads to a hard power-law spectrum from the presence of the hot inner accretion flow often accompanied by radio emission from a jet. At high luminosities, Compton cooling is efficient leading to the breakdown of the hot coronal plasma. The accretion flow collapses into a thin disc which produces a soft black-body spectrum. Intermediate states are also observed where the spectra show signs of both a hot coronal plasma and a disc component.

Other modulations of the X-ray luminosities of XRB and their spectra on short timescales are also observed which we will briefly highlight here. So-called X-ray bursts can be observed in XRB hosting a neutron star. These bursts are thermonuclear explosions of material deposited on the neutron star's surface and last up to several minutes. The accretion disc in LMXB may show signs of precession and warps which have periods different from the orbital period of the binary. Eccentric orbits in Be-HMXB lead to transient behavior because the compact object may only accrete sufficiently in the orbital periastron. Some HMXB show signs of pulsations due to wind

instabilities of fast-rotating Wolf-Rayet stars. Quasi-periodic oscillations are also seen in BH XRB which are either caused by the frame-dragging Lense-Thirring effect of a rotating compact object or oscillatory instabilities in the accretion disc.

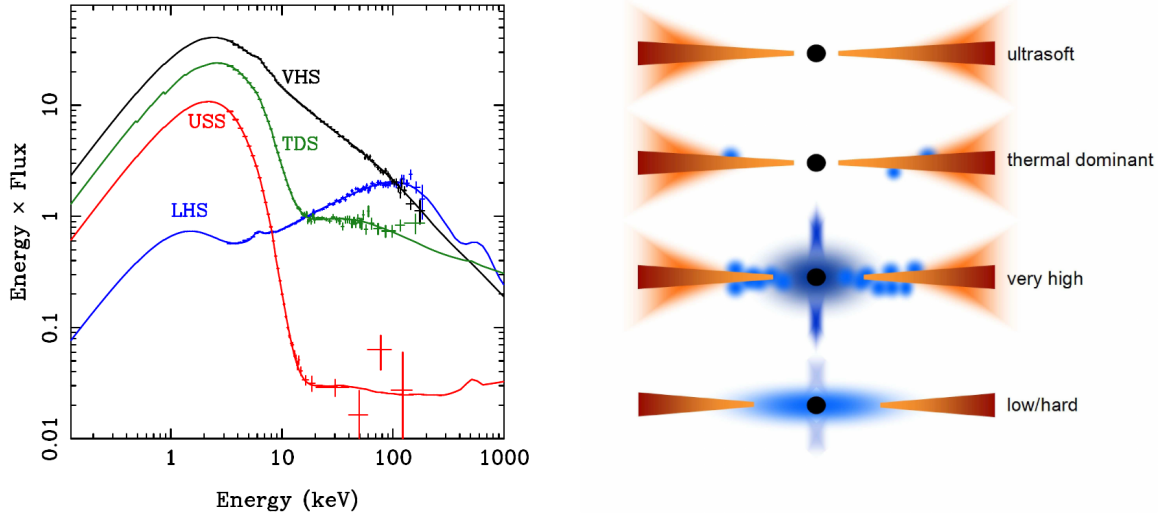


Figure 3.7: Transitions of the accretion flow in BH LMXB causing different spectral states. The left panel shows the X-ray spectrum of the associated state in the right panel. The ultra-soft state (USS) arises from a stable thin accretion disc. The thermally dominant state (TDS) shows a black body spectrum from the disc in addition to a weaker power-law tail caused by pockets of hot coronal plasma from the increasing temperature in the disc. The very high state (VHS) is the transition point where the inner disc starts to break down because of evaporation and a large inner Comptonization region emerges. In this phase, a radio jet is forming. In the low/hard state, the hot Comptonizing plasma replaces the thin accretion disc such that the hard X-ray power law emerges together with a radio jet. Figure directly taken and description adapted from (Done et al., 2007)

### 3.4 Scaling relations

With the advent of the *Chandra* X-ray telescope and its high spatial resolution, the detailed study of extragalactic XRB systems became possible. In this section, we will highlight some of the key findings regarding the populations of XRB and their properties while mostly following the summary of Gilfanov et al. (2022).

From the evolutionary considerations for XRB and binary systems we discussed above, HMXB should dominate young stellar environments because of the short timescales involved in stellar evolution and binary interaction. In contrast, the evolution of LMXB requires significantly more time, such that LMXB lose their connection with the star-formation event that created them. Therefore, a commonly used proxy discriminating the two XRB populations is the specific star-formation rate (sSFR) which is the ratio of SFR and stellar mass ( $M_*$ ) over a region of a

galaxy

$$\text{sSFR} = \frac{\text{SFR}}{M_*}. \quad (3.28)$$

Typically, a galaxy is dominated by the emission from HMXB if  $\text{sSFR} \geq 10^{-10} \text{ yr}^{-1}$  while LMXB are dominant in galaxies with  $\text{sSFR} \leq 10^{-12} \text{ yr}^{-1}$  (Lehmer et al., 2010).

The study of LMXB in QG led to the conclusion that the number of LMXB,  $N_{\text{LMXB}}$ , and their collective X-ray luminosity in the 0.5 – 8 keV band,  $L_X^{\text{LMXB}}$  is proportional to the stellar mass (Gilfanov, 2004; Zhang et al., 2011, 2012), such that

$$N_{\text{LMXB}}(l_X > 10^{37} \text{ erg s}^{-1}) \approx 14 \times \frac{M_*}{10^{10} M_\odot}, \quad L_X^{\text{LMXB}} \approx 8 \cdot 10^{38} \times \frac{M_*}{10^{10} M_\odot} \text{ erg s}^{-1}, \quad (3.29)$$

where  $l_X$  is the X-ray luminosity of an individual XRB. The distribution of LMXB mainly follows the stellar density profiles (Zhang et al., 2013). Still, there is evidence for contribution from globular cluster seeding both from LMXB density being higher than expected at a few effective radii of the galaxy and a higher formation efficiency in globular clusters (Borson et al., 2011; Zhang et al., 2011; Lehmer et al., 2020). The number of LMXB systems is expected to increase over time because of the long X-ray bright phase of these systems, more low-mass stars evolving with  $\tau_{\text{nuc}} \geq 1 \text{ Gyr}$ , and an increase in tidal interactions in globular clusters. Indeed, there is observational evidence for old QG hosting more LMXB compared to young QG (Zhang et al., 2012; Lehmer et al., 2019).

For HMXB it was convincingly shown that their number and total X-ray luminosity scales linearly with SFR (Grimm et al., 2003; Lehmer et al., 2010; Mineo et al., 2012a; Sazonov & Khabibullin, 2017a) such that the X-ray emission of SFG can be used as an independent tracer for star-formation compared to traditional estimators such as  $H_\alpha$ , UV or far-infrared emission. The resulting scaling relations are of the order

$$N_{\text{HMXB}} \approx 10 \times \frac{\text{SFR}}{M_\odot \text{ yr}^{-1}}, \quad L_X^{\text{HMXB}} \approx 2 \cdot 10^{39} \times \frac{\text{SFR}}{M_\odot \text{ yr}^{-1}} \text{ erg s}^{-1}. \quad (3.30)$$

A time dependence of the number of HMXB sources in a galaxy is also observed from spatially resolved studies of the star-formation history of individual galaxies (Shtykovskiy & Gilfanov, 2007; Antoniou et al., 2019). From binary evolution, it is expected that HMXBs start appearing with a delay compared to a star-formation event also given a decline in supernova rate with time (Shtykovskiy & Gilfanov, 2005b; Antoniou et al., 2019). We show the scaling relations between XRB X-ray luminosity and SFR or stellar mass of the host galaxies for HMXB and LMXB, respectively, in Fig. 3.8, based on Eq. (3.30) and (3.29). Since both types of XRB are present to varying degrees in galaxies, their disentanglement can be particularly challenging for distant galaxies even with high spatial resolution. A useful alternative formulation for the scaling relations was employed by Lehmer et al. (2010) which allowed for simultaneous determination of the contribution from the two classes

$$\frac{L_X}{\text{SFR}} = \beta + \alpha \text{ sSFR}^{-1}, \quad (3.31)$$

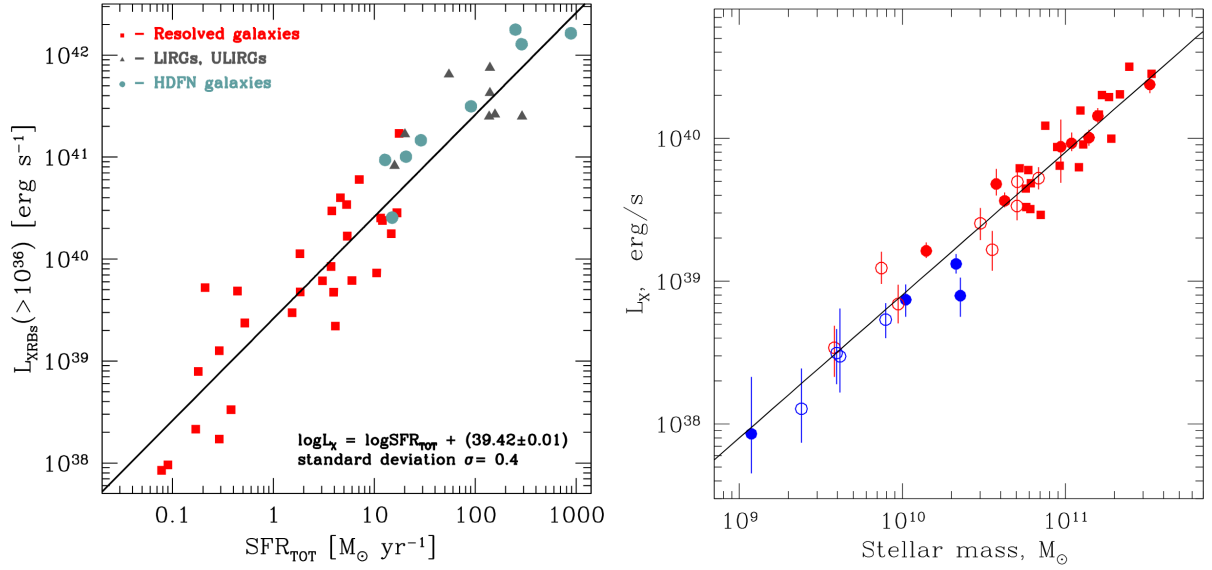


Figure 3.8: *Left*: Dependence of the total X-ray luminosity of HMXB on star-formation rate for resolved star-forming galaxies (red). The solid black line indicates the best-fit linear relation with numbers given in the figure legend. Additional data points are given for star-burst galaxies (ULIRGs, grey) and unresolved Chandra deep field galaxies (teal) for which total luminosities including gas and potentially AGN emission are included. Figure is directly taken from Mineo et al. (2012a). *Right*: Dependence of the total X-ray luminosity of LMXB on stellar mass for elliptical (red) and spiral galaxies (blue). The luminosity of some galaxies is additionally taken within smaller annuli (thus smaller mass) denoted as open symbols. The solid black line indicates the linear regression of the data. Figure is directly taken from Gilfanov et al. (2022).

where  $\log \beta [\text{erg s}^{-1} (\text{M}_{\odot} \text{yr}^{-1})^{-1}] = 39.71^{+0.14}_{-0.09}$  and  $\log \alpha [\text{erg s}^{-1} \text{M}_{\odot}^{-1}] = 29.25^{+0.07}_{-0.06}$  track the contribution from HMXB and LMXB, respectively (see also Lehmer et al., 2019; Inoue et al., 2021). The simultaneous occurrence of both XRB types leads to a combined X-ray luminosity function (XLF) where the respective contribution of LMXB and HMXB depends on the age of the underlying stellar population (Lehmer et al., 2017; Gilbertson et al., 2022). Therefore, the clear dependence of the X-ray luminosity of galaxies on stellar mass and SFR prompted studies on the redshift evolution of the galaxy main sequence (Lehmer et al., 2016; Aird et al., 2017).

The luminosity distribution of individual XRB can be summarized in an X-ray luminosity function (XLF). The shape of the XLF for HMXB follows a simple power-law relation

$$\frac{dN}{dl_X} \propto \text{SFR} \times l_X^{-1.6}, \quad (3.32)$$

where the power-law slope appears to be universal and only the normalization scales linearly with SFR (Grimm et al., 2003; Mineo et al., 2012a; Sazonov & Khabibullin, 2017a; Lehmer et al., 2019). Similarly, the normalization of the XLF for LMXB scales with the total stellar mass  $M_*$ , however, it has a more complex shape with up to two breaks. One of the breaks coincides with the

Eddington luminosity of an accreting neutron star,  $l_X \approx 3 \cdot 10^{37} \text{ erg s}^{-1}$ , suggesting a luminosity limit for neutron star systems with an accretion disc (Revnivtsev et al., 2011). The nature of the second break at higher luminosities,  $l_x \approx 5 \cdot 10^{38} \text{ erg s}^{-1}$ , is still unclear (Gilfanov et al., 2022).

Studies on the effect of metallicity showed an anti-correlation between the integrated X-ray luminosity of HMXBs in galaxies and their metallicity (Mapelli et al., 2009; Brorby et al., 2016; Fornasini et al., 2020; Lehmer et al., 2021). In Lehmer et al. (2021), they also showed that the luminosity function of HMXB is sensitive to metallicity such that low metallicity environments harbor more luminous HMXB. This behavior may be attributed to weaker stellar winds in massive stars with low metallicity allowing for tighter orbits of the compact object. This leads to a higher probability of systems undergoing atmospheric RLO due to the evolution of the massive donor and thus a higher number of luminous X-ray sources (Linden et al., 2010; Wiktorowicz et al., 2017). Consequently, RLO HMXBs are a strong candidate for ultra-luminous XRB sources with luminosities  $L_X \geq 5 \cdot 10^{39} \text{ erg s}^{-1}$  which share many of the properties discussed here (Linden et al., 2010; Sazonov & Khabibullin, 2017b; Wiktorowicz et al., 2017; Gilfanov et al., 2022).

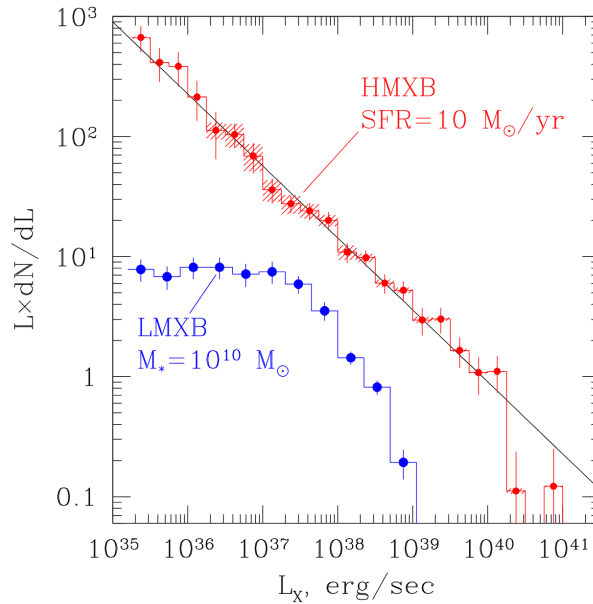


Figure 3.9: Example X-ray luminosity functions for HMXB (red) and LMXB (blue) for a galaxy with stellar mass  $M_* = 10^{10} M_{\odot}$  and star-formation rate  $\text{SFR} = 10 M_{\odot} \text{ yr}^{-1}$ . The figure is directly taken from (Gilfanov et al., 2022).

## **Part II**

### **X-ray binaries in simulated galaxies**



## 4 | Magneticum Pathfinder Simulations

While observations of astrophysical objects can in general only provide a snapshot of their current physical state, their full evolution across cosmic time happens on timescales much longer than the rise and fall of human civilization. In that respect, assembling the full history of e.g. galaxy evolution in the universe can only be done in a statistical manner by connecting observations of similar objects across different epochs of the universe. With the advent of increasingly powerful computational resources by the end of the 20th century however, it became possible to simulate accurate numerical representations of astrophysical processes in much higher resolution and precision.

### 4.1 A brief history on cosmological simulations

In the context of cosmic structure formation for instance, pioneering simulations of non-linear gravitational collapse of overdensities established the current picture of the CDM scenario (Davis et al., 1985; Frenk et al., 1985; White et al., 1987; Frenk et al., 1988), also due to remarkable resemblance to the observed clustering of matter in the real universe. For such simulations of collisionless matter, it is sufficient to solve the equation of motions by solely relying on gravitational interaction between  $N$  particles which is achieved by employing dedicated numerical techniques. Their goal is to try to minimize the computational cost while still retaining sufficient accuracy and can be based on particle-particle (PP) or particle-mesh methods (PM), tree structures, or hybrid methods such as the Tree-PM solver implemented in GADGET 2 (Springel, 2005).

While these early simulations only included dark matter, including baryonic matter in such large-scale simulations could also be useful in predicting observables directly from the simulations. Unavoidably, the treatment of baryons requires solving hydrodynamical equations of motion due to significant interaction between fluid elements in addition to gravity. There are two main methods to numerically approach hydrodynamic interactions: the grid-based, Eulerian codes or the Smoothed-Particle Hydrodynamics (SPH), Lagrangian codes. The grid-based approach spatially discretizes a fluid into grid cells and solves the fluid equations for each grid cell (Kravtsov et al., 1997). The SPH approach discretizes the fluid density into particles and hydrodynamical properties at their location are computed by smoothing over their respective neighboring particles (see e.g. Price, 2012).

Within a simulated sub-volume, the formation of structure can now be followed self-consistently and observables in principle arise directly from the baryonic component tracked by simulations.

However, because of the scales involved in a cosmological setting as well as computational restrictions, it is not feasible to implement arbitrarily detailed prescriptions of physical processes, i.e. for star formation, mechanical or radiative feedback, in such simulations. Instead, such phenomena are typically treated either in an effective manner and depend on the scientific goal. Nevertheless, they produce sufficiently robust results for a large range of astrophysical applications.

For instance, star-formation models within a multi-phase medium calibrated to density and temperature criteria (Katz, 1992; Katz et al., 1996; Springel & Hernquist, 2003) or to empirical relations of the surface density of molecular hydrogen in galaxies (Murante et al., 2015) or the inclusion of SN feedback (Navarro & White, 1993; Scannapieco et al., 2006) are employed in a cosmological framework. Of particular importance for X-ray emission of galaxies are descriptions for chemical enrichment and gas cooling (Yoshida et al., 2003; Tornatore et al., 2004, 2007; Maio et al., 2007, 2010), as well as the treatment of AGN feedback (Di Matteo et al., 2005; Sijacki & Springel, 2006; Sijacki et al., 2007; Fabjan et al., 2010; Teyssier et al., 2011) and thermal conduction (Dolag et al., 2005; Beck et al., 2016).

With ever-improving computational resources at large computational facilities in recent years, increasingly larger volumes could be simulated at higher resolution. Up to now, several large simulation campaigns, such as *Magneticum* (Dolag et al., 2016), *Illustris* (Vogelsberger et al., 2014), *EAGLE* (Schaye et al., 2015), *Horizon-AGN* (Kaviraj et al., 2017), *IllustrisTNG* (Pillepich et al., 2018) or *SIMBA* (Davé et al., 2019), made use of a large variety of different physics modules and hydrodynamic solvers in order to specifically target galaxy evolution experiments. The goal of these large cosmological box simulations is to have a statistical representation of a sub-volume of the universe. Within those sub-volumes the population of emerging galaxies can be studied in different environments. Their resulting properties can then be benchmarked and compared to the properties of galaxies in the real universe in order to better understand the physics involved in their formation.

### **Aim of the thesis**

This thesis will aim to analyze predictions of hydrodynamical cosmological simulations regarding galaxy evolution. In particular, the main focus will be on the X-ray properties of galaxies by analyzing their simulated ISM, CGM, and their connection to the large-scale filamentary structure. For this purpose, we will first describe the particular cosmological simulation used for the analysis in this work, namely *Magneticum Pathfinder Simulations* (or just *Magneticum*). Rather than including directly the X-ray emission of astrophysical objects and its influence on structure formation in the simulation, we perform a post-processing step in which intrinsic properties of the simulation are used to infer their X-ray emission (see Chap. 5). A novelty in the post-processing step of the simulation is the inclusion of XRB populations which are based on scaling relations and evolutionary pathways presented in previous chapters. The exact description of this model, its verification, and its predictions are presented in Chap. 6. We then use this model to further analyze the predictions of X-ray emission in the large-scale environment of simulated galaxies and how XRB contribute as a source of contamination (Chap. 7). Lastly, we will give preliminary results on X-ray emission from filaments in the cosmic web in which galaxies are embedded.

In the following, we will introduce *Magneticum* in more detail as a series of state-of-the-

art hydrodynamical cosmological simulations on which the results of this work are based. We will further highlight important physical modules employed in the simulation that are needed to interpret the results presented in this thesis.

## 4.2 Magneticum

– *This section has partially been published in Vladutescu-Zopp et al. (2023).*

*Magneticum*<sup>1</sup> is a series of state-of-the-art hydrodynamical cosmological simulations that explore varying ranges in particle number, volume, and resolution. They are based on an improved version of the N-body code GADGET 3, which is an updated version of the code GADGET 2 (Springel, 2005), which uses the SPH approach for the hydrodynamics. The code introduces several improvements regarding the SPH implementation by including a treatment of viscosity and artificial conduction (Dolag et al., 2005; Beck et al., 2016). The inclusion of thermal conduction is based on Jubelgas et al. (2004) with improvements by Arth et al. (2014).

Additional physical processes describing the evolution of the baryonic component have been implemented. They encompass radiative gas cooling as described in Wiersma et al. (2009), heating from a uniform time-dependent UV background (Haardt & Madau, 2001) and a sub-resolution model for star-formation with mass-loading rate proportional to SFR and resulting wind-velocities of  $v_w = 350 \text{ km s}^{-1}$  (Springel & Hernquist, 2003). A treatment for chemical enrichment of the gaseous component through stellar evolution has been implemented following the prescription of Tornatore et al. (2004, 2007). Furthermore, a prescription of SMBH growth through mergers and gas accretion, powering energy feedback for AGN, was implemented following Springel et al. (2005) and Di Matteo et al. (2005) with modifications following Fabjan et al. (2010). It was further improved and tested in the works by Hirschmann et al. (2014); Steinborn et al. (2015).

Further details on the description of the simulations can be found in Dolag et al. (2016). Table 4.1 summarizes all available simulated volumes of the simulation together with their resolution. For the results presented in chapter 6 and 7 we made use of the *Box4/ubr* volume which is highlighted in table 4.1.

The advantage of *Box4/ubr* is its ultra-high resolution together with the large simulated volume. The former allows for a physically reliable picture of galaxies with total stellar mass  $M_* > 10^{10} M_\odot$  at or below the stellar mass of the MW<sup>2</sup> and for which included physical processes are resolved. In the case of *Box4/ubr*, stellar particles have a mass of  $0.25 m_{\text{gas}}$  (see Sec. 4.2.1 which would correspond to a few thousand stellar particles per galaxy. The total volume of  $(48 \text{ cMpc } h^{-1})^3$  allows probing smaller wavenumbers in the initial power spectrum of density fluctuations and can thus represent larger overdensities. In this case, this leads to the formation of a few galaxy groups and small galaxy clusters below  $M_{\text{halo}} \lesssim 10^{14} M_\odot$  which offers a diverse environment for galaxies. Initial conditions for the simulations are generated using standard  $\Lambda$ CDM cosmology using results from the Wilkinson Microwave Anisotropy Probe (WMAP) (Komatsu et al., 2011), with Hubble parameter  $h = 0.704$ , matter density  $\Omega_M = 0.272$ , dark

<sup>1</sup>Project web page: [www.magneticum.org](http://www.magneticum.org). PI: Klaus Dolag

<sup>2</sup>The MW stellar mass is estimated to be  $M_*^{\text{MW}} \approx 5 \cdot 10^{10} M_\odot$ .

	Size [cMpc $h^{-1}$ ]	Resolution	$N_{\text{part}}$	$m_{\text{DM}}$ [ $M_{\odot} h^{-1}$ ]	$m_{\text{gas}}$ [ $M_{\odot} h^{-1}$ ]	$\epsilon_{\text{DM/gas}}$ [ckpc $h^{-1}$ ]	$\epsilon_{\text{star}}$ [ckpc $h^{-1}$ ]
Box0	2688	mr	$2 \times 4536^3$	$1.3 \times 10^{10}$	$2.6 \times 10^9$	10	5
Box1	896	mr	$2 \times 1526^3$	$1.3 \times 10^{10}$	$2.6 \times 10^9$	10	5
Box2b	640	hr	$2 \times 2880^3$	$6.9 \times 10^8$	$1.4 \times 10^8$	3.75	2
Box2	352	mr	$2 \times 594^3$	$1.3 \times 10^{10}$	$2.6 \times 10^9$	10	5
		hr	$2 \times 1584^3$	$6.9 \times 10^8$	$1.4 \times 10^8$	3.75	2
Box3	128	mr	$2 \times 216^3$	$1.3 \times 10^{10}$	$2.6 \times 10^9$	10	5
		hr	$2 \times 576^3$	$6.9 \times 10^8$	$1.4 \times 10^8$	3.75	2
		uhr	$2 \times 1536^3$	$3.6 \times 10^7$	$7.3 \times 10^6$	1.4	0.7
<b>Box4</b>	48	mr	$2 \times 81^3$	$1.3 \times 10^{10}$	$2.6 \times 10^9$	10	5
		hr	$2 \times 216^3$	$6.9 \times 10^8$	$1.4 \times 10^8$	3.75	2
		<b>uhr</b>	<b><math>2 \times 576^3</math></b>	<b><math>3.6 \times 10^7</math></b>	<b><math>7.3 \times 10^6</math></b>	<b>1.4</b>	<b>0.7</b>
Box5	18	hr	$2 \times 81^3$	$6.9 \times 10^8$	$1.4 \times 10^8$	3.75	2
		uhr	$2 \times 216^3$	$3.6 \times 10^7$	$7.3 \times 10^6$	1.4	0.7
		xhr	$2 \times 576^3$	$1.9 \times 10^6$	$3.9 \times 10^5$	0.75	0.25

Table 4.1: Available volumes for *Magneticum* with their respective resolution. Sizes are the side length of the box in comoving units.  $N_{\text{part}}$  is the total initial particle number including dark matter and gas.  $m_{\text{DM}}$  and  $m_{\text{gas}}$  are the particle masses of dark matter and gas, respectively.  $\epsilon$  is the gravitational softening for dark matter, gas and stars assuming a Plummer potential.

energy density  $\Omega_{\Lambda} = 0.728$ , baryon density  $\Omega_b = 0.0451$  and normalization of the fluctuation amplitude at 8 Mpc  $\sigma_8 = 0.809$ .

### 4.2.1 Sub-grid star-formation

One of the main goals of this thesis is the introduction of a post-processing step to sample XRB from simulation data. It is therefore necessary to briefly introduce the core aspects of the star-formation model in *Magneticum*. The star-formation model in *Magneticum* is based on the model of [Springel & Hernquist \(2003\)](#). Baryons are distinguished into an ISM, with a hot and cold phase, and stars. The phases are allowed to interact through various processes. For instance, radiative cooling enables hot gas to move into the cold phase. Feedback from SNe leads to the heating of the cold ISM and the evaporation of cold clouds, the ejection of galactic winds, and the enrichment of the ambient gas with metals. The equilibrium temperature of the hot phase is regulated by SNe under the assumption that the timescale to reach thermal equilibrium,  $t_{\text{cool}}$  (see Eq. (1.10)), is shorter than dynamical timescale  $t_{\text{dyn}}$  (see Eq.(1.11)). The model requires a free parameter for the star-formation timescale  $t_0^* \approx 2.1$  Gyr which is calibrated to the observationally

constrained Schmidt-Kennicutt relation between surface gas density and SFR density (Kennicutt, 1998; Springel & Hernquist, 2003).

The ISM is then described by spatially averaged properties and global dynamics of the underlying ambient gas distribution. Each SPH fluid element represents a portion of the ISM assuming that supposed cold clouds are in pressure equilibrium with the hot ambient gas above a given threshold density  $\rho_{th}$ . In fact, cold clouds remain unresolved in this scheme where their statistical properties are inferred from energy transfer rates calculated in the background. Further heating of the hot ambient gas by energy injection from SNe ultimately sets the cloud evaporation efficiency. The threshold density is then computed self-consistently by requiring that the hot-phase temperature at the threshold is equal to the thermal instability temperature and the specific effective energy changes continuously (Springel & Hernquist, 2003; Tornatore et al., 2004, 2007).

If the density threshold is exceeded ( $\rho > \rho_{th}$ ), the gas particle will be transformed into a stellar particle on a characteristic timescale

$$t_* = t_0^* \left( \frac{\rho}{\rho_{th}} \right)^{-\frac{1}{2}}. \quad (4.1)$$

The resulting star-formation rate  $\dot{m}_*$  can then be expressed following the stochastic approach of Katz et al. (1996)

$$\dot{m}_* = (1 - \beta) \frac{x \cdot m}{t_*}, \quad (4.2)$$

where  $\beta = 0.1$  is the fraction of stars exploding as SNe type II,  $m$  the total mass of the gas particle and  $x$  the cold gas fraction in the particle which is computed in the background. The expected mass of stars formed in a time interval  $\Delta t$  follows from Eq.(4.2) as

$$m_* = m \left\{ 1 - \exp \left( - \frac{(1 - \beta)x \Delta t}{t_*} \right) \right\}. \quad (4.3)$$

In the simulation, a star particle will then be created from a gas particle if a uniform random number  $p \in [0, 1]$  falls below the probability

$$p < \frac{m}{m_*} \left\{ 1 - \exp \left( - \frac{(1 - \beta)x \Delta t}{t_*} \right) \right\}. \quad (4.4)$$

The newly formed star particle will copy the dynamical state and position of its former parent gas particle whose mass will be reduced by  $m_*$ . This setup allows gas particles to be the site of multiple such star-formation events, if the resulting mass of the star particle only has a fraction of the mass of its parent,  $m_* = m/N_*$ . Up to  $N_* = 4$  generations of stars can be created from a single gas particle in *Magneticum*, where the gas particle vanishes if the gas particle forms its  $N_*$ -th generation of stars. From the point of their creation, star particles will decouple from the SPH

treatment and act collisionless, only interacting through gravity. While the global SFR is well approximated within the simulated volume, the stochastic approach presented in Eq. (4.4) can lead to localized bursts of star formation. Each newly formed star particle represents a Simple Stellar Population (SSP) in which a collection of stars follow a common IMF and share metallicity at a common time of birth.

In *Magneticum*, stars within SSPs are distributed according to a Chabrier-like IMF (Chabrier, 2003). The mass fraction of stars above  $40 M_{\odot}$  in a SSP is immediately returned to the ISM through SN feedback after the formation of the SSP because the lifetime of those stars is shorter than the temporal resolution of the simulation (see Eq.(6.6)). In addition, the mass of stellar particles decreases continuously during the simulation because of stellar evolution which returns metal-enriched gas to the hot phase (Tornatore et al., 2007).

### 4.2.2 AGN feedback

Another physical process crucial to understanding galaxy evolution is feedback from actively accreting SMBHs because it can directly regulate star formation (see Sec. 1.2.1 and 2.2). In *Magneticum*, SMBHs are treated as collisionless sink particles<sup>3</sup> following the implementation of Springel et al. (2005) with improvements regarding their dynamics and feedback model. SMBHs are seeded during the runtime of the simulation by identifying gravitationally bound stellar structures (i.e. galaxies) using a friends-of-friends algorithm. If the mass of the bound stellar structure exceeds a mass threshold  $M_{*,\text{th}}$ , the star particle at the bottom of the potential is converted to a SMBH particle. The seed mass of SMBH particles is thereby firmly below observed relations between total stellar mass and SMBH mass (see e.g. McConnell & Ma, 2013) to prevent abrupt heating of the surrounding gas.

Their mass growth through mergers is only allowed if the relative velocity of two close SMBH particles is less than half the sound speed of the surrounding gas if their relative distance is small compared to the softening length, and if they are gravitationally bound. Mass growth through gas accretion follows Eq. (3.12) with an additional boost factor  $\alpha = 100$  to account for the limited resolution of the simulation (Springel et al., 2005). Since the actual accretion flow onto the SMBH particles is unresolved, gas particles in the vicinity of the SMBH particle lose a fraction of their mass which is added to the SMBH

$$\Delta M_{\bullet} = (1 - \eta) \dot{M} \Delta t, \quad (4.5)$$

with  $\eta$  being the fraction of mass remaining in the ISM. In this way, gas particles can contribute to accretion more often which allows for a more continuous description of accretion (Springel et al., 2005).

The total radiated energy for SMBH particle can be estimated from the accretion rate as

$$L_{\bullet, \text{bol}} = \epsilon_r \dot{M} c^2, \quad (4.6)$$

---

<sup>3</sup>Sink particles are a numerical workaround in collapse calculations to avoid issues with time integration. They effectively mask high-density regions beyond a certain threshold.

with radiative efficiency  $\epsilon_r \approx 0.1$  according to accretion disc theory for a Schwarzschild BH (Shakura & Sunyaev, 1973; Springel et al., 2005), and  $c$  the speed of light. This follows from equation (3.23) using three Schwarzschild radii as the innermost stable orbit for a non-rotating BH  $R_{in} = 3R_S = 6GM/c^2$ . Missing factors and uncertainties in the actual accretion geometry are then accounted for by  $\epsilon_r$ . The fraction of the radiated energy that is then coupled back to the surrounding gas in the simulation can be expressed as

$$\dot{E}_f = \epsilon_f \epsilon_r \dot{M} c^2, \quad (4.7)$$

with  $\epsilon_f = 0.15$  as a free efficiency parameter for feedback (Steinborn et al., 2015) tuned to reproduce observed scaling relations between total stellar mass and SMBH mass (McConnell & Ma, 2013). Following the prescription in Fabjan et al. (2010), the radiated power is distributed thermally to the surrounding gas by increasing its internal energy with a radiative efficiency set to  $\epsilon_r = 0.2$ .

### 4.2.3 Results on galaxy properties

Previous studies using the *Magneticum* simulations showed that predicted kinematic and morphological features of simulated galaxies are consistent with observations. Particularly Teklu et al. (2015) devised a classification criterion of star-forming and quiescent galaxies based on the intercept of galaxies in the stellar mass, angular momentum plane. About the kinematical properties of galaxies, it was shown that distinct classes of rotation patterns can emerge in the simulation in accordance with observational results (Teklu et al., 2017; Schulze et al., 2018, 2020).

Furthermore, it was demonstrated that tidal features of galaxies as well as their morphology and dynamical state are connected to their formation history and the shape of the dark-matter halo (Remus et al., 2017; Valenzuela et al., 2024; Valenzuela & Remus, 2024). The effects of the environment on galaxy quenching and properties of post-starburst galaxies were analyzed in Lotz et al. (2019, 2021). Recent observational results of massive quenched galaxies at high redshift could be reproduced as a result of environmental effects and feedback under specific conditions in the early evolution of galaxies (Kimmig et al., 2023). Chemical properties of galaxies and clusters reliably reproduce observations (Dolag et al., 2017) and simple analytic lookback models are in good agreement with galaxy populations at different redshifts in the simulation (Kudritzki et al., 2021).

The population of SMBH, their statistical properties, and their influence on structure formation were studied in Hirschmann et al. (2014); Steinborn et al. (2016). In Biffi et al. (2018a), the X-ray properties of the AGN and their relative contribution to the X-ray emission in galaxy clusters were analyzed, estimating the expected count rates for the eROSITA mission. They also showed that the XLF of AGN is well reproduced within the simulation. Rihtaršič et al. (2024) showed the effects of environment on AGN and star-formation activity in the outskirts of galaxy clusters.

Overall, the predictions of *Magneticum* regarding properties of simulated galaxies have shown to reliably reproduce observations, giving a strong foundation for our analysis presented in this thesis.



## 5 | Let the Simulations Shine in X-ray

Although cosmological simulations are a powerful tool to study the properties of cosmic structures and their surroundings in full 3D space, it is not straightforward to compare observations to simulations. Namely, all 3D properties of an observed object in the real universe are hidden behind projection effects from only having a fixed line of sight (LOS) as well as response functions of the instruments used to conduct the specific observations. In most cases, including the explicit treatment of photons in simulations would require costly on-the-fly modeling of the emitting component. It is therefore advisable to translate the hydrodynamic 3D properties of the simulation into the required photon information using a post-processing procedure. In post-processing, each eligible resolution element of the simulation is assigned a specific type of emission using appropriate models. In this context, eligible means that the resolution element fulfills the conditions required by the model, e.g. density or temperature thresholds in the case of X-ray emitting gas.

### 5.1 PHOX X-ray photon simulator

The virtual X-ray photon simulator PHOX is a post-processing tool for hydrodynamical cosmological simulations tailored to convert intrinsic properties of the simulations into synthetic and realistic X-ray emission (Biffi et al., 2012, 2013). While there have been numerous approaches to the extraction and processing of these quantities (X-Mass/X-Mass2 Gardini et al., 2004; Rasia et al., 2008) the novelty introduced with PHOX lies in the separation of the photon generation from adequate emission models and the projection of simulated photons along a line of sight. Each step of a synthetic observation can thus be carried out individually, requiring the initial photon generation to be executed only once and independent of the projection.

PHOX itself consists of a C code leveraging the programming interface provided by the publicly available X-ray Spectral Fitting Package (XSPEC) (Arnaud, 1996) to calculate model emission spectra. It further utilizes auxiliary libraries GSL<sup>1</sup> and CFITSIO<sup>2</sup> both bundled together with XSPEC in the HEASOFT<sup>3</sup> package. PHOX is structured into three independent units and its input is required to be the output of hydrodynamical cosmological simulations. Each snapshot of a cosmological simulation contains information about the current redshift, assumed cosmology, and

---

<sup>1</sup><https://www.gnu.org>

<sup>2</sup><https://heasrc.gsfc.nasa.gov/fitsio/>

<sup>3</sup><https://heasrc.gsfc.nasa.gov>

intrinsic quantities of the tracked resolution elements such as position, velocity, mass, density, and more. While PHOX is tailored towards particle-based SPH codes, in particular GADGET2 (Springel, 2005), the very general approach can be adapted for grid-based simulations (see e.g. pyXSIM<sup>4</sup> by John ZuHone). Currently, PHOX can produce model emission for the gaseous component (Biffi et al., 2012), actively accreting SMBH (Biffi et al., 2018a), and XRB (Vladutescu-Zopp et al., 2023). We show a basic flowchart of the algorithm in Fig. 5.1.

PHOX has been previously applied to study properties of the inter-cluster medium (ICM) of simulated galaxy clusters (Biffi et al., 2012, 2013, 2014; Biffi & Valdarnini, 2015; Cui et al., 2016), the contamination of ICM emission by AGN (Biffi et al., 2018a) and to study the contribution of XRB emission in galactic X-ray scaling relations and spectra for simulations of galaxies (Vladutescu-Zopp et al., 2023, 2024). Furthermore, it was used in Marini et al. (2024) to study X-ray faint galaxy groups in eROSITA mock observations. The PHOX code is constructed in a general manner such that it can be expanded easily to include the treatment of various X-ray sources which can be constrained from source properties tracked by the simulations.

### 5.1.1 Unit 1

The first module is responsible for the conversion of hydrodynamical simulation input into a discrete photon distribution. This is done by considering each possible source in the simulation and computing an idealized spectrum before applying any projections, guaranteeing a high spatial and spectral resolution. Various model spectra are available per source type and energy range and the corresponding number of spectral bins can be specified beforehand. The fiducial integration quantities, namely the fiducial effective area,  $A_{\text{eff, fid}}$ , and exposure time  $T_{\text{obs, fid}}$ , are crucial in determining the number of associated photons per resolution element. By successively iterating over every resolution element in the simulation, an emission model is assigned to each element according to its intrinsic properties. The simulator then produces a photon package for each resolution element by sampling the emission model stochastically in a Monte-Carlo-like fashion, where the total number of produced photons is

$$N_{\text{ph}} \propto A_{\text{eff, fid}} \times T_{\text{obs, fid}} . \quad (5.1)$$

The resulting photons are therefore characterized by their energy, and share all other quantities, e.g. position and velocity, with its associated resolution element. This allows for a convenient method for storing photon data, where the information on each active element is stored separately from the information on photon energies. Each element then contains an index into the array of photon energies. Ideally, the fiducial integration values are chosen such that the resulting spectra are largely over-sampled to permit a dramatic reduction in photon number after applying geometrical selection, projection, and instrumental response in the following modules. Finally, Unit 1 creates a spatially equivalent distribution of photons from the distribution of provided resolution elements.

<sup>4</sup><https://hea-www.cfa.harvard.edu/jzuhone/pyxsim/>

### Gas emission model

The gas emission model is based on thermal Bremsstrahlung (Eq. (1.15)) with the addition of emission lines from metal species within the plasma (see Sec. 1.3). Both are dependent on the density, temperature, and metallicity of the resolution element and there are dedicated emission models available to calculate the appropriate spectra, such as APEC (Smith et al., 2001) or MEKAL (Kaastra & Mewe, 1993). In addition to classic models available through XSPEC, we implemented a new emission model based on tables provided by Khabibullin & Churazov (2019) which includes scattering of photons from a background CXB source and local photo-ionization equilibrium. Within XSPEC, several variations of the aforementioned emission models exist allowing for the detailed adjustment of individual ion species.

### SMBH emission model

The emission model for SMBH sources is detailed in Biffi et al. (2018a). From the accretion rate of a SMBH in the simulation, the standard approach to calculate the bolometric luminosity is given by Eq. (4.6). An alternative approach is given by Churazov et al. (2005) who distinguish radio mode and quasar mode accretion, such that

$$\frac{L_{\text{bol}}}{L_{\text{edd}}} = \begin{cases} \epsilon_r \left( 10 \frac{\dot{M}}{\dot{M}_{\text{edd}}} \right) & , \frac{\dot{M}}{\dot{M}_{\text{edd}}} \geq 0.1 \\ \epsilon_r \left( 10 \frac{\dot{M}}{\dot{M}_{\text{edd}}} \right)^2 & , \frac{\dot{M}}{\dot{M}_{\text{edd}}} < 0.1 \end{cases} . \quad (5.2)$$

However, the reconstructed X-ray luminosity functions for AGN, compared to data from Hopkins et al. (2007), only weakly depend on the employed estimation for the bolometric luminosity. Therefore, the standard estimator is typically assumed. Using the bolometric corrections presented in Marconi et al. (2004), the bolometric luminosity can be converted to the soft X-ray band (SXR: 0.5 – 2 keV) and the hard X-ray band (HXR: 2 – 10 keV) with

$$\log \left( \frac{L_{\text{HXR}}}{L_{\text{bol}}} \right) = -1.54 - 0.24\mathcal{L} - 0.012\mathcal{L}^2 + 0.0015\mathcal{L}^3 , \quad (5.3)$$

$$\log \left( \frac{L_{\text{SXR}}}{L_{\text{bol}}} \right) = -1.65 - 0.22\mathcal{L} - 0.012\mathcal{L}^2 + 0.0015\mathcal{L}^3 , \quad (5.4)$$

where  $\mathcal{L} = \log(L_{\text{bol}}/L_{\odot}) - 12$ , derived for the luminosity range  $8.5 < \log(L_{\text{bol}}/L_{\odot}) \leq 13$ . These corrections are derived from redshift-independent template spectra which are closer to the intrinsic luminosity of an accreting SMBH and thus closer to theoretical estimates of  $L_{\text{bol}}$  from simulations. Judging from Fig. 2.5 and Eq. (3.27), describing well the emission spectrum of an actively accreting SMBH, an adequate approximation for the emission spectrum is a power-law of the form

$$A(E) = K [E(1+z)]^{-\Gamma} , \quad (5.5)$$

with  $K$  being the normalization of the observed spectrum at  $E = 1$  keV and  $z$  the redshift of the source. The luminosity of the soft and hard bands are then related by

$$\begin{cases} L_{\text{SXR}} = F \int_{0.5/(1+z)}^{2/(1+z)} K [E(1+z)]^{-\Gamma} E dE, \\ L_{\text{HXR}} = F \int_{2/(1+z)}^{10/(1+z)} K [E(1+z)]^{-\Gamma} E dE, \end{cases} \quad (5.6)$$

forming a system of equations that can be solved to obtain the spectrum normalization  $K$  and slope  $\Gamma$  by assuming that both luminosities originate from the same underlying power-law. An additional uniform noise with  $\sigma = 0.1$  is added on top of  $L_{\text{SXR}}$   $L_{\text{HXR}}$  resulting in slopes of  $\Gamma = 1.4 - 2.8$  peaked at  $\Gamma \sim 1.9 - 2.0$ . In the end, an intrinsic absorption component is given to each SMBH source by stochastically sampling the distribution of absorption columns of obscured AGN given in [Buchner et al. \(2014\)](#).

### XRb emission model

The exact details of the XRb model are presented in Chap. 6.

#### 5.1.2 Unit 2

The second module takes the output of Unit 1 and applies the geometrical selection and projection of the specified target in the simulation, creating a mock observation. In particular, a field of view containing a sub-volume of the photon cube can be specified along with the depth along an arbitrary line of sight. Photons outside the specified volume will be discarded and the remaining photons will be corrected for their Doppler-shift induced by the velocity component along the LOS,  $v_{\text{los}}$ , such that

$$E' = E \sqrt{\frac{1 - \beta}{1 + \beta}}, \quad (5.7)$$

where  $\beta = v/c$  with  $c$  the speed of light. The fiducial LOS is parallel to the simulation intrinsic  $z$ -coordinate, however, the geometry of the remaining photons will be rotated into the correct reference frame if a new line of sight direction is specified. In the next step, a detection probability will be determined for every photon within the specified geometry depending on the user-defined values for the collecting area  $A_{\text{eff}}$ , exposure time  $T_{\text{obs}}$ , or redshift  $z$ . The rescaling factor becomes

$$p_o = \frac{A_{\text{eff}} T_{\text{obs}}}{A_{\text{eff, fid}} T_{\text{obs, fid}}} \times \frac{\mathcal{D}_{\text{L, fid}}^2}{\mathcal{D}_{\text{L}}^2}, \quad (5.8)$$

where the chosen redshift in Unit 2 ultimately determines the distance to the observer. We note that the rescaling uses the luminosity distance  $\mathcal{D}_{\text{L}}$  in order to be flux-conserving.

The Hubble flow gives another factor contributing to the detection probability. Specifically, in volumes with large elongation along the LOS, foreground and background sources may already be sufficiently distant from the observational center to require a significant correction to their energy. Thus, the exact distance to each photon along the LOS is determined in co-moving space from which a new redshift  $z'$  can be derived to give the correction for the photon energy and flux conservation

$$E' = E \left( \frac{1 + z'}{1 + z} \right), \quad p_z = \frac{\mathcal{D}_L^2}{\mathcal{D}_L'^2}. \quad (5.9)$$

Furthermore, a specific absorption model, e.g. wabs (Morrison & McCammon, 1983) or tbabs (Wilms et al., 2000), and corresponding column densities can be specified mimicking an absorber located at a specific redshift and a given optical depth. The resulting absorption coefficient gives another contribution to the detection probability as a function of photon energy

$$p_E = \exp(-\sigma(E) N_H), \quad (5.10)$$

where  $\sigma(E)$  is the model and energy-dependent absorption cross-section and  $N_H$  is corresponding column density. The final detection probability can thus be expressed as

$$p = p_o \cdot p_z \cdot p_E, \quad p \geq 0. \quad (5.11)$$

There is a chance that, depending on the specified geometry,  $p > 1$  for a given photon, in which case the algorithm will duplicate the photon. Finally, all photons associated with a resolution element will be redistributed in 3D space according to radial Gaussian with standard deviation  $\sigma_r$  equal to the smoothing length of the resolution element. Alternatively, the smoothing length for a given type of resolution element can be chosen manually before executing the algorithm. Since Unit 2 acts independently, it no longer requires the original input used for Unit 1, i.e. the output of the hydrodynamic simulation. As such, specifications regarding the mock observation can be adjusted easily allowing for multiple studies of the same source from many different LOS. Unit 2 then outputs a photon list in a format suitable for convolution with the technical response of a specific instrument or for an external software dedicated to simulating a specific X-ray satellite, such as SIXTE<sup>5</sup> (Dauser et al., 2019).

It is also possible to create lightcone slices of the original simulation at specific redshift intervals to create a more realistic mock observation with a continuous redshift distribution and specified opening angle. The original implementation of this mode produced misalignments between the actual source position and its associated photons due to an oversight regarding redshift corrections. We corrected this issue and made the treatment of redshifts consistent enabling the study of Marini et al. (2024).

### Unit 3

In the final third module, the characteristics of a real X-ray telescope are considered to complete the mock observation. In particular, the technical aspects of a specific instrument are defined

<sup>5</sup><https://www.sternwarte.uni-erlangen.de/sixte/>

by its redistribution matrix (RMF) and its ancillary response file (ARF). The RMF defines which energy channel a photon with specific energy is sorted in. The ARF defines additional information about the instrument such as the point spread function and the effective area as a function of energy. Convolution of the photon lists obtained in Unit 2 with the RMF and ARF yields event files satisfying the standards of real X-ray observations. This enables analysis with the same procedures and tools used for real data. Generally, the RMF and ARF are provided externally and are not predetermined in Unit 3. Special care has to be taken for the effective area's normalization as defined in the ARF concerning the fiducial effective area assumed during the projection in Unit 2 to avoid the unphysical overabundance of observed photons.

In figure 5.2 we show the result of running Unit 1 and Unit 2 on a face-on disc galaxy from our sample, identified as a “poster-child” star-forming disk galaxy in [Vladutescu-Zopp et al. \(2023\)](#). The white outer solid circle corresponds to the virial radius of the galaxy while the inner white dashed circle corresponds to 10% of the virial radius. The color indicates the photon counts per pixel within the energy range of 0.5-2 keV, assuming a fiducial exposure of 1 Ms and effective area 1000 cm<sup>2</sup>. Black pixels have no photon counts. Each panel shows the same field of view of the galaxy with a different X-ray emitting component indicated in the top left corner of the panel.

## 5.2 General code updates

In this section, we highlight major code updates with respect to the original version of PHOX described in [Biffi et al. \(2012, 2018a\)](#).

PHOX Unit 1 used explicit C system calls to execute XSPEC from within PHOX and calculate the required template spectra for each component using predefined XSPEC scripts. Those scripts would calculate the templates and write the result into files, which would, in turn, again be read by PHOX. Three major problems with this approach are: *(i)* that the main PHOX algorithm remained idle while waiting for the XSPEC application to finish writing the files; *(ii)* the waiting times required to finish writing the file containing the template spectrum are severely limited by the speed of I/O processes of the filesystem; *(iii)* writing of temporary files prevented parallelization of the PHOX algorithm due to race conditions in data access. By replacing the system calls to XSPEC with actual C functions provided by the XSPEC programming interface, the overall runtime of PHOX Unit 1 was reduced by more than a factor of 10.

Removing the direct dependence on the filesystem also enabled the algorithm to be parallelized using MPI thread parallelization. A rudimentary version was therefore implemented as a proof-of-concept, allowing for a much faster processing of entire simulations.

Modeling of foreground absorption was moved from Unit 1 to Unit 2 because it allows for more flexibility regarding the generation of mock observations using different prescriptions of absorption. A disadvantage is that Unit 1 will produce drastically more photons in the ultra-soft X-ray range ( $E \lesssim 0.3$  keV) which results in larger files. This change does not affect absorption required to describe the intrinsic emission model of the source such as for SMBH or XRB.

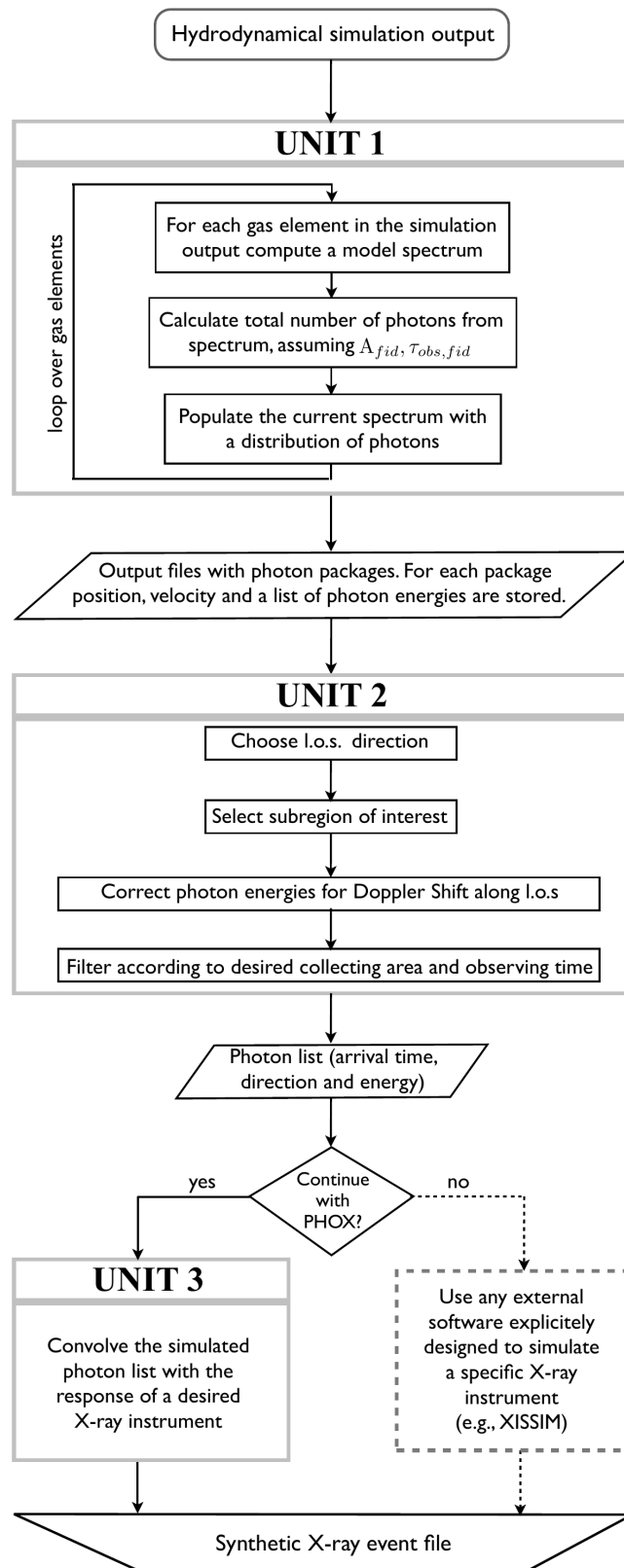


Figure 5.1: Schematic flow chart illustrating the main modules of PHOX. The dashed box denotes the possibility of invoking an external software package designed to simulate observations of a certain X-ray telescope in conjunction with the output of Unit 2. Graphic directly taken from Biffi et al. (2012).

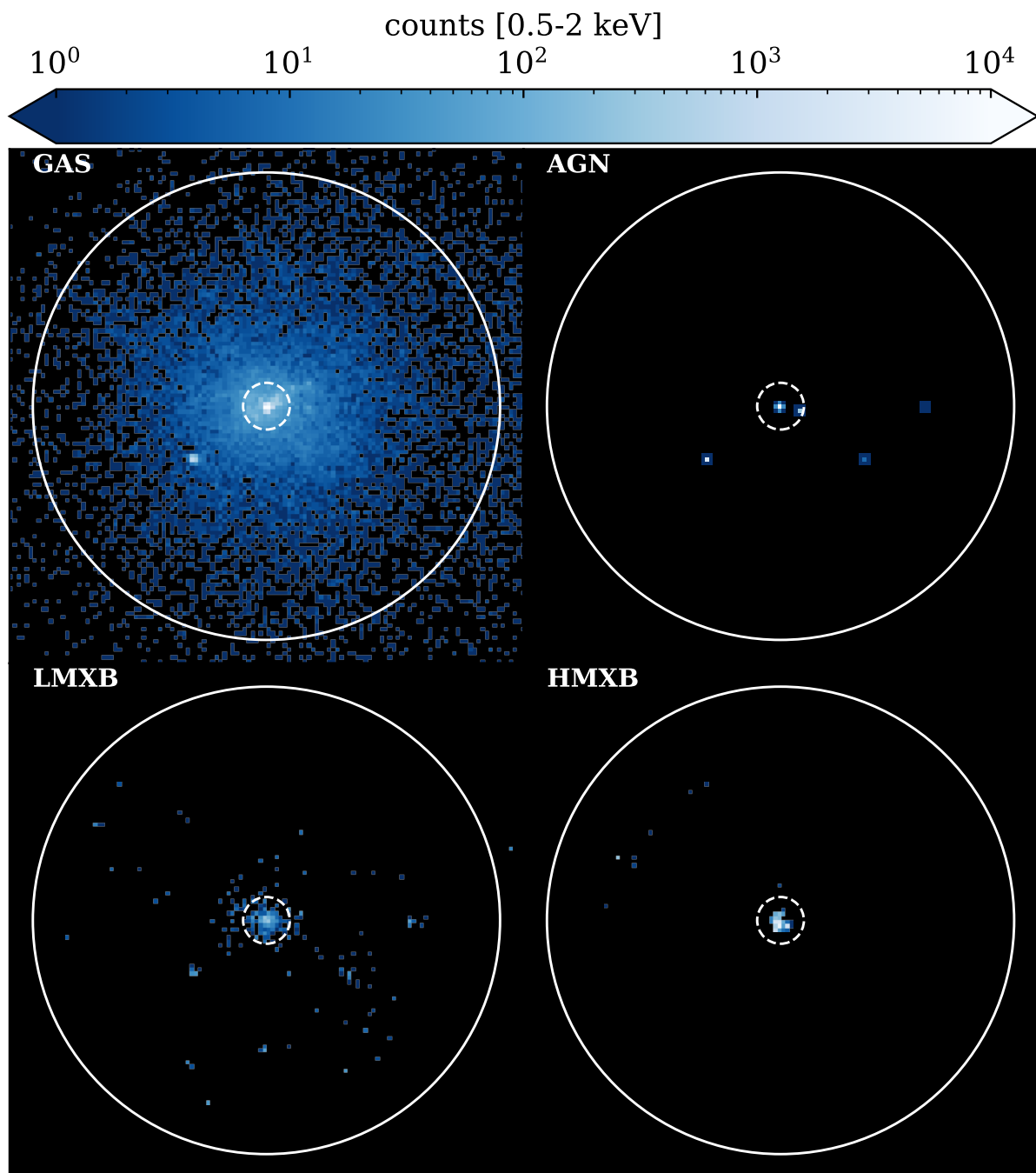


Figure 5.2: X-ray mock images of the poster-child star-forming disk galaxy from [Vladutescu-Zopp et al. \(2023\)](#). The fiducial orientation of its stellar component is face-on. The outer solid white circle indicates the virial radius and the inner dashed circle indicates 10% of the virial radius. The color indicates the total photon in the SXB per pixel.

## 6 | Seeding X-ray binaries in the simulations (Paper 1)

- This chapter has been published in [Vladutescu-Zopp et al. \(2023\)](#) and received some minor adjustments.

X-ray properties of local normal galaxies have been extensively studied in the past, where “normal” describes galaxies without a luminous active galactic nucleus (AGN). One of the most challenging tasks has been the identification of the physical processes that produce the observed X-ray emission from those galaxies. It is a well-established fact that most of their X-ray power output originates from diffuse hot gas in the interstellar medium (ISM) and accretion-powered point sources called X-ray binaries (XRBs; see the reviews [Fabbiano, 1989, 2006, 2019](#)), excluding the emission from actively accreting super-massive black holes (SMBHs).

Numerous studies of the hot diffuse ISM in star-forming normal galaxies have revealed a tight linear relation between the total X-ray luminosity,  $L_X$ , and the star-formation rate (SFR; [Strickland & Stevens, 2000](#); [Ranalli et al., 2003](#); [Tyler et al., 2004](#); [Mineo et al., 2012b](#); [Li & Wang, 2013](#); [Kouroumpatzakis et al., 2020](#)) due to feedback from young stellar objects and energy injection from supernovae (SNe), which heat up the ISM. Recent studies suggest that the ISM emission normalization in X-rays declines with increasing total gas-phase metallicities, possibly due to the effect of metal absorption and changes in stellar feedback within the ISM ([Garofali et al., 2020](#); [Lehmer et al., 2022](#)).

The ISM of normal elliptical galaxies (EGs) depends on their dynamical state ([Kim & Fabbiano, 2015](#); [Babyk et al., 2018](#)) and strongly correlates with the ISM temperature ([Boroson et al., 2011](#); [Kim & Fabbiano, 2015](#)) and dynamical mass ([Kim & Fabbiano, 2013](#); [Forbes et al., 2017](#); [Babyk et al., 2018](#)). The ISM of core EGs, where “core” denotes slow rotating systems with cored central surface brightness and an overall old stellar population, appears to follow gas X-ray luminosity scaling relations consistent with virialized systems, similar to brightest cluster galaxies (BCGs) and groups. Other types of gas-poor EGs behave similarly to disk galaxies in these relations: they do not show significant correlations between hot gas temperature and the X-ray luminosity of hot gas, suggesting secondary effects such as rotation, flattening, and SN feedback dissipating the ISM (see, e.g., [Fabbiano, 2019](#)).

Separate scaling relations are found for collective XRB X-ray luminosity depending on the type of XRB: low-mass X-ray binaries (LMXBs) are accreting compact objects (COs) where the low-mass companion undergoes Roche-lobe overflow at the end of its life. Thus, LMXBs are

generally correlated with the integrated stellar light ( $L_K$ ) and, by extension, with the total stellar mass of the host galaxies because of the long evolutionary timescales of the low-mass ( $< 1 M_\odot$ ) donor star in the binary system (Gilfanov, 2004; Boroson et al., 2011; Zhang et al., 2012; Lehmer et al., 2019). This relation seems to be enhanced by the globular cluster (GC) specific frequency,  $S_N = N_{GC} 10^{0.4(M_V^T + 15)}$ , where gravitationally dissolving GCs seed LMXBs into the galactic field, which join the LMXBs formed in situ (Irwin, 2005; Zhang et al., 2011; Boroson et al., 2011; Zhang et al., 2012; Lehmer et al., 2020). In high-mass X-ray binaries (HMXBs) the donor star is a massive O/B star ( $> 8 M_\odot$ ) that fuels accretion onto the CO with intense stellar winds. Due to the short lifetimes of such massive stars ( $< 100\text{Myr}$ ), HMXBs provide an independent tracer of the galactic star-formation history (SFH). It was found that the combined X-ray luminosity of HMXBs relates linearly to the SFR (Grimm et al., 2003; Shtykovskiy & Gilfanov, 2005b; Mineo et al., 2012a; Lehmer et al., 2010, 2016, 2019). Broadband X-ray luminosity functions (XLFs) of XRBs follow distinct power-law (PL) or broken-power-law (BPL) distributions in the local Universe (see, e.g., Grimm et al., 2003; Gilfanov, 2004). The exact shape of XRB luminosity functions in normal galaxies is a function of stellar age and evolves on timescales consistent with the stellar evolution timescales of the XRB donor, transitioning from HMXB dominated to LMXB dominated at a stellar population age of  $\gtrsim 100\text{Myr}$  (Lehmer et al., 2017; Gilbertson et al., 2022).

By combining the scaling relations of both XRB types, we expect a distinct relation between SFR-normalized  $L_X$  and the specific star-formation rate (sSFR = SFR/ $M_*$ ) of the form  $L_X/\text{SFR} = \alpha \text{sSFR}^{-1} + \beta$ , where  $\alpha$  describes the contribution from LMXBs and  $\beta$  the contribution from HMXBs. This relation is especially useful in galaxies where XRB candidates cannot be resolved: it shows which of the two XRB types is the dominant contributor to the galactic  $L_X$ . In previous works, it has been shown that this relation generally holds for local galaxies (Lehmer et al., 2010, 2016, 2019), with modifications for high redshift galaxies (Lehmer et al., 2016). The turnover from LMXB to HMXB domination occurs at  $\log \text{sSFR} \sim -10.5$ . Recently, Soria et al. (2022) performed *Chandra* observations of normal galaxies in the Virgo cluster that were marginally compatible with scaling relations for local galaxies, indicating non-negligible environmental effects on this relation. A similar dependence was found by Inoue et al. (2021) in the form of a fundamental plane:  $L_X \sim \text{SFR} + \alpha M_*$ .

Numerous studies on generalizing locally derived XRB scaling relations for the high redshift Universe have used computationally expensive population synthesis codes for XRB evolution (Fragos et al., 2013a,b; Madau & Fragos, 2017; Wiktorowicz et al., 2017). Taking into account the metallicity evolution and SFH of the universe constrained with the help of cosmological simulations (MILLENNIUM II in the case of Fragos et al. 2013b) suggests a more complex evolution of local XRB scaling relations, with redshift and HMXB emissivity dominating above  $z \sim 2$ , where the cosmic SFR density peaks. This is supported by constraints from the VANDELS survey<sup>1</sup> on HMXB emission in high redshift galaxies (Saxena et al., 2021). Additional evidence for the metallicity dependence of HMXB emissivity comes from a recent study by Lehmer et al. (2021), who used the gas-phase oxygen fraction of their galactic sample to further refine the

<sup>1</sup>The VANDELS project is an ESO-funded spectroscopic survey within the *Chandra Deep Field South* targeting high-redshift galaxies.

$L_X$ -SFR relation. They demonstrate that galaxies with lower metal content consistently show an increased number of luminous HMXBs and a higher total luminosity. Similarly, earlier studies from [Brorby et al. \(2016\)](#) and [Fornasini et al. \(2020\)](#) find anticorrelated metallicity enhancements in the  $L_X$ -SFR relation, which is consistent with findings by [Lehmer et al. \(2021\)](#). Additionally, data from the eROSITA Final Equatorial Depth Survey (eFEDS) show an elevated total X-ray luminosity for low-metallicity dwarf galaxies with high sSFRs ([Vulic et al., 2022](#)). This paper introduces a numerical modeling to study the composition of galactic X-ray emission from a theoretical point of view, using state-of-the-art hydrodynamical cosmological simulations from the *Magneticum* set. Instead of applying computationally expensive population synthesis codes, we associated XRB populations with the stellar component within the cosmological simulation by making use of observationally derived XRB luminosity functions. We use observationally derived local scaling relations to constrain seeding parameters and describe the numerical setup used to extend the capabilities of the virtual X-ray photon simulator PHOX. PHOX has been successfully used in conjunction with *Magneticum* to study galaxy cluster  $L_X$ -temperature relations as well as AGN luminosity functions. Additionally, it was used to predict the contamination of cluster X-ray emission by AGN for the eROSITA mission (see [Biffi et al., 2012, 2013, 2018a](#)). The inclusion of an XRB component enables the study of galactic X-ray spectra from a theoretical standpoint. We validate our approach by retrieving well-known XRB and gas scaling relations of galaxies while maintaining a low computational cost.

## 6.1 Modeling of XRB populations within SSPs

In this section, we describe the process of modeling the population size of LMXBs and HMXBs, given a stellar resolution element in the cosmological simulation. Stellar elements describe a collection of stars as an SSP that shares the same time of birth and initial metallicity, distributed according to a common initial mass function (IMF). The main difficulty lies in connecting the XLFs, which are derived from observed galactic properties, with SSP properties traced by the simulation. In order to preserve the generality of our approach, we do not a priori assume a galactic environment of the SSP in the simulation but rather investigate scaling relations and arising XLFs by processing each SSP individually.

### 6.1.1 Theoretical estimation of the LMXB population size

The modeling of LMXB is based on the fact that they cannot be associated with previous star formation events in a galaxy, which is due to the long lifetime of their low-mass stellar companions. Thus, LMXBs are more typically found in old galactic stellar regions, which connects the LMXB population to the total stellar mass of their host galaxy ([Gilfanov, 2004](#); [Zhang et al., 2012](#); [Lehmer et al., 2017, 2019](#)). By requiring that an SSP must be older than 1 Gyr for it to be eligible to host an LMXB population, we can simply obtain the LMXB population size by re-normalizing the LMXB XLF to the mass of the SSP. In particular, we use the BPL XLF from [Zhang et al.](#)

(2012) throughout this paper, which has the form

$$\frac{dN_{\text{LMXB}}}{dL} = A_{\text{LMXB}} \frac{M_*}{10^{11} M_\odot} \begin{cases} L^{-\alpha_1}, & L < L_{b,1} \\ L_{b,1}^{(\alpha_2 - \alpha_1)} L^{-\alpha_2}, & L_{b,1} < L < L_{b,2} \\ L_{b,2}^{(\alpha_3 - \alpha_2)} L^{-\alpha_3}, & L_{b,2} < L < L_{\text{cut}} \\ 0, & L \geq L_{\text{cut}} \end{cases}, \quad (6.1)$$

where  $L_{b,1} = 0.546$  and  $L_{b,2} = 5.99$  are break luminosities,  $L_{\text{cut}} = 500$  is the cutoff luminosity,  $A_{\text{LMXB}} = 54.48$  is the normalization,  $M_*$  is the total stellar mass of a galaxy, and  $\alpha_1 = 1.02$ ,  $\alpha_2 = 2.06$ ,  $\alpha_3 = 3.63$  are the respective PL slopes. Luminosities are given in units of  $10^{38} \text{ erg s}^{-1}$ . In fact, LMXBs appear to not only be dependent on the stellar mass of the host galaxy, but also be connected to the GC specific frequency ( $S_N$ ), which enhances the XLF normalization by accounting for dynamically formed LMXBs in GCs (Irwin, 2005; Boroson et al., 2011; Zhang et al., 2012; Lehmer et al., 2020). In Lehmer et al. (2020), they were successful in estimating the field LMXB contribution from different formation channels while earlier studies like Zhang et al. (2012) combine these channels into a single XLF. Since it is not feasible to account for GCs in the context of a cosmological simulation, because of mass resolution limits, integration of Eq. (6.1) is sufficient to describe the LMXB population in an SSP as

$$\tilde{N}_{\text{LMXB}} = \int_{L_{\text{min}}}^{L_{\text{cut}}} \frac{dN_{\text{LMXB}}}{dL} (M_{\text{SSP}}) dL, \quad (6.2)$$

where we use the current SSP mass  $M_{\text{SSP}}$  in solar masses instead of  $M_*$ . The total stellar mass of a galaxy would then be recovered by the sum over each single SSP within its boundary.

### 6.1.2 Theoretical estimation of the HMXB population size

Due to the short lifetime of their massive companions, HMXBs are typically associated with young stellar regions of a galaxy, which implies a connection to the SFR. It was shown that HMXBs are a robust independent tracer for recent star formation activity in their host galaxy (Grimm et al., 2003; Mineo et al., 2012a). In particular, the XLF normalization of HMXBs depends linearly on the SFR. A standard HMXB XLF that we use throughout the paper is given in Mineo et al. (2012a) as

$$\frac{dN_{\text{HMXB}}}{dL} = A_{\text{HMXB}} \frac{\text{SFR}}{M_\odot \text{ yr}^{-1}} \begin{cases} L^{-\gamma}, & L < L_{\text{cut}} \\ 0, & L \geq L_{\text{cut}} \end{cases}, \quad (6.3)$$

where  $A_{\text{HMXB}}$  is the normalization constant, SFR of a galaxy is given in units of  $M_\odot \text{ yr}^{-1}$ ,  $\gamma = 1.59$  is the PL slope, and  $L_{\text{cut}} = 10^3$  is the cutoff luminosity. The luminosity  $L$  is given in units of  $10^{38} \text{ erg s}^{-1}$ . One can obtain the number of individual HMXBs in a galaxy with

$$N_{\text{HMXB}} = \int_{L_{\text{min}}}^{L_{\text{cut}}} \frac{dN_{\text{HMXB}}}{dL} dL. \quad (6.4)$$

The main difficulty in transferring the SFR scaling property to SSPs in a cosmological simulation lies in determining the SFH of these SSPs. Since SSPs are created in an instantaneous star-formation event in the simulation (see Sec. 4.2.1), their SFH resembles a  $\delta$ -function at their time of creation (Tornatore et al., 2007). To circumvent this issue, we can adapt the procedure in Mineo et al. (2012a) by obtaining the fraction  $f_X$  of COs becoming a XRB, which is derived from the birth rate of massive stars ( $> 8 M_\odot$ ) in a star-formation event. Instead of using the birthrate  $\dot{N}_{\text{CO}}$  of COs following a star-formation event, which is directly dependent on the IMF and SFR, we can equally use the type II supernova (SNII) rate  $R_{\text{SNII}}$ , which hides the SFR dependence in the stellar lifetime function. Following Tornatore et al. (2007), we can express the SNII rate as

$$R_{\text{SNII}}(\tau) = \Phi(m(\tau)) \times \frac{dm(\tau)}{d\tau}, \quad (6.5)$$

where  $\Phi(m)$  is a mass-normalized IMF, which gives the number of stars given the mass  $m$ , and  $m(\tau)$  is the inverse stellar lifetime function of Padovani & Matteucci (1993) (PM93), which gives the mass of stars dying at an age of  $\tau$ . The SNII rate  $R_{\text{SNII}}$  is given in units of  $\text{Gyr}^{-1}$  for a SSP of mass  $1 M_\odot$ . The PM93 lifetime function has the form

$$\tau(m) = \begin{cases} 10^{(1.338 - \sqrt{1.79 - 0.2232 \cdot (7.764 - \log m)}) / 0.1116 - 9}, & m \leq 6.6 M_\odot, \\ 1.2 \cdot m^{-1.85} + 0.003, & m > 6.6 M_\odot, \end{cases} \quad (6.6)$$

with mass  $m$  of the star given in  $M_\odot$  and  $\tau$  in units of Gyr. We employed the modified Chabrier IMF (Chabrier, 2003) used in the simulation, which has the form

$$\Phi(m) \propto \begin{cases} m^{-2.3}, & 1.0 M_\odot < m < 100 M_\odot \\ m^{-1.8}, & 0.5 M_\odot < m < 1.0 M_\odot \\ m^{-1.2}, & 0.1 M_\odot < m < 0.5 M_\odot \end{cases}. \quad (6.7)$$

Using the SNII rate, we followed the calculations in Mineo et al. (2012a) to obtain an estimate of the HMXB population size.

First we determined the product of the X-ray-bright fraction,  $f_X$ , and the average bright-phase duration,  $\bar{\tau}_X$ , assuming an XLF

$$f_X \bar{\tau}_X \sim \frac{N_{\text{HMXB}}(> L_{\text{min}})}{\dot{N}(> 8 M_\odot)}, \quad (6.8)$$

where  $\dot{N}(> 8 M_\odot)$  is the birthrate of massive stars. The birthrate can be obtained from the IMF to the first order using

$$\dot{N}(> 8 M_\odot) = \frac{\int_8^{M_u} \Phi(m) dm}{\int_{M_l}^{M_u} \Phi(m) m dm} \times \text{SFR}, \quad (6.9)$$

with integration limits defined by the IMF. Mineo et al. (2012a) determined instead the term in Eq. (6.8) as  $f_X \sim 0.18 \frac{0.1 \text{ Myr}}{\bar{\tau}}$ , based on binary evolution calculations for the most common type of Be HMXB and assuming  $\bar{\tau}_X \sim 0.1 \text{ Myr}$ , therefore making the factor explicitly dependent on

the bright phase duration. In our case, by computing directly the product of  $f_X$  and  $\bar{\tau}$  as in Eq. (6.8), we can conveniently bypass uncertainties connected to assumptions for the bright phase duration. Given the proportionality to SFR in Eq. (6.9) and of  $N_{\text{HMXB}}$  (see Eq. (6.4)), then the dependence of  $f_X \bar{\tau}_X$  on SFR disappears.

Then, from Eq. (6.8), we can replace the birthrate,  $\dot{N}$ , with the SNII rate,  $R_{\text{SNII}}$ , given the age of the SSP, and multiply by the current SSP mass to get the expected HMXB population size:

$$\tilde{N}_{\text{HMXB}} = \begin{cases} M_{\text{SSP}} \times R_{\text{SNII}}(t_{\text{SSP}}) f_X \bar{\tau}_X, & t_{\text{SSP}} \leq \tau(8 M_{\odot}) \\ 0, & t_{\text{SSP}} > \tau(8 M_{\odot}) \end{cases}. \quad (6.10)$$

Additionally, we require  $t_{\text{SSP}}$  to be smaller than the lifetime of stars with mass  $8 M_{\odot}$ , in line with mass limits for HMXBs in the literature (see, e.g., [Lewin & van der Klis, 2006](#)), which, according to Eq. (6.6), gives  $\approx 30$  Myr. Therefore, in the simulation, a stellar particle older than 30 Myr should no longer represent a SSP containing stars with masses greater than  $8 M_{\odot}$ . The same procedure can be repeated for different IMFs and XLF models.

In order to study the metallicity dependence of HMXBs, we also included the model proposed by [Lehmer et al. \(2021\)](#) (L21):

$$\frac{dN_{\text{HZB}}}{dL} = A_{\text{HZB}} \text{SFR} \exp[-L/L_c(Z)] \begin{cases} L^{-\gamma_1}, & L < L_b \\ L_b^{\gamma_2(z)-\gamma_1} L^{\gamma_2(Z)}, & L \geq L_b \end{cases}, \quad (6.11)$$

with

$$\gamma_2(Z) = \gamma_{2,\odot} + \frac{d\gamma_2}{d \log Z} [12 + \log(\text{O}/\text{H}) - 8.69] \quad (6.12)$$

and

$$\log L_c(Z) = \log L_{c,\odot} + \frac{d \log L_c}{d \log Z} [12 + \log(\text{O}/\text{H}) - 8.69]. \quad (6.13)$$

Both  $\gamma_{2,\odot} = 1.16$  and  $\log L_{c,\odot} = 1.98$  are reference values at solar metallicity. The other parameter values are the normalization  $A_{\text{HZB}} = 1.29$ , break luminosity  $\log L_b = 0.54$ , slope  $\gamma_1 = 1.74$  and first-order metallicity corrections  $\frac{d\gamma_2}{d \log Z} = 1.34$  and  $\frac{d \log L_c}{d \log Z} = 0.6$ . Luminosities are given in units of  $10^{38} \text{ erg s}^{-1}$  in Eq. (6.11). We labeled the L21 model ‘‘HZB’’ to indicate the metallicity dependence,  $Z$ .

## 6.2 XRB emission model

Following the modeling of AGN and hot gas emission in the PHOX code, we similarly determined the X-ray emission coming from a stellar resolution element of the simulation. We made use of the SSP properties determined in Sect. 6.1 to calculate an expected number of point sources  $\tilde{N}$  per stellar element. We then sampled the respective XLF based on the following recipe. We selected the correct XLF from a stellar age criterion: if the age of the SSP is  $\tau < 30$  Myr, we classified it as HMXB hosting. If  $\tau > 1$  Gyr we classified the SSP as LMXB hosting. Both choices are based on expectations from binary evolution simulations (see, e.g., the review by [Lewin & van](#)

der Klis, 2006) and are well motivated from observations. In the HMXB case Shtykovskiy & Gilfanov (2007) found peak formation efficiency in the Small Magellanic Cloud at  $\approx 50$  Myr, Garofali et al. (2018) found peak formation efficiency in M33 at  $\approx 40$  Myr, and Antoniou et al. (2019) find peak formation efficiency again in the Small Magellanic Cloud at  $\approx 30 - 40$  Myr, all by correlating the specific SFH of observed stellar regions with HMXBs. Since these values are dependent on the stellar models assumed for the observed regions we settled for the value given by the lifetime function (see Sect. 6.1). In the LMXB case the 1 Gyr boundary yields a donor mass limit of  $1.75 M_{\odot}$ , which reflects the Roche-lobe overflow scenario of accretion onto a CO.

From the XLF we constructed a pseudo cumulative density function (pCDF). This requires setting a luminosity interval  $[L_{\min}, L_{\max}]$  at which the pCDF  $C(L)$  will be defined:

$$C(L) = 1 - \frac{N(> L)}{N(> L_{\min})}, \quad (6.14)$$

with  $N(> L)$  being the integrated XLF from step 1, and  $C(L) \in [0, 1]$ . Typically,  $L_{\max}$  is chosen to be the cutoff luminosity of the respective XLF. It should be noted that  $C(L)$  is sensitive to the choice of  $L_{\min}$  due to the PL dependence of the XLF. We then calculated  $\tilde{N}$  from Eqs. (6.2) and (6.10) and chose  $[\tilde{N}]$  uniformly distributed random numbers  $p_i \in [0, 1]$ . If a separate uniform random number  $\tilde{p}$  satisfies  $\tilde{p} < \tilde{N} - [\tilde{N}]$ , we draw an additional random number  $p_i$ . For each  $p_i$  we determined a corresponding luminosity  $L_i$ , at which  $C(L_i) = p_i$ . From this we can calculate the total luminosity of the SSP as

$$L_{\text{SSP}} = \sum_i L_i. \quad (6.15)$$

This recipe yields a SSP with a single X-ray luminosity in the same energy range the XLFs have been defined in. As such, it will be treated as a single XRB-like point source. Specifically, we described XRB emission spectra as redshift-dependent, absorbed PLs of the form

$$A(E) = w(E(1+z)) \times K [E(1+z)]^{-\Gamma}, \quad (6.16)$$

where  $K$  is the spectrum normalization at 1 keV and  $\Gamma$  is the photon index as given in the XSPEC manual (Arnaud (1996)). Absorption was modeled after the Wilms et al. (2000) photo-ionization cross sections, and the model includes gas, grain, and molecule components in the ISM, which is expressed in Eq. (6.16) with  $w(E)$ . The redshift dependence of the spectrum allows for consistent modeling in a cosmological context. The total observed luminosity of the SSP (Eq. (6.15)) in a certain energy band  $E \in [E_1, E_2]$  is then related to Eq. (6.16) by

$$L_{\text{SSP}} = F \int_{E_1}^{E_2} A(E) E dE, \quad (6.17)$$

with  $F = 4\pi \mathcal{D}_L(z)^2 \times 1.602 \cdot 10^{-9} \text{ erg keV}^{-1}$  being the rescaling factor between flux and luminosity and  $\mathcal{D}_L(z)$  is the luminosity distance inferred from the underlying cosmology. The energy range  $[E_1, E_2]$  has to be chosen in correspondence to the range in which the XLFs were defined, which is commonly adopted as  $E_1 = 0.5 \text{ keV}$  and  $E_2 = 8 \text{ keV}$  in the observed frame. We are then able

to constrain the spectrum normalization  $K_{\text{SSP}}$  using Eqs. (6.15) and (6.17), obtaining

$$K_{\text{SSP}} = \frac{\sum_i L_i}{F \int_{E_1}^{E_2} w(E)[E(1+z)]^{-\Gamma+1} dE}. \quad (6.18)$$

A fully detailed description of XRB spectra is not possible in our modeling. For instance, the cosmological context of our approach makes it impossible to capture XRB variability on small timescales, so changes in spectral hardness have to be accounted for statistically. Therefore, we opt for an average X-ray emission spectrum for the two XRB types, in line with typical values found in the literature. For our analysis, we chose the PL slope  $\Gamma_{\text{LMXB}} = 1.7$  in the LMXB case and  $\Gamma_{\text{HMXB}} = 2$  in the HMXB case. Both slopes are motivated from observational data where the  $\Gamma_{\text{HMXB}}$  follows assumptions of Mineo et al. (2012a) and  $\Gamma_{\text{LMXB}}$  follows the median slope of all high-confidence XRBs in Lehmer et al. (2019). For the absorption component we assume the median column density  $N_H^{\text{xrb}} = 2 \cdot 10^{21} \text{ cm}^{-3}$  from the same sample of XRBs in Lehmer et al. (2019). This choice of parameters results in spectra resembling typical XRBs in their low/hard-state (see Remillard & McClintock, 2006; Done et al., 2007; Sazonov & Khabibullin, 2017b). Additionally, it was found that  $\Gamma_{\text{LMXB}} \sim 1.4 - 1.8$  is sufficient to describe the hot atmosphere of EGs (Boroson et al., 2011; Wong et al., 2014; Babyk et al., 2018). We do not include any other form of stellar X-ray sources such as active binaries or cataclysmic variables since their cumulative luminosity is at least an order of magnitude below the total XRB luminosity (see, e.g., Boroson et al., 2011; Babyk et al., 2018). Typically applied corrections for unresolved X-ray emission of cataclysmic variables and active binaries are  $\sim 8 \cdot 10^{27} \text{ erg s}^{-1} \text{ M}_{\odot}^{-1}$  according to Babyk et al. (2018). For young stellar objects, Mineo et al. (2012b) estimate a collective unresolved emission of  $\sim 2 \cdot 10^{38} \text{ erg s}^{-1}$  per unit SFR.

Having determined  $K$ ,  $\Gamma$  and  $N_H^{\text{xrb}}$  of a single SSP, we can compute the resulting XRB spectrum by adopting the ztbabs and zpowerlw model embedded in XSPEC, from which we calculated an ideal photon list associated with each SSP.

### 6.3 Simulated data set

For our analysis we extracted galaxy sized halos at redshift  $z = 0.07$  from the Box4/ubr cosmological volume of the Magneticum Pathfinder simulation set and artificially placed them at  $z = 0.01$ . Assuming fiducial values for effective area  $A_{\text{eff}} = 1000 \text{ cm}^2$  and exposure time  $T_{\text{exp}} = 10^5 \text{ s}$ , we selected all halos generated by the SUBFIND algorithm (Springel et al., 2001; Dolag et al., 2009) that have a total stellar mass  $M_* > 10^{9.7} \text{ M}_{\odot}$  within a sphere of  $R_{2500}$  around the halo center, which also includes a few massive group-like objects with stellar masses of  $M_* \sim 10^{12} \text{ M}_{\odot}$ . Halos with stellar masses below a threshold of  $M_* < 10^{10} \text{ M}_{\odot}$  are resolution limited: the SPH implementation fails to correctly reproduce the required star-formation for low-mass halos. We illustrate the  $M_{\text{gas}} - M_*$  relation in Fig. 6.1. Halos that have high stellar masses and low gas masses were subjected to feedback processes and were depleted of their gas content, which is connected to resolved physical processes within the simulations.

The selected set consists of 1480 objects of which 335 are considered actively star-forming, based on the limit  $\text{SFR} > 0.4 \text{ M}_{\odot} \text{ yr}^{-1}$ , with SFR derived from the total mass of stars born in

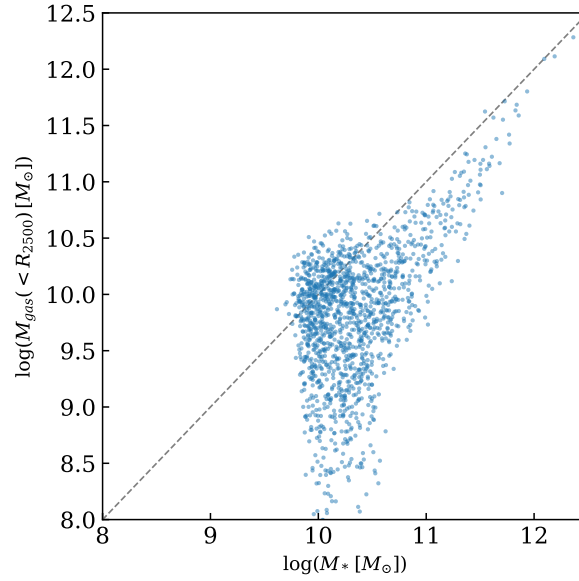


Figure 6.1:  $M_{\text{gas}} - M_*$  relation of our simulated galaxy sample. The dashed diagonal line indicates a one-to-one ratio.

the past 100 Myrs within the projected volume of each galaxy. This SFR estimator thus probes similar timescales of the SFH as typical tracers used in the literature such as in Mineo et al. (2012a). X-ray luminosities were calculated from the photon list obtained from a cylindrical volume around each galaxy with radius  $R_{2500}$  and projected along the l.o.s. for a length of  $2R_{2500}$ . The l.o.s. direction coincides with the  $z$ -axis of the simulation box. We chose  $R_{2500}$  as the smallest available scale invariant size from the halo catalog and to focus our analysis on the inner regions of selected galaxies in our sample. Reported comparison values probe projected radii on ISM scales consistently smaller than  $R_{2500}$ : Strickland et al. (2004) and Mineo et al. (2012a) within the  $D_{25}$  isophotes, Bogdan et al. (2013) within 0.05-0.15  $R_{200}$  (20-60 kpc), Lehmer et al. (2016) within  $\gtrsim 10$  kpc (see chapter on stacking procedure) and Lehmer et al. (2022) within  $\sim 50$  kpc.

Because PHOX was originally conceived as a tool to study the X-ray emission of galaxy clusters, the calculated emission for the hot gas component in galaxies does not account for self-absorption from the ISM. We attempt to model self-absorption following observational derivations of intrinsic ISM emission by employing an additional TBABS model with  $N_H^{\text{gas}} = 5 \cdot 10^{21}$  cm at the source redshift (see, e.g., Mineo et al., 2012b; Gilbertson et al., 2022; Lehmer et al., 2022). In Fig. 6.2 we show our galactic sample on the SFR- $M_*$  plane color coded by the  $b$  value, which is a measure of galaxy morphology from the intercept of  $M_* - j_*$  relation (Romanowsky & Fall, 2012; Teklu et al., 2015). We adopt the classification scheme by Schulze et al. (2020) with  $b > -4.35$  for disk galaxies (*blue*),  $-4.73 < b < -4.35$  for intermediates (*green*) and  $b < -4.73$  for spheroids (*red*). To increase the sample size of low-metallicity star-forming galaxies, we followed the approach taken by Weinmann et al. (2010), assigning a uniformly distributed log sSFR in the range -12.4 to -11.6 for halos with SFR = 0. This can be seen in Fig. 6.2 as an apparent strip of

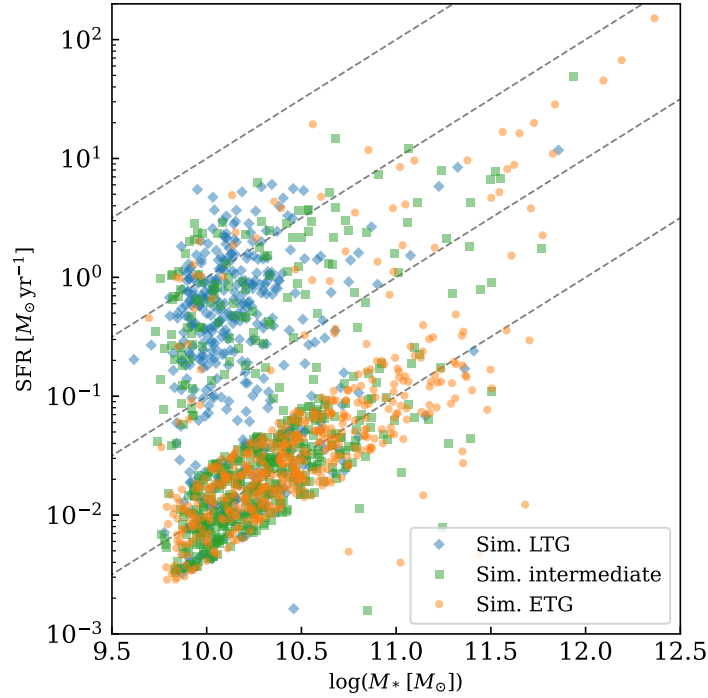


Figure 6.2: SFR –  $M_*$  relation of our sample. The dashed diagonal lines correspond to constant  $\log$  sSFR of  $-9$  (top) to  $-12$  (bottom) in increments of 1. Each galaxy was color-coded by its respective  $b$  value (Teklu et al., 2015) with the classification scheme from Schulze et al. (2020) (*red*: elliptical, *green*: intermediate, *blue*: disk). Galaxies clustered at  $\log$  sSFR =  $-12$  were given a SFR estimate based on the Weinmann et al. (2010) approach (see text).

mostly spheroidal galaxies located around the  $\log$  sSFR =  $-12$  line. We emphasize that galaxies distributed according to this criterion will not be used to derive hot gas properties in star-forming halos since the assigned SFR is not connected to gas properties within the simulations.

Subsequent analysis of the generated ideal photons will concentrate on the unfolded photon lists without taking into account any instrumental response.

## 6.4 Validation of the modeling

### 6.4.1 Spatial distribution of XRB emission

As a first step, we show that the XRB seeding follows the correct spatial distribution of XRB emission. We selected a poster-child late-type galaxy from our sample with  $M_* = 10^{11.3} M_\odot$ ,  $\text{SFR} = 8.4 M_\odot \text{yr}^{-1}$  and  $R_{2500} = 91$  kpc that appears face on to the line of sight. We focus our showcase on the inner 60 kpc to better capture the main stellar body of the galaxy. In Fig. 6.3 we show the percentile contours of photons emitted by HMXBs (*black*) and LMXBs (*red*) on top of the line-of-sight projected stellar mass map of the galaxy. As expected, the LMXB emission

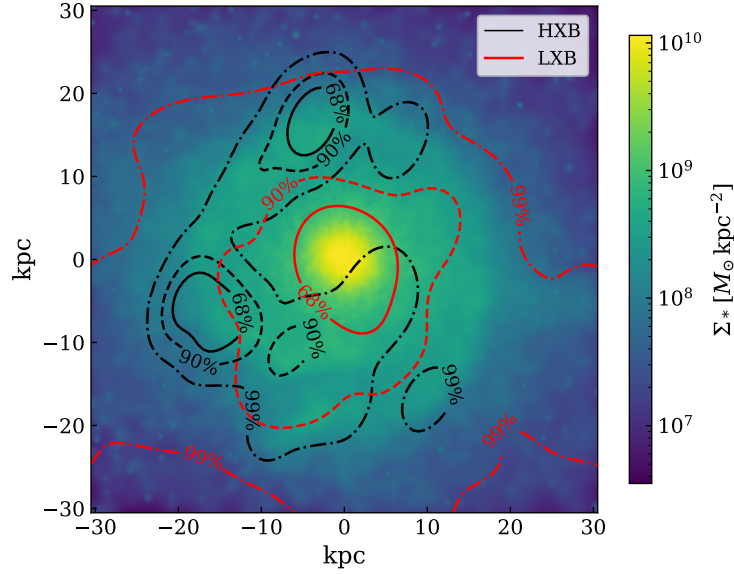


Figure 6.3: Projected stellar surface mass density ( $\Sigma_*$ ) of the poster-child disk galaxy in Box4 of Magneticum with halo ID 13633. Contours indicate the 68th, 90th, and 99th percentiles of X-ray photon positions for HMXBs (*black*) and LMXBs (*red*).

spans the whole field of the galaxy with its center over the galaxy bulge and decreasing with distance from the center reflecting the stellar surface density ( $\Sigma_*$ ). In contrast, HMXB emission is confined to the stellar mass overdensities surrounding the galaxy center. The reason for this can be seen in Fig. 6.4 where we show the same X-ray contours on top of the mass-weighted stellar age map of the galaxy. It shows that HMXB emission is bound to much younger stellar fields of the galaxy. In particular, the stellar age map shows the complex intersection of the two XRB components in the galactic field (e.g., [Lehmer et al., 2017](#); [Gilbertson et al., 2022](#)). While this general behavior for the two XRB types is expected, the ability to clearly distinguish the origin of X-ray emission of a galaxy is a major advantage and enables predictions on theoretical aspects of X-ray spectra of unresolved galaxies in high redshift observations. We note that the spatial distribution of emitted photons was smeared out according to a Gaussian, positioned at the projected particle location with a standard deviation equal to the simulation intrinsic smoothing length of the SSP. Because of that, XRBs are not visible as point sources.

### 6.4.2 XLFs

For the XLF reconstruction, we chose a lower luminosity limit of  $L_{\min} = 10^{35} \text{ erg s}^{-1}$ , since all XLFs are expected to have a turn-over at luminosities  $\lesssim 10^{35} \text{ erg s}^{-1}$ . This is due to neutron star XRBs generally experiencing lower Eddington accretion rates than their black hole counterparts, as well as a strong magnetic field influencing the accretion flow ([Shtykovski & Gilfanov, 2005a,b](#)). In addition, the integrated luminosity from the XLF will be dominated by the high

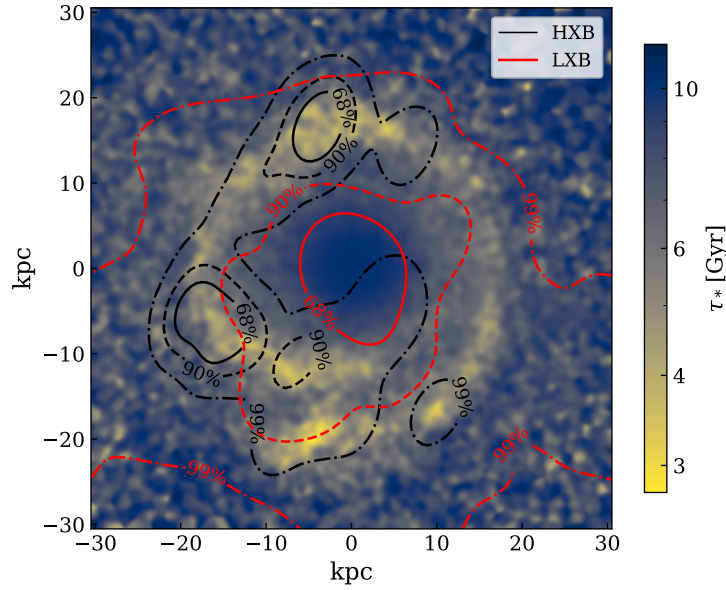


Figure 6.4: Mass-weighted stellar age ( $\tau_*$ ) of the poster-child disk galaxy in Box4 of Magneticum with halo ID 13633. Contours indicate the 68th, 90th, and 99th percentiles of X-ray photon positions for HMXBs (*black*) and LMXBs (*red*).

luminosity end, so lower value choices of  $L_{\min}$  will not change the integrated luminosity significantly. In Fig. 6.5 we compare the integrated XLFs (colored), reconstructed from the approach outlined in Sect. 6.2, with their original model (black). Corresponding XLFs are indicated with the same linestyle. Luminosities of individual XRBs were calculated from the simulated photon lists associated with the SSP element hosting the XRB. In detail, each colored line is derived from the total photon box produced for each SSP in the simulation. The apparent turn-over of the reconstructed lines is unrelated to any physical effects associated with neutron star XRBs but can be explained by the following: (1.) low luminosity XRBs are unlikely to produce observable photons given the distance of the simulation box (low flux); and (2.) in cases where the XRB population size is greater than one per SSP, low luminosity XRBs are removed from the XLF through the summation process of Eq. (6.15). The corresponding luminosity for a XRB emitting a single photon in our setup, assuming an absorbed PL spectrum, is marked by the vertical gray band at  $L_X \sim 10^{37} \text{ erg s}^{-1}$ , which roughly coincides with the turnover given the energy range of 0.5 – 8 keV. The solid vertical gray line is the luminosity of a photon with mean energy  $\sim 3 \text{ keV}$  according to Eq. (6.16). Thus, SSPs with  $L_{\text{SSP}} < 10^{37.4} \text{ erg s}^{-1}$  will produce at most one single photon given the discrete photon sampling in PHOX. We note that our setup is not dependent on background flux calibration, since our goal in Unit 1 of PHOX is to create an ideal photon list. We find excellent agreement between the reconstructed XLFs (colored lines) and their original model (*black*, same linestyle) above the single photon luminosity limit. The average reconstructed XLF for the L21 model (*orange*) is consistent with solar values for  $12 + \log[\text{O}/\text{H}]$ , which is almost indistinguishable from the Mineo et al. (2012a) XLF. Also shown is the L21 model at

$12 + \log[\text{O}/\text{H}] = 9.2$  and  $7.2$ , which are not good descriptions of the average HZB XLF.

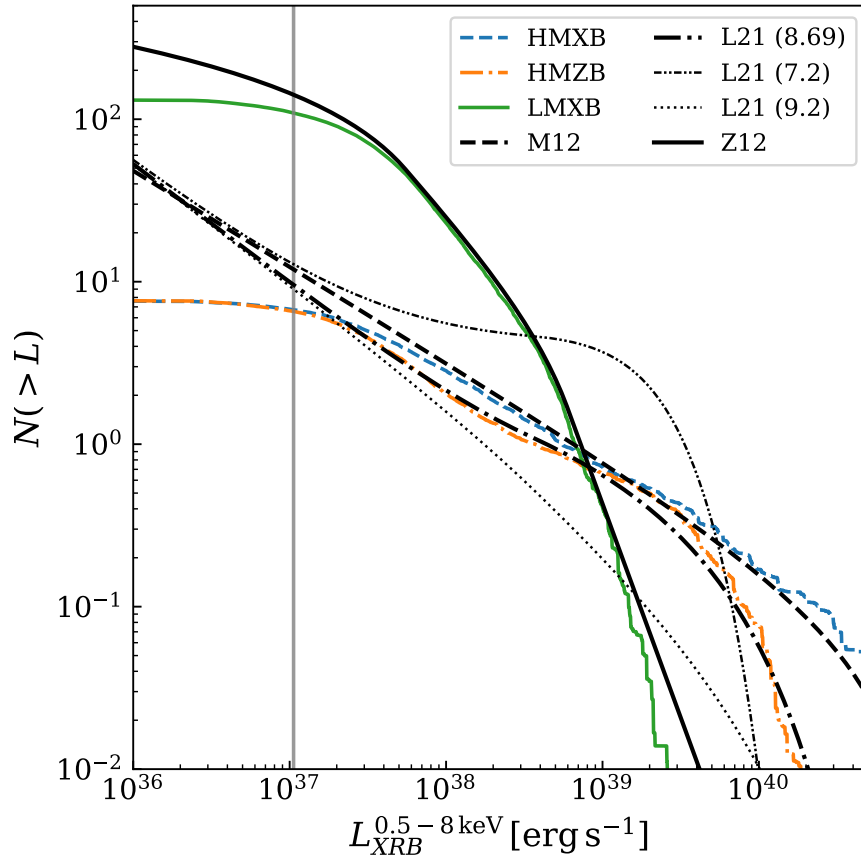


Figure 6.5: Integrated XLFs from Eqs. (6.1), (6.3), and (6.11) normalized by their respective scaling (SFR and  $M_*$ ). The *dash-dot-dotted* line is the XLFs of the L21 model, for  $\log[\text{O}/\text{H}] + 12 = 7.2$ , and the *dotted* line for  $\log[\text{O}/\text{H}] + 12 = 9.2$ . Colored lines are average XLFs obtained from the luminosity sampling in PHOX: from Mineo et al. (2012a) (M12) in *dashed blue*, Lehmer et al. (2021) in *dash-dotted orange* (L21), and Zhang et al. (2012) in *solid green* (Z12). Corresponding lines share the same line style. The *gray* vertical line at  $\log L \sim 37$  marks the maximum luminosity of a source emitting one single photon with an average energy of 0.5-8 keV.

### 6.4.3 Scaling relations

Since our approach to assigning luminosities to SSPs is agnostic to its environment, that is, if the SSP is part of a star-forming halo within the simulation, we first verified the self-consistent emergence of well-known galactic X-ray scaling relations.

Studies of the diffuse galactic X-ray emission revealed a linear relationship with SFR in the soft X-ray band, which is associated with ISM heating through SN remnants and stellar wind from heavy stars (Ranalli et al., 2003; Gilfanov et al., 2004a; Mineo et al., 2012b; Bogdán et al., 2013). However, it is observationally challenging to separate pure ISM emission from unresolved

emission from point sources. In fact, Mineo et al. (2012b) and Anderson et al. (2013) show that two-thirds of the galactic extended emission in the soft band can be attributed to XRB emission, which they estimated from XRB scaling relations. Since PHOX was designed to reproduce X-ray emission from galaxy clusters, we have to verify that galactic ISM properties are appropriately reproduced. In Fig. 6.6 we show the relationship between the hot gas X-ray luminosity and SFR in the soft X-ray band (0.5-2 keV). The blue contours enclose the 68th, 90th, and 99th percentiles of galaxies in our simulated sample also indicated by underlying green dots. We only show galaxies with  $\log \text{sSFR} > -11.6$ , which removes all galaxies falling in the Weinmann et al. (2010) criterion. This is done to reduce the influence of unresolved galaxies on the relation as well as removing weakly star-forming galaxies. Also shown is best-fit linear relation from Lehmer et al. (2022) with  $\log(L_X^{0.5-2\text{keV}}/\text{SFR}) = 39.58^{+0.17}_{-0.28}$ , using spectral energy distribution (SED) fitting to derive the SFH for each galaxy in their sample. We include absorbed ISM luminosities from Mineo et al. (2012b) (*red squares*) with SFR derived from a combination of UV and IR tracers. Their reported values in the soft X-ray band are smaller compared to the L22 relation, which may be caused by differences in sample properties like metallicity. They argue, however, that their normalization might be higher by at least a factor of 2, due to uncertainties in observed column densities and depending on their fitting procedure. Additional bolometric gas luminosities are obtained from Bogdán et al. (2013) (B13) (*black pentagons*) in the 0.5-2 keV energy range and a radial range of 0.05-0.15  $R_{\text{vir}}$  for late-type galaxies, with SFRs derived from the total IR luminosity. Although B13 aimed to study extended X-ray coronae around large spiral galaxies, the measured luminosities are consistent with a linear  $L_X - \text{SFR}$  relation prompting a connection between SFR and galactic outflows. From Strickland et al. (2004) (S04) we obtained data points for absorption-corrected total gas luminosities in late-type galaxies in the 0.3-2 keV energy range (*black stars*), which also show a linear SFR relation. They derived SFRs from the far IR band luminosity. Assuming the same energy range of 0.5-2 keV and no absorption correction for S04 values, resulting luminosities would be slightly lower. Within the 90th percentile contours, our galaxy sample is consistent with observational data of the extended galactic emission. We notice, however, that while a linear trend exists in our data, the relation is less tight and contaminated by low-luminosity galaxies at  $\text{SFR} \sim 1$ . Low-luminosity galaxies may have been the result of feedback processes removing large fractions of gas from the central halo, which we discuss in more detail in Sect. 6.6. The intrinsic scatter in our data of  $> 1$  dex is concerning, but might be a result of an uncurated sample. An important caveat is the limited resolution of the underlying simulation. Halos with stellar mass below the Milky Way stellar mass suffer greatly from the resolution restriction. In those cases, the total gas and stellar halo are composed of only a few hundred resolution elements, giving rise to a large intrinsic scatter due to the SPH implementation of the simulation as well as an eventual cutoff where a halo was not able to form stars (see Fig. 6.1).

The primary goal of this paper is to model the stellar X-ray emission in the form of XRBs using data from cosmological simulations. In Figs. 6.7 and 6.8 we show the principal scaling relations for HMXBs and LMXBs, respectively. The contours have the same meaning as in Fig. 6.6. The solid black line indicates the expected scaling relation from integrating the luminosity functions in Eqs. (6.3) and (6.1). In the HMXB case in Fig. 6.7 the reconstructed scaling relation is consistent with observations from Mineo et al. (2012a) but shows significant deviation from

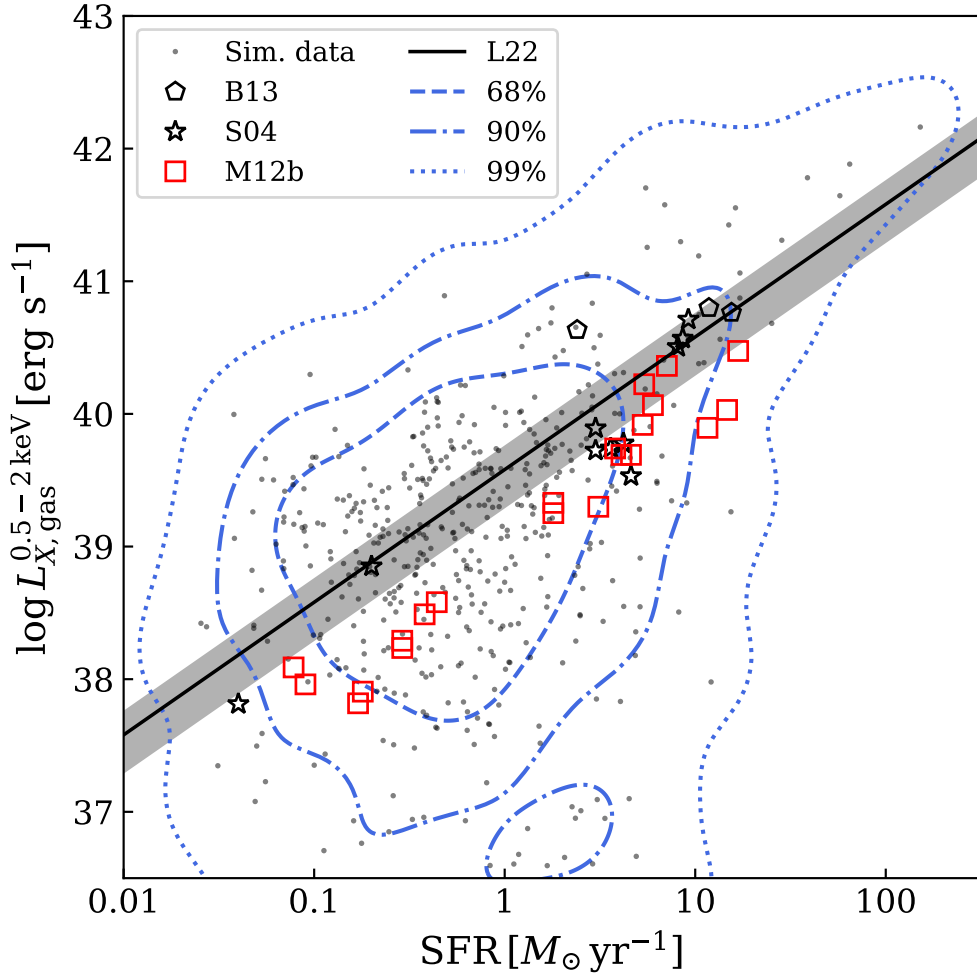


Figure 6.6: Relation between hot gas X-ray luminosity (0.5-2 keV) and the SFR for star-forming galaxies in the simulations. We only show galaxies with  $\log(\text{sSFR}) > -11.6$ , which removes all galaxies that fulfill the [Weinmann et al. \(2010\)](#) criterion. This is done to reduce the influence of unresolved galaxies on the relation as well as remove weakly star-forming galaxies. The *solid black* line indicates the linear relation from [Lehmer et al. \(2022\)](#). The gray shaded area is the corresponding  $1\sigma$  standard deviation. Data points are bolometric luminosities of the diffuse emission taken from [Strickland et al. \(2004\)](#) (S04) in the 0.3-2 keV band, [Mineo et al. \(2012b\)](#) (M12b) in the 0.5-2 keV band, and [Bogdán et al. \(2013\)](#) (B13) in the 0.5-2 keV band.

the expected linear SFR dependence at low SFR values. This apparent deviation was noticed in observations of star-forming galaxies as well (Grimm et al., 2003; Gilfanov et al., 2004a) and explained in Gilfanov et al. (2004b) where the transition between linear and PL regime of the SFR relation is caused by low-number sampling of a single sloped XLF. The approximate relation calculated from Gilfanov et al. (2004b) for the XLF in Eq. (6.3) is shown as the dashed black line and has a slope  $\frac{1}{\gamma-1}$ . For the LMXB case in Fig. 6.8, the linear stellar mass dependence is well reproduced but our data systematically underestimates the expected relation by a factor of  $\approx 0.15$  dex. This is a manifestation of the one-photon limit associated with the XLF sampling. Also shown in Fig. 6.8 is the integrated luminosity function of Z12 (Eq. (6.1)) for  $L_{min} = 5 \cdot 10^{37} \text{erg s}^{-1}$ , which is approximately the upper bound of the one-photon luminosity limit. Accounting for the under-sampling of the LMXB XLF caused by the one-photon limit thus improves the relation. A similar effect is not seen in the HMXB since the under-sampled XLF only contributes less than 5%. We do not observe a break in the LMXB- $M_*$  relation since our stellar mass limit ( $M_* = 10^{9.7} M_\odot$ ) is relatively high compared to the XLF normalization (Eq. (6.1)), which allows for sufficient sampling points. In the stellar mass regime of dwarf galaxies ( $M_* \lesssim 10^9$ ) we expect breaks in the  $L_X - M_*$  relation as well (Gilfanov et al., 2004b).

When combining the SFR-normalized emission from HMXBs and LMXBs, we expect a sSFR-dependent relation of the form

$$L_X/\text{SFR} = \alpha \text{sSFR}^{-1} + \beta, \quad (6.19)$$

where  $\alpha$  contains the linear mass dependence of the total LMXB luminosity and  $\beta$  contains the linear SFR dependence of the total HMXB luminosity (Lehmer et al., 2010, 2016, 2019). In Fig. 6.9 we show the sSFR dependence of the SFR-normalized combined XRB luminosity of our sample with contours as in Fig. 6.6. Additionally, we show data points from Mineo et al. (2014b) (M14) (SFRs as in M12a) from nearby galaxies and a study performed on star-forming galaxies within the Virgo cluster by Soria et al. (2022) (S22) with SFR values derived from the  $12 \mu\text{m}$  WISE W3 measurement. We include an observationally derived relation (*black, dash-dotted*) for local galaxies from Lehmer et al. (2019) (L19) where SFRs were derived from a combination of far UV and 24  $\mu\text{m}$  maps. The red dashed diagonal line represents the theoretical contribution from LMXBs given our model choice (Fig. 6.8) and the blue dashed line corresponds to contributions from HMXBs (Fig. 6.7). Because of the HMXB scaling relation being more similar to a BPL, the combined luminosity of LMXBs and HMXBs, normalized by SFR, takes a different shape (*dashed purple*) compared to the L19 relation: it reaches a minimum value at  $\text{sSFR} \sim -10$  after which it begins to approach the linear HMXB regime. Our sample is in agreement with the purple relation and is broadly consistent with the relations from L19 for  $\log \text{sSFR} \lesssim -10.5$ . However, due to the lack of high sSFR halos in the simulated sample, we are not able to reliably demonstrate the expected turnover predicted by our model in purple. Interestingly, we find remarkable agreement between the simulated data and S22 data obtained from star-forming galaxies in the Virgo cluster. Furthermore, data from M14 connects seamlessly to both the S22 sample and our sample. We also compare model 5 of Aird et al. (2017) (*solid cyan*) in which they quantify the total  $L_X$  of a star-forming galaxy as a function of  $M_*$ , SFR and redshift. They take into account their whole  $0.1 < z < 2$  sample of galaxies and convert the total count rate of each galaxy from the 0.5-2

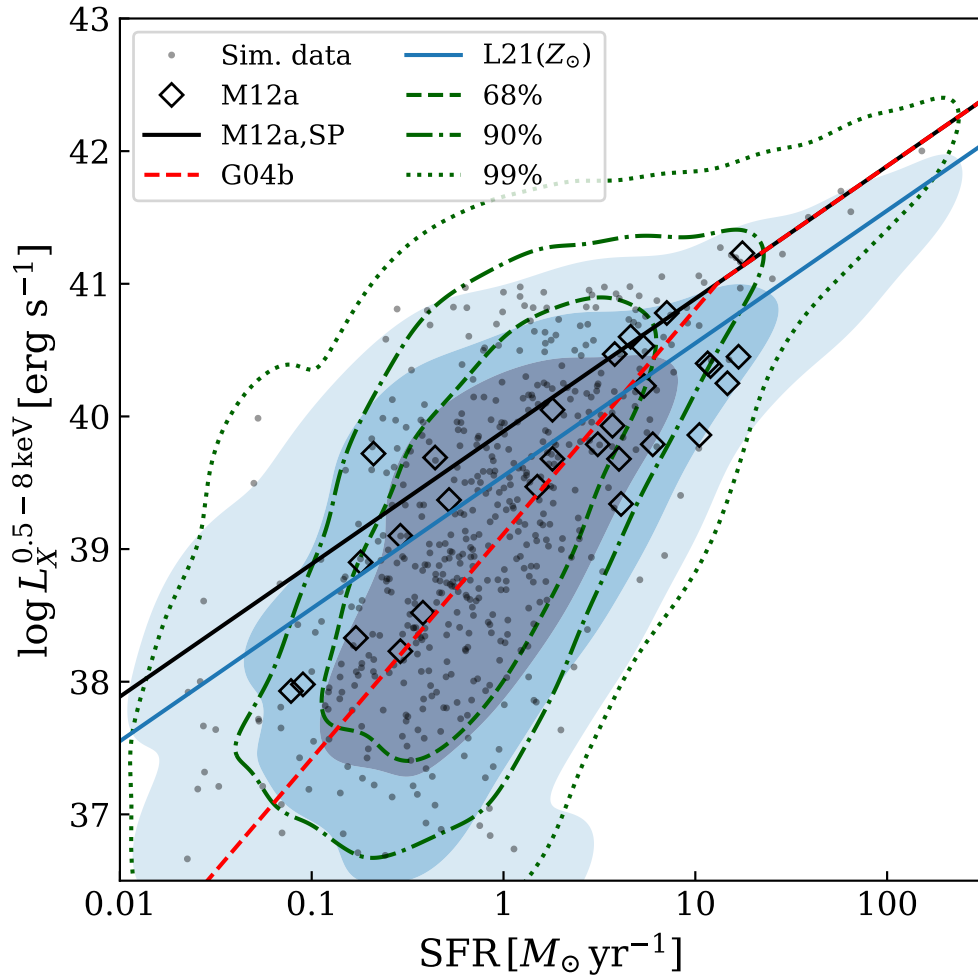


Figure 6.7: Same as Fig. 6.6, but for HMXB luminosity in the 0.5-8 keV band. The filled *blue* contours represent the same halos with HMXBs sampled from the L21 model (Eq. (6.11)). The *solid black* line is the expected relation from the employed HMXB model in Eq. (6.3), and the *dashed red* line is the predicted relation for discretely sampling data points from a PL distribution (Gilfanov et al., 2004b). The *solid blue* line is the expected relation from the employed L21 model. Data points are taken from Mineo et al. (2012a).

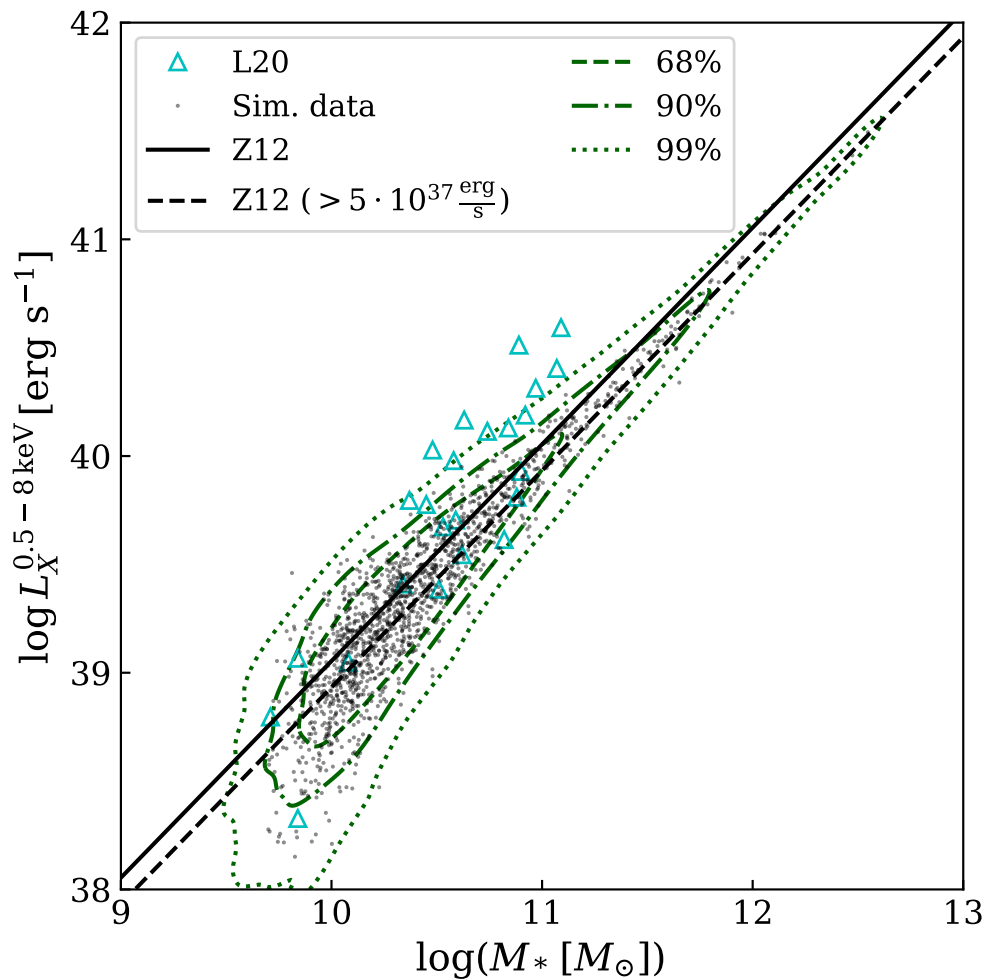


Figure 6.8: Same as Fig. 6.7, but for LMXB emission in the 0.5-8 keV band. The *solid black* line is the expected relation from the employed LMXB model in Eq. (6.1). The *dashed black* line is the same relation for a luminosity limit  $L_{min}$  of  $5 \cdot 10^{37} \text{erg s}^{-1}$ . Data points (*cyan* triangles) are taken from [Lehmer et al. \(2020\)](#).

keV band to the 2-10 keV band using a constant conversion factor based on an absorbed PL with  $\Gamma = 1.9$ . It takes the form

$$L_X = \alpha(1+z)^\gamma M_* + \beta(1+z)^\delta \text{SFR}^\theta, \quad (6.20)$$

with  $\log \alpha [\text{erg s}^{-1}] = 28.81$ ,  $\log \beta [\text{erg s}^{-1}] = 39.5$ ,  $\gamma = 3.9$ ,  $\delta = 0.67$ ,  $\theta = 0.86$ ,  $M_*$  in  $M_\odot$  and SFR in  $\text{erg s}^{-1}$ . We fixed the redshift to  $z = 0.01$  in line with our sample. Due to the nonlinear SFR dependence, model 5 falls off for higher SFR values. From a visual inspection alone, both our broken SFR scaling relation and model 5 appear to adequately describe the SFR-normalized luminosities from S22 at high sSFR. However, model 5 underpredicts luminosities in the low sSFR regime compared to our simulated data. In their study, S22 show that most of their data points with  $\log$  sSFR lie below the median tracks of Monte-Carlo simulations of L19 for various populations of galaxies. They argue that inclination effects and differences in the used galaxy population are causing this discrepancy.

#### 6.4.4 Metallicity relation of HMXB

Numerous studies on the total HMXB emission in individual galaxies associate an increase in HMXB emissivity per unit SFR with a lower-metallicity environment of the HMXB (Fragos et al., 2013b; Garofali et al., 2020; Lehmer et al., 2021; Saxena et al., 2021; Vulic et al., 2022). In this section we try to verify if our modeling allows us to capture the metallicity dependence of the HMXB luminosity function proposed by Lehmer et al. (2021) (L21) (see Eq. (6.11)). They obtained SFRs similar to L19 using far-UV and 24  $\mu\text{m}$  maps and gas-phase metallicities from emission-weighted oxygen line ratios. In Fig. 6.10 we show the SFR-normalized X-ray luminosity of our star-forming galaxy sample against the metallicity derived from the mass-weighted oxygen fraction of the young stellar population ( $< 30$  Myr). We binned our sample according to metallicity and SFR with horizontal bars representing the bin width in metallicity and vertical bars representing the 25th-75th percentile in luminosity. Black crosses are the median values for the whole star-forming sample while colored symbols correspond to different SFR bins. The SFR bins are displaced with respect to the metallicity bin center for illustrative purposes. Our full sample (*black crosses with error bars*) is consistent with the theoretical model and shows the expected increase in luminosity for lower metallicities. Similarly, the high SFR sample ( $\gtrsim 5 M_\odot \text{ yr}^{-1}$ , blueish colors) is also consistent with the global model up to an oxygen fraction of 8-8.5. Our sample did not include highly star-forming galaxies with lower metallicities. For the sample at  $\text{SFR} \sim 1 M_\odot \text{ yr}^{-1}$  (green) we find lower median luminosities compared to the global model but are consistent within the 25th percentile margin. From the Markov chain Monte Carlo simulation performed in L21, it is however expected that the median luminosity decreases with lower SFR values due to worse HMXB count statistics. Despite this, the median luminosity for the low SFR sample (*orange*) lies more than an order of magnitude above the relation predicted in L21 for  $\text{SFR} \lesssim 0.1$ . Given our approach to retrieve HMXB luminosities for SSPs in the simulation, we find that, with the given mass resolution of the simulation, a single eligible SSP in a low SFR galaxy might already overcount the expected number of HMXBs. Additionally, only luminous SSPs will be sampled by PHOX (see Fig. 6.5). Since we did not take into account

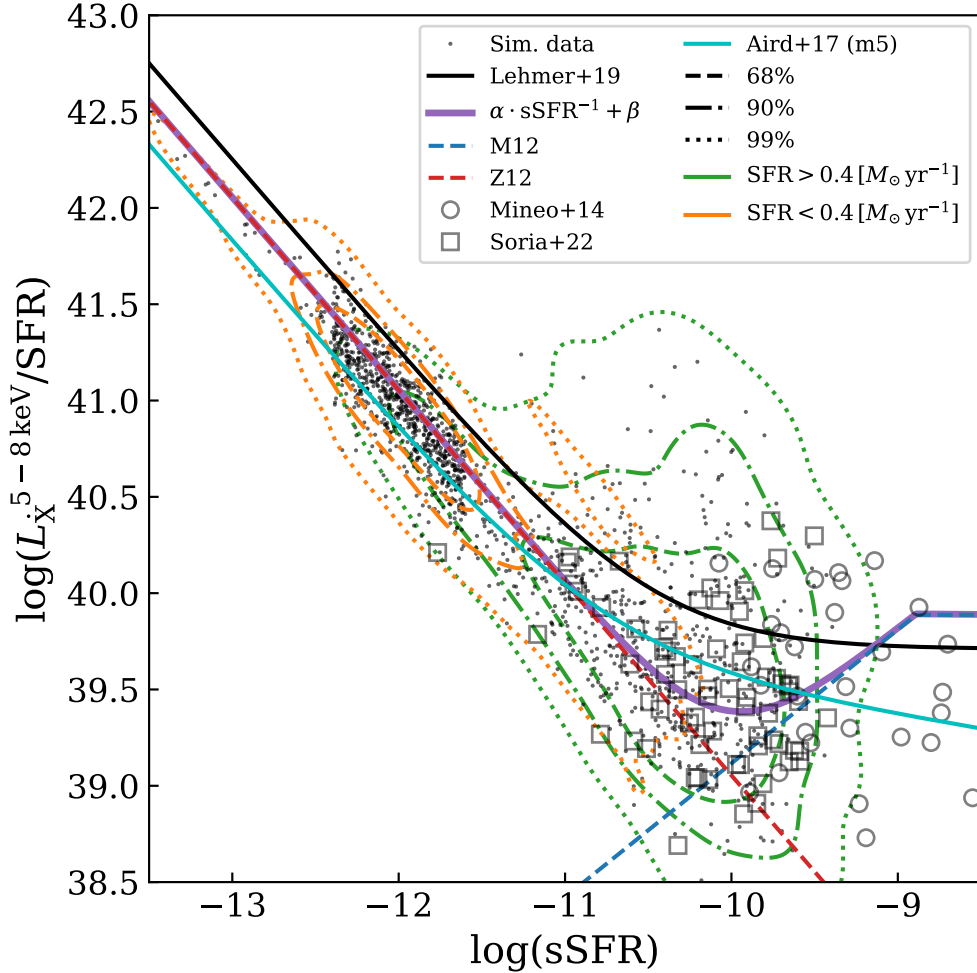


Figure 6.9: Relation between SFR-normalized total X-ray luminosity (both XRB types) and sSFR, for star-forming galaxies in Box4of Magneticum (contours: percentiles). The *solid black* line is the relation of observed normal galaxies at  $z \sim 0$  from [Lehmer et al. \(2016\)](#). The *dash-dotted* line represents the relation for a set of local galaxies from [Lehmer et al. \(2019\)](#). The *solid cyan* line is the relation obtained from model 5 (m5) in [Aird et al. \(2017\)](#), where we fixed  $z = 0.01$ . The *dashed red* line depicts the expected scaling relation for a pure LMXB contribution given our XLF choice. The *dashed blue* line shows the expected broken SFR scaling relation of a pure HMXB contribution. Data points are taken from [Soria et al. \(2022\)](#) (S22) and [Mineo et al. \(2014b\)](#) (M14).

galaxies that do not have HMXB emission despite being star-forming, we are biased toward a low SFR sample with comparatively large luminosities and too large HMXB population.

### 6.4.5 Additional Validation

This subsection is not included in the original paper (Vladutescu-Zopp et al., 2023) and was produced as a supplementary addition for this thesis. While the application of the LMXB model is straightforward, because of the direct scaling between the number normalization of LMXB with the stellar mass of the SSP, additional verification was needed for the HMXB case. In particular, we investigated the robustness of the proposed approach against the produced total number of HMXB on a large range of star-formation rates and compared formation efficiencies to the literature. By assuming different lifetime functions, we also investigated their influence on the result while not considering changes in the IMF since, in the high-mass regime, the IMF shape is similar across various sources.

For the theoretical experiment, we constructed 1000 artificial star-forming regions. Each region hosts a collection of SSPs in the age range of  $t_{\text{SSP}} \in [4, 200]$  Myr and with mass  $m_{\text{SSP}} \in [1, 4] \cdot 10^6 M_{\odot}$ . All SSPs within the region are distributed uniformly within the age and mass ranges and contribute towards the SFR if they are younger than 100 Myr. The assumption of a uniform age distribution is motivated by the age distribution of stars given within Magneticum in the considered range. In detail, we populated each region with an increasing number of SSPs starting from 1 up to 1000 SSPs which corresponds to an SFR range of  $[0.1, 12] M_{\odot} \text{ yr}^{-1}$ . For each region, and thus SFR, we re-seeded the corresponding SSP population 100 times and calculated the number of resulting HMXB according to the prescription given in Sec. 6.1.2. We show the result of this experiment in Fig. 6.11 where we illustrate the mean number of HMXB,  $N_{\text{HMXB}}$ , produced per unit SFR using the lifetime functions of Padovani & Matteucci (1993) (PM, blue circles) and Maeder & Meynet (1989) (MM, red squares). Vertical error bars indicate the  $1\sigma$  standard deviation, horizontal error bars indicate the width of the SFR bin, and cyan circles consider star-forming regions with no HMXB in the PM case. The black dotted line corresponds to the expected value of the underlying luminosity function given by Mineo et al. (2012a) and a lower luminosity limit of  $L_{\text{min}} = 10^{35} \text{ erg s}^{-1}$ . Blue and red symbols have been slightly offset from the central bin for visual clarity.

For high star-formation rates ( $\text{SFR} > 0.5 M_{\odot} \text{ yr}^{-1}$ ), both the PM and MM models reach a constant value as expected from observations and cyan circles coincide with the blue circles. However, the mean of the PM model falls short of the expected value of Mineo et al. (2012a) by a factor of  $\approx 1.2$ . In contrast, the MM model perfectly aligns with the expected value. With decreasing star-formation rates, both models drastically overestimate the number of HMXB per unit SFR if the star-forming region hosts an eligible SSP. The reason for this is the limited mass resolution representing the star-forming region. On average, the correct constant value can be reproduced when including the zero cases, indicated by the cyan circles. In cases where the low star-formation rate is represented by a single SSP, the normalization from the SNII rate is too high for the given SFR. This effect can however be mitigated, if the mass resolution of the SSP is higher, i.e. there are more SSPs with lower mass. We thus repeated the experiment for SSPs within the mass range  $m_{\text{SSP}} \in [1, 4] 10^5 M_{\odot}$  and found much better agreement with the expected

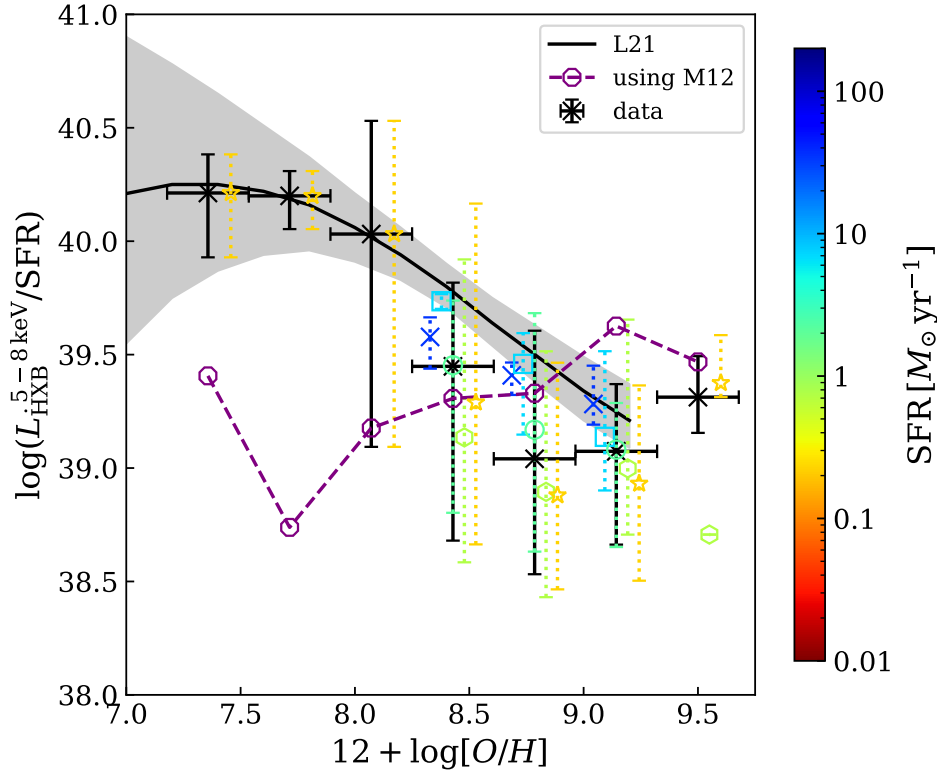


Figure 6.10: Metallicity dependence on the linear SFR scaling relation of HMXB luminosity. Oxygen fractions are derived from mass-weighted stellar metallicities of SSPs younger than 30 Myr. The *black solid* line is the mean global model calculated by L21 in the limit of perfect luminosity function sampling. The shaded *gray* area is its 16th-84th percentile margin. Our data are binned by oxygen fraction and SFR; SFR bins are indicated by color. Vertical error bars correspond to the 25th-75th percentile margin of the data within each metallicity bin, and horizontal *black* bars indicate the width of the metallicity bin. Colored symbols corresponding to the SFR bins are displaced horizontally with respect to the metallicity bin center for illustrative purposes. The dashed *purple* line is the corresponding M12a model where no explicit metallicity dependence is assumed.

value, shifting the problematic SFR range by an order of magnitude. Thus, our HMXB model performs better when the underlying cosmological simulation has a higher resolution.

In a separate validation study, we compared the formation efficiency of HMXB per unit stellar mass with the formation efficiency in the small Magellanic cloud (SMC). The HMXB population of the SMC has been extensively studied since its proximity allows for the detection of even low-luminosity HMXB down to  $L_X^{\text{HMXB}} \simeq 10^{34} \text{ erg s}^{-1}$  (Haberl & Sturm, 2016). In general, the formation efficiency,  $\eta$ , is defined as

$$\eta_{\text{HMXB}}(t) = \frac{N_{\text{HMXB}}}{M}, \quad (6.21)$$

where  $M$  is the total stellar mass of the star-forming region (Shtykovskiy & Gilfanov, 2007; Antoniou et al., 2019). In our setup, the formation efficiency is directly proportional to the SN rate (Eq. (6.5)). We therefore show the formation efficiency derived from our model in the right panel of Fig. 6.11. As before, blue lines are associated with the PM lifetime function whereas red is associated with the MM lifetime function. Solid lines represent the formation efficiency of our HMXB prescription following the SNII rate rescaled to the number of known HMXB in the SMC ( $\sim 130$ ) (Haberl & Sturm, 2016; Antoniou et al., 2019). The green dashed line is the formation efficiency derived for the SMC by Shtykovskiy & Gilfanov (2007) using XMM-Newton data, rescaled to account for a different definition of the formation efficiency, and the purple error bars are the values given in Antoniou et al. (2019) using *Chandra* data. The vertical dotted lines are the corresponding ages for an SSP at which a star of  $8 M_{\odot}$  would reach the SNII phase.

While the values for the formation efficiency are broadly consistent with the literature, a key feature not reproduced by our model is the maximum formation efficiency at  $\tau \approx 40 \text{ Myr}$  which is also seen in other galaxies such as M33 (Garofali et al., 2018). We would therefore expect our model to underpredict the number of HMXB resulting from a star-formation event. Indeed, when the PM lifetime function is assumed, the model marginally underpredicts the expected number of HMXB as discussed before. Assuming the MM lifetime function increases the maximum allowed SSP age while keeping a comparable formation efficiency. This increases the number of eligible SSPs from  $\approx 12\%$  to  $\approx 16\%$  in this setup<sup>2</sup> and exactly accounts for the missing HMXBs. We caution, however, that this effect may be pure coincidence and rather reflects the amount of finetuning present in our model prescription. In addition, our model relies on evolutionary prescriptions of single stars which introduces further uncertainty. Despite this, our model proved to be robust when applied to the environment of *Magneticum* which encouraged us to proceed.

## 6.5 Relative emission of hot gas and XRBs

In this section, we used the ideal photon list generated with `PHOX` to obtain relative count ratios between the gas and XRB components in our galaxy sample. Additionally, we built average spectra of normal galaxies by first looking at the whole sample and subsequently dividing the sample according to different galactic properties. Average spectra are obtained by first normalizing each

<sup>2</sup>Assuming the environment of this experiment with  $\tau \in [4, 200] \text{ Myr}$ .

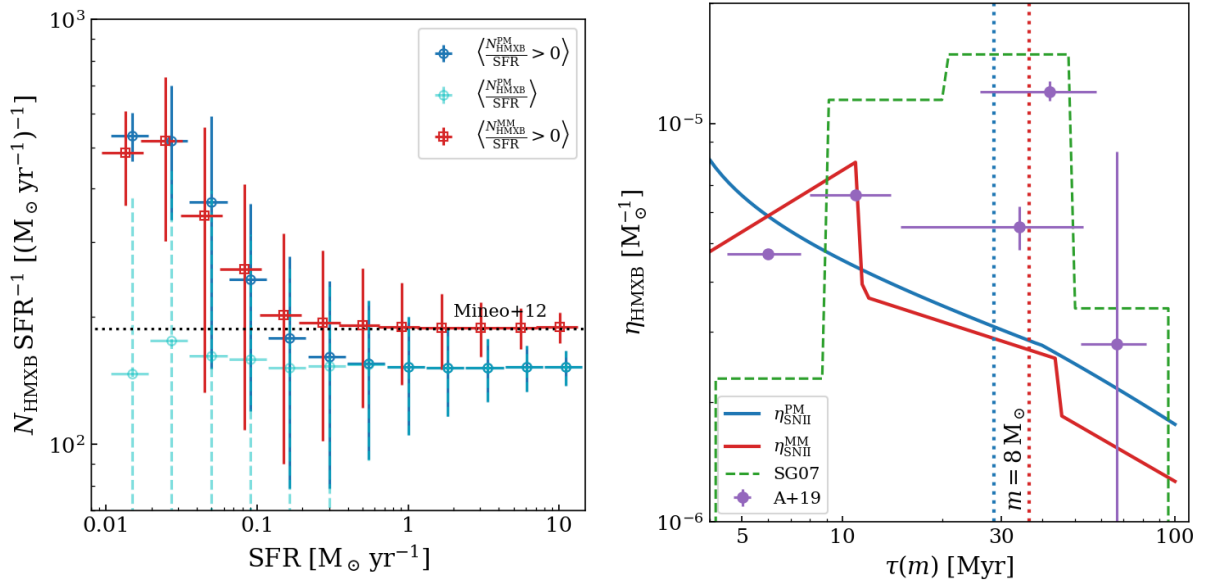


Figure 6.11: **Left:** Result of the model validation for the number of HMXB per unit SFR as a function of SFR for artificial star-forming regions. Each star-forming region is populated 100 times with 1 to 1000 SSPs, uniformly distributed in the age range [4, 200] Myr and mass range  $[1, 4]10^6 \text{M}_{\odot}$ . Colored symbols indicate the mean number of HMXB per unit SFR for a given SFR range assuming different lifetime functions (blue circles for [Padovani & Matteucci \(1993\)](#) (PM) and red squares for [Maeder & Meynet \(1989\)](#) (MM)). Cyan circles also consider regions with zero HMXB per unit SFR. The dotted black line indicates the expected scaling for the underlying luminosity function from [Mineo et al. \(2012a\)](#) assuming a  $L_{\text{min}} = 10^{35} \text{erg s}^{-1}$ . **Right:** Formation efficiency of HMXB per unit stellar mass. The red (MM) and blue (PM) solid lines represent the formation efficiency of our model as given by the SNII rate for the number of HMXB in the small Magellanic cloud (SMC) ([Haberl & Sturm, 2016](#)). The vertical dotted lines show the maximum allowed age of an SSP to still be eligible for HMXBs. The green dashed line is the formation efficiency of the SMC rescaled from [Shtykovskiy & Gilfanov \(2007\)](#) (SG07) to account for a different definition of the formation efficiency. The purple symbols with error bars are the formation efficiency as given by [Antoniou et al. \(2019\)](#) (A+19) using *Chandra* data.

galaxy spectrum with its total emission in the 0.5-10 keV band and afterward taking the average in each energy bin of the stacked spectra.

### 6.5.1 Relative count ratio

In order to investigate the relative contribution of the hot gas and XRB components in our galaxy sample, we compared the respective photon counts coming from each component. We split the contribution into different energy bands (0.5-2 keV, 2-8 keV, and 0.5-8 keV) and binned our galaxies according to the count ratio,  $r$ , which is defined as

$$r = 1 + \frac{c_{\text{XRB}}}{c_{\text{GAS}}}, \quad (6.22)$$

where  $c_i$  stands for the number of photon counts from the respective component. A value of  $r > 2$  indicates a dominant XRB component in our setup. In Fig. 6.12 we show the differential and cumulative fraction of galaxies in our sample with respect to the ratio  $r$ . We show the LMXB contribution, the HMXB contribution, and the summed contribution of LMXBs and HMXBs. Different line styles correspond to the different energy bands. Regarding the combined contribution of both XRB types we notice that  $\sim 90\%$  of our galaxies are dominated by XRB emission in the hard X-ray band (2-8 keV). Interestingly, this high fraction is almost exclusively caused by the LMXB emission. One has to keep in mind, however, that HMXBs only occur in galaxies with sufficient star formation. Thus, the low HMXB contribution is rather an expression of the rareness of star-forming galaxies compared to non-star-forming ones in our sample. If we include the soft band (0.5-2 keV), where the hot gas emission is stronger, only  $\lesssim 40\%$  of our galaxies are still dominated by XRB emission.

### 6.5.2 Average galaxy spectra

In addition to comparing the total counts received from each component, we construct an average spectrum from a star-forming galaxy sample and quantify the contribution of each component in each energy bin. To do this we first normalize each galaxy spectrum to its 0.5-10 keV emission and taking the average in every energy bin. The results can be seen in Fig. 6.13, which shows the total average spectrum, the average combined spectrum of both XRB types, and the average spectrum of hot gas. In the bottom panel of Fig. 6.13 we show the relative contribution of each component toward the total spectrum as a function of energy. Additionally, we added the average spectrum from [Lehmer et al. \(2022\)](#), which was derived for low-metallicity dwarf galaxies (*dashed red*) and values for the relative XRB contribution in different energy bands at redshift  $z = 0$  from [Lehmer et al. \(2016\)](#) (L16) in the lower panel of Fig. 6.13. From a visual inspection, the combined average spectrum is similar to the L22 spectrum in the energy range 0.8-10 keV despite differences in mass and metallicity regimes in their sample. Below 0.8 keV our average spectrum falls off more steeply than the L22 spectrum. This is connected to differences in assumptions made for the different component spectra in L22. They use a two-temperature APEC model with intrinsic absorption column densities similar to our  $N_H^{\text{gas}} = 5 \cdot 10^{22} \text{ cm}^{-3}$  but use a weaker absorption coefficient  $N_H^{\text{Xrb}} = 6 \cdot 10^{20} \text{ cm}^{-3}$  compared to our  $2 \cdot 10^{21} \text{ cm}^{-3}$ . Because

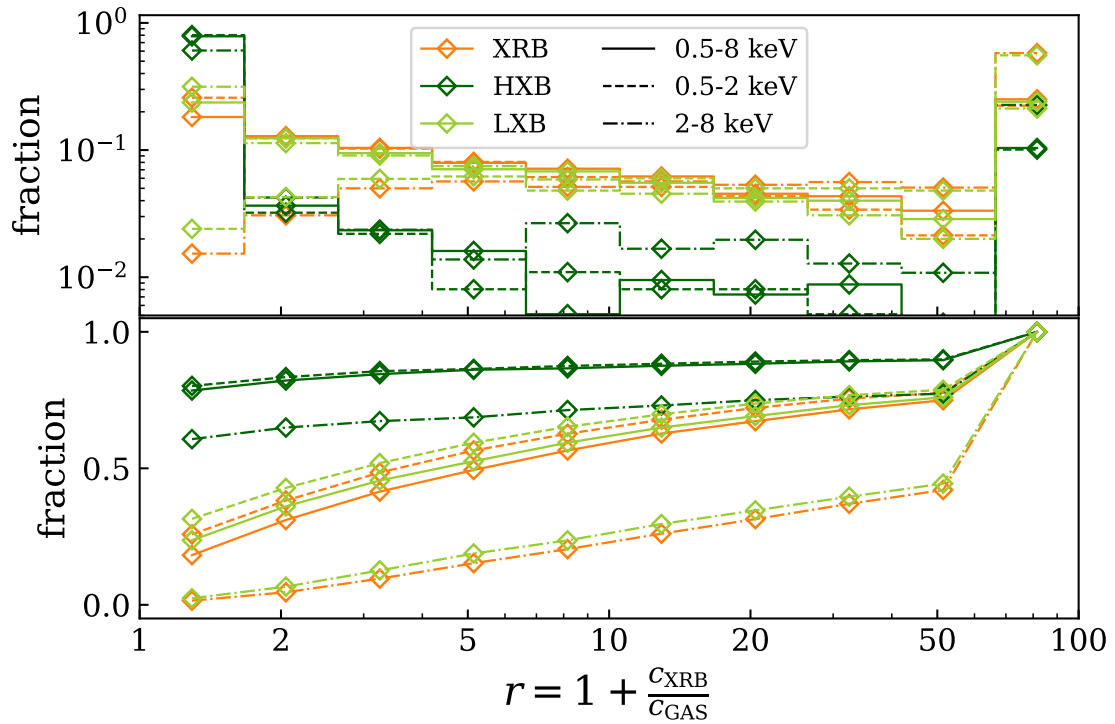


Figure 6.12: X-ray photon count ratio between the XRB and the hot gas component including all galaxies in our sample. Colors represent the component and line styles the energy range in the observed frame. The label “XRB” shows the sum of HMXB and LMXB emission. *Top*: Differential fraction of galaxies with a given count ratio,  $r$ . *Bottom*: Cumulative fraction of galaxies. Here, a ratio of  $r \geq 2$  means that the XRB component is dominant. Ratios exceeding the given range are collected in the last bin.

of this, the XRB contribution is much higher for low energies. The sensitive behavior of the spectrum at low energies can also be seen when comparing the relative contributions of XRB with values from L16 in the lower panel. In L16 they build an average spectrum for massive star-forming galaxies from observations by Wik et al. (2014), Lehmer et al. (2015), and Yukita et al. (2016). While we predict strong contributions of XRBs in the 0.5-1 keV energy range with >30%, L16 find much lower values of  $\sim 10\%$ . Our predictions agree well with L16 for harder energy bands (>1.5 keV). Interestingly, Wik et al. (2014) also find high XRB contributions in the 0.5-1 keV band that are similar to our values, again highlighting the strong model dependence of the XRB contribution in the soft X-ray. Given our simple choice for the XRB emission model in the form of a single absorbed PL, we fail to capture the expected steepening of the XRB PL for  $E > 6$  keV that is predicted by Lehmer et al. (2016) for normal galaxies, by population synthesis performed in Fragos et al. (2013b), and by, for example, Persic & Rephaeli (2002) for star-burst galaxies. A more sophisticated model of the XRB spectrum would be needed to fully reproduce observed spectral shapes.

Further disentanglement of the sample into increasing SFR bins yields a more refined view of the underlying galactic properties influencing the spectral composition. In Fig. 6.14 we show the same decomposition of galactic spectra as in Fig. 6.13 for four SFR bins. While the average XRB contribution stays consistent with previously discussed values, we see slight variations between each SFR bin. Specifically, in the lowest SFR bin (*top left*) we notice a very strong XRB component that generally exceeds estimates from L16. By comparing to Fig. 6.6, where we found galaxies with  $\text{SFR} \lesssim 1 M_{\odot} \text{ yr}^{-1}$  having low  $L_X$  within the 99th percentile contour, we attribute the strong XRB component to under-luminous gas-poor galaxies in the probed SFR regime and normalization issues when determining  $\tilde{N}_{\text{HMXB}}$  from Eq. (6.10), which leads to more HMXBs per unit SFR. In the next higher SFR bin (*top right*) the normalization of the spectrum drops slightly, mainly in the HMXB component because the normalization issue no longer applies here. Simultaneously, the hot gas component increases normalization in the hard band due to more massive galaxies contributing to the bin with hotter gaseous atmospheres. The relative contribution of the XRB component is consistent with L16 values in this case in the hard band. Further increasing SFR in each following bin yields even more prominent hot gas contributions in the hard band (see *bottom left* and *bottom right*). While the SFR-normalized total XRB luminosity stays almost constant in the two last bins, the XRB contribution is diminished by strong contributions from the hot gas atmospheres around massive, BCG-like galaxies with their deep gravitational potential. In these cases, the L16 values become less suitable to compare against since the considered samples have vastly different properties. In the highest SFR bin (*bottom right*) the inclusion of group-like mass regimes also disfavors the comparison against the L22 spectrum that was derived using high redshift analogs for normal galaxies.

Since the two lowest SFR bins present the largest contribution in terms of sample number, the total average spectrum from Fig. 6.13 will mostly resemble to the upper panels of Fig. 6.14. An important question associated with galactic X-ray spectra is their influence on the cosmic X-ray background. Upcoming planned X-ray missions such as Athena or the Light Element Mapper are sensitive enough to receive significant contributions from galactic emission to their background calibration. We plan to investigate this issue in an upcoming study.

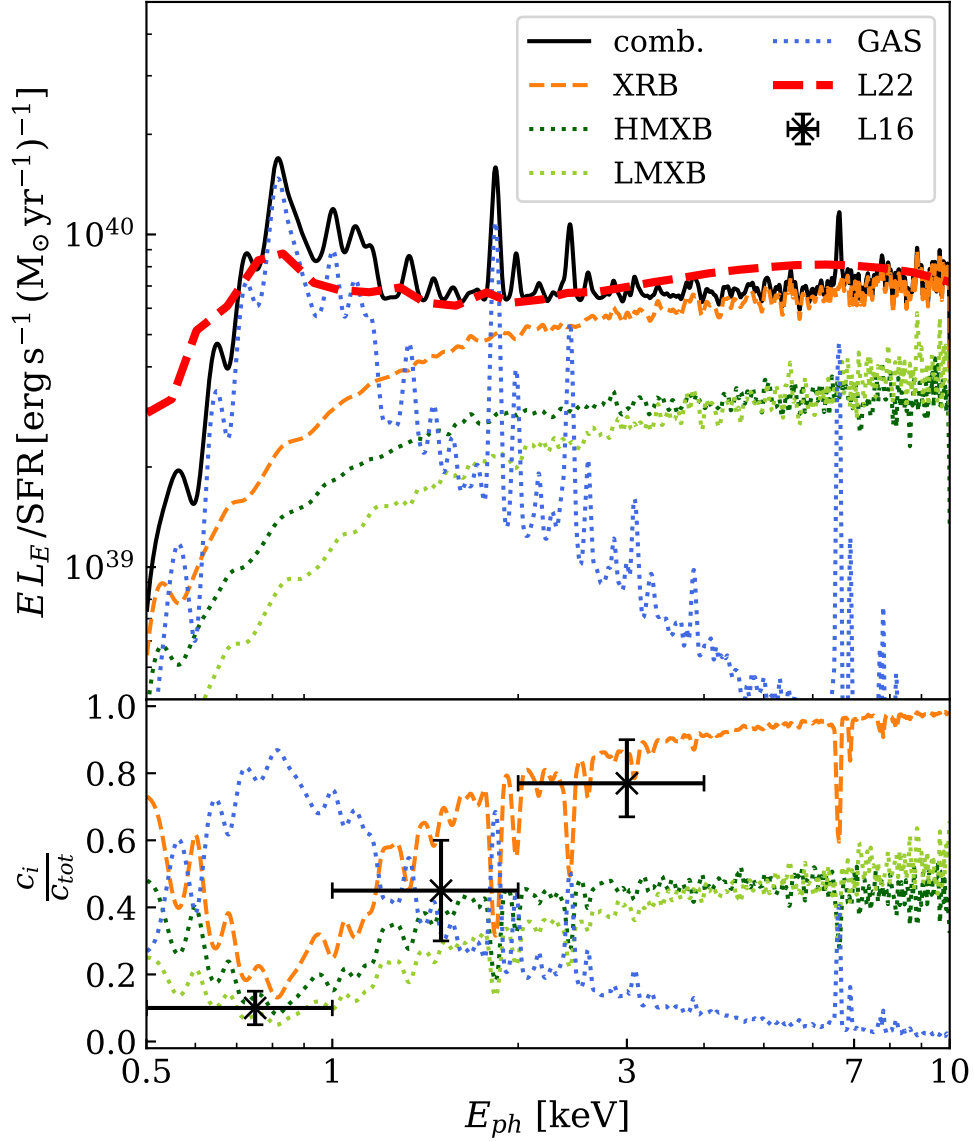


Figure 6.13: SFR-normalized average X-ray spectrum of our star-forming sample ( $\text{SFR} > 0.4 \text{M}_\odot \text{yr}^{-1}$ ). The combined spectrum (*black*) is made up of the HMXB (*dark green*), the LMXB (*lime green*), and the hot gas (*blue*) component. The combined XRB emission is given in *orange*. The *red* line is the L22 average spectrum derived from observations of dwarf galaxies.

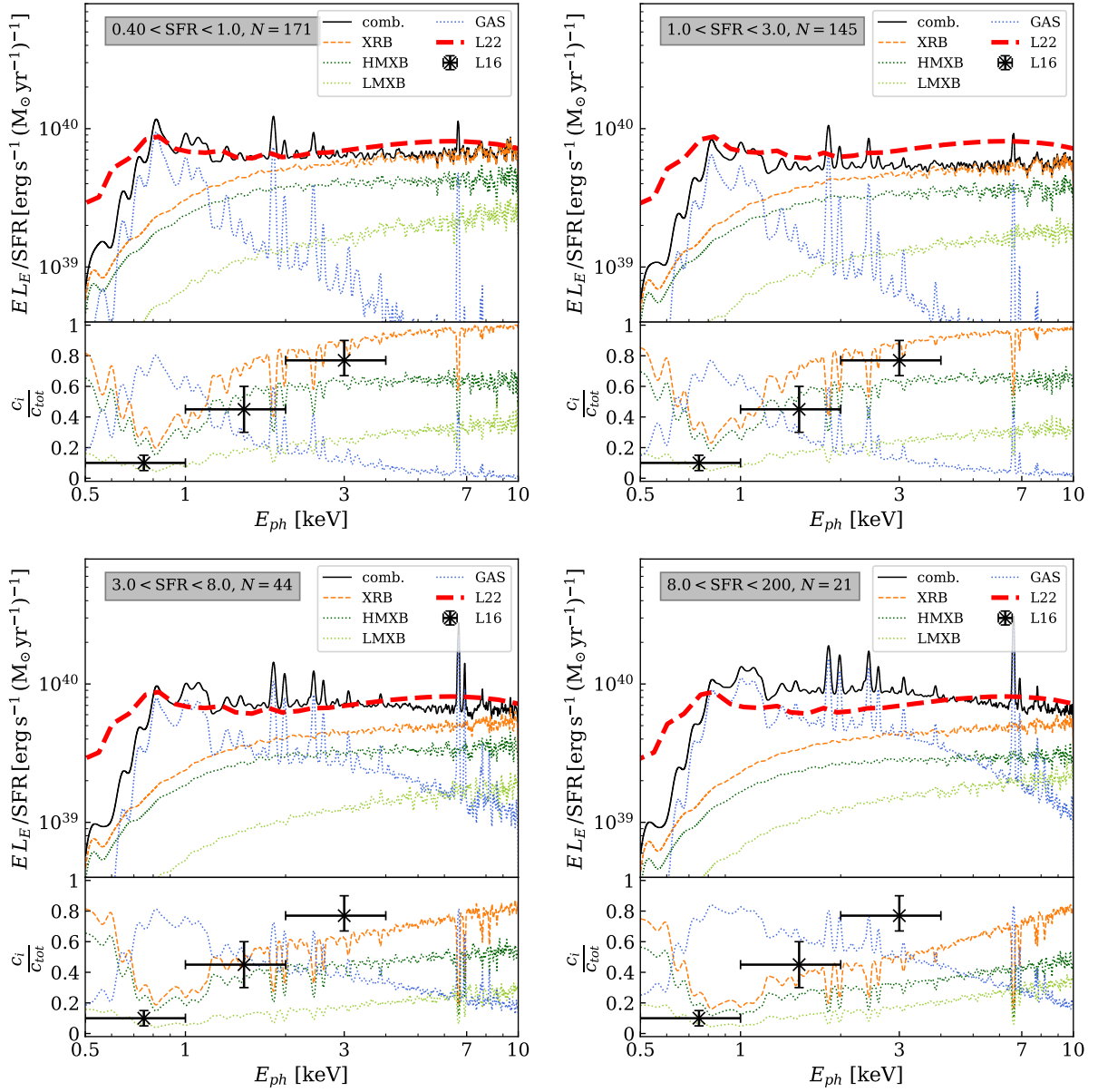


Figure 6.14: Mean X-ray spectrum (*solid black*) of our star-forming galaxy sample binned by SFR from lowest (*upper left* panel) to highest (*bottom right*) in the energy range 0.5-10 keV. The mean spectrum was calculated by normalizing each galaxy spectrum to its total 0.5-10 keV emission and taking the average in each energy bin. *Dotted* lines represent the different components that contribute to the total spectrum: hot gas emission (*blue*), LMXB (*lime green*), and HMXB (*dark green*). “XRB” (*orange*) stands for LMXB+HMXB emission. The *red* line is the L22 average spectrum derived from observations of dwarf galaxies. The lower part of each panel shows the fractional contribution of each component to the mean spectrum together with the XRB count ratios from L16. The gray box highlights the bin size and the number of galaxies,  $N$ , within each bin.

## 6.6 Discussion

### 6.6.1 Gas luminosity scaling relation

Compared to observational data we found that the  $L_X - \text{SFR}$  relation in the 0.5-2 keV band for the hot gas component has a large intrinsic scatter of  $\sim 1$  dex at  $\text{SFR} \lesssim 1$  with observers typically reporting lower luminosities of  $L_X \sim 10^{39} \times \text{SFR}$  with significantly smaller scatter (Strickland et al., 2004; Mineo et al., 2012b; Bogdán et al., 2013). We propose six explanations as to why we expected the scatter to be larger for the hot gas component.

First, in its core, the PHOX code was perceived as a tool to study X-ray emission from galaxy clusters with relatively hot atmospheres of  $T > 10^7$  K (Biffi et al., 2012). Thus, an intrinsic dusty absorption component was not required to realistically model cluster emission. In order to emulate a dusty absorber intrinsic to each selected galaxy of our data set, we applied a constant absorption model at the redshift of the selected halo consistent with ISM absorption column densities. While it improved the global relation compared to when no absorption is applied, it is not clear whether a strong absorption component is suited for halo outskirts beyond  $0.5 R_{2500}$ . Furthermore, numerous studies explicitly mention that intrinsic absorption is highly dependent on the observed galaxy and may vary significantly (e.g., Mineo et al., 2012b; Lehmer et al., 2016, 2019, 2022).

Second, in several galaxies with elevated  $L_X$  we found isolated pockets of dense hot gas clumps, despite specifically filtering out overheated star-forming gas elements from the simulation. This issue has to be investigated further but may be connected to the chosen projected volumes, which we explain in one of the following points.

Third, recent studies have shown that the extended hot gas atmosphere can significantly impact the total observed luminosity depending on the chosen projection radius (Nica et al., 2022; Comparat et al., 2022). In Comparat et al. (2022) they studied the X-ray emission of the circumgalactic medium for halos of stellar mass  $2 \cdot 10^{10} - 10^{12} M_\odot$  for different projection radii (80 kpc, 300 kpc). They further differentiated between star-forming and quiescent galaxies. They found that the enclosed luminosity in the 0.5-2 keV band increases by a factor of at least 2 for star-forming galaxies and  $> 10$  for quiescent galaxies if the enclosing projected radius is increased from 80 kpc to 300 kpc. In addition, they find that while quiescent galaxies clearly have an extended hot halo, star-forming galaxies share radial profiles with an expected diffuse unresolved component and weak AGN. This may indicate that, in order to more properly study gas scaling relations for the ISM, the projected radius has to be chosen more carefully.

Fourth, regarding the influence of AGN toward ISM properties, the Magneticum simulations include a thermal feedback model for SMBH described in Hirschmann et al. (2014). While SMBH properties are tracked by the simulations we did not specifically check for AGN activity in each of our selected halos. It is however known, that AGN experience different behavior compared to normal galaxies with respect to their X-ray radial profiles and scaling relations (Comparat et al. (2019); Vulic et al. (2022)). A proper disentanglement of AGN contribution to these relations goes beyond the scope of this paper. We prefer to more thoroughly analyze their effects in a future study.

Fifth, another influencing factor for gas properties in the ISM is ongoing mergers between

galaxies. In some instances we found that our selected halos had equally massive companions within  $R_{2500}$ , possibly introducing an additional heating source through merger-triggered interaction. We did not exclude merging halos from our sample since we selected for a good representation of different classes of objects for our XRB model.

Finally, the driving factor for uncertainty, especially toward low  $L_X$ , is probably the resolution limit of the total gas mass in the cosmological simulation. SPH simulations usually derive hydrodynamical quantities by interpolating between neighboring SPH elements with a set number of neighbors. As soon as a halo gas mass reaches below a lower mass limit, hydrodynamical effects like star formation can no longer be consistently resolved since the number of SPH elements in the halo becomes smaller than the needed neighbor number. The scatter is then dominated by the stochastic process with which sub-grid star-formation is handled in the implementation (see [Springel & Hernquist, 2003](#)).

We want to emphasize again that the hot gas component was not a major focus of this paper. Nonetheless, our approach shows that the simulation can recover a linear trend between gas X-ray luminosity and SFR if we select sufficiently resolved galaxies. However, the large scatter of over  $\sim 1$  dex shows that a simple approach to model the ISM is not optimal and needs more careful investigation.

### 6.6.2 XRB scaling relations

The main purpose of this paper was to introduce the viability of a semi-analytic approach to model X-ray emission from XRBs using hydrodynamical cosmological simulations. We connected locally derived luminosity functions of XRBs and their intrinsic behavior to hydrodynamical quantities from the simulations and showed the self-consistent emergence of expected scaling relations and spatial distribution. Here we discuss some interesting aspects regarding our results.

The strong scatter in the  $L_X - \text{SFR}$  relation of HMXBs is a major concern. While the expected Poissonian noise from a discrete sampling of the luminosity functions was predicted by [Gilfanov et al. \(2004b\)](#), additional uncertainties arise from our SFH proxy (see Sect. 6.1 and 6.4.5). For the birthrate of massive stars (Eq. (6.9)) we assumed a linear dependence on SFR that is only true as a first-order approximation and is highly sensitive to the underlying IMF. One would need to model the complete SFH of the star-forming region to account for time dependence. Since we are not able to recover this information from SSPs in cosmological simulations, this first-order approximation is the best we can achieve. For the lifetime function of stars, we assumed the prescription of [Padovani & Matteucci \(1993\)](#) (PM93), which is also implemented in the simulations ([Tornatore et al., 2007](#)). The advantage of the PM93 model is its simple functional form. There are more recently developed stellar lifetimes using evolutionary tracks calculated by PARSEC ([Bressan et al., 2012](#)). Such lifetime functions are nonetheless derived for single stars despite it being known that the evolution of massive binary systems heavily depends on orbital, stellar wind, and common envelope interactions (see, e.g., [Lewin & van der Klis, 2006](#), as a review on XRB evolution), which might drive inconsistencies in stellar age determination. For this reason, we decided to keep the PM93 model.

One of the most important drivers of uncertainty in the  $L_X - \text{SFR}$  relation for HMXBs at low SFR values, is the limited mass resolution of SSPs in the simulation. If the mass resolution

decreases the probability of having SSPs in the required age range of  $\tau_{\text{SSP}} \in [0, 30]$  Myr becomes smaller. Because there will be fewer SSPs per galaxy to resolve SFR, it adds another layer of Poisson noise. With smaller SSP masses we would be able to more accurately estimate the HMXB population size for each galaxy as is already seen in the LMXB case where the scatter in the  $L_X - M_*$  relation is much smaller. In fact, [Kouroumpatzakis et al. \(2020\)](#) showed that the  $L_X - \text{SFR}$  relation on sub-galactic scales should be consistent with galaxy-wide scaling relations. They argue that their shallower slopes in the sub-galactic relation is caused by LMXB contamination and differences in local SFH. Nonetheless, the overall trend in our recovered  $L_X - \text{SFR}$  relation is still consistent with observations.

In our investigation of the metallicity dependence we concluded that there is only a weak link between the SFR and the mass-weighted stellar metallicity in the simulation since the HMXB model from [Mineo et al. \(2012a\)](#) shows no significant increase in total luminosity with decreasing oxygen fraction. In fact, it instead suggests that there is a positive correlation between oxygen content and total luminosity, as indicated in Fig. 6.10, in contrast to observations by [Lehmer et al. \(2021\)](#). We attribute this behavior of the M12 model to our small low Z sample and to the fact that our approach does not account explicitly for metallicity. Sampling from the metallicity-dependent L21 model performs as expected and correctly reproduces observational results. We note that our low SFR sample (*yellow*) for  $12 + \log[\text{O}/\text{H}] \leq 8.5$  has much higher luminosities than predicted by the Monte Carlo Markov chains of L21 for  $\text{SFR} \sim 0.1$ . Apart from the number normalization issues discussed above for low resolution SSPs, we speculate that this difference might be caused by either a different zero-point in metallicity or differences between mass-weighted stellar metallicities and gas-phase metallicities, the latter of which is used in observations. We have to compare to the mass-weighted stellar metallicity in the simulations since we rely on the metallicity estimates of the SSPs. Considering the formation process of SSPs in the [Springel & Hernquist \(2003\)](#) prescription and the [Tornatore et al. \(2007\)](#) metal distribution, both gas-phase and stellar metallicities should be comparable in the simulations (see, e.g., [Dolag et al., 2017](#)).

In Fig. 6.9 we compare the  $L_X - \text{SFR} - M_*$  relation of our sample with recent observations of galaxies within the Virgo cluster from [Soria et al. \(2022\)](#) (S22). We find excellent agreement with our data. Due to the break in our  $L_X - \text{SFR}$  relation for HMXBs our expected transition of LMXB to HMXB dominated galaxies, around  $\log \text{sSFR} \approx -10.5$ , allows for slightly lower  $L_X$  compared to a linear scaling in  $L_X - \text{SFR}$ . The normalization of our  $L_X - \text{SFR}$  relation in the limit of high sSFR appears to be higher compared to the selected studies. In fact our model does not rule out the purely linear  $L_X - \text{SFR} - M_*$  relation and is equally consistent to the model in Eq. (6.19) if we consider a lower normalization for the  $L_X - \text{SFR}$  relation. Interestingly, model 5 of [Aird et al. \(2017\)](#) shows a sublinear normalization in the SFR component that also leads to a much better representation of the S22 data compared to the L19 model. They argue that the nonlinear SFR dependence may arise from differences in the properties of the stellar population, such as age and metallicity (see, e.g., [Fragos et al., 2013a](#)), across a given mass range of galaxies. Combining galaxies of different redshifts thus neglects changes in stellar properties contributing to differences in the total X-ray emission per unit SFR. A similar line of argument is raised by [Soria et al. \(2022\)](#) who claim that their observed incompatibility with the L19 models is caused either by the galaxy cluster environment or by unaccounted properties such as metallicity.

### 6.6.3 Average galaxy spectra

When we investigated the different components contributing to galactic X-ray spectra, we only used the ideal photon lists and did not perform a full mock observation using instrumental response with subsequent unfolding of spectra. While different instruments are more or less suited to detect X-ray point sources like XRBs, we did not think that a full mock observation would prove to be beneficial in order to present the XRB algorithm. Since real observations on X-ray spectra of galaxies report unfolded spectra, we skipped the instrumental response and reconstruction in favor of cleaner and better data. Our analysis of the average galactic spectra showed that XRBs can have significant contribution for energies  $E \leq 2$  keV. We note, however, that our approach suffers from the same spectral simplification as discussed in [Sazonov & Khabibullin \(2017a\)](#). They argue that variability of XRB spectra has to be accounted for individually including intrinsic absorption and spectral hardness for each source. Otherwise, the luminosity estimates for soft sources can be significantly different. They suggest taking ISM maps of the host galaxies into account and individually resolving spectral shapes to improve upon luminosity estimates for XRBs. Given the modular design of our XRB module for the photon simulator PHOX, spectral models for XRBs can easily be updated to account for XRBs in different hardness states, for example using spectral characteristics from [Sazonov & Khabibullin \(2017b\)](#). From the same arguments, the estimated count ratios might also be slightly different if some sources had higher flux in the soft band.

The mean X-ray spectrum of our star-forming sample is consistent with estimates from [Lehmer et al. \(2022\)](#) although their derived SED is based on observations of dwarf galaxies with sub-solar metallicity as high redshift analogs to local galaxies. The good agreement with our data is caused by our hot gas luminosity estimates being in part 0.5 dex above conventional values for the ISM (see Fig. 6.6). An increase of gas luminosity for lower-metallicity environments from L22 thus improves the visual overlap but does not correspond to a lower metallicity in our sample. Another issue is the strong suppression of metal lines in the tabulated SED in L22. We accounted for that by convolving our derived spectrum with a fairly wide Gaussian kernel, which still does not suppress some very prominent line features at high energies. We also find that the shape of our simulated SEDs are flatter at  $E \sim 1 - 2$  keV compared to the L22 SED. Differences in spectral shape, especially in the soft energy regime, are highly dependent on the adopted absorption models as discussed for Fig. 6.13, which leads in our case to overestimation of the XRB component compared to values from [Lehmer et al. \(2016\)](#). In the hard band, the L16 estimates are consistent with our derived values. Splitting the average spectrum into different SFR bins revealed stronger contributions from the hot gas component in high SFR galaxies as well as a higher normalization in general. This is due to the influence of massive BCG-like galaxies in the sample with hot gaseous atmospheres. In those cases, the L16 values are no longer suited to compare our derived values against. [Gilbertson et al. \(2022\)](#) show that the expected influence of the hot gas component is also a function of stellar population age, with the hot gas contribution declining to less than 5% in older populations, which was not investigated in our presented sample. In addition to an SFR-normalized emission model that is consistent with the L22 spectrum, [Gilbertson et al. \(2022\)](#) also report stellar-mass-normalized average spectra, which we did not compare against as it goes beyond the scope of this paper. We will conduct a future, more detailed investigation of the influence of the hot gas component to the average spectrum,

where we will also drill down on line properties within the ISM and circumgalactic medium.

## 6.7 Summary and conclusions

Based on SNII rate estimates made using SSP ages and masses tracked by numerical cosmological simulations, we are able to self-consistently reconstruct an SFR proxy suitable for Monte-Carlo-like sampling of XRB luminosity functions. We have presented a possible implementation within the PHOX code and verified the validity of our approach using simulated galaxies from the Magneticum Pathfinder simulations. We extracted galaxy-sized halos from the simulation based on a stellar mass criterion ( $10^{9.5} M_{\odot} \leq M_* \leq 10^{12} M_{\odot}$ ) and produced ideal photon lists for the hot gas and the XRB component using the stochastic photon simulator PHOX. We assumed XRB emission followed a static PL with photon index  $\Gamma = 1.7 - 2$ , while hot gas was modeled assuming a single temperature APEC model with thermal line-broadening and varying metal abundance for each gas element in the simulation. To account for the self-absorption of the ISM at the source location, we additionally required an intrinsic absorption component for both hot gas and the XRB component with column density  $N_H^{\text{gas}} = 5 \cdot 10^{21} \text{cm}^{-2}$  and  $N_H^{\text{xrb}} = 2 \cdot 10^{21} \text{cm}^{-2}$ , respectively. For each halo in our sample, we constructed cylindrical volumes around the center of mass with  $R = R_{2500}$  and  $h = 2 R_{2500}$  and projected the enclosed photons, accounting for the redshift and peculiar motion of the source with respect to the line of sight. Our findings from the resulting galactic X-ray spectra can be summarized as follows:

1. The global reconstructed XRB luminosity functions perfectly resemble the underlying analytic shape. The observed flattening of the reconstructed XLFs below  $\log L_{XRB} \approx 37$  is consistent with the expected one-photon luminosity. The reconstructed XLF derived from the metallicity-dependent model from [Lehmer et al. \(2021\)](#) most closely resembles the XLF shape for solar metallicity, which is almost indistinguishable from the [Mineo et al. \(2012a\)](#) model. A more curated sample of galaxies would be needed to reliably disentangle the effects of metallicity on the XLF shape, which may be analyzed in a separate study.
2. The  $L_X$ - $M_*$  relation for LMXBs is tightly constrained and is in excellent agreement with the [Zhang et al. \(2012\)](#) relation. More recent measurements of this relation by [Lehmer et al. \(2020\)](#) are also consistent with our data.
3. The  $L_X$ -SFR relation for HMXBs suffers greatly from low-number statistics for  $\text{SFR} \lesssim 1 M_{\odot} \text{yr}^{-1}$ . Additionally, the SFR proxy used to determine the number of HMXBs per SSP has large intrinsic uncertainties stemming from the limited mass resolution of the simulation and assumptions for stellar lifetime and IMF. Despite these drawbacks, our approach is still consistent with a BPL relation, which is expected to arise from incomplete sampling of the HMXB XLF dominated by Poissonian noise ([Gilfanov et al. \(2004b\)](#)).
4. The  $L_X$ -SFR-Z relation as proposed by [Lehmer et al. \(2021\)](#) does not arise when sampling from the M12a relation, indicating a weak correlation between SFR and Z within the simulation. When employing the L22 model directly, the correlation becomes more obvious but continues to suffer from the same uncertainties inherent to the HMXB sampling.

5. The  $L_X/\text{SFR-sSFR}$  relation we recovered from studying the combined effect of both XRB types is in remarkable agreement with recent studies of field galaxies within the Virgo cluster from [Soria et al. \(2022\)](#). The shape of our derived relation shows more complex behavior at  $\log \text{sSFR} \sim -10$  compared to the conventional relation found in the literature ([Lehmer et al., 2010, 2016, 2019](#)) due to the observed break in the HMXB relation.
6. As expected, we find that HMXBs spatially coincide with the star-forming regions of their host galaxies and that the spatial LMXB distribution follows the stellar-mass surface density.
7. We find that approximately 40-50% of our galaxy sample is dominated by the combined XRB emission compared to emission from the hot gas component in the 0.5-8 keV energy band. In the soft band only 30-40% of galaxies are dominated by gas emission, while more than 90% are dominated by XRB emission in the hard band. The surprisingly low contribution of HMXBs to these percentages reflects the relatively small portion of high SFR galaxies within our sample.
8. We constructed average SFR-normalized galactic X-ray spectra from our complete star-forming sample ( $\text{SFR} > 0.4$ ) and measured the relative contribution of the two XRB types and the hot gas component toward the total spectrum. The average spectrum of the total star-forming sample is consistent with the spectral fits from [Lehmer et al. \(2022\)](#) in terms of magnitude and shape, assuming an average SFR of 1. Contributions from XRBs to the soft part of the spectrum are inconsistent with values from [Lehmer et al. \(2016\)](#) but consistent with those from [Wik et al. \(2014\)](#), which reflects different model assumptions for absorption and XRB spectra. Additionally, the normalization of the spectrum only shows minimal variations across different SFR bins and is mostly influenced by the presence of massive galaxies in the sample.

In this paper we have presented an approach to modeling galaxy X-ray spectra from cosmological simulations. In addition to the hot gas component in the simulation, we took the properties of stellar elements into account and implemented a fast and consistent algorithm to compute XRB emission from these elements while reliably separating the two different XRB types. The presented method proves its viability as a supporting tool for observers with its highly modular design, which also allows for alterations to employed model spectra for individual components. Future studies that build upon the suggested implementation will improve the sample selection and focus on the influence of X-ray AGN emission on scaling relations, on the background, and on the retrieved spectra.



# 7 | The X-ray atmospheres of simulated galaxies (Paper 2)

- This chapter has been published in [Vladutescu-Zopp et al. \(2024\)](#) and received minor adjustments.

In the standard cosmological framework, dark matter (DM) halos attract baryonic matter to form galaxies and galaxy clusters. The infalling baryonic matter is then shock-heated to X-ray temperatures ( $T \gtrsim 10^6 K$ ) in equilibrium with the gravitational potential well ([White & Rees, 1978](#); [White & Frenk, 1991](#)), forming a gaseous circum-galactic medium (CGM). Due to long cooling times compared to the dynamical time, the CGM is expected to be quasi-static where the majority of cooling processes occur through thermal Bremsstrahlung and line-dominated cooling from different metal species. In addition, there are several feedback mechanisms, such as star-formation and feedback from accreting super-massive black holes (SMBHs) powering active galactic nuclei (AGN), which inject metals and energy into the CGM and cause the CGM to be multi-phase. The interplay between different feedback mechanisms from e.g. AGNs and stellar evolution as well as the refueling of the inner gas reservoir through cooling processes in the CGM play a crucial role in the quenching and growth of galaxies (see review [Tumlinson et al., 2017](#)).

The multi-phase structure of the CGM is apparent from observations. Studies of the absorption and emission lines of hydrogen and metals in the UV band revealed the presence of the warm ( $T \sim 10^{5-6} K$ ) phase of the CGM ([Tumlinson et al., 2013](#); [Werk et al., 2016](#); [Burchett et al., 2019](#)) for nearby galaxies which provides further evidence that most of the baryonic matter, including metals, is likely bound to the CGM ([Stocke et al., 2013](#); [Werk et al., 2014](#)). Direct X-ray emission from the CGM revealed its hot phase ( $T \gtrsim 10^6 K$ ) in a few nearby massive galaxies ([Humphrey et al., 2011](#); [Bogdán et al., 2013, 2015](#); [Buote, 2017](#); [Li et al., 2017](#); [Das et al., 2019, 2020](#)) where the signal to noise (S/N) ratio allowed them to have reliable detection up to  $0.15 R_{200c}$ <sup>1</sup>. One of the main challenges in determining the properties of the CGM is the low surface brightness (SB) of hot gas at large galactocentric distances, due to declining gas density. Because the X-ray emissivity of hot plasmas in collisional equilibrium scales with the square of the density, the X-ray SB thus declines faster than the density. In addition, the X-ray foreground of our own Milky Way (MW) is present in all directions ([McCammon et al., 2002](#)) and drowns out most of the signal coming from the low-SB CGM. By performing a stacking analysis of survey galaxies,

---

<sup>1</sup>In the linear collapse model of structure formation,  $R_{200c}$  denotes the radius at which the mean halo density reaches 200 times the critical density

foreground effects can be somewhat mitigated to obtain a statistical signal from the CGM in the soft X-ray band (SXB) (Anderson et al., 2013, 2015; Li et al., 2018; Comparat et al., 2022; Chadayammuri et al., 2022; Zhang et al., 2024b) which however hampers our ability to quantify other global properties of the CGM such as mass, metallicity and temperature. Recent results from the extended ROentgen Survey with an Imaging Telescope Array (eROSITA) (Predehl et al., 2021) claim the detection of the CGM out to a radius of 300 kpc, close to the virial radius of MW-mass galaxies (Comparat et al., 2022; Chadayammuri et al., 2022; Zhang et al., 2024b). Both UV and X-ray observations are complemented by analytic models of the temperature and density distribution in the CGM (Faerman et al., 2017, 2020).

Most of the emissivity in the SXB is due to specific metals (e.g. oxygen, neon, and iron) which have their transition lines of different ionization states in the energy range of 0.5-2 keV. Recent studies showed that with high-resolution X-ray spectroscopy, it may be possible to directly measure the emissivity of specific metal transitions in certain redshift ranges outside of the MW foreground (Barret et al., 2018; Tashiro et al., 2020; Kraft et al., 2022). This would enable more detailed studies on metal abundances and temperature of the CGM (Wijers & Schaye, 2022; Truong et al., 2023; Bogdán et al., 2023) and give insights into large-scale anisotropies within the hot X-ray atmosphere (Truong et al., 2023; Schellenberger et al., 2023; ZuHone et al., 2024).

A major component of contamination in X-ray emission are unresolved point sources in the form of X-ray binary (XRB) systems in the stellar field of galaxies. Low-mass XRBs (LMXBs), whose cumulative total luminosity scales linearly with the total stellar mass of the galaxy (Gilfanov, 2004; Zhang et al., 2012; Lehmer et al., 2016, 2019), are mostly associated with elliptical galaxies with low SFR (Boroson et al., 2011; Bogdán & Gilfanov, 2011; Lehmer et al., 2020). High-mass XRBs (HMXBs) are mostly found in galaxies with high SFR (Grimm et al., 2003; Mineo et al., 2012a). From these earlier studies of HMXBs, it is known that both the total number and total luminosity of HMXBs scale linearly with the SFR of galaxies. More recent studies found evidence for flatter dependence on SFR for galaxies with low SFR (Kouroumpatzakis et al., 2020; Kyritsis et al., 2024). Deviations from a linear relation can in principle be connected to a redshift dependence (Lehmer et al., 2016; Aird et al., 2017), to metallicity (Lehmer et al., 2022) or to stellar age distributions (Lehmer et al., 2017; Gilbertson et al., 2022). However, the observed flatter relation at low SFR is not consistent with low number sampling of HMXB luminosity functions (Gilfanov et al., 2004b; Vladutescu-Zopp et al., 2023; Kyritsis et al., 2024). Typically, the total XRB contribution to the total galaxy X-ray luminosity is not exactly known in observations and is modeled empirically for distant galaxies (see e.g. Anderson et al., 2015; Comparat et al., 2022). Typically, an absorbed power-law spectrum is assumed for unresolved XRB sources. Conservative estimates place the contribution of unresolved XRBs at around  $< 50\%$  in the SXB (Lehmer et al., 2016; Vladutescu-Zopp et al., 2023). This has been recently challenged by Kyritsis et al. (2024) who estimate the contribution from XRB to be  $\sim 80\%$ , which is considerably higher compared to previous studies (Mineo et al., 2012b, 2014b; Lehmer et al., 2019; Vladutescu-Zopp et al., 2023; Riccio et al., 2023), using stacking results from the eROSITA all-sky survey 1 (eRASS:1).

This paper aims to shed light on the intrinsic X-ray emission of the CGM in simulated galaxies and connect it to global properties such as halo temperature, gas fraction, and stellar mass. In order to complement results from stacking procedures where information about these global

properties is partially lost, we investigate simulated galaxies from the Magneticum Pathfinder suite of hydrodynamic cosmological simulations. We make use of the virtual X-ray photon simulator PHOX (Biffi et al., 2012, 2018a) which allows for a self-consistent and detailed multi-component modeling of the X-ray emission coming from various resolution elements of the simulations. In particular, we will be able to make use of this more accurate modeling to account for signals coming from the broad range of temperatures, metallicities and densities present in the hot gas of galaxy-sized halos. Additionally, we can directly account for the emission of XRB (Vladutescu-Zopp et al., 2023) and SMBH (Biffi et al., 2018a) sources and give accurate estimates of their contribution.

## 7.1 Simulated data set

From the selected cosmological volume described in section 4.2 we extract 1319 galaxy-sized halos at redshift  $z = 0.0663$  which roughly corresponds to an angular diameter distance of  $\mathcal{D}_A \approx 260$  Mpc. They were selected using the SUBFIND algorithm (Springel et al., 2001; Dolag et al., 2009) which defines halos according to a density threshold. We only considered the main central sub-halo within each parent-halo. We further require them to have stellar mass  $10^{10}M_\odot < M_* < 10^{12}M_\odot$  within a sphere of the virial radius  $R_{\text{vir}}$  around the halo center. The lower mass cut accounts for resolution limitations, the higher mass cut excludes the most massive group-sized halos. Resolution limitations arise for halos in which the total number of particles is of the order of the minimum number required for the SPH interpolation, which makes hydrodynamical quantities unreliable. Our initial selection is the same as in Vladutescu-Zopp et al. (2023) and consists of 324 star-forming (SF) and 995 quiescent (QU) galaxies. The classification into SF and QU galaxies is based on the specific star-formation rate (sSFR = SFR/ $M_*$ ), where SF galaxies have  $\log \text{sSFR} > -11$ . For each galaxy we derive SFRs from the stellar mass born in the past 100 Myrs of the simulation, in line with typical estimators from the literature for X-ray studies of galaxies (Mineo et al., 2012a,b; Lehmer et al., 2016, 2019; Kouroumpatzakis et al., 2020).

Following our initial selection, we obtain X-ray photons for each galaxy by first applying UNIT 1 with a fiducial exposure time of  $T_{\text{exp}} = 2$  Ms and effective area  $A_{\text{eff}} = 1000$  cm<sup>2</sup> on the full simulation volume. For the gaseous component, the idealized spectrum follows an APEC model scaled with the total metallicity of each gas source. In contrast to Vladutescu-Zopp et al. (2023), we however did not impose an intrinsic ISM-absorption component on the gas emission for star-forming galaxies in addition to the global foreground Galactic absorption (see further discussion in section 7.3). Emission from SMBH and XRB follow the modeling by Biffi et al. (2018a) and Vladutescu-Zopp et al. (2023) respectively.

Next, we apply UNIT 2 on each selected galaxy by projecting the produced photons within a cylindrical volume with base radius of  $R_{\text{vir}}$  and depth of  $2 \cdot R_{\text{vir}}$  around the galaxy center. The galaxy center is the position of the most-bound particle according to SUBFIND. The chosen l.o.s. is parallel to the  $z$ -axis  $\hat{e}_z$  of the underlying simulated volume. We chose  $R_{\text{vir}}$  as a scale-free radius to have a sufficient representation of the gravitationally bound region. In our analysis, we will not include an instrumental response because we opted to predict intrinsic properties from

the simulations.

From the projected photons we construct surface brightness (SB) profiles by radially binning photons in the plane perpendicular to the l.o.s. centered on the minimum of the gravitational potential. For each radial bin, we take the sum of all photon energies in a chosen energy range and normalize by the area of the annulus. We thus obtain

$$S_X \left( R_{i+\frac{1}{2}} \right) = \frac{\sum_{j, R_i < r_j < R_{i+1}} \epsilon_j}{A_{\text{eff}} T_{\text{exp}} \pi \left( R_{i+1}^2 - R_i^2 \right)} \times 4\pi \mathcal{D}_L^2, \quad (7.1)$$

for the SB profile, with  $\mathcal{D}_L$  being the luminosity distance,  $\epsilon_j$  and  $r_j$  the photon energy and its projected radial distance from the center,  $R_i$  the edges of the radial bins and  $i + \frac{1}{2}$  assigns the determined SB value to the center of the radial bin. The same construction applies to all considered X-ray components.

Throughout this work, luminosities are given in the rest-frame in the energy range of 0.5-2 keV, if not otherwise noted. For the total luminosity  $L_{\text{tot}}$  of each galaxy, we integrate SB profiles up to  $R_{\text{vir}}$  and take the sum of each component. By construction, the X-ray emission of each galaxy is derived from the photons emitted by all the X-ray sources (gas, SMBHs, XRBs) within the galaxy  $R_{\text{vir}}$ , with no distinction between the central galaxy and substructures.

### 7.1.1 Sample cleaning

After determining the luminosity of each component, we further clean our initial galaxy sample by applying exclusion criteria for AGN galaxies which we partially adapt from [Lehmer et al. \(2016\)](#). In this way, we can focus our investigation on a well-behaved subsample of galaxies, in which there is no dominant contamination from AGN emission. This will provide us with a more solid base to interpret the behavior of SB profiles in typical galaxies. In particular, we use the following criteria:

1. If the total luminosity of a galaxy is

$$L_{\text{tot}}^{0.5-7 \text{ keV}} > 3 \cdot 10^{42} \text{ erg s}^{-1}, \quad (7.2)$$

in the 0.5-7 keV energy band, we consider the source to be an AGN. This is directly taken from [Lehmer et al. \(2016\)](#) and was also recently employed by [Riccio et al. \(2023\)](#) as an exclusion proxy.

2. If the integrated luminosity ratio  $\ell$  between SMBH sources ( $L_{\text{BH}}^{\text{vir}}$ ) and the other components ( $L_{\text{gas}}^{\text{vir}}$  and  $L_{\text{xrb}}^{\text{vir}}$  respectively) within the virial radius is

$$\ell = \frac{L_{\text{BH}}^{\text{vir}}}{L_{\text{xrb}}^{\text{vir}} + L_{\text{gas}}^{\text{vir}}} > 3, \quad (7.3)$$

we also consider the source to be an AGN. This second condition was inspired by the requirement to fulfill a pure Lx-SFR scaling relation in [Lehmer et al. \(2016\)](#). They allowed

the total X-ray luminosity to be three times larger than the SFR scaling relation from [Alexander et al. \(2005\)](#) which is based on the radio luminosity at 1.9 GHz. The argument is that at this frequency, radio emission should mostly come from star formation while any excess would be associated to an AGN. Without appropriate tracers for radio emission from the simulation however, we reformulate their criterion to be instead the ratio between the X-ray power from SMBH sources and the combined X-ray power of gas and XRBs. With this, we can exclude galaxies that are clearly dominated by an AGN.

3. If  $L_{\text{BH}}^{\text{vir}}$  exceeds the expected luminosity of the central SMBH ( $L_{\bullet}$ , see below for definition)

$$\log L_{\text{BH}}^{\text{vir}} > \log L_{\bullet}, \quad (7.4)$$

we remove the source from our sample. By construction, each SMBH source gets assigned its spectral parameters dependent on its bolometric luminosity such that

$$\log L_{\bullet} \leq \log L_{\text{bol}} + \sigma - 1.65 - 0.22\mathcal{L} - 0.012\mathcal{L}^2 + 0.0015\mathcal{L}^3, \quad (7.5)$$

where  $\mathcal{L} = \left(\log \frac{L_{\text{bol}}}{L_{\odot}} - 12\right)$  (see [Marconi et al., 2004](#); [Biffi et al., 2018a](#)). The second term  $\sigma = 0.1$  denotes the maximum of randomized uniform noise which was added to the bolometric correction by [Biffi et al. \(2018a\)](#). The latter four terms denote the bolometric correction for the soft X-ray band (0.5-2 keV). The bolometric luminosity ( $L_{\text{bol}}$ ) of the central SMBH is  $L_{\text{bol}} = \varepsilon_r \dot{M}_{\bullet} c^2$ , where  $\dot{M}_{\bullet}$  is the accretion rate of the central SMBH,  $\varepsilon_r = 0.1$  is the radiative efficiency,  $c$  is the speed of light. In our modeling, this acts as an upper limit for the luminosity of a single SMBH source, because we employ an effective torus model with intrinsic absorption for SMBH sources which effectively lowers the power output in the soft band. In general, multiple emitting SMBH sources can be present in our simulated galaxies. Thus, the criterion expressed by eq. (7.4) is equivalent to excluding systems hosting more than one luminous SMBH source within  $R_{\text{vir}}$ .

In figure 7.1 we show  $L_{\text{BH}}^{\text{vir}}$  of the projected volume against  $\dot{M}_{\bullet}$  of the central SMBH for the complete sample of galaxies. Colors indicate the ratio  $\ell$  (eq. (7.3)). Galaxies that were classified as an AGN according to our exclusion criteria are marked as diamonds. The dashed diagonal line indicates the upper limit that we impose for the collective emission of SMBH sources (see eq. (7.4)). From the total sample, 86 SF and 128 QU galaxies are classified as an AGN according to criterion 1. According to criterion 2, 11 SF and 1 QU galaxies have large  $\ell$  and are mostly found for central accretion rates  $10^{-5} \text{ M}_{\odot} \text{ yr}^{-1} < \dot{M}_{\bullet} < 10^{-3} \text{ M}_{\odot} \text{ yr}^{-1}$ . With criterion 3 we find 31 SF and 21 QU galaxies for which the integrated luminosity  $L_{\text{BH}}^{\text{vir}}$  is above the upper limit set by the central SMBH accretion and thus hosts more than one bright SMBH source within  $R_{\text{vir}}$ . Accounting for overlaps, all criteria together thus reduce the full sample to 338 SF and 727 QU normal galaxies.

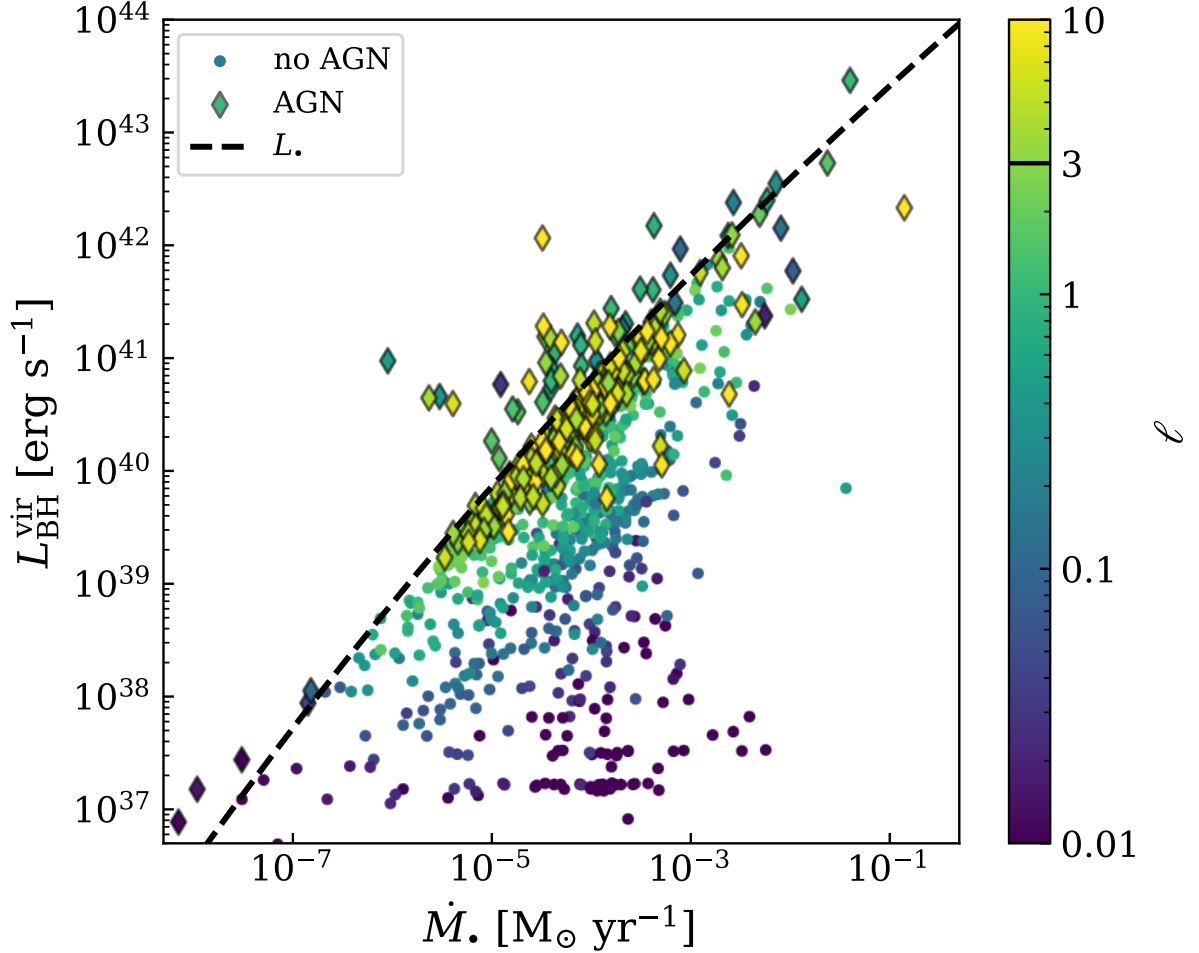


Figure 7.1: The integrated luminosity of SMBH sources ( $L_{\text{BH}}^{\text{vir}}$ ) for each galaxy in the 0.5-2 keV energy band as a function of the accretion rate of the central SMBH ( $\dot{M}_{\bullet}$ ). The dashed line indicates the upper limit set by the bolometric luminosity of the central SMBH (see criterion 3). Data points above the dashed curve host more than one X-ray bright SMBH source within  $R_{\text{vir}}$ . Each galaxy is color-coded by the ratio  $\ell$  (eq. (7.3)) between the integrated luminosity of SMBH sources and the other two components (gas + XRB). Galaxies that have been excluded following our AGN classification scheme are highlighted by thick edges and have been removed for the final sample.

### 7.1.2 Determination of galaxy properties

In this section we outline the direct estimate of galactic properties from the simulation. In contrast to the X-ray data retrieval, we do not limit ourselves to 2D projected quantities but make full use of the 3D information available from the simulation. We first select all resolution elements within a sphere of  $R_{\text{vir}}$  around each galaxy center. Then we filter for all particles which are gravitationally bound to the central halo according to the `SUBFIND` identification. This procedure allows us to remove the substructures for each considered system from our analysis, and derive the properties of the central galaxies only. For the stellar mass  $M_*$ , we take the sum of the mass of each stellar particle in the matched list. For the hot gas fraction  $f_{\text{gas}}$  and the halo temperature  $k_B T$ , we first select gas particles from the matched list that are considered X-ray emitting. Specifically, we select those that are not star-forming and not multiphase (do not represent cold gas), that have a temperature  $10^5 \text{ K} \leq T \leq 5.85 \cdot 10^8 \text{ K}$  and an intrinsic density of  $\rho < 5 \cdot 10^{-25} \text{ g cm}^{-3}$ . To obtain  $f_{\text{gas}}$ , we take the ratio between the summed mass of X-ray emitting gas particles and all gravitationally bound particles (including stars, dark matter and gas). To derive a single halo temperature, we calculate the emissivity weighted average of the selected gas particles. This approach will yield values close to a spectral temperature. The emissivity weights were calculated directly from the Astrophysical Plasma Emission Database (APED)<sup>2</sup> tables used by APEC (Smith et al., 2001) accounting for individual metal abundances assuming solar abundance from Anders & Grevesse (1989).

## 7.2 Galaxy X-ray surface brightness

In this section we present our findings on the correlation between X-ray surface brightness and global intrinsic properties of our galaxies. We quantify the contribution of XRBs and SMBH sources to the SB as possible contaminants when determining properties of the CGM.

Throughout our investigation we split our full sample into the SF and QU sub-samples. In this way we probe different mechanisms responsible for maintaining a hot, X-ray-bright gas atmosphere in different galaxy populations. Furthermore, we show SB profiles as a function of a normalized scale-free radius in order to make the sub-sample intrinsically more comparable irrespectively of differences in physical size. As a reference scale we choose the virial radius  $R_{\text{vir}}$ .

We first investigate general properties of the QU and SF sample by constructing mean and median profiles of the full subsamples. In figure 7.2(a) we show the mean (thin lines) and median (thick lines) SB profiles of our complete sample accounting for every source component. The shaded area shows the 16-84 percentile ranges of the median profiles. The median profiles are always lower than the mean profiles because the latter is more sensitive towards extreme outliers as seen from the 84 percentile boundary. Since we include every galaxy irrespectively of stellar mass when constructing the mean and median here, we are naturally dominated by the brightest and presumably most massive galaxies. Additionally, the mean enhances the presence of substructures which is noticeable by the noisy behavior of the mean at large radii. The median is a more stable estimator here although it is less suited for capturing the SB in the outermost

<sup>2</sup><http://www.atomdb.org>

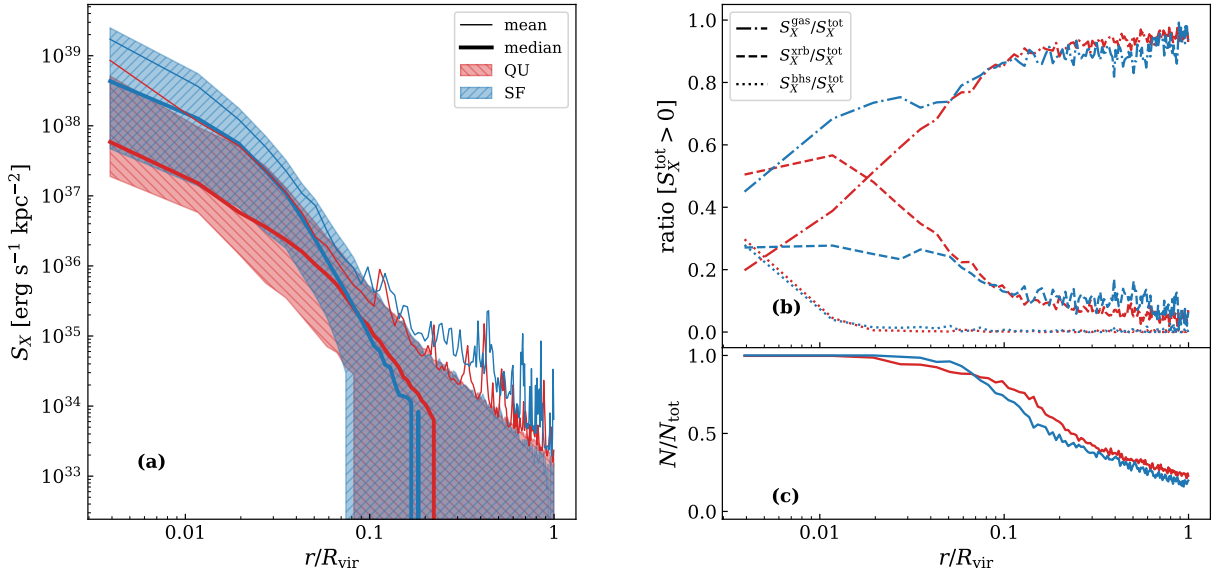


Figure 7.2: (a): Average SB profiles (blue for SF, red for QU) of the normal galaxy sample in the 0.5-2 keV energy band. Thin solid lines indicate the mean total SB. Thick lines indicate the median total SB. The shaded area around the thick lines corresponds to the 16-84 percentile ranges. (b): Mean ratio of the SB profiles of one component (gas: dash-dotted; XRB: dashed; SMBH: dotted) towards the total SB. At each radius we determine the ratio between the SB of one component and the total SB for every galaxy. We take the mean of that ratio by only accounting for galaxies with non-zero SB. (c): The sample completeness of the mean ratio in (b). Lines indicate the fraction of galaxies which have non-zero SB at a given radius and thus contribute to the mean ratio in (b).

regions, where it is more sensitive to the large number of galaxies with zero emission. The median profile drops to zero SB at  $\sim 0.17 R_{\text{vir}}$  for the SF sample and at  $\sim 0.22 R_{\text{vir}}$  for the QU sample. This means that less than 50% of the galaxies have detectable SB beyond those radii, respectively. This can be visualized in figure 7.2(c), where we show the sample completeness as the fraction of galaxies with non-zero SB at a given radius. When comparing the two sub-samples, the SF sample is centrally brighter than the QU sample both in the median and mean. For radii larger than  $0.1 R_{\text{vir}}$  the mean SB profiles of both samples are comparable with similar normalization and slope while median profiles are steeper for SF galaxies. For QU galaxies the median indicates a slightly more extended SB. According to figure 7.2(c) this behavior is a result of more galaxies that are bright at larger radii. We note that for large radii, the 16-84 percentiles of the QU and SF sample are identical which indicates that their CGM has similar properties.

In order to disentangle the contribution of different components to the SB profiles, we compute the ratio between the SB of each component and the total SB for each galaxy. This is shown in figure 7.2(b). In each radial bin, we then compute component-wise the mean of these ratios only accounting for galaxies with non-zero total SB. In this way, we effectively reduce the number of available galaxies in our sample (cf. figure 7.2(c)) especially at larger radii and can consequently inspect details of the SB profile in luminous galaxies. Different line styles in 7.2(b) indicate the mean ratio of gas (dash-dotted), XRB (dashed) and SMBH (dotted) sources towards the total surface brightness of each galaxy, with SF and QU samples in the same colors as in panel (a). We note that the mean ratio of each component is not biased by extreme outliers. We verified this by also computing the median ratio of each component, which yielded similar results.

Comparing these trends with the mean and median SB profiles from panel (a) of figure 7.2, we conclude that the central increase of the SB in SF galaxies is mainly caused by an enhanced contribution from hot gas within  $\lesssim 0.05 R_{\text{vir}}$ . This is most likely due to the presence of a hot ISM where stellar feedback from active star-forming regions injects energy into the surroundings. Conversely, the XRB component is more dominant for QU galaxies in the central regions. Due to the expected density distributions of stars and hot gas in quenched galaxies, the ISM contribution should be less pronounced in the center compared to XRB. The contribution from SMBH sources is mostly insignificant except for the very center where every galaxy hosts a SMBH. We note, that the SMBH considered here would be X-ray faint due to our AGN exclusion. Beyond  $\sim 0.05 R_{\text{vir}}$  both the SF and QU sample reach similar contribution levels in all components. Interestingly, the average XRB contribution is  $\gtrsim 10\%$  for radial bins close to  $R_{\text{vir}}$ . We attribute this fact to the presence of stellar sub-structures.

Given the scatter in each sample, the mean SB profiles of the two classes of galaxies show little qualitative differences. The median SB however hints at SF galaxies being slightly less extended and having steeper profiles compared to QU galaxies. Looking at relative contributions from different sources of the non-zero SB galaxies, we see that most of the difference is coming from the behavior of the ISM gas. In X-ray observations, the distinction between these two classes is also apparent on the ISM level (Bogdán et al., 2013; Kim & Fabbiano, 2015; Goulding et al., 2016; Babyk et al., 2018) and is supported by other independent simulation studies using the IllustrisTNG-100 (TNG100) suite (Truong et al., 2020).

### 7.2.1 Connection to galaxy properties

In this section we will investigate the shape and slope of median SB profiles of our QU and SF galaxy subsample while accounting for differences in their global properties. In the self-similar scenario, thermodynamic properties of the hot gaseous atmospheres are directly determined by the depth of the gravitational potential well of the underlying dark matter halo (see e.g. Sarazin, 1988). Assuming that the main cooling mechanism is thermal bremsstrahlung, the X-ray luminosity  $L_X$  of a halo can be expressed as

$$L_X \propto f_{\text{gas}}^2 T_{\text{vir}}^{0.5} M_{\text{vir}}, \quad (7.6)$$

with

$$f_{\text{gas}}(< R_{\text{vir}}) = \frac{M_{\text{gas}}(< R_{\text{vir}})}{M_{\text{vir}}}, \quad (7.7)$$

as the gas fraction. Note, that the gas fraction is assumed to be constant with mass in the self-similar scenario, while the true gas fraction of a halo is strongly dependent on stellar and AGN feedback, as well as replenishing and depletion of the gas reservoir. These effects lead to deviations from the self-similar picture which are found in observations of elliptical galaxies as well as of star-forming galaxies (Fabbiano, 2019, see review by). Based on eq. (7.6), we explore the gas fraction  $f_{\text{gas}}$  and halo temperature  $k_B T$  (estimated as in section 7.1.2) of our galaxies and connect them to the SB profiles. We further inspect the relation to their total stellar mass  $M_*$ .

Measurements of the gas fraction in galaxies have been historically difficult and are typically limited to the innermost regions of the galaxy. For instance, studies using survey data make use of stacking procedures to enhance the signal of weakly X-ray emitting gas in the outskirts which however makes quantitative statements on gas fractions in individual galaxies impossible. Constraints on the hot gas fraction of individual galaxies are indeed sparse and mostly feasible for massive systems (see e.g. Bogdán et al., 2013; Li et al., 2017; Babyk et al., 2018).

In cosmological simulations, we are able to estimate directly the galaxies intrinsic gas fractions and connect them to X-ray properties. In figure 7.3 we show the gas fraction for each galaxy in our sample against its stellar mass. Points are colored blue for SF and red for QU galaxies respectively. Additionally, we show histograms of the stellar mass ( $M_*$ ) and the gas fraction ( $f_{\text{gas}}$ ) distributions of our sample which are attached to the respective axis. Dotted lines in the  $f_{\text{gas}}$  histograms indicate the median value of the respective distribution. The magenta dotted line in the main panel shows the cosmic baryon fraction  $f_{\text{bary}}$  from the simulation. For comparison, we also include measurements of gas fraction and stellar mass from galaxies in the local universe: NGC 720 (Humphrey et al., 2011) and NGC 1521 (Humphrey et al., 2012) (stars); NGC 1961 and NGC 6753 (squares) (Bogdán et al., 2013); star-forming galaxies from (Li et al., 2017); fossil group NGC 6482 (Buote, 2017) and compact elliptical galaxy Mrk 1216 (Buote & Barth, 2018). We selected these specific observational examples because the gas fractions were obtained from a detailed analysis of mass and density profiles resulting from deep X-ray observations. The mass profiles were then extrapolated to a radius of  $R_{200c}$  to calculate the gas fraction. Furthermore, we include gas fraction estimates of the MW (Miller & Bregman, 2015; Nicastro et al., 2016) which were obtained from modeling of O VII and O VIII emission and O VII absorption lines in the MW CGM, respectively and also quote the gas fraction at  $R_{200}$ . While our sample is consistent with the selected observations in terms of gas fractions, the observational values are biased towards

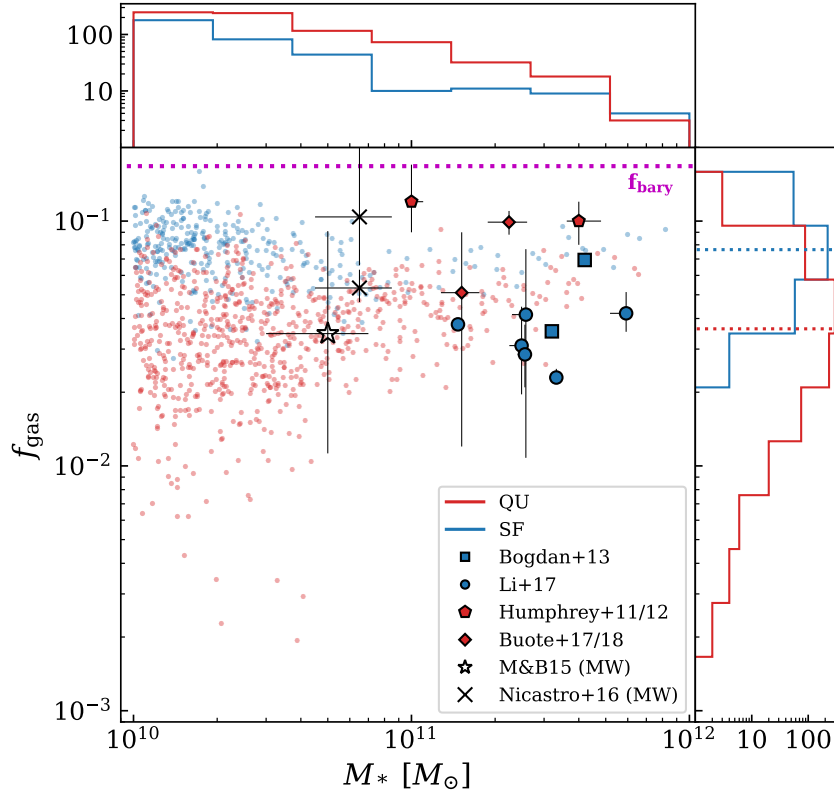


Figure 7.3: Gas fraction against the stellar mass of our galaxy sample with  $f_{gas}$  computed according to eq.(7.7). SF and QU galaxies are shown in blue and red respectively. Additional symbols with error bars represent values obtained from the literature for comparison. The color of each symbol indicates SF / QU classification. The magenta line corresponds to the cosmic baryon fraction  $f_{bary} = 0.167$  adopted in the simulation.

X-ray bright galaxies which may not be representative of the average galaxy population. In the simulated sample, QU galaxies have in general lower gas fractions than SF galaxies and span a larger range of values. In particular, we note that the low-value tail of the gas fraction distribution in simulations is dominated by low-mass QU galaxies. For comparison, we also report the cosmic  $f_{bary}$  value, which is as expected larger at all masses.

In figure 7.4 we report total SB profiles for the QU (upper panels) and SF (lower panels) samples, for different global intrinsic properties, i.e.  $f_{gas}$  (left),  $M_*$  (middle) and  $k_B T$  (right). Lines with different colors are median profiles binned by the respective property, using the same intervals for both QU and SF galaxies. Given that the property bins do not contain equal numbers of galaxies, constraints would be less strong on the low-number bins. For comparison, we also report the median of the whole SF/QU subsample (dashed black line) from figure 7.2. For a better interpretation of observed profiles and for comparisons among different sizes, we define

the quantity

$$\xi_i = \frac{300 \text{ kpc}}{R_{\text{vir},i}}. \quad (7.8)$$

We chose 300 kpc as a reference scale because it is close to the virial radius of a MW-mass halo and corresponds to the physical galactocentric distance for which CGM emission was detected (Comparat et al., 2022; Chadayammuri et al., 2022; Zhang et al., 2024b). This is used to highlight the distribution of sizes for the halos in each bin, visualized by the violins. In Fig. 7.4, we also report observed SB profiles for the BCG-like QU galaxies NGC 6482 and Mrk 1216 (Buote, 2017; Buote & Barth, 2018) and for several local SF galaxies from Bogdán et al. (2013, 2015); Li et al. (2017). We color code the observational data points according to the considered property.

### Gas fraction

We investigate the impact of the gas fraction on median SB profiles in the first column of figure 7.4. Within the QU sample, median SB profiles have lower normalization and appear less extended with decreasing  $f_{\text{gas}}$ . Their slope becomes slightly steeper with decreasing  $f_{\text{gas}}$ . For the lowest  $f_{\text{gas}}$  bins, the median SB profiles drop to zero before  $0.1 R_{\text{vir}}$ . From the distribution of  $\xi$  within each bin (violins), we can infer that more massive QU galaxies tend to have higher gas fractions. Compared to NGC 6482 and Mrk 1216, our sample has lower normalization. In fact, NGC 6482 and Mrk 1216 are BCG-like and are expected to be brighter than normal elliptical galaxies (see e.g. Kim & Fabbiano, 2015).

For SF median profiles, the normalization in the central regions decreases with decreasing  $f_{\text{gas}}$ . At the same time, galaxies with lower gas fractions seem to have more extended profiles. This is because the  $f_{\text{gas}}$  bins are dominated by small galaxies which have less extended profiles. Visually, the SF median profiles seem to be steeper compared to the QU sample for the same  $f_{\text{gas}}$  bins. We caution, however, that the interpretation of trends in the SF sample is more difficult here because of the narrower range in  $f_{\text{gas}}$  compared to the QU sample. Since we use the same binning for both subsamples, this leads to fewer non-empty bins in the SF sample with similar size distributions  $\xi$  among the bins. A more quantitative approach regarding the steepness of the profiles w.r.t. the gas component will be shown in section 7.2.2 later on. The median SB profiles of the SF sample are broadly consistent with estimates from observations of massive spiral galaxies (Bogdán et al., 2013; Li et al., 2017). As shown in Fig. 7.3, reported observations probe similar gas fractions compared to our SF sample but are more massive than the bulk of our SF galaxies. We also note that the annuli for which the SB was extracted in these observations are rather large and thus provide loose constraints. The measured SB for massive spiral galaxies from Bogdán et al. (2013) is higher than our median profiles which is due to the median being dominated by low mass SF galaxies.

### Stellar mass dependence

In the central column of figure 7.4, we show the stellar mass dependency of median SB profiles. The normalization of median profiles in the QU subsample increases with increasing stellar mass. The slope of the profiles remains mostly unaffected by changes in stellar mass and the

extent of the profiles decreases with decreasing stellar mass. The distribution in  $\xi$  confirms that larger galaxies have higher stellar mass. The median profiles of all stellar mass bins in the QU case are below the observational sample for the same reason as before. For median SF profiles, the normalization appears to be unaffected by stellar mass. Instead, decreasing stellar mass leads to a steepening of the profiles. The distribution in  $\xi$  for each bin shows the same trend as in the QU case. Our median SF profiles are in agreement with observational results in the  $0.05 - 0.15 R_{\text{vir}}$  radial range. For the  $0.15 - 0.3 R_{\text{vir}}$  radial range, our data is consistent with observations. However, the high stellar mass galaxies from [Bogdán et al. \(2013\)](#) are below our median profiles for a similar stellar mass bin while the slightly less massive galaxies from [Bogdán et al. \(2015\)](#) are above median profiles for similar stellar mass bins in the  $0.15 - 0.3 R_{\text{vir}}$  radial range. This is likely caused by a selection effect of the observational sample compared to our statistical sample. The stellar mass dependency of galaxy X-ray luminosity has been well studied in recent years. Clear correlations have been found for elliptical and spheroidal galaxies with the integrated stellar light ([Kim & Fabbiano, 2013](#)), for elliptical galaxies with their dynamical mass ([Kim & Fabbiano, 2015](#); [Forbes et al., 2017](#)). For star-forming galaxies, [Aird et al. \(2017\)](#) showed a connection between the stellar mass and mode of X-ray luminosity. Recent results from the EFEDs field of eROSITA also indicate the presence of a correlation between stellar mass and the SB normalization ([Comparat et al., 2022](#); [Chadayammuri et al., 2022](#); [Zhang et al., 2024b](#)).

Generally, a stellar mass trend in the SB should be expected as it can be connected to the gas mass through halo mass relations. The steepening of the profiles in the SF sub-sample indicates a change in the gas density distribution depending on total stellar mass, since the profiles are dominated by gas emission in the outskirts (see fig. 7.2). We will quantify this effect and highlight differences between the QU and SF subsamples in section 7.2.2.

## Temperature

In the right column of figure 7.4 we show the temperature dependence of median SB profiles. With increasing temperature, the median profile of the QU sample in the top panel shows an increase in normalization and becomes more extended. Except for the highest temperature bin, the  $\xi$  distribution indicates that larger galaxies have higher temperatures. The median profile of the highest bin lies in between the other bins in terms of normalization and extent and mostly consists of galaxies with large  $\xi$ , and thus of smaller halos. This is not expected from empirical scaling relations, where higher temperatures are associated with more massive galaxies ([Kim & Fabbiano, 2015](#); [Goulding et al., 2016](#); [Babyk et al., 2018](#), see e.g.). Upon inspection, 4 out of the 6 galaxies within the highest temperature bin showed no gas emission and some XRB emission in the central  $0.1 R_{\text{vir}}$ . They have low stellar mass ( $< 2 \cdot 10^{10} M_{\odot}$ ) and slightly lower  $f_{\text{gas}} (\approx 0.06)$ . Outside of  $0.1 R_{\text{vir}}$ , they have very shallow gas SB profiles with low normalization and little XRB contribution. We thus argue, that some recent events removed the central gas of these galaxies and simultaneously heated their gaseous atmosphere at larger radii. The SF sample shows a weak increase in normalization and radial extent with increasing halo temperature. With decreasing temperature, the profiles again become steeper because the low-temperature bins consist of more small galaxies. The distribution in  $\xi$  consistently indicates higher temperatures for larger halos. The SF sample is again in agreement with observations in terms of normalization for all the

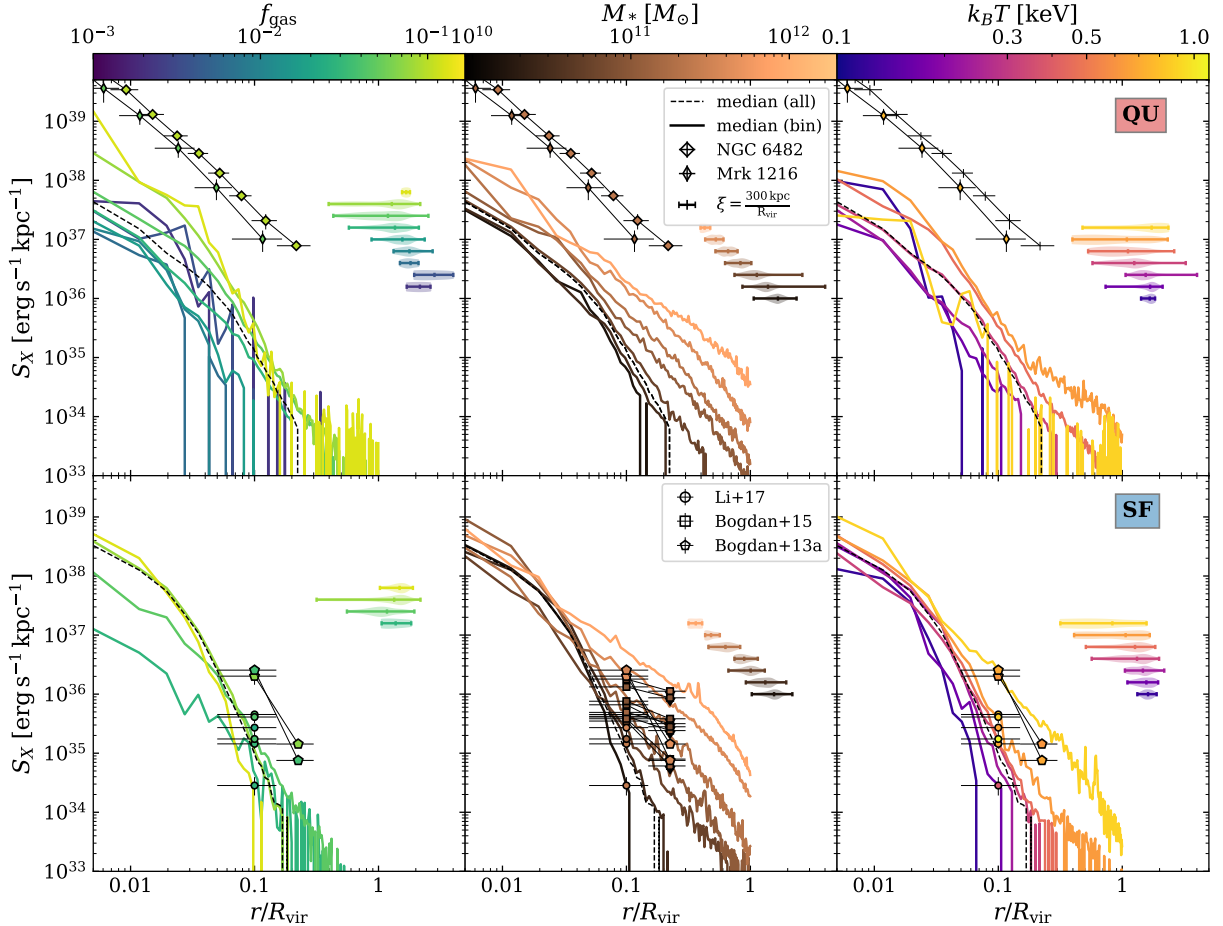


Figure 7.4: Scale-free median SB profiles of quiescent (*top*) and star-forming (*bottom*) galaxies. Galaxies are binned by gas fraction  $f_{\text{gas}}$  (*left*), stellar mass  $M_*$  (*center*), and emissivity weighted temperature  $k_B T$  (*right*). Colors indicate the central value of each bin for the respective quantity. We include SB profiles for NGC 6482 (Buote, 2017) and Mrk 1216 (Buote & Barth, 2018) in the QU panels and measurements of the extended emission in SF galaxies from (Bogdán et al., 2013, 2015; Li et al., 2017) for the SF panels. The violin plots indicate the distribution of  $\xi$  (eq. (7.8)) within each quantity bin. The horizontal extent of each violin indicates the minimum and maximum value of  $\xi$  within the respective bin. The central tick indicates the mean value of  $\xi$ . The height of each violin is proportional to the number density of  $\xi$  in the bin. The black dashed line is the median profile of the QU and SF sub-sample respectively.

radial ranges shown. In particular, one galaxy in the sample from Li et al. (2017) has a higher temperature than the highest temperature bin. Again we argue that differences between properties are a result of selection effects in observations.

### 7.2.2 SB profiles of the gas component

As shown in Fig. 7.2, the hot gas is responsible for most of the X-ray emission in our AGN-cleaned sample of galaxies, throughout the majority of the galaxy volume. It is thus interesting to further inspect the gas SB properties separately. This is directly possible in simulations, where we can predict for each galaxy the emission of the contaminating components (i.e. SMBH and XRB) individually. In observations, the study of the hot gas distribution of galaxies is more difficult, due to uncertainties regarding contaminants such as the central emission of the SMBH, point sources in the galactic field, background modeling and instrumental response. Nonetheless, studies of the CGM emission can be attempted through stacking of galaxy spectra, as shown by (Oppenheimer et al., 2020), based on mock observations of simulated galaxies extracted from IllustrisTNG and EAGLE simulations. In fact, recent observational studies based on eROSITA data, successfully employed stacking to find emission above the background level from the CGM of MW/M31-like galaxies (Comparat et al., 2022; Chadayammuri et al., 2022; Zhang et al., 2024b).

Here, we confront our findings with these recent eROSITA results, as shown in figure 7.5. In particular, we report the stacking results for the QU\_M10.7 and the SF\_M10.7 sample from the eFEDs field (Comparat et al., 2022) (Comp22). We use the same mass selection as their M1 mask which removes the signal from bright AGN and is comparable to our AGN cleaned sample. The QU\_10.7 sample consists of 7267 quiescent ( $\log(\text{sSFR} [\text{yr}^{-1}]) < -11$ ) GAMA matched galaxies in the mass range of  $M_* = 10^{10-11} M_\odot$  and the SF\_M10.7 sample with 9846 star-forming galaxies in the mass range  $M_* = 10^{10.4-11} M_\odot$ . The mass ranges were chosen such that the mean stellar mass in each sample is  $M_* = 10^{10.7} M_\odot$ . The average redshift is 0.2 and 0.23 for QU\_M10.7 and SF\_M10.7 respectively. In figure 7.5, we also include the best fit  $\beta$  model for the CGM of 30825 eROSITA stacked central galaxies in the MW mass range ( $M_* \sim 10^{10.5-11}$ ) and a median redshift  $z \sim 0.08$  from Zhang et al. (2024b) (Z24a) (dash-dotted black line). The associated shaded area corresponds to the  $1\sigma$  uncertainty in the best-fit parameters of their  $\beta$ -model. The contamination of XRBs, AGNs and satellite galaxies was accounted for through empirical modeling and the fitting was performed on the background-subtracted stacked SB profile. Furthermore, they do not distinguish between star-forming and quiescent galaxies such that both are included in their mass range. An improvement w.r.t Comp22 is a more detailed treatment of contamination from satellite galaxies which leads to a steeper profile. We note that their best-fit  $\beta$ -model for the MW mass regime has large errorbars in general but is representative of their full gas profile.

For a more faithful comparison, we restrict here to a subsample of our simulated galaxies that more closely resembles the observational selection. By applying exactly the same mass ranges as the QU\_M10.7 and SF\_M10.7 on our galaxy sample, we obtain 93 SF and 645 QU galaxies, which does not reflect the same galaxy number ratio and fails to give the correct mean mass of  $\bar{M}_* = 10^{10.7} M_\odot$ . We thus define our mass ranges such that  $\bar{M}_* = 10^{10.7} M_\odot$ , which results in 71 SF ( $M_* = 10^{10.48-11} M_\odot$ ) and 247 QU ( $M_* = 10^{10.46-11} M_\odot$ ) galaxies. We did not try to recreate an exact match of their stellar mass distribution (see Table 1 in Comp22), because we can not

account for the redshift distribution given the fixed redshift of our simulation box. Nonetheless, our chosen mass ranges do in fact overlap with the mass ranges and mean redshift presented in Z24a.

In figure 7.5, we plot the mean (thin solid) and median (thick solid) SB profiles of the gas component for our  $\bar{M}_*$ -matched sub-sample, in blue for SF galaxies and red for QU galaxies. The shaded area corresponds to the 25-75 percentiles and we additionally apply a median filter on the mean profiles to mask out satellite contribution. Compared to the profiles by Comp22, we find overall steeper profiles for both QU and SF galaxies. We note nonetheless that this difference is stronger for the QU subsample, as the SF mean profile by Comp22 indicates a moderately steeper trend in the central bins (up to  $\sim 100kpc$ ) but is mostly constrained by upper limits in the outer regions. While hinting at a flatter shape than simulations, no strong conclusions on the comparison can be therefore drawn for the SF subsample. Furthermore, the procedure in Z24a showed that satellite contamination in Comp22 may be significant. We find that our mean and median SB profiles are in good agreement with results from Z24a, given the uncertainties. In the central 10 kpc, our median SB profiles appear generally brighter than in Z24a. Nevertheless, the QU median stack is compatible with results from Z24a within the 25 percentile. Another detail in the observational analysis is the treatment of point sources and nuclear emission in each galaxy. Typically, excess in nuclear emission is attributed to SMBH activity and is consequently removed from the analysis. This could lead to an underestimation of the central SB in observations if the emission is originating from the gas component instead of an AGN.

### Beta profiles of the gaseous component in individual galaxies

The shape of the SB profile associated to the gas component can be further inspected by modeling it with a  $\beta$  profile, as often done in observations. Specifically, we model the SB profiles of the hot gaseous component by fitting both a single  $\beta$ -profile ( $S\beta$ ) with 3 free parameters,

$$S_X(r) = S_0 \left( 1 + \left( \frac{r}{r_c} \right)^2 \right)^{0.5-3\beta}, \quad (7.9)$$

where  $S_0$  is the normalization at  $r = 0$ ,  $r_c$  is the core radius and the slope  $\beta$  (Cavaliere & Fusco-Femiano, 1978), and a double  $\beta$ -profile ( $D\beta$ ) with 6 free parameters. The  $\beta$ -profile assumes spherical symmetry of the gas density distribution where the gas is in isothermal equilibrium within the gravitational potential of the galaxy. We use a standard  $\chi^2$  least-square algorithm in log-space with equal-size radial bins in units of  $R_{\text{vir}}$  for each halo to fit the SB radial profile. We assume Poissonian uncertainties on the SB in each radial bin based on the photons counts. In order to account for substructures in the halo outskirts during the fitting procedure, we apply a median filter on the SB profiles which removes sharp spikes in SB and effectively functions as a mask. We use the reduced  $\chi^2$  value to determine the best fit. If the reduced  $\chi^2$  of single and double  $\beta$ -profile fits are both close to 1, we prefer the single  $\beta$ -profile, which has less free parameters. If the best fit is a double  $\beta$ -profile but relative uncertainties in the fitting parameters are large ( $\frac{\Delta x}{x} > 0.8$ ) due to degeneracies, and the single  $\beta$ -model also yields a good fit, we prefer the latter. In cases where neither a single nor a double  $\beta$ -profile adequately describe the data, we

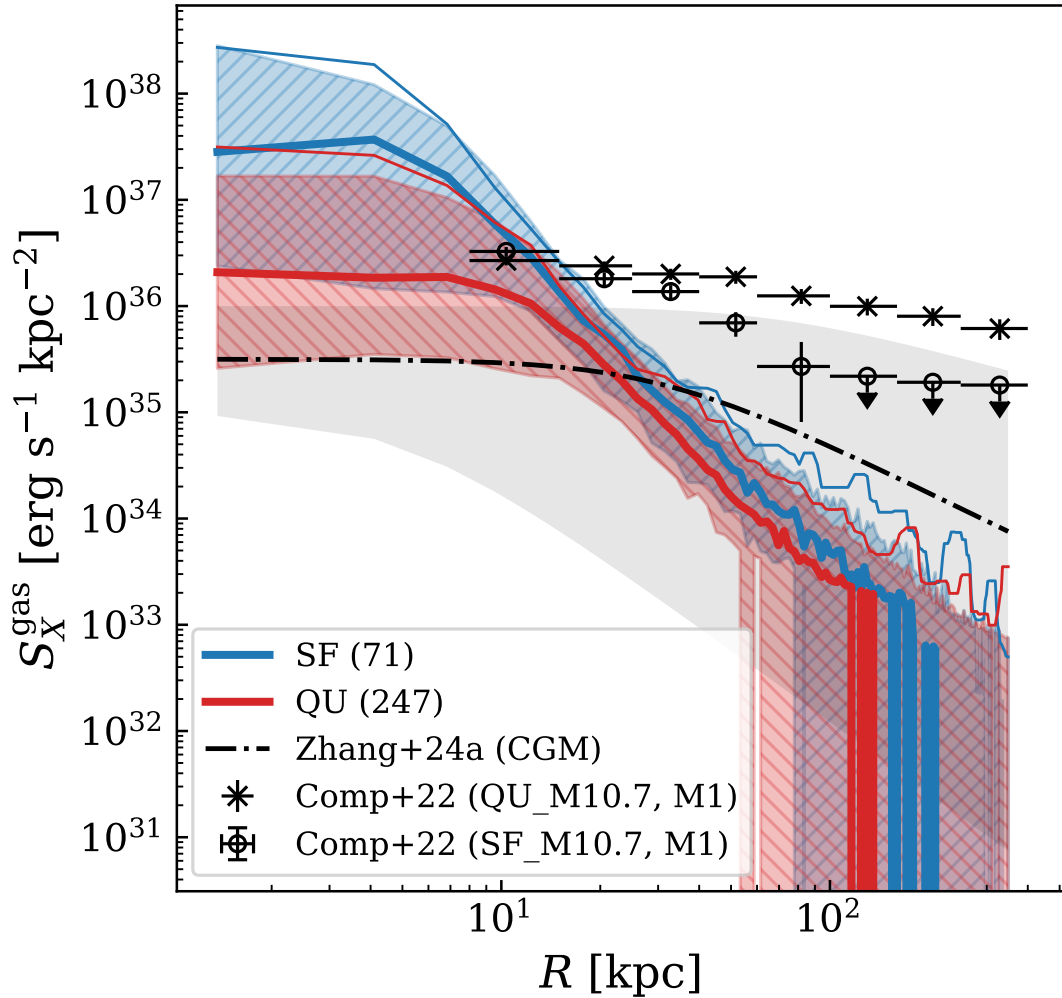


Figure 7.5: X-ray SB profile of the hot gas component recreating the mass cuts from [Comparat et al. \(2022\)](#). We recreate the observational sample from eFEDs galaxies ([Comparat et al., 2022](#)) by replicating their M1 mask for the SF\_M10.7 and QU\_M10.7 mass bins and show their background-subtracted results. Thin and thick solid lines are mean and median SB profiles of our sample of galaxies. We apply mass cuts on our sample ranging from  $M_* = 10^{10.46-11} M_\odot$  for QU galaxies and  $M_* = 10^{10.48-11} M_\odot$  for SF galaxies and report the total number of galaxies in each stack in the legend. We apply a median filter on the mean stacked profiles (thin solid) to remove substructures. Additionally, we show the best-fit SB profile for the CGM of MW-mass galaxies from [Zhang et al. \(2024b\)](#) which probes a similar stellar mass range.

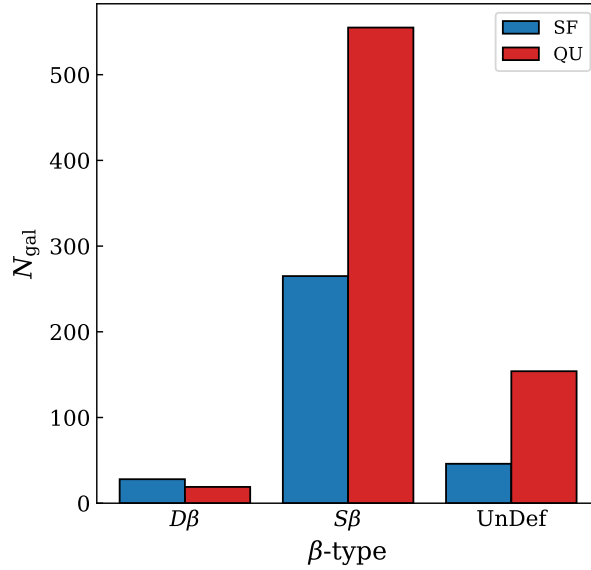


Figure 7.6: Result of the labeling process after fitting each SB profile with a single and double  $\beta$  profile. The main classification criterion is based on the reduced  $\chi^2$  as well as parameter degeneracy (see text).

label the galaxy as an "undefined" case, and do not consider those for the subsequent analysis. In figure 7.6 we show the results of this fitting process. The blue and red colored histograms show the distribution of QU and SF galaxies. Most galaxies in our sample are consistent with a  $S\beta$  profile. The most massive galaxies in our sample are instead better described by the  $D\beta$  model. We show exemplary profiles of both categories in appendix 7.5.2 (7.12). The undefined cases are galaxies which do not have any surface brightness or have too few ( $<10$ ) non-zero radial bins and are exclusively found at low halo masses.

As a second step, we investigate the relation between the shape of the density profile (quantified via the slope  $\beta$  of the  $\beta$ -profile) and the global properties of the galaxies. To this scope, we restrict our analysis to the subsample of galaxies that are best modeled by a  $S\beta$  profile. In figure 7.7, we show the best-fit single slope  $\beta$  as a function of total gas luminosity  $L_{X,\text{gas}}$ , stellar mass  $M_*$ , hot gas fraction  $f_{\text{gas}}$  and emissivity-weighted hot gas temperature  $k_B T$ , in panels (a), (b), (c) and (d) respectively. The simulation data points, with error bars, are marked in red and blue to distinguish QU from SF galaxies respectively. The thick colored lines represent the median  $\beta$  of the respective sample for equal-count bins.

In general, we find that the SB profiles in the SF sample have steeper slopes compared to the QU sample in all examined properties. Furthermore, uncertainties on the slope increase for larger values of  $\beta$ , due to degeneracy with the core radius  $r_c$ . We also note that the overall scatter is large and the two subsamples have significant overlap.

In panel (a) we find a strong positive correlation between the slope of the SB profile and  $L_{X,\text{gas}}$  up to  $L_{X,\text{gas}} \approx 5 \cdot 10^{40} \text{ erg s}^{-1}$  for QU galaxies and  $L_{X,\text{gas}} \approx 10^{41} \text{ erg s}^{-1}$  for SF galaxies. This indicates that the gas emission becomes more centrally concentrated for more luminous halos in

these cases. At higher luminosities, the median slope levels between  $\beta \sim 0.6$  (for QU galaxies) and 0.8 (for SF galaxies). Panel (b) indicates that the simulated galaxies span the largest range in  $\beta$  values at the lowest stellar masses. Despite the large scatter, in this stellar mass regime we still find a moderate tendency for steeper profiles in SF galaxies. For stellar mass above  $10^{11}M_{\odot}$ ,  $\beta$  remains around  $\sim 0.6$ , for both the SF and QU sample. In panel (c) we find that  $\beta$  is positively correlated with  $f_{\text{gas}}$  for both galaxy samples. We also notice that the median slopes of the two subsamples seem to connect across the full  $f_{\text{gas}}$  range. This suggests that the distribution of hot gas tends to be more centrally concentrated in galaxies with higher gas fractions. A small fraction of the central increase can be attributed to a hot ISM component in SF galaxies due to SN feedback from newly formed stars. However, in panel (d) we do not find a clear correlation between steeper slopes and the temperature of the halo. Since the slope is most sensitive to SB outside the core region, this suggests that the steep profiles are an intrinsic property of the halo.

In order to better interpret the origin of the largest  $\beta$  values, we inspect directly the corresponding profiles. We find that these galaxies either have also large uncertainties on the core radius  $r_c$ , or present sharp drops in SB at  $r \gtrsim 0.1R_{\text{vir}}$ . The latter corresponds to a few effective radii for those galaxies. Since we found the steepest slopes in low-mass galaxies, the compactness of the profiles may be caused by resolution limits in the simulation. In this case the low density of the halo outskirts is represented by a few resolution elements only which leads to stochastic effects. At the same time, the smallest values of  $\beta$  are also found in low-mass systems, and this is likely a result of extreme feedback events displacing the gas beyond the galaxy boundary.

In order to cross-validate our statistical results with observations, we compare to several observational studies. In all panels, we show  $\beta$  for a sample of nearby QU galaxies (gray hexagons), where X-ray properties were obtained from deep CHANDRA observations including extensive modeling of background sources and contaminants (Babyk et al., 2018). Their studied sample also includes BCG and cG galaxies which we exclude for the comparison. Luminosities and temperatures were directly taken from the aforementioned study. We inferred stellar masses from the central stellar velocity dispersion given for each galaxy in their study using scaling relations from Zahid et al. (2016). Gas fractions were obtained from the given gas masses and the given dynamical mass. We note, that X-ray quantities derived in Babyk et al. (2018) were extracted within five effective radii which is smaller than the  $R_{\text{vir}}$  in our analysis. While the given profile slopes and halo temperatures should not change significantly at larger radii, properties such as stellar mass and gas fraction are likely lower bounds. In panels (a) and (d) we additionally show a different sample of massive elliptical galaxies (black empty diamonds), by O’Sullivan et al. (2003) who used ROSAT data to obtain SB profiles of massive elliptical galaxies. In panel (b) we include best-fit slopes for the CGM of MW-mass and M31-mass galaxies from Zhang et al. (2024b) (black filled diamonds) derived from stacking analysis of the first eROSITA full-sky survey (eRASS:1). We also show a sample of massive SF galaxies in all panels from Li et al. (2017) who used XMM-Newton data for their analysis. In panels (b) and (c) there are also values for the Milky Way (MW) derived by Miller & Bregman (2015) and Nicastro et al. (2016). The data by Miller & Bregman (2015) result from a symmetric  $\beta$ -like profile which has been flattened along the axis perpendicular to the galactic disk, and uses XMM-Newton data of O VII and O VIII emission lines from the MW CGM. The values from Nicastro et al. (2016) (model A in their study) refer to a true spherical symmetric profile derived from X-ray absorption lines in Chandra data

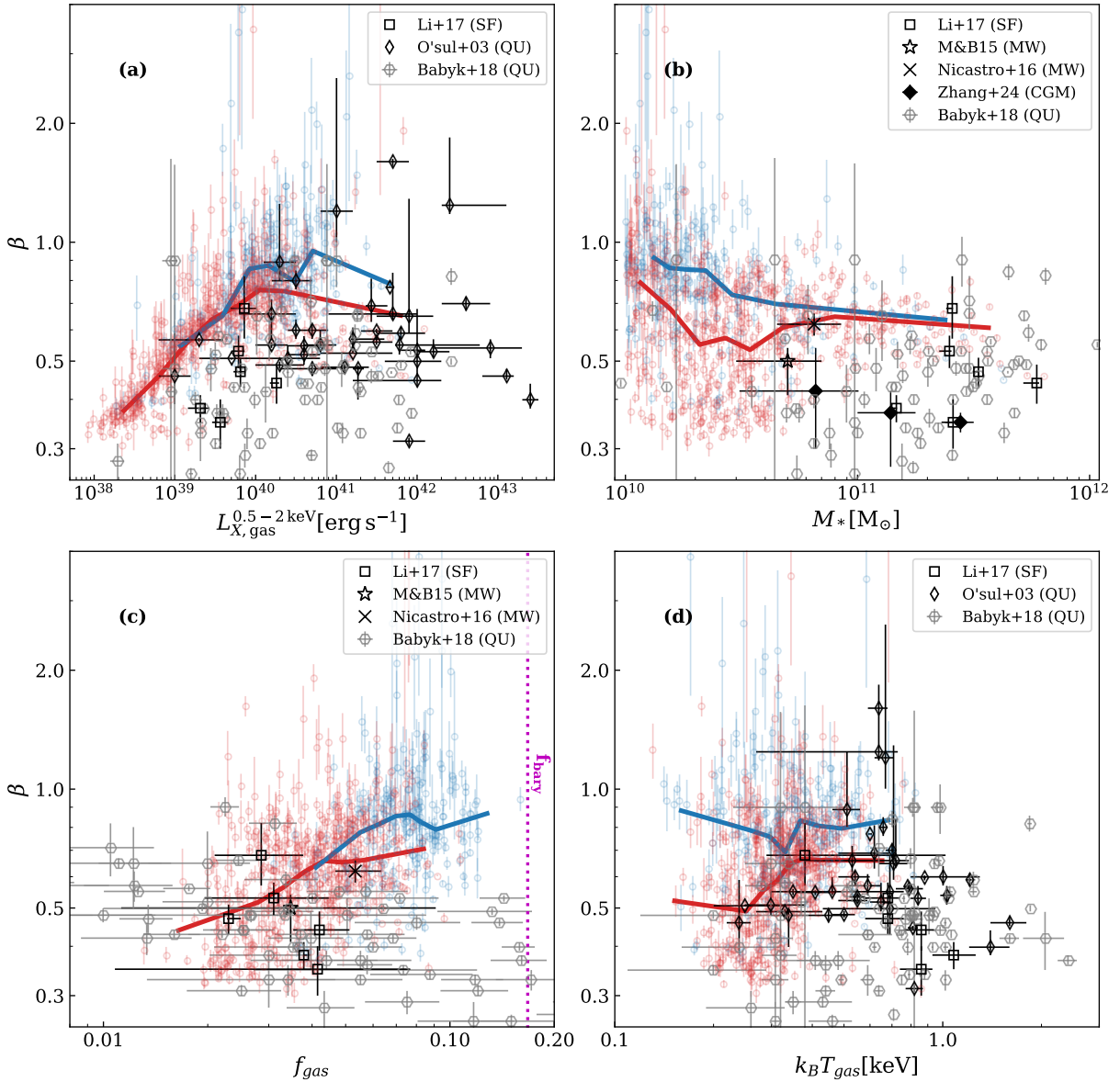


Figure 7.7: Best-fit slope  $\beta$  of each galaxy’s gas SB profile labeled as a  $S\beta$  profile (eq. (7.9)) against various halo properties within  $R_{\text{vir}}$ : (a) gas luminosity  $L_{X,\text{gas}}$ ; (b) stellar mass  $M_*$  obtained from stellar resolution elements bound to the parent halo; (c) gas fraction  $f_{\text{gas}}$  derived from gas resolution elements bound to the parent halo excluding star-forming and low-temperature ( $< 10^5$  K) gas. In panel (c) the *dotted magenta* line indicates the cosmic baryon fraction in the simulation; (d) emissivity weighted hot gas temperature  $T_{\text{gas}}$ . The exact retrieval of these quantities are outlined in section 6.3. The thick solid line in each panel indicates the median value of  $\beta$ . For comparison, we include the sample of massive elliptical galaxies from O’Sullivan et al. (2003) (O’sul+03) and massive star-forming galaxies of Li et al. (2017). Additionally, we compare to  $\beta$  models of the MW from Miller & Bregman (2015) (M&B15) and Nicastro et al. (2016) (model A) in (b) and (c).

associated with the MW CGM. We note that our slopes for the SF sample are systematically larger than the slopes from [Li et al. \(2017\)](#) and compared to the MW. Additionally, the gas fractions of the MW and the sample from [Li et al. \(2017\)](#) are lower than those of our SF sample. Interestingly, the slopes from [Li et al. \(2017\)](#) seem to agree better with our QU sample, especially in terms of  $L_{X,gas}$  and  $f_{gas}$  but are still on the lower side. Our derived slopes are in broad agreement with the  $\beta$  values derived in [Babyk et al. \(2018\)](#), despite being typically higher. While luminosities in their study are similar to ours, they have more high mass galaxies. Especially in the high stellar mass regime, their SB profiles are shallower. Regarding gas fractions, their sample has a larger range compared to ours. Interestingly, their sample shows a decline in slope with increasing  $f_{gas}$  which is in contrast to our results. Furthermore, they probe higher temperatures compared to our analysis which is connected to the higher stellar mass of their galaxies. In general, the temperature of the gaseous halo in observed galaxies is consistent with our sample and also does not show a clear correlation with  $\beta$ . The sample from [O’Sullivan et al. \(2003\)](#) is consistent with slopes derived for our galaxy sample and also contains a few galaxies with  $\beta \gtrsim 1$ . In their case, larger slopes are likely connected to the environment of their galaxy sample. Most of their targets lie in a cluster or group environment which can in principle affect X-ray properties of the galaxy even after accounting for the cluster emission in spectral modeling.

### 7.2.3 Global X-ray luminosity

In figure 7.8 we show total X-ray luminosities of our complete sample (including AGN) as a function of the total mass  $M_{500c}$  (gray dots) and compare to scaling relations from [Anderson et al. \(2015\)](#) (cyan boxes), [Lovisari et al. \(2015\)](#) (red dashed line) and [Zhang et al. \(2024c\)](#) (magenta dash-dotted line). We additionally include 6 group-like halos with  $M_* > 10^{12} M_\odot$  ( $M_{500c} > 5 \cdot 10^{13} M_\odot$ ) from the same simulated volume in Fig 7.8 and highlight them as black triangles. For the total luminosity of our sample, we combine the emission of hot gas, XRBs and SMBHs. Instead of considering the whole  $R_{vir}$  extent for the simulated galaxies, we extract the properties in the same regions used by [Anderson et al. \(2015\)](#), namely within  $R_{500c}$  and  $[0.15-1] R_{500c}$ . They obtained their SB measurements from a bootstrapped stacking procedure with data from the Rosat All-Sky Survey (RASS) of SDSS (Sloan Digital Sky Survey) confirmed galaxies in a stellar mass range of  $10^{10-12} M_\odot$ . Luminosities  $L_{tot}$  and  $L_{CGM}$  in their study were extracted from stacked SB profiles of central galaxies. They derive total masses for their stellar mass bins by forward-modeling of the  $L_X - M_{500c}$  relation using  $L_{tot}$  from their stacks. With this approach, they did not attempt to derive total masses for halos with  $M_* < 10^{10.8} M_\odot$  ( $M_{500c} < 10^{12.4} M_\odot$ ) due to significant contamination from XRBs. We note, that [Anderson et al. \(2015\)](#) referred to the radial range  $[0.15-1] R_{500c}$  as CGM, which we also adopt here for convenience. The best fit  $L_X - M_{500c}$  relation from [Lovisari et al. \(2015\)](#) is accounting for selection bias and was derived from a sample of galaxy groups and clusters using *XMM-Newton* observations. The relation from [Zhang et al. \(2024c\)](#) results from a stacking analysis of central galaxies in eRASS:4 and accounts for source contamination from a central SMBH and XRBs. Thick solid lines in figure 7.8 represent the median of our sample. Colored lines and shaded area represent the contribution of HMXBs (green) and LMXBs (orange) together with their 16-84 percentile which is a direct prediction of our XRB model (see [Vladutescu-Zopp et al., 2023](#), for details). We are thus also

able to provide constraints of XRB contribution for the CGM regime. The thin black line is the mean of our sample.

Generally, the median total luminosity of our galaxy sample within  $R_{500}$  (panel (a)) is in very good agreement with the reported scaling relations from the literature. At intermediate masses,  $2 \cdot 10^{12} \lesssim M_{500c} [M_{\odot}] \lesssim 10^{13}$ , the simulated median relation naturally shows increasing deviations from the relation by [Lovisari et al. \(2015\)](#), whose sample does not include low-mass systems. At lower masses,  $M_{500c} \lesssim 2 \cdot 10^{12} M_{\odot}$ , simulation data show a large scatter in luminosity but we still find a broad agreement with the observed relations. The increasing scatter flattens the mean and median at these low halo masses and is driven by extreme outliers, especially at high luminosities. We note that the scaling relations from [Zhang et al. \(2024c\)](#) and [Lovisari et al. \(2015\)](#) have very similar slopes, despite being derived for vastly different halo masses. This hints at a common mechanism shaping the overall matter distribution of all halos.

The median LMXB luminosity follows an almost linear relation with  $M_{500c}$ . By construction, LMXB contribution should linearly increase with the stellar mass of the galaxy ([Vladutescu-Zopp et al., 2023](#)). Deviations from a linear relation with  $M_{500c}$  arise from a non-linear stellar mass function. For the lowest luminosities in our sample, the emission from LMXBs dominates with respect to HMXBs, although the major emitting component remains the hot gas. The median HMXB luminosity increases with halo mass, but its contribution to the total  $L_X$  is significantly lower compared to LMXBs, except for the highest halo masses.

We note, however, that HMXB contribution is highly dependent on the sample and model assumptions. In A15 for instance, they use a SFR indicator that probes the star formation of the past 300 Myr while we probe star formation in the past 100 Myr. Furthermore, they employed simple scaling relations between SFR and HMXB luminosity while we directly sample the HMXB luminosity functions (see [Vladutescu-Zopp et al., 2023](#)). The latter introduces Poissonian noise in the  $L_{\text{HMXB}}$  scaling relation which steepens the slope of the relation at low SFR ([Gilfanov et al., 2004b](#); [Vladutescu-Zopp et al., 2023](#)). Moreover, A15 argue that the population of star-forming galaxies increases with lower stellar mass. While this is true in our case as well (see figure 7.3), each stellar mass bin has nonetheless more quiescent galaxies than star-forming galaxies. We also inspected the main sequence for our galaxy sample (shown in figure 7.13, in appendix 7.5.3) and found that there are indeed few SF galaxies that are close to the main sequence at low stellar mass. Hence, we expect SF galaxies below the main sequence to have less contribution from HMXBs, given their SFR, compared to a linear relation.

The mean and median CGM luminosity of our sample (panel (b)) is in excellent agreement with the stacking results of A15 (cyan) where we used the same values for  $M_{500c}$  as in panel (a). The contribution of LMXBs and HMXBs to the total CGM luminosity shows steeper trends compared to the total luminosity within  $R_{500}$ . We argue that there is more substructure in the outskirts of more massive halos which amplifies the contribution from XRBs. Moreover, especially LMXBs can contribute significantly towards the CGM luminosity of the least luminous galaxies at low halo masses. In these cases, the hot gas fraction is close to zero and residual LMXB emission must either be associated with satellites or a diffuse stellar component outside the central  $0.15R_{500c}$ . We note, that the median and mean CGM luminosity for low-mass halos ( $M_{500c} < 10^{12} M_{\odot}$ ) is significantly lower than the total luminosity by at least an order of magnitude. For larger masses, the CGM luminosity becomes comparable to the total luminosity. This implies that most of the

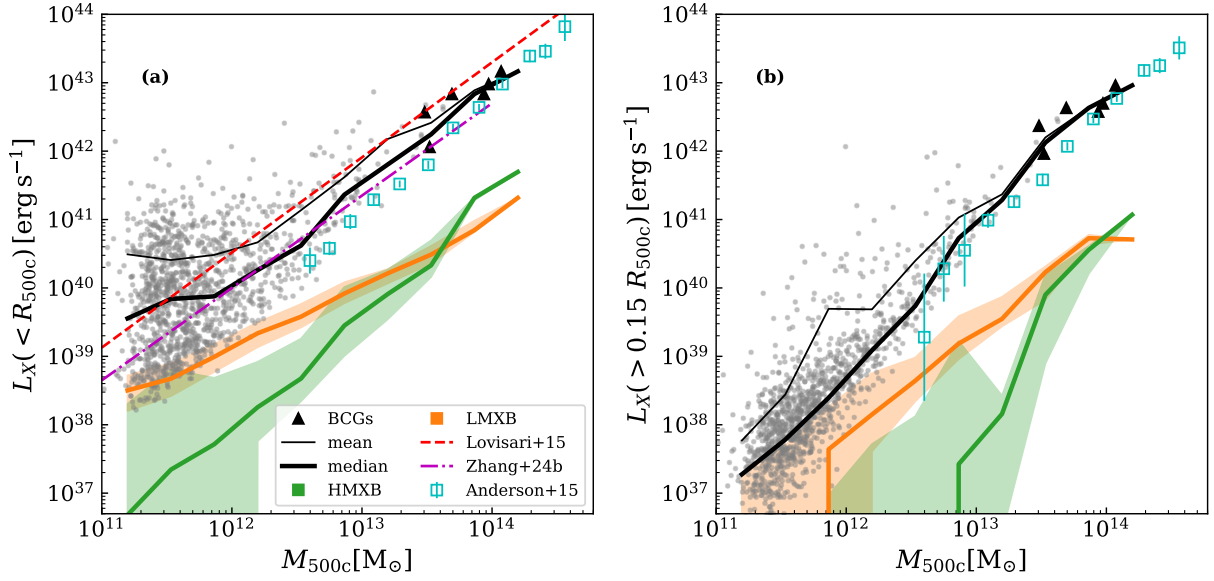


Figure 7.8: Total X-ray luminosity as a function of halo mass ( $M_{500c}$ ) (a) within  $R_{500c}$  of each galaxy, (b) within  $(0.15 - 1) R_{500c}$ . Grey dots represent all galaxies in our full sample, including the AGN systems, with BCG galaxies marked as black triangles. Thin and thick lines represent the mean and median luminosity of our sample, respectively. The contribution from HMXBs and LMXBs in our sample is shown in *orange* and *green* together with the 16-84 percentile range as the shaded area. Additionally, we show data from Anderson et al. (2015) (*cyan squares*) for the total X-ray luminosity within  $R_{500}$  in (a) and CGM luminosity within  $0.15 - 1 R_{500}$  in (b). The sample consists of central galaxies and results from a stacking analysis using ROSAT data. Their total mass is derived from forward modeling of the  $L_X - M_{500c}$  relation of gas-dominated halos in their sample. The magenta dash-dotted line is the best fit  $L_X - M_{500c}$  relation for stacked galaxies in eRASS:4 from Zhang et al. (2024c). The red dashed line shows the bias-corrected best fit  $L_X - M_{500c}$  relation from Lovisari et al. (2015).

emission is centrally concentrated in our sample, which is in line with steeper  $\beta$ -profiles from section 7.2.2.

## 7.3 Discussion

### 7.3.1 Inclusion of absorption

By including a weak foreground absorption to model the idealized emission assigned to each gas element, we effectively reduce the X-ray emission in the soft part. Therefore the luminosity retrieved directly from the photon counts, without modeling the spectrum, is in principle a lower limit to the true intrinsic luminosity, even if no instrumental response is included and the ideal photon emission is employed. However, we verified that the foreground absorber does not

significantly impact the derived luminosity for each halo, by conducting a simple experiment. We again applied unit 1 of the PHOX algorithm on a sub-volume of the simulation box without the weak foreground absorption component. All other settings were left the same as described in section 6.3. We compare the total number of photons produced in the case with no absorption and the original setup for the same sub-volume in the energy range 0.5-2 keV. Since we take into account all particles within the simulated sub-volume, we probe a wide range of temperatures and metallicities being affected by absorption. Ultimately, the foreground absorption component, with column density  $N_H = 10^{20} \text{ cm}^{-2}$ , reduces the total number of photons by  $\approx 5\%$  in the considered sub-volume. We thus recompute the luminosities as in section 7.2 and find that the true intrinsic luminosity is typically underestimated by up to 5% when absorption is included.

Another point worth considering is the inclusion of an intrinsic component mimicking ISM absorption in SF galaxies which we did not include in this study. Typical values for ISM absorption in observed SF galaxies are of the order of  $\sim 10^{21} \text{ cm}^{-2}$  (see e.g. [Lehmer et al., 2022](#)), which would lead to a reduction of SB in the central  $0.1 R_{\text{vir}}$  in the gas component of SF galaxies by  $\gtrsim 30\%$ , ultimately reducing the normalization of the profiles.

### 7.3.2 Beta profiles

We chose a least-squares algorithm in logarithmic space to fit the SB profiles with a single or double  $\beta$ -model. We used the reduced  $\chi^2$  as the main criterion for comparison, to decide between a  $S\beta$  and  $D\beta$  model. We manually validated the resulting choice for all galaxies in the AGN cleaned sample and confirmed if the fits reached convergence. Additionally, we cross-validated the resulting best-fit parameters using other fitting techniques. On the most massive galaxies within our sample ( $M_* > 5 \cdot 10^{11} M_\odot$ ), we employed a likelihood minimization using a C-statistic ([Cash, 1979](#)), a gradient-descent algorithm as implemented in `scipy` ([Virtanen et al., 2020](#)) and a Markov-Chain Monte-Carlo (MCMC) approach with flat and informed priors using the software package `EMCEE` ([Foreman-Mackey et al., 2013](#)). Both the C-statistic and the gradient-descent method yielded similar best-fit values and agreed with the least-squared method. The MCMC approach was sensitive to the assumed priors and slow to converge. It yielded median fit parameters that were more degenerate than the ones found with the other methods and were systematically lower by  $\sim 10\%$ . Given these results, we decided to rely on the least-square results.

The strong positive correlation between the slope of  $S\beta$  galaxies and their total gas luminosity  $L_{X,\text{gas}}$  indicates that gas at the center of those galaxies is emitting more than in the outskirts. This suggests that a feedback mechanism is probably in place, injecting more energy into the central gas. One of the primary sources of energy can be the activity of the SMBH at the center of each galaxy on which we will focus here. In order to quantify the central feedback in each galaxy in our AGN-cleaned sample, we show  $L_{X,\text{gas}}$  as a function of the current accretion rate of the central SMBH ( $\dot{M}_\bullet$ ) in figure 7.9. Each data point is colored by the stellar mass of the host galaxy. We observe a tight coupling between the total luminosity of the gas component and the current accretion rate of the SMBH. This suggests that the main source of energy in our AGN-cleaned sample appears to be connected to the activity of the central SMBH at all stellar masses. Since we excluded overly X-ray bright AGN from this sample, this correlation is not driven by extreme cases and holds for faint AGNs as well. While the strong link between the

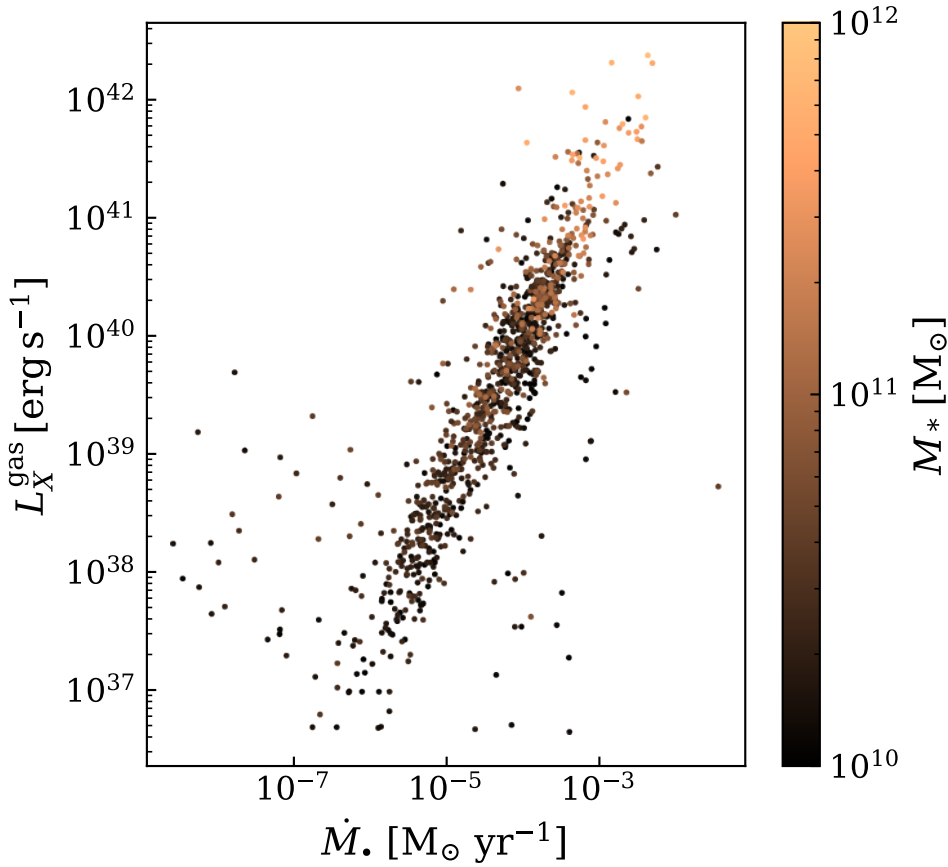


Figure 7.9: Gas luminosity within  $R_{\text{vir}}$  of the AGN cleaned sample as a function of the current accretion rate of the central SMBH  $\dot{M}_\bullet$ . The color indicates stellar mass of the galaxy

SMBH and the regulation of the gas phase is expected (e.g. [Hirschmann et al., 2014](#); [Steinborn et al., 2015](#); [Gaspari et al., 2019](#); [Truong et al., 2020, 2021b, 2023](#)), high accretion rates generally also indicate a large gas reservoir in the vicinity of the SMBH. The results in figure 7.9 indicate that the injected energy in the innermost region heats up this gas quickly so that this is immediately reflected in the gas luminosity. An additional mechanism injecting energy into the gas phase is associated with SN feedback. Especially in SF galaxies, SNII feedback can additionally heat up the gas and increase its luminosity and may trigger outflows that leave imprints in the CGM SB of SF galaxies ([Strickland et al., 2004](#); [Mineo et al., 2012b](#); [Li et al., 2018](#)).

While the  $\beta$ -profile is a simple and well-established model, it is also assuming the gas to be in an isothermal state. Thus it can not account for the expected temperature gradients which are observed for galaxies and galaxy clusters alike ([Pratt et al., 2007](#); [Kim et al., 2020](#)). Since the  $\beta$ -profile is a spherically symmetric profile, it can not account for asymmetries in the gas distribution either. In an idealized scenario for disk galaxies, distinct flow patterns are expected to arise with outflows primarily happening perpendicular to the stellar disk and inflows circularizing at the edges of the stellar disk (see e.g. [Tumlinson et al., 2017](#); [Stern et al., 2023](#)). Recently,

eROSITA revealed large-scale lobes perpendicular to the galactic disk of the MW (Predehl et al., 2020) which are compelling evidence for the aforementioned asymmetries. Simulations showed the presence of such asymmetries in mock X-ray images of simulated galaxies (Truong et al., 2021b, 2023; ZuHone et al., 2024). However, a recent study of edge-on star-forming galaxies in the Virgo galaxy cluster yielded only weak evidence for the presence of extraplanar hot gas (Hou et al., 2024) perpendicular to the stellar disc. We investigated our galaxy sample with respect to possible asymmetries by selecting disk-like SF galaxies. We binned them by their inclination angle with respect to the chosen l.o.s. (i.e. the z-axis of the simulation box.) We describe the exact setup in appendix 7.5.4 and show the result in figure 7.14. We do not find any variation of the SB profiles with inclination angle in our sample. In low mass galaxies, the resolution limit of the simulation may smooth out emerging asymmetries. Moreover, the feedback from the central SMBH is distributed isotropically in its surroundings which further suppresses asymmetries. A spherically symmetric profile is thus a fair description in our case.

We also verified the validity of the  $\beta$ -model description by reconstructing the X-ray emitting gas mass from the best-fit profiles of the simulated galaxies represented by a single  $\beta$  model. The deprojected 3D density profile derived from the  $\beta$ -model takes the form

$$\rho(r) = \rho_0 \left( 1 + \left( \frac{r}{r_c} \right)^2 \right)^{-\frac{3\beta}{2}}, \quad (7.10)$$

where the central gas density is

$$\rho_0 = 2.21 \mu m_p n_0, \quad (7.11)$$

with  $\mu$  being the mean molecular weight,  $m_p$  the proton mass, and

$$n_0 = \sqrt{\frac{S_0}{r_c \epsilon B(3\beta - 0.5; 0.5)}}. \quad (7.12)$$

In eq. (7.12),  $n_0$  denotes the central number density at  $r = 0$ ,  $\epsilon$  is the emissivity,  $B(a, b)$  represents the validity of the beta function and  $S_0$ ,  $\beta$  and  $r_c$  are the same as in eq. (7.9) (see also Babyk et al., 2018, for details). The resulting value For each galaxy we compute  $\epsilon$  assuming an APEC model with the emissivity-weighted average temperature and mass-weighted metallicity of the X-ray emitting gas within  $R_{\text{vir}}$ . The resulting total gas mass is then obtained from the integration of eq. (7.10) up to the virial radius. We show the comparison between the mass of the total X-ray emitting gas in the simulation and the reconstructed gas mass from the beta profile in figure 7.10. We find good correspondence between intrinsic and reconstructed values for high gas masses ( $M_{\text{gas}} > 10^{11} M_{\odot}$ ), with some possible bias underestimating the reconstructed gas mass at intermediate mass ranges ( $10^{10} \lesssim M_{\text{gas}} [M_{\odot}] \lesssim 10^{11}$ ). The scatter at very low masses ( $M_{\text{gas}} < 10^{10} M_{\odot}$ ) might be driven by a combination of the underlying simplifications as well as large uncertainties on the best-fit  $r_c$  and  $\beta$  values, originating from a poorly resolved atmosphere.

Since the plasma in galaxies is generally cooler than in clusters, X-ray emission is mostly dominated by emission lines of various metal species. We therefore investigated possible trends between the slope of  $S\beta$  galaxies and their mass weighted total metallicity. We did not find any

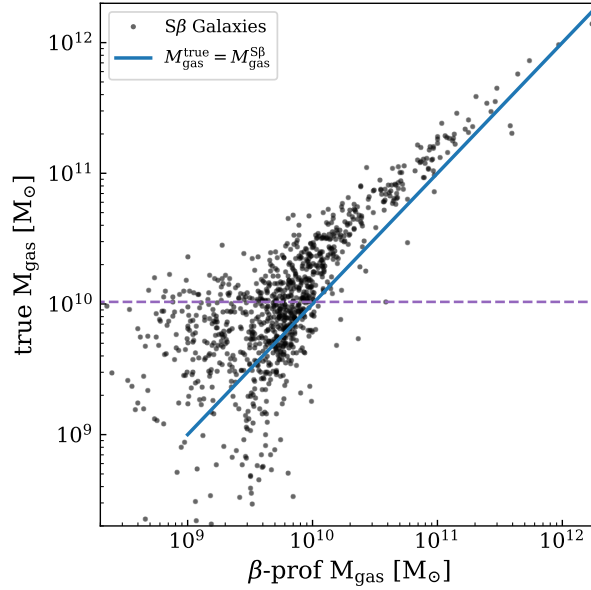


Figure 7.10: Comparison of the X-ray emitting gas mass from the simulation and the gas mass retrieved from single  $\beta$ -profiles using eq.(7.10)-(7.12). The solid blue diagonal line indicates equality between the two methods. The horizontal purple dashed line indicates  $M_{\text{gas}}^{\text{true}}$  for a halo with 1000 gas resolution elements. Galaxies with  $M_{\text{gas}}^{\text{true}} \lesssim 10^{10} M_{\odot}$  have more poorly resolved atmospheres.

correlation between  $\beta$  and the metallicity within  $0.1R_{\text{vir}}$  or  $R_{\text{vir}}$ , which means that the shape of our profiles is not determined by a metallicity gradient. Therefore the  $\beta$ -profile is an adequate description of the gas density in our case.

### 7.3.3 Contamination of the CGM emission

A major aspect when dealing with the SB of the CGM is the contamination by satellite galaxies (see also Zhang et al., 2024b). With their stellar mass and potentially high star-formation rates, satellite galaxies can host additional XRB sources. As indicated in figure 7.2(b), not only does the gas component contribute towards the extended SB but XRB emission can have non-negligible contribution as well. The show-case galaxy in figure 5.2 illustrates how especially LMXBs can appear as a diffuse component in the outskirts of a galaxy. The exact contribution from XRBs is however highly dependent on the assumed spectral model (Lehmer et al., 2016; Vladutescu-Zopp et al., 2023). In our case, we use a relatively high column density when modeling the absorbed power-law spectrum of XRBs compared to other studies (Lehmer et al., 2021; Riccio et al., 2023; Kyritsis et al., 2024). Lower column densities would obviously yield higher contributions from XRBs in the soft band. Figure 5.2 also shows the presence of actively accreting SMBH point sources which correlate with the position of the subhalos and would be likely masked in observations. Since our AGN-exclusion criteria (section 7.1.1) ensure that SMBHs associated to

subhalos are less luminous than the central SMBH, we do not expect significant contamination.

In order to explicitly mask radial bins where subhalos are dominant, we used a median filter on the gas SB profiles when fitting  $\beta$ -profiles and when constructing our mean profiles of figure 7.5. While the median filter reliably detected substructure, the resulting masking of the affected radial bins rendered some of the SB profiles unusable. In those cases, the profile was either dominated by substructures or had too few radial bins left and was consequently undetermined.

Another aspect of XRB contamination comes from the association of XRBs with the main stellar body of a galaxy (see Grimm et al., 2003; Gilfanov, 2004). Our detailed model of XRB emission enabled us to quantify XRB contamination not only for the total luminosity (see figure 7.8) but also for the core-excised luminosity. Especially for low-mass galaxies, XRBs can have a significant contribution to the total luminosity of galaxies with low SB.

In Fig. 7.8 we showed that scaling relations between the halo mass  $M_{500c}$  and both the total luminosity as well as the core-excised luminosity are in excellent agreement with observations. Especially in the group regime  $M_{500c} > 10^{13} M_{\odot}$ , where the gas component is most dominant, observed scaling relations are perfectly reproduced. Since we include all major emitting components for the total luminosity  $L_X$ , we also verified that scaling relations are still consistent when only accounting for the gas component. We note that the largest luminosities at low halo masses are associated to galaxies with a bright AGN.

### 7.3.4 Scaling with global quantities

Both the QU and SF sample show distinct behavior at different radii with respect to variations in their global properties. In the QU case, all investigated properties mostly affect the normalization of the binned profiles. In the SF case normalization stays the same while the extent of the profiles change. We know from observations, that the hot atmospheres of elliptical galaxies are in hydro-static equilibrium with the gravitational potential such that global properties have a tight relation with the halo mass (Kim & Fabbiano, 2015; Forbes et al., 2017; Fabbiano, 2019). In SF galaxies this relation is less clear and observations have shown that the total X-ray luminosity of SF galaxies is only weakly related to halo properties such as temperature (Kim & Fabbiano, 2015). Concerning  $f_{\text{gas}}$  in our SF sample, we would have expected a stronger dependence on the normalization of the SB profiles. From the violin plots in figure 7.4 we can infer that the highest gas fraction bin is comprised preferentially of low mass galaxies for SF galaxies while there are preferentially more massive galaxies in the QU case. This would suggest that a high fraction of the hot gas is located in the halo outskirts of QU galaxies since the whole structure of the SB changes with  $f_{\text{gas}}$ . This is in line with typical formation scenarios of QU galaxies where energetic feedback events from the central SMBH or major mergers redistributed and heated the gas. In turn, the hot gas appears to be more concentrated towards the center for our SF sample since the normalization of the SB profiles only changes for the inner  $0.1 R_{\text{vir}}$  and is also supported by Fig. 7.7(c). This behavior is however not supported in the literature where shallower profiles are typically observed (Bogdán et al., 2013; Li et al., 2017; Zhang et al., 2024b). The slope also increases for SF galaxies at low masses in our case where the resolution of the simulation may already be too low to properly resolve the hot gas atmosphere outside of  $0.1 R_{\text{vir}}$ .

### 7.3.5 Comparison to other simulations

Similar works on the X-ray SB in simulated galaxies have been conducted using different simulation suites. Notably, [Oppenheimer et al. \(2020\)](#) analyzed full eROSTIA mock observations based on EAGLE ([Schaye et al., 2015](#)) and IllustrisTNG-100 (TNG100) ([Pillepich et al., 2018](#)) simulations. They made use of the pyXSIM package<sup>3</sup>, which is a python implementation of the PHOX algorithm used in this work (see Sec.5.1). When generating the initial photon events from the simulation, they include a model for the MW foreground emission and absorption as well as a model for the background sources. However, they do not directly model the contribution from AGN and X-ray binaries. Additionally, they used SIXTE to account for instrumental effects on the resulting SB profiles. They split their galaxy sample in low ( $M_* = 10^{10.2-10.7} M_\odot$ ) and high mass ( $M_* = 10^{10.7-11.2} M_\odot$ ) star-forming and quiescent galaxies for both simulation sets and performed a stacking analysis on each respective subsample in a radial range of [10-300] kpc. Their low-mass sample (see their Fig. 2, left) is therefore in a comparable MW mass range w.r.t. our analysis in Fig. 7.5, on which we will focus here. In general, they find flatter SB profiles for both simulations in the MW mass range compared to our findings, with EAGLE predicting less luminous star-forming galaxies than TNG100. Especially at ( $r > 100$  kpc) we predict an order of magnitude lower SB. At smaller radii, our findings are consistent but interestingly show larger object by object variations, which we attribute to the differences in the details of the AGN feedback treatment in the simulations. Both EAGLE and TNG100 confirm the significant increase in central SB for star-forming galaxies compared to quiescent galaxies which we observe in our simulations. Furthermore, [Truong et al. \(2020\)](#) found that blue galaxies in TNG are an order of magnitude brighter in X-ray than red galaxies at fixed stellar mass, confirming this dichotomy. For radii  $r > 50$  kpc, we find that SF and QU galaxies have similar SB profiles which is consistent with EAGLE galaxies in [Oppenheimer et al. \(2020\)](#), whereas TNG100 predicts larger SB for star-forming galaxies at all radii. We note that [Oppenheimer et al. \(2020\)](#) considered the X-ray photon emission from the gas included within a sphere of  $3 \cdot R_{200}$  around each galaxy, which is significantly larger than the volume inspected here (see Sec. 6.3). Some contamination in the outskirts, due to gas in the galaxy surrounding not associated to the galaxy itself, can thus be present and contribute to the flattening of the SB profiles. Moreover, those authors performed full mock observations aiming to test CGM detectability, while we focused on intrinsic emission and its connection to the global properties of our galaxies. We thus expect some differences introduced by the instrumental effects, such as in the central SB due to effects from the eROSITA PSF or in the galaxy outskirts due to the treatment of the background in observations and full mocks.

## 7.4 Summary

In this study, we present results on the X-ray SB of simulated galaxies from the *Magneticum Pathfinder* set of simulations. We made use of the virtual X-ray photon simulator PHOX ([Biffi et al., 2012, 2018a; Vladutescu-Zopp et al., 2023](#)) to produce highly sophisticated spectral models

<sup>3</sup><http://hea-www.cfa.harvard.edu/jzuhone/pyxsim/>

of individual galaxies where we properly account for the multi-temperature and metallicity distribution of the gaseous component. The emission from SMBH sources and XRBs can be accounted for individually and self-consistently without the need for empirical modeling of their contribution. We accounted for an AGN population in our galaxy sample by applying exclusion criteria motivated by the literature. We focused our analysis on an AGN-cleaned sample uncovering the following aspects:

- We determined mean and median SB profiles of normal star-forming ( $\log(\text{sSFR}) > -11$ ) and quiescent galaxies and quantified the contribution of different components. We find that SF galaxies have elevated total SB in their central regions compared to QU galaxies up to a scale-free radius of  $0.1 R_{\text{vir}}$  and comparable SB in the outskirts. The average contribution from XRBs towards the total SB is between 30%-50% in the inner  $0.1 R_{\text{vir}}$ , and  $\gtrsim 10\%$  for larger radii, which we attribute to the presence of substructures.
- We compared median SB profiles of the gas component in a  $M_*$ -matched subsample of our galaxies to recent observational results from the eROSITA collaboration, where they obtained CGM SB from stacking MW-mass galaxies. We are in moderate agreement with results from [Zhang et al. \(2024b\)](#) who have a similar median redshift distribution in their sample compared to our fixed redshift. We find no significant difference between the mean CGM profiles of SF and QU galaxies in our sample for the MW mass range ( $M_* = 10^{10.5-11}$ ). Results from [Comparat et al. \(2022\)](#) are in disagreement with our sample which may be due to instrumental effects.
- We computed hot gas fractions and temperatures of each galaxy and found positive correlations between the extent and normalization of SB profiles and the respective properties. Correlations are generally stronger for QU galaxies than for SF galaxies. All our galaxies have  $f_{\text{gas}} < f_{\text{bary}}$  accounting for hot gas within  $R_{\text{vir}}$ . We compared the SB of our sample with SB of observed galaxies for which the same properties ( $M_*$ ,  $f_{\text{gas}}$ ,  $k_B T$ ) were available and found good agreement for SF galaxies. We found lower normalization for our QU sample compared to the selected observations. The selected observations are however more consistent with our excluded AGN sample. We attribute this fact to the observational sample including more BCG galaxies which makes them brighter than typical QU galaxies.
- We fitted  $\beta$ -models to SB profiles of the gas component of our AGN-cleaned galaxy sample using a least-square algorithm. We found that most of our sample is best reproduced by a single slope  $\beta$ -profile. We compared the profile slope to intrinsic properties for each galaxy and found that SF galaxies have consistently steeper profiles compared to QU galaxies. We found a strong correlation between steepness and total gas luminosity, in agreement with observational results. We found a large scatter in the slope of low  $M_*$  galaxies in both the QU and SF sample. The slope of the SB profiles seems uncorrelated with  $f_{\text{gas}}$  and  $T_{\text{gas}}$  for SF galaxies and weakly correlated for QU galaxies while being consistent with observational results.
- We compared the  $M_{500c} - L_X$  relation of our galaxy sample to stacking results of A15 and Z24b for galaxy-mass halos and also compared to the scaling relations for galaxy groups

from [Lovisari et al. \(2015\)](#). While the intrinsic scatter in our sample increases for low halo masses we found excellent agreement with observational results at all halo masses. The scatter is a result of subgrid physics in the underlying cosmological simulation. The estimated median XRB contribution is consistent with theoretical models and can account for the total luminosity of galaxies with the lowest SB.

- Additionally, we compared the CGM luminosity of our galaxies by using an annulus similar to A15 ( $r > 0.15 R_{500c}$ ) and found median luminosities in excellent agreement with their stacking results. At low halo masses, LMXBs can contribute significantly to the overall CGM luminosity which may be due to satellite galaxies or a diffuse stellar component outside of the central galaxy.
- We find that the main engine for the gas luminosity and consequently the increase in steepness in our galaxy sample is the central SMBH of each galaxy. We find a strong dependence of the global gas luminosity on the current accretion rate of the central SMBH, in the whole range of host galaxy stellar masses investigated. While the SMBH injects feedback energy isotropically into the surroundings in the simulation, the internal energy of neighboring gas is increased. A higher  $\dot{M}_\bullet$  generally also suggests that there is more gas in the vicinity of the SMBH in order to sustain the accretion. The energy is then released close to the SMBH which leads to a centrally localized increase in luminosity and consequently to a steeper SB profile.

Ultimately, we were able to show that the CGM of galaxies can be resolved in modern cosmological simulations and can offer a unique way of benchmarking observational results. Empirically well studied relations for the X-ray emission of galaxies arise from the simulation self-consistently and provide predictions for the distribution of the gaseous halo out to the virial radius. However, it is challenging to directly observe the hot CGM in emission due to the emissivity being proportional to the density squared. The detection of the CGM out to large radii has been confirmed in emission using stacking procedures. While stacking can retrieve average properties of the underlying sample, information about the diversity of trends and scatter in those properties, such as metallicity, temperature or gas fraction, is lost. Our study can be therefore useful to better understand the underlying properties of galaxies and their systematics in commonly used observational techniques. In the future, current and proposed X-ray missions using calorimetry-based detectors, such as XRISM ([Tashiro et al., 2020](#)) or LEM ([Kraft et al., 2022](#)), may provide additional insights by directly measuring gas emission lines and setting more stringent constraints on feedback models and enrichment in the CGM.

## 7.5 Appendix

### 7.5.1 Behavior of the AGN sample

In Fig. 7.11 we present the mean and median SB profiles of all galaxies excluded by our exclusion criteria from Sec. 7.1.1. The excluded sample mostly comprises X-ray AGN-dominated galaxies

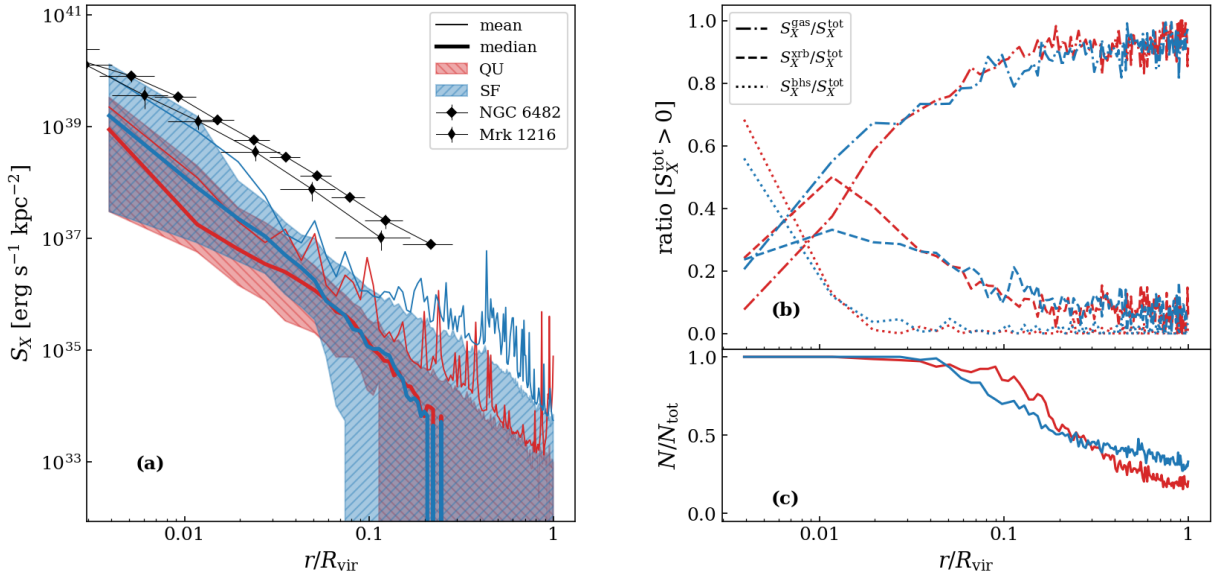


Figure 7.11: Same as figure 7.2 for the excluded AGN sample. Additionally, we include SB profiles from BCG like galaxies NGC 6482 and Mrk 1216.

as well as 6 brightest group galaxies (BGGs) with a stellar mass  $M_* > 10^{12} M_\odot$ . Compared to the cleaned sample, the excluded sample is more than an order of magnitude brighter in the center, which is due to the X-ray bright AGN emission. This can be seen in Fig. 7.11(b) where the emission of the central SMBH contributes more than 60% towards the total SB in the center. Furthermore, the difference between SF (blue) and QU (red) galaxies in the central  $0.1 R_{\text{vir}}$  is weaker in the excluded sample than in the cleaned sample. At large radii, profiles are similar to those reported in Fig. 7.2 for normal galaxies. However, the excluded sample shows slightly more extended emission for SF galaxies. This is caused by the BGGs in the excluded sample which are also highly star-forming. In Fig. 7.11 we also include the SB profiles of BCG-like galaxies NGC 6482 (Buote, 2017) and Mrk 1216 (Buote & Barth, 2018), which are in better agreement with the excluded sample compared to the cleaned sample.

## 7.5.2 Examples

In Fig. 7.12 we show two exemplary SB profiles (black) from our sample. The left panel shows a galaxy from the  $S\beta$  category which is best represented by a single  $\beta$ -profile (blue). The right panel shows a galaxy from the  $D\beta$  category which is best represented by a double  $\beta$ -profile (red). For reference, we also included the best fit single  $\beta$  profile in the right panel to illustrate the difference. We note, that the  $D\beta$  example also has some substructure within  $R_{\text{vir}}$  which is seen as large jumps in the SB profile. Those were masked using a median filter before fitting the profile.

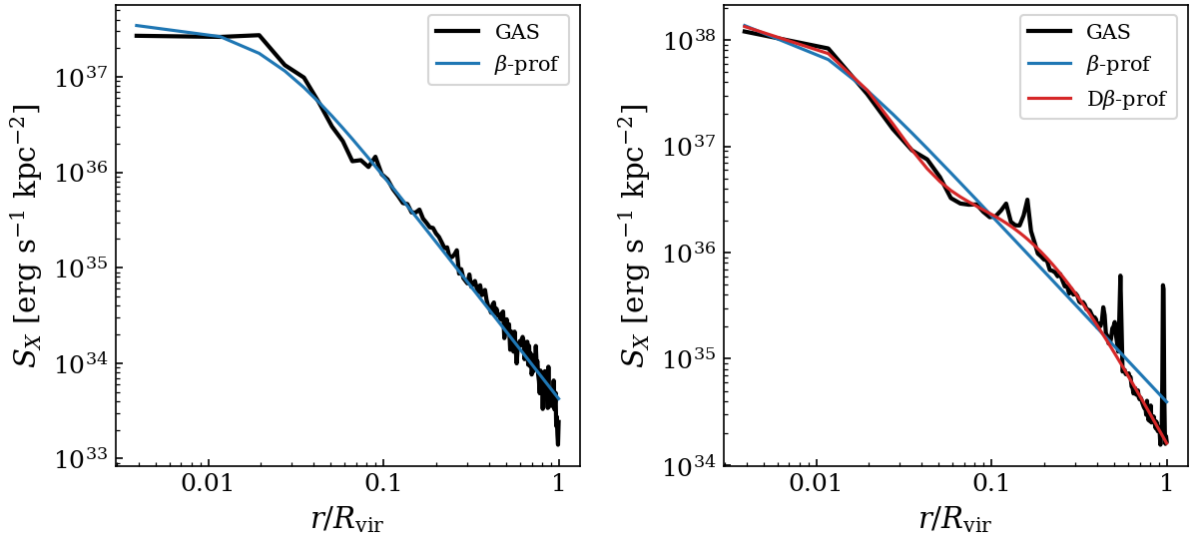


Figure 7.12: Exemplary SB profiles (*solid black*) from the  $S\beta$  category (*left*) and  $D\beta$  category (*right*). The solid blue line shows the best-fit single  $\beta$ -profile and the solid red line shows the best-fit double  $\beta$ -profile.

### 7.5.3 Galaxy main sequence

In Fig. 7.13 we show the SFR- $M_*$  relation for our galaxy sample, color-coded by SF (blue) and QU (red) galaxies. The black solid line indicates the observed main sequence from [Pearson et al. \(2018\)](#) in the redshift range  $0.2 < z < 0.5$ . The gray dashed diagonal lines indicate the relation for constant values of sSFR.

We note that low-mass SF galaxies lie below the main sequence by 0.5 dex, indicating that they typically have less star formation than expected.

### 7.5.4 Inclination

In order to quantify the imprints of galaxy orientation with respect to the l.o.s., we investigate the inclination dependence of SB profiles in star-forming disk galaxies. In our framework, the inclination angle  $i$  of each galaxy can be computed from the scalar product between the fiducial l.o.s. ( $\hat{e}_z$ ) and the specific angular momentum of the stellar component ( $\mathbf{j}_*$ ), such that

$$\cos i = \frac{\hat{e}_z \cdot \mathbf{j}_*}{\|\mathbf{j}_*\|}.$$

The galaxy would be seen edge-on for  $\cos i = 0$  and face-on for  $\cos i = 1$ . For this test, we only consider star-forming galaxies with a  $b$ -value  $b > -4.35$ , where

$$b = \log \left( \frac{j_*}{\text{kpc km s}^{-1}} \right) - \frac{2}{3} \log \left( \frac{M_*}{M_\odot} \right),$$

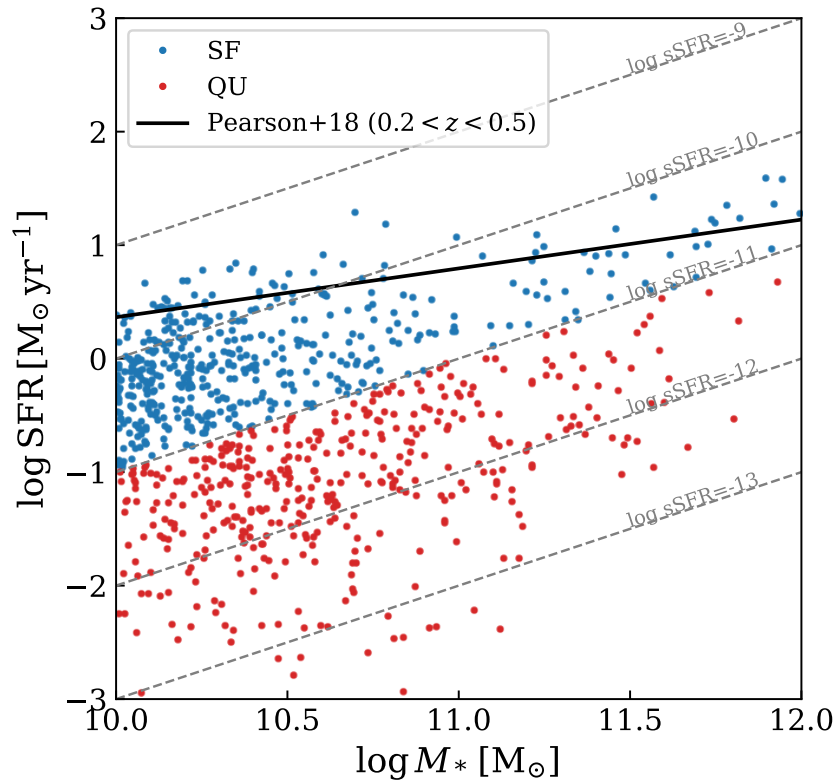


Figure 7.13: The main sequence of our total galaxy sample was extracted from the simulations. The dashed diagonal lines indicate constant specific star-formation rates in  $\text{Gyr}^{-1}$ . The solid black line indicates the empirical main sequence from (Pearson et al., 2018) for the redshift range  $z = 0.2 - 0.5$ . Blue colors are SF galaxies and red is QU galaxies which we distinguish using the  $\log \text{sSFR} [\text{yr}^{-1}] = -11$

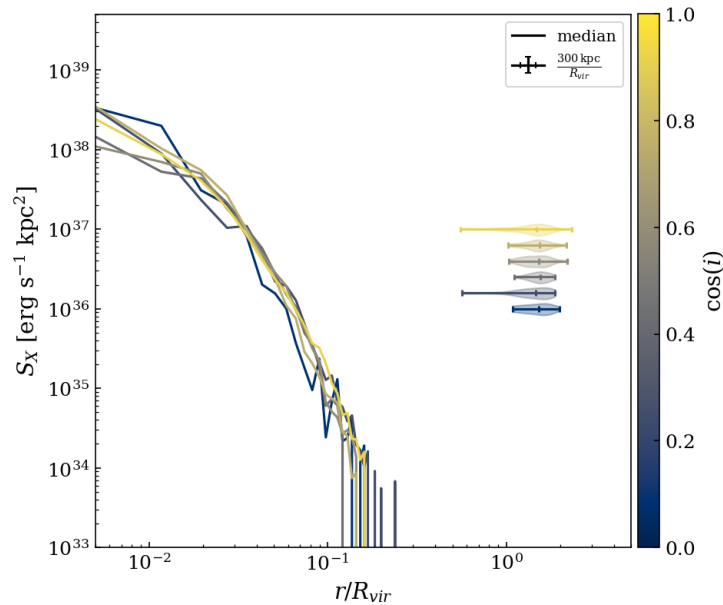


Figure 7.14: Similar to figure 7.4. Colors indicate the cosine of the inclination angle of star-forming disk galaxies within each bin.

is a measure of the galaxy morphology (Teklu et al., 2015) and the numerical value was chosen according to Schulze et al. (2020) for disk galaxies. This constrains our sample to only include truly disk-like galaxies, allowing for a meaningful interpretation of the inclination angle. In figure 7.14 we show mean SB profiles of our disk-like subsample, where galaxies were binned according to the value of  $\cos i$  (with colors indicating the bin centers). Colored violins have the same meaning as in Fig. 7.4. We do not find any strong dependence of the SB profile on the galaxy inclination angle. From a theoretical perspective, it is intuitive to assume preferential outflow directions perpendicular to the galactic disc due to the path of least resistance. Numerical studies using different simulations find in fact asymmetric outflow patterns in X-ray mock observations of disc galaxies Truong et al. (2021a); Schellenberger et al. (2023); Truong et al. (2023). Observationally, studies of X-ray emission around disk galaxies did not find however any enhanced signal perpendicular to the disc (Bogdán et al., 2013; Li et al., 2018; Hou et al., 2024).



## **Part III**

# **Inter-Galactic X-ray emission from cosmic filaments in simulations**



# 8 | Emissivity of low-density gas in cosmic filaments: a case study

- This chapter will be part of a future publication (Vladutescu-Zopp et al., 2025, in prep)

In this part of the thesis, we want to connect the previously investigated properties of galaxies to their larger-scale environment. Having previously discussed the interaction between ISM and CGM, we will now highlight the X-ray properties of the cosmic web in which galaxies are embedded. The specific study presented here was developed during the proposal phase of the Line Emission Mapper (LEM) probe concept mission (see [Kraft et al., 2022](#)).

## 8.0.1 Line Emission Mapper

The design of LEM specifically targeted and was optimized for the soft X-ray energy range (0.2 – 2 keV) where the most abundant ion species in the CGM and IGM have bright emission lines. The single telescope would have consisted of a grazing-incidence X-ray mirror with a large effective area (1600 cm<sup>2</sup>), a moderate angular resolution (15''), and a large field of view (30' × 30'). The main detector was planned to have an energy resolution of at least 2 eV made possible through a cryogenic microcalorimeter array, a similar technique employed in the short-lived *Hitomi* satellite ([Takahashi et al., 2016](#)) and its successor *XRISM* ([Tashiro et al., 2020](#)) as well as the future facilities *HUBS* ([Cui et al., 2020](#)) and *Athena* ([Barret et al., 2018](#)). Since the faint emission of the IGM and CGM of distant galaxies would be screened by the foreground emission of the MW's CGM, a microcalorimeter array would be able to distinguish the emission lines of the IGM from the MW foreground due to the redshifted line emission, improving the signal-to-noise by at least an order of magnitude. The optimal redshift windows needed to observe various emission lines against the MW foreground are shown in Fig. 8.1. Within these windows, the emission lines of the IGM are sufficiently separated from their counterparts in the MW foreground. Together with its unprecedented grasp (effective area times field-of-view), LEM would have been an ideal instrument to target the long-standing problem of the X-ray emission from the warm ( $\sim 10^6$  K) low-density gas ( $\lesssim 10^{-4}$  cm<sup>-3</sup>) which is believed to make up a large fraction of the cosmic baryon budget ([Cen & Ostriker, 1999](#)).

The observatory's science cases focused on its exceptional resolution of emission lines. In particular, the shape and strength of different lines are direct indicators of various physical

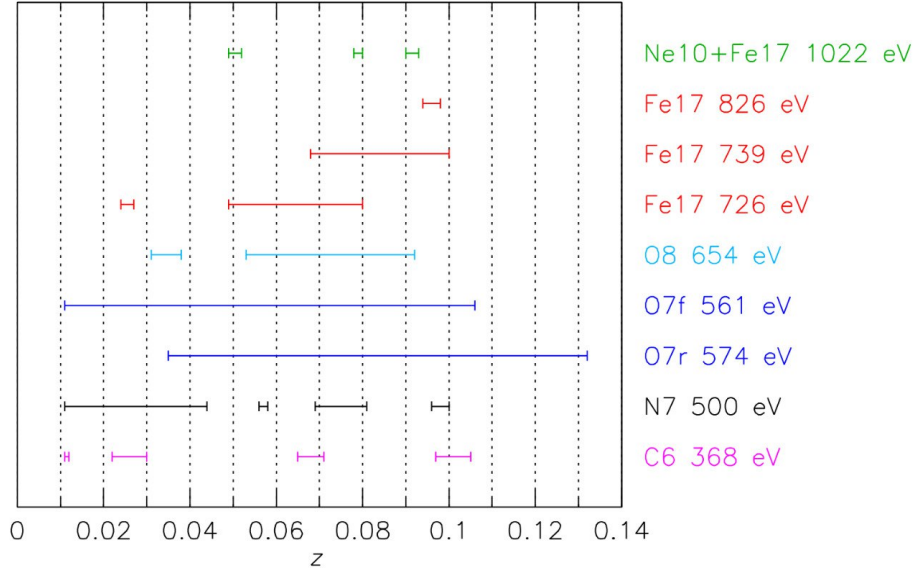


Figure 8.1: Optimal redshift windows to observe various emission lines of the IGM against the MW foreground. Courtesy of Maxim Markevitch, from the IGM science group within the LEM collaboration.

properties such as cooling, galactic outflows induced by AGN and stellar feedback, gas mixing, and turbulence (Kraft et al., 2022). A planned all-sky survey would have enabled statistical studies of extra-galactic sources and constrained the foreground emission of the MW as well as the local hot bubble (Khabibullin et al., 2023). Regarding galaxies, the ionization state of the hot ISM could have been determined directly to reassess the CIE paradigm (Kraft et al., 2022), and XRB populations could have been identified spatially by monitoring their time variability concerning relativistically broadened line emission in their spectra (Pinto et al., 2024).

Several studies have been published on the capabilities of LEM. For instance, the velocity structure of the CGM in galaxies, and the IGM is directly accessible for such high energy resolution due to line centroid shifts (ZuHone et al., 2024). Additionally, information on the feedback processes shaping galaxy evolution can be gained from the spatial distribution of emissivity in different ion lines and their respective ratios (Truong et al., 2023; Schellenberger et al., 2024). The interplay between feedback processes in galaxies and the cosmic web plays a crucial role in understanding the origin of pre-enriched gas in the IGM and its physical characteristics (Biffi et al., 2017; Mernier et al., 2023). A dedicated all-sky survey would enable the study of a plethora of physical phenomena from stellar astrophysics, SN remnants, the MW CGM, to extra-galactic science of galaxy groups and clusters (Khabibullin et al., 2023). Therefore, a primary target of the mission concerns the evolution of structure formation and enrichment of the IGM. While the continuum emission of the IGM is low compared to the line emission of e.g. O VII or Fe XV, resonant X-ray lines can be significantly enhanced through the scattering of CXB photons (see Khabibullin & Churazov, 2019).

Unfortunately, at the time of writing this thesis, NASA's Astrophysics Probe Explorer (APEX) selection had not approved the mission concept for further review in the program. Nevertheless,

the science conducted within the collaboration remains generally applicable to all future X-ray missions employing microcalorimeters and may serve as a reference for the science goals of such missions.

In the following, we will present our results for a project started within the LEM collaboration targeting the IGM. In particular, we will focus on the physical properties of the IGM, such as temperature and underlying density structure, and relate to its X-ray emission lines using an exemplary cosmic filament from the *Magneticum* simulation.

## 8.0.2 The IGM in cosmic filaments

The cosmic web is a result of the gravitational collapse of matter and is an emerging pattern connecting the densest nodes of cosmic structures through sheets and filaments at the edges of underdense voids (Bond et al., 1996; Cautun et al., 2014). Numerical simulations have shown that up to half of the baryons in the universe reside within the connecting filaments, shock-heated from the gravitational collapse of the filaments to a temperature of  $T = 10^5 - 10^7$  K (Cen & Ostriker, 1999; Davé et al., 2001; Cautun et al., 2014; Martizzi et al., 2019; Tuominen et al., 2021). This Warm-Hot Intergalactic Medium (WHIM) phase of the cosmic baryon distribution has been the subject of extensive observational studies trying to close the gap of missing baryons in the universe (Péroux & Howk, 2020). However, its low density and high temperatures shift the thermally excited emission into the UV and soft X-ray regime where absorption and the MW foreground are strong. Additionally, the high degree of ionization in hydrogen and helium within the filaments makes detecting this phase in X-ray absorption rather difficult and requires favorable conditions (Nicastrò et al., 2018).

Allowing the WHIM phase to be sufficiently enriched with metals, the direct emission and absorption in metal lines is nevertheless the most promising approach to observing this medium directly (Paerels et al., 2008; Richter et al., 2008) and effects of different metallicity enrichment models on the emissivity of the WHIM across redshift have been investigated (Ursino et al., 2010). Indeed, direct X-ray emission from filaments within the virial radii of massive clusters has been found in individual cases (Werner et al., 2008; Eckert et al., 2015; Bulbul et al., 2016) and filaments connecting cluster pairs showed an X-ray excess beyond several virial radii in eROSITA data (Reiprich et al., 2021; Biffi et al., 2022; Dietl et al., 2024). Churazov et al. (2023) investigated the detectability of filaments as a function of the line-of-sight integrated emission measure using the *Magneticum* simulations and archival observations of the Coma cluster. They concluded that the emissivity of filaments is highest at a few turnaround radii ( $\sim 10$  Mpc) of the cluster, where the density contrast is enhanced from the cluster potential.

Identifying filaments in a statistically rigorous manner is difficult due to their low intrinsic density and complex morphology. Nevertheless, there are several dedicated algorithms used for the identification such as Spineweb (Aragón-Calvo et al., 2010), DisPerSE (Sousbie, 2011; Sousbie et al., 2011), or Bisous (Tempel et al., 2014). Applied to observational data, these algorithms identify the filamentary structure from the distribution of galaxies from dedicated sky surveys such as the Sloan Digital Sky Survey (SDSS, Gunn et al., 2006) (e.g. Tempel et al., 2014; Malavasi et al., 2020). Equally, the algorithms can also be applied to cosmological numerical simulations, which were used to understand the structure and physical properties of the WHIM

in more detail (Galárraga-Espinosa et al., 2020, 2021, 2024; Ilc et al., 2024). Concerning the X-ray emission from the WHIM gas phase in filaments, several studies employed the stacking technique to enhance the X-ray faint signal. For instance, Tanimura et al. (2020) detected direct X-ray emission from large cosmic filaments using ROSAT data, constraining the temperature  $T$  and relative overdensity  $\delta$  in the spine of the filament to  $T \sim 0.9_{-0.6}^{+1.0}$  keV and  $\delta \sim 30 \pm 15$ , respectively. They also forecasted the potential of eROSITA to further constrain the parameter space. They also showed that the gas density follows a  $\beta$ -model with  $\beta = 2/3$  in agreement with results from numerical simulations. Recently, Zhang et al. (2024a) performed a similar analysis on eROSITA data of 4 complete all-sky scans (eRASS:4, Merloni et al., 2024) where they also accounted for unresolved emission from galaxies within the filaments.

With the advent of future X-ray missions employing microcalorimeter technology, a new avenue to directly detect the emission of individual filaments will be possible using spectroscopy. By resolving individual emission lines or using line intensity mapping in the X-ray spectra of filaments (Bregman et al., 2023), it will be possible to directly assess the temperature and density of the WHIM phase but simultaneously constrain its metal enrichment and turbulent pressure. Current and future missions such as *XRISM Resolve* (provided the gate valve opens for the soft X-ray regime, Tashiro et al., 2020) or *HUBS* (Cui et al., 2020) and *Athena* (Barret et al., 2018) will give new insight into properties of the intergalactic medium. A forecast study based on the supercluster catalog from eRASS:1 was performed for the upcoming *HUBS* mission, which showed that model assumptions for the WHIM phase could be successfully reproduced using the large field of view and eV spectral resolution of *HUBS*. (Zhao et al., 2024).

In the following study, we will present preliminary results on the intrinsic properties of an individual cosmic filament regarding the WHIM phase. The filament was extracted from the hydrodynamic cosmological simulation volume *Box2/hr* of the *Magneticum* which is described in Sec 8.1. Using the PHOX algorithm (Biffi et al., 2012) we create virtual X-ray photons from the intrinsic properties of the simulation in conjunction with the WHIM emission model presented in Khabibullin & Churazov (2019), also described in Sec. 8.1. Similar to observations we trace the underlying large-scale distribution of galaxies, dark matter, and gas temperature in the filament and correlate them to the X-ray line emissivity in Sec. 8.2, while accounting for the X-ray emission of galaxies. In Sec. 8.3, we bring our results into a broader context and discuss future steps for the analysis of this study.

## 8.1 Data Set

### 8.1.1 Filament extraction

For the filament extraction, we considered all clusters with a total mass of  $M_{\text{vir}} \sim 10^{15} M_{\odot}$  in the *Box2/hr* volume of the *Magneticum* set of cosmological simulations (see 4.1) at a simulation redshift of  $z = 0.252$ . We selected regions around each cluster corresponding to a few turnaround radii of each cluster and constructed halo catalogs from the subfind output of the same regions.

For each cluster, we then constructed cluster-centric HEALPix<sup>1</sup> maps of the galaxy distribution and determined the pixel containing the highest galaxy number density. If the galaxy distribution in the identified direction additionally showed a radial distribution with respect to the cluster center, we considered the direction to host a filament.

With the approach outlined here, we specifically exclude directions containing galaxy groups, where the number density would not show a radial trend. This approach is thus similar to the DisPerSE algorithm (Sousbie, 2011) in which we follow the overall galaxy density along a filament. We applied this approach to our selected cluster sample and selected the second most massive cluster in *Box2/hr* for the case study because it hosted the most promising filament with the highest galaxy number density. We generated a  $30 \text{ Mpc} \times 15 \text{ Mpc} \times 15 \text{ Mpc}$  sub-volume of the selected cluster, only containing the identified filament and excluding the cluster center. We rotated the sub-volume such that the elongation of the filament lies perpendicular to the line of sight. The underlying dark matter surface density and the gas temperature distribution are shown in the top and bottom panels of Fig. 8.2, respectively, where the cluster center is to the right of the image and coordinates on the  $x$  and  $y$ -axis measure the distance from the cluster center. For the dark matter surface density, we binned dark matter particles contained in the sub-volume according to a regular grid with a pixel area of  $\sim 133 \text{ kpc} \times 133 \text{ kpc}$  and a corresponding integration depth of 15 Mpc. We used the same regular grid for the temperature map and distributed each gas particle's temperature according to its hydrodynamic kernel weighted by the particle's intrinsic density. Black circles overlaid on each map correspond to the virial radii of halos within the filament sub-volume with a halo mass greater than  $10^{10} M_{\odot}$ . The position of galaxies often coincides with pockets of cold gas ( $< 5 \cdot 10^5 \text{ K}$ ) as seen in the temperature map. This behavior is expected as density-weighted temperatures are dominated by the low temperatures and high densities of the ISM.

To better reflect the optical selection of galaxies determining a filament in real observations, we construct a map of the halo number density using the same regular grid as in Fig. 8.2 by binning halo positions. The resulting histogram is then smoothed with a Gaussian kernel assuming a standard deviation of  $\sigma = 4 \text{ Mpc}$  which we show in Fig. 8.3. Black lines indicate iso-density contour levels for visual clarity and the corresponding line per level is indicated directly in the colorbar.

### 8.1.2 Emission model

For the X-ray analysis of the filament, we employ the PHOX algorithm to produce virtual X-ray photons from the simulation (see Chap. 5). In particular, we make use of the WHIM specific emission model introduced by Khabibullin & Churazov (2019, KC19) in which a thermal plasma is subjected to irradiation from the CXB. Not only does this additional photon field change the ionization balance of the plasma, but it also contributes an additional scattered component where background photons are resonantly scattered toward the line of sight enhancing the line emissivity. The more realistic treatment of this phase makes the emissivity explicitly dependent on the underlying density of the plasma, in contrast to a standard APEC model based on collisional

<sup>1</sup><https://healpix.sourceforge.io/credits.php>

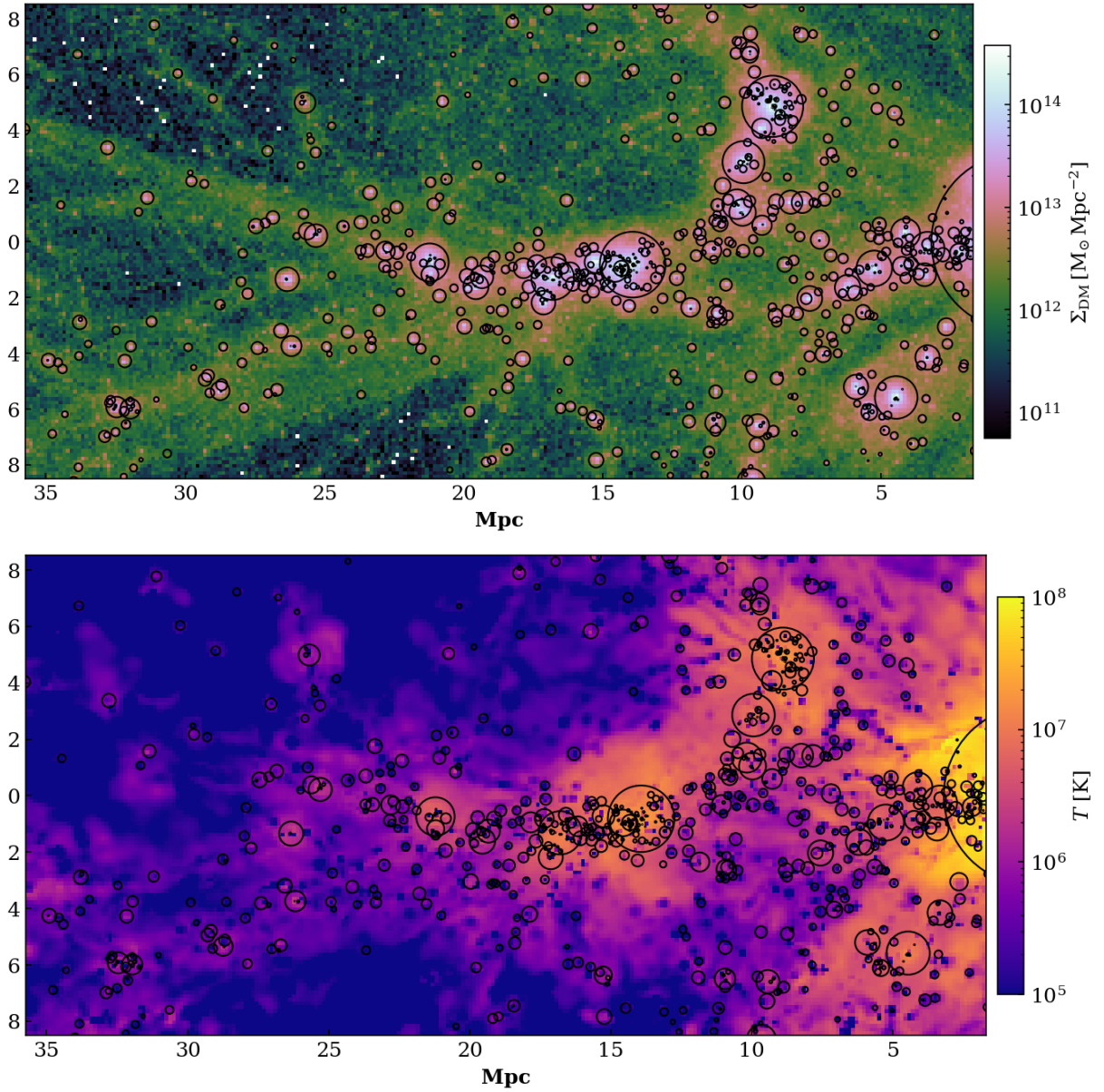


Figure 8.2: Dark matter surface density (top) and density-weighted gas temperature map (bottom) of the filament region. The parent cluster is to the right of the image and coordinates denote the distance from the cluster center. Black circles indicate the position of identified halos within the field of view with their corresponding virial radii.

equilibrium. Above a temperature of  $T \sim 10^7$  K and densities above  $n \sim 10^{-4} \text{ cm}^{-3}$ , the KC19 model converges towards the APEC model.

In order to produce the initial set of photons, we shifted the filament closer to a redshift of  $z \sim 0.035$  setting the required fiducial integration time to  $\tau_{\text{obs}} = 5 \text{ Ms}$  and the fiducial flat collecting area  $A_{\text{obs}} = 1000 \text{ cm}^2$ . In this redshift range, the two most prominent oxygen lines should be

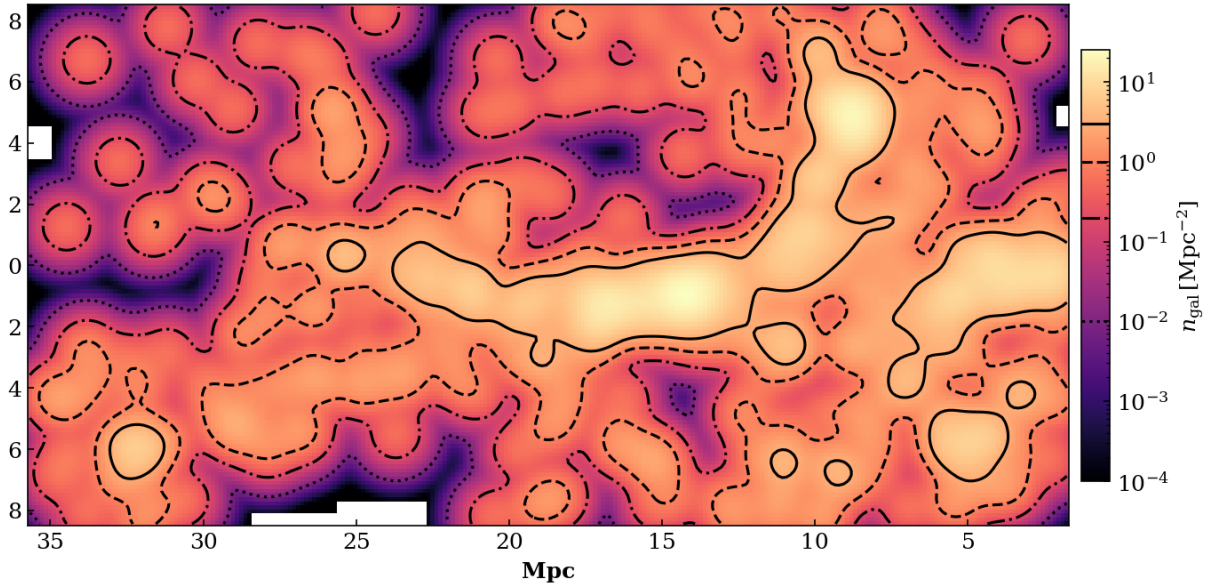


Figure 8.3: Surface number density of identified halos within the filament region. The parent cluster is to the right of the image and coordinates denote the distance from the cluster center. Halo positions were binned on a regular grid and the resulting histogram was smoothed using a Gaussian kernel with  $\sigma = 4$  Mpc. Black lines indicate iso-density contours indicated in the color bar with their corresponding line style.

easily discernible from the MW foreground for an X-ray telescope with microcalorimeters. We note that the WHIM phase in *Magneticum* appears to be metal-poor compared to the other gas phases resulting from the chemical feedback implementation in the simulation (Biffi et al., 2022; Churazov et al., 2023). For this reason, we implemented a metallicity floor for the gas particles at  $Z = 0.1 Z_{\odot}$  (Anders & Grevesse, 1989), boosting the line emission from the otherwise faint WHIM signal and to better reflect radial abundance gradients for galaxy cluster outskirts which appear to be flat around  $Z \sim 0.2 - 0.3 Z_{\odot}$  (Biffi et al., 2018b; Mernier et al., 2018, 2023, see e.g.). The resulting photon packages are then projected along the line of sight, accounting for the peculiar motion of the gas and assuming no foreground absorption. Finally, the projection is stored as photon lists containing information about the associated parent particle from the cosmological simulation.

For the following analysis, we focus on the hydrogen and helium-like oxygen ions OVIII and OVII for which prominent emission lines exist in the soft X-ray spectrum at  $O_8 = 0.654$  keV and  $O_{7(r)} = 0.574$  keV, where ( $r$ ) denotes the resonant line of the OVII triplet. We chose to focus on a single element since both species are dependent on the same abundance. Other metal species can be considered as well for this analysis, however, more care has to be taken for the specific abundance ratio in addition to temperature and density dependencies. From the simulated photon lists, we select specific energy ranges around each of the considered oxygen lines in a narrow band of 10 eV and produce maps on the same regular grid as in Fig. 8.2. The result is shown in Fig. 8.4, where the color indicates the surface photon flux per unit time and collecting area with blue

for OVII (top panel) and orange for OVIII (bottom panel). Overplotted black circles are again the positions of identified halos with their virial radii. From a visual inspection, it appears that OVIII is more extended than OVII which in our framework hints at a temperature dependence. The exact details of the strength and spatial distribution from each line will be subject to the following analysis.

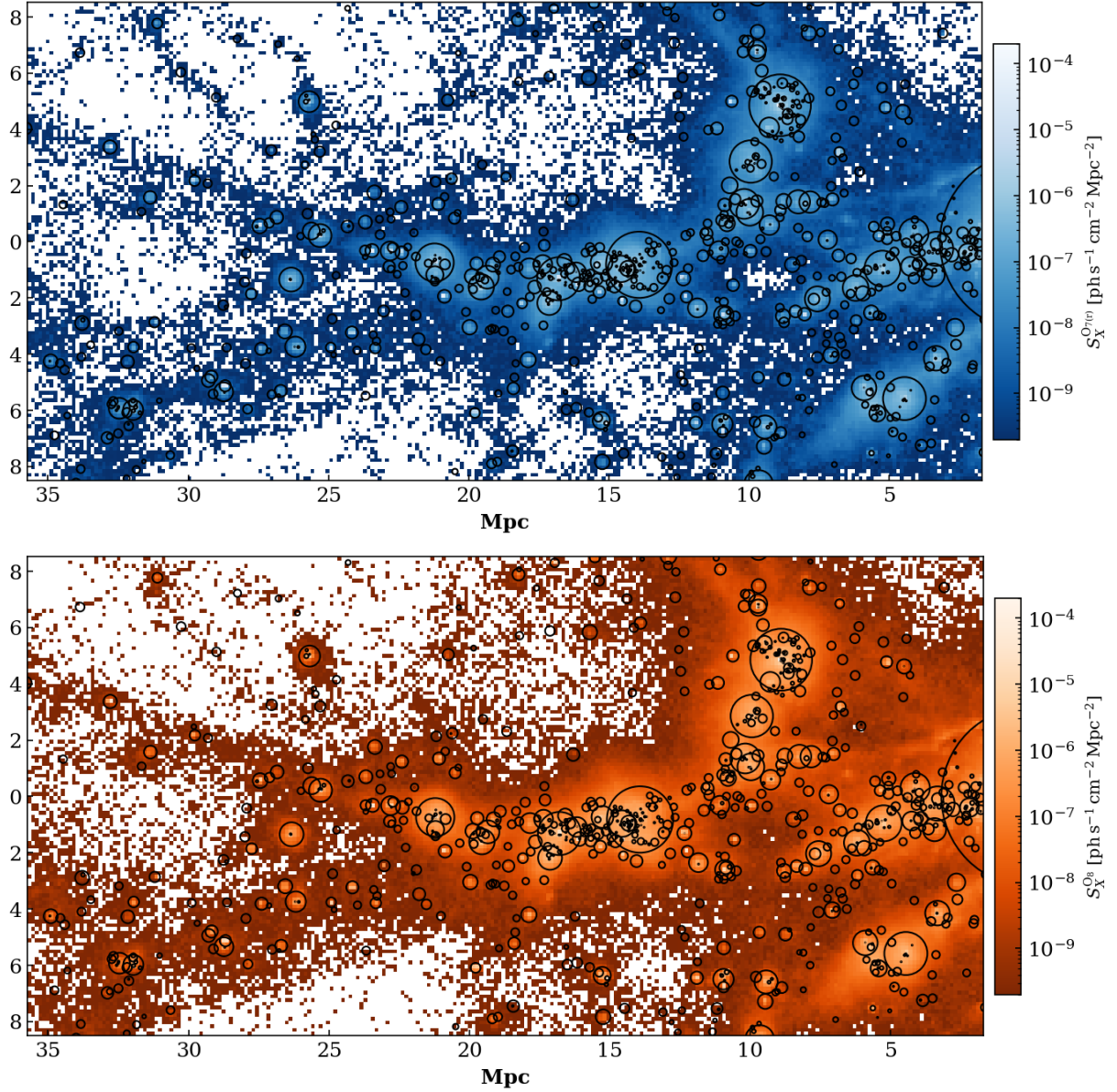


Figure 8.4: Integrated surface photon flux of the filament region for the resonant OVII line (blue, top panel) and the OVIII line (orange, bottom panel). Black circles indicate the position of identified halos with the field of view with their corresponding virial radii.

## 8.2 Intrinsic filament emission

### 8.2.1 Line emissivity as a tracer for dark matter

Various studies on the matter distribution inside filaments yielded consistent results across both cosmological simulations (Galárraga-Espinosa et al., 2020, 2021, 2024) and observations (Tanimura et al., 2020, 2022; Zhang et al., 2024a; Zhao et al., 2024). Namely, all matter components (dark matter, stars, and gas) follow a  $\beta$ -model (Galárraga-Espinosa et al., 2022) with similar slope but varying core density. As such, the gas density inside filaments is traced by the dark matter component and consequently the distribution of halos along the filament. With the X-ray emissivity being a strong function of density, the emissivity indirectly traces the dark matter component as well. We investigate this possible connection from the intrinsic line emissivity in O<sub>VIII</sub> and O<sub>VII</sub> on both the true underlying dark matter density and the halo number density. Additionally, we test the same correlation while masking bins that overlap within the virial radius of any identified halo in our filament region.

In Fig. 8.5 we show the line emissivity of  $O_7$  (blue) and  $O_8$  (orange) as a function of the surface halo density by cross-correlating the maps shown in Fig. 8.3 with Fig. 8.4. In the top row, we include all pixels in the map ( $S_X$ ), while in the bottom row, we mask pixels overlapping with the virial radius of a halo ( $R_X$ ). The black dashed line indicates a power-law relation with slope 2 between the surface brightness and the underlying density. The  $r$ -value represents the Pearson correlation coefficient for pixels containing more than 5 photons. Both correlations for  $O_7$  and  $O_8$  are similar with  $O_8$  reaching slightly higher surface brightness. Judging from the  $r$ -value in the top row, the two quantities are only weakly correlated, dominated by large outliers at high surface brightness and low halo density. By masking pixels overlapping with identified halos in the bottom row, the correlation improves because of the missing outliers at high surface brightness. The bulk of data points is located close to a halo number density of 1 with surface brightness  $S_X \sim 5 \cdot 10^{-10} \text{ ph s}^{-1} \text{ cm}^{-2} \text{ Mpc}^{-2}$ . While the indicated square dependence seems to be a good fit of the correlation, we performed a proper least square fit of the data which yielded a shallower slope at  $\sim 1.0 - 1.2$ .

We performed the same analysis using the dark matter surface density which is shown in Fig. 8.6. The dark matter correlation is more confined than the halo density at low surface brightness because of fewer outliers at low densities but similarly shows outliers at high surface brightness. Furthermore, the  $r$ -value suggests a stronger correlation with dark matter surface density caused by the comparatively few halos used in the halo density map. When including the halo contribution (top row) the relation between surface brightness and dark matter density is visibly flatter than a power law with slope 2 at high density. When masking the halo contribution (bottom row) the correlation may be consistent with a power law, however, a least-square fit again yields shallower slopes at  $\sim 1.0 - 1.2$ .

### 8.2.2 Line ratios as a tracer for temperature

In general, line ratios in the 0.3 – 1.1 keV band are sensitive to the temperature of the plasma since the temperature sets not only the ionization but also the recombination balance of ions (Dopita &

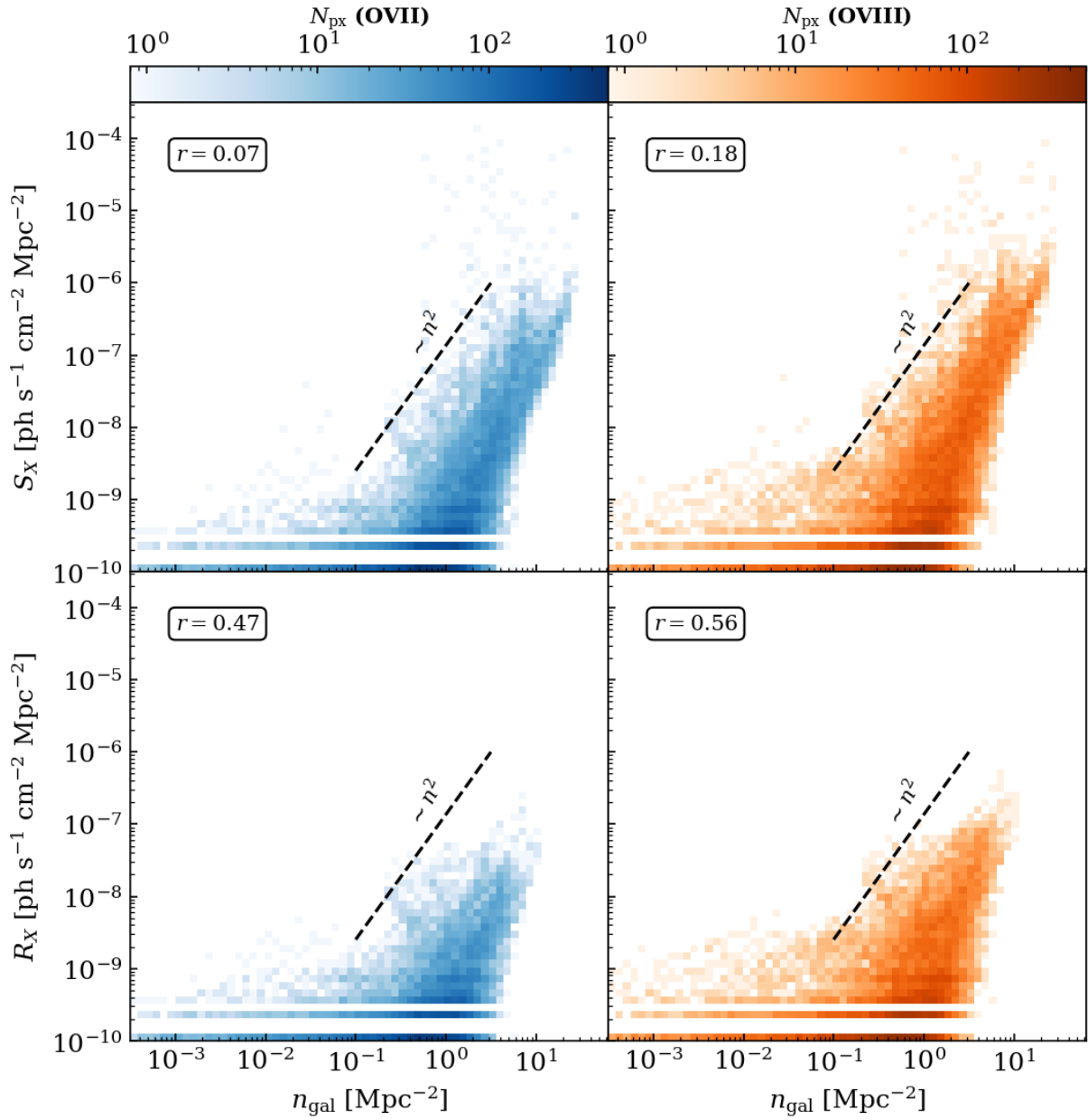


Figure 8.5: Cross-correlation of the halo number density and the line emissivity in  $O_7$  (blue) and  $O_8$  (orange). In the top row, all pixels are considered and in the bottom row, pixels overlapping with the virial radius of an identified halo are masked. The color bar indicates the number of pixels per bin. The black dashed line shows a power-law relation with slope 2 between surface brightness and underlying halo density.

Sutherland, 2003). Depending on the model assumptions, such as collisional or photoionization equilibrium, the expression of lines can be vastly different across models. As such, line ratios are

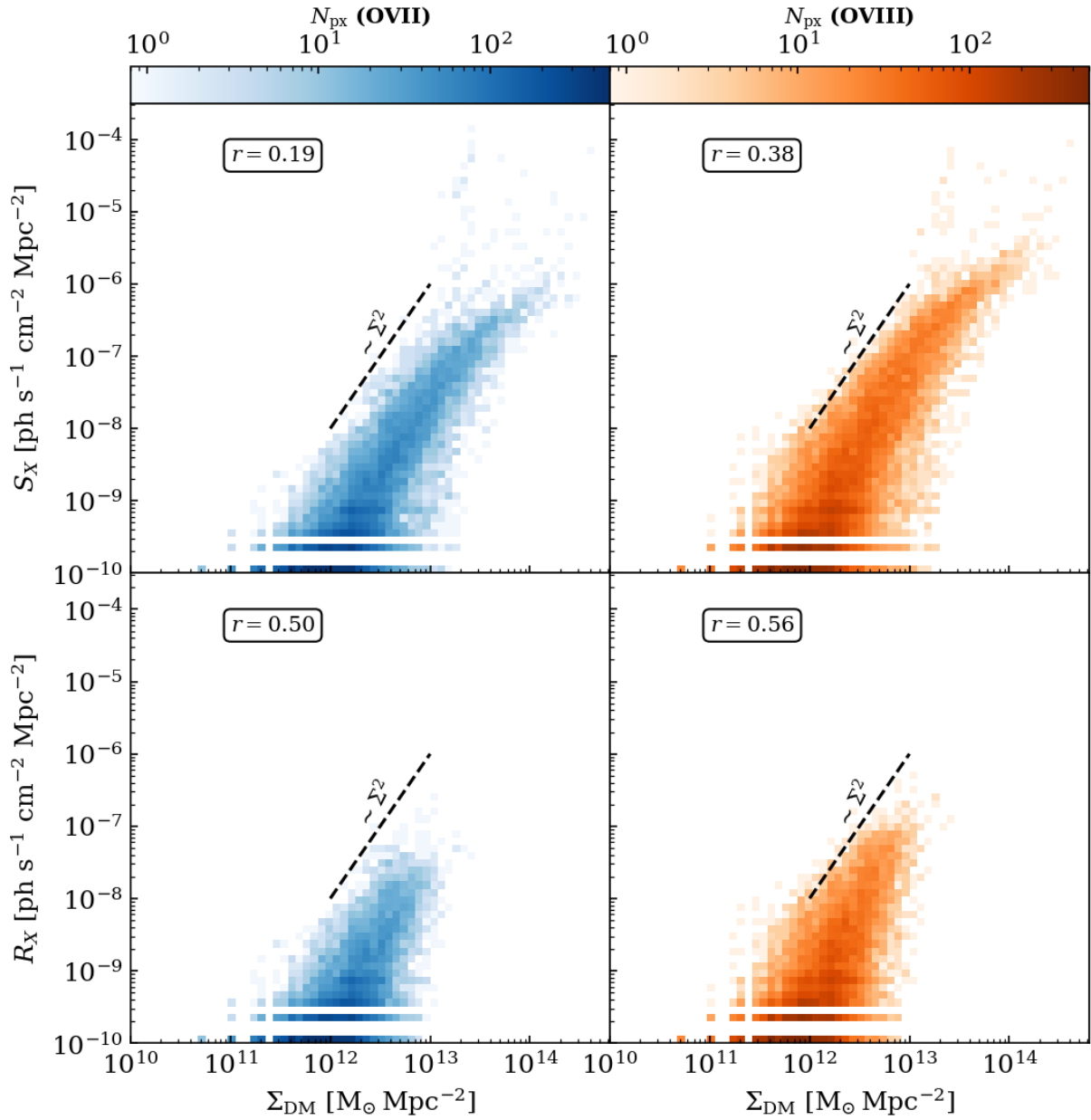


Figure 8.6: Same as Fig. 8.5 using the dark matter surface density instead of the halo density.

not only a tracer of the plasma's underlying temperature but also give insights into the physical processes governing equilibrium. Microcalorimeters should be able to distinguish between different models. We will therefore investigate the line ratios of the previously constructed  $O_{7(r)}$  and  $O_8$  maps as a potential tracer for the underlying temperature. We only focus on one element to mitigate the effects of degeneracy in abundance variation between different elements but in principle, other line ratios can be used to probe different temperature regimes.

We constructed the  $O_{7(r)}$  to  $O_8$  ratio maps by dividing the previously created maps of the same lines which we show in Fig. 8.7. High ratios are given in blue and low ratios are given in red colors. Again we overplot the position of identified halos with their virial radii as black circles. Notably,  $O_8$  is dominant in most regions of the filament including near the most massive halos. However, smaller halos in the outskirts of the filament show a clear increase in  $O_{7(r)}$  to  $O_8$  ratio. We further

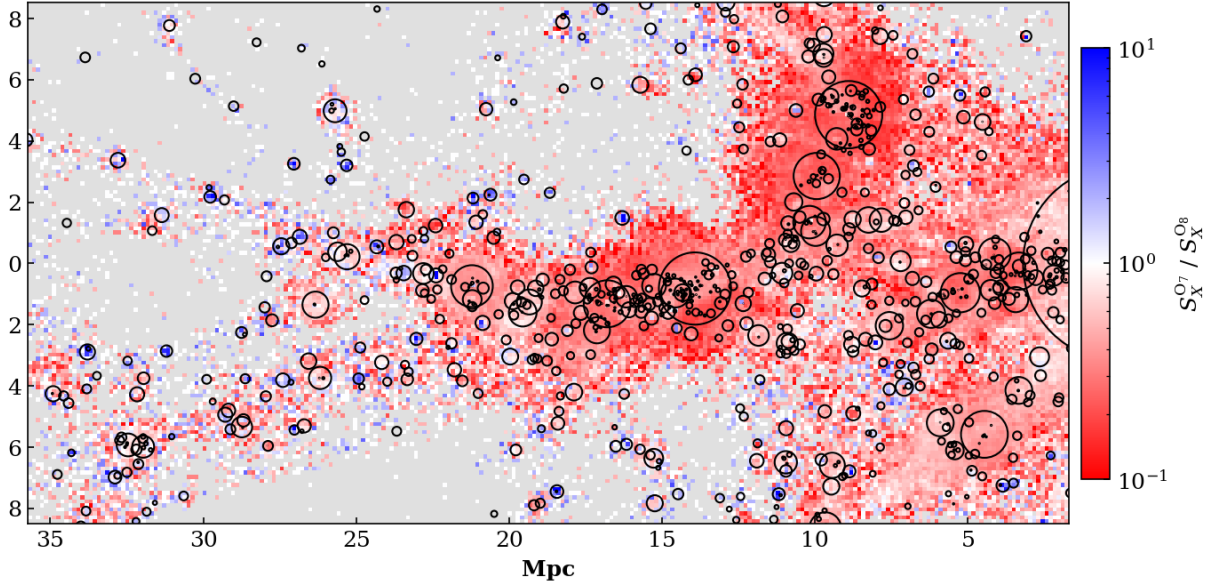


Figure 8.7: Similar to Fig. 8.4 where we divide the  $O_{7(r)}$  by the  $O_8$  map to obtain their ratio. The black circles indicate the position of halos with their virial radii.

investigated the oxygen ratio by cross-correlating the ratio map with the gas temperature map which we show in Fig. 8.8. The left panel shows the entire region while the right panel shows the same relation excluding pixels overlapping with halos. In both cases, a clear correlation is seen for the temperature range of  $T = 10^{5.5-7}$  K. For higher temperatures, oxygen would be completely ionized such that the ratio only depends on the shape of the continuum. In order to understand the origin of the large spread within the distribution we also show the theoretically expected line ratios from the KC19 model as green dashed lines for various plasma densities. The logarithmic ion number density  $n_i$  is shown in the green boxes next to the corresponding line. For completeness, the cyan dash-dotted line shows the theoretical ratio assuming an APEC model. We note, that the KC19 model is defined only for temperatures  $T < 10^7$  K and is replaced by an APEC model at higher temperatures. From visual inspection, the temperature dependence aligns well with the KC19 model prediction for ion densities of  $\log n_i [\text{cm}^{-3}] = [-5.2; -4.5]$  showing an even spread across. We therefore conclude that the spread in the distribution is caused by a superposition of gas at various densities consistent with densities expected for the WHIM phase and the tail at high temperatures is well explained by the behavior of the APEC model.

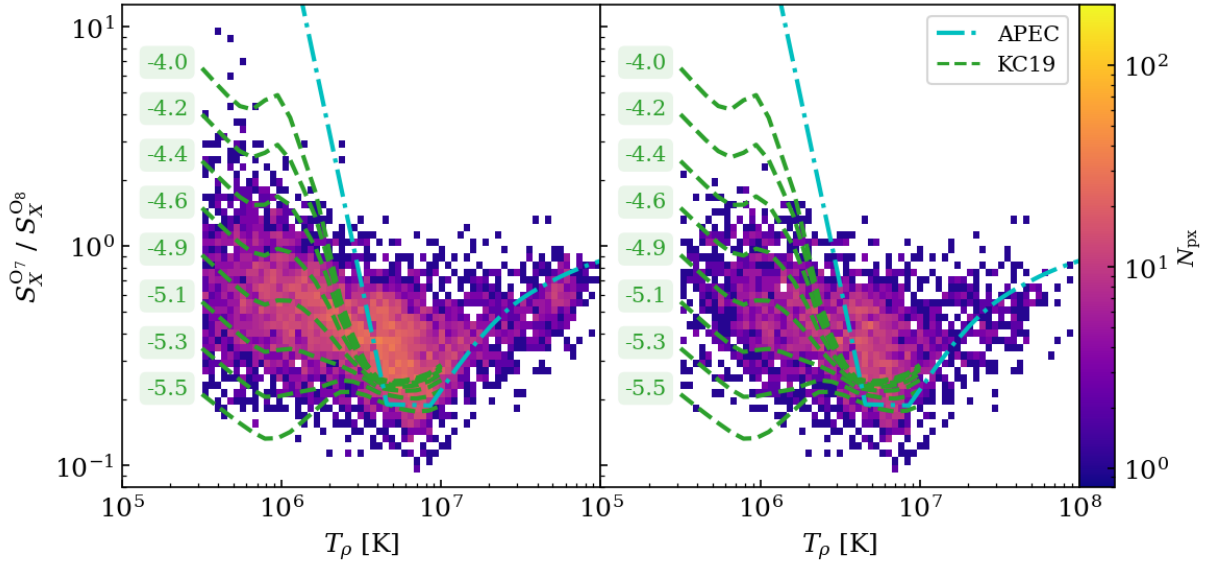


Figure 8.8: Cross-correlation of the temperature map (Fig. 8.2, bottom) and the  $O_{7(r)}$  to  $O_8$  ratio map. Dashed green lines indicate the expected temperature dependence of the line ratio for various ion densities assuming the model by [Khabibullin & Churazov \(2019\)](#) which was used for the photon simulation. The corresponding logarithmic ion density is given in the green boxes next to its line ( $\log n_i [\text{cm}^{-3}] = [-5.5; -4]$ ). The cyan dash-dotted line is the line ratio predicted by the APEC model. The color bar indicates the number of pixels from the original map within each bin.

### 8.3 Outlook

Due to time constraints, the analysis presented here is not yet complete and we will thus briefly outline plans to continue this project for a final publication. So far, we have only examined the filament's intrinsic properties, limited to the most prominent oxygen lines in the soft X-ray band. A simple extension of the analysis would be the focus on other X-ray lines for chemical elements tracked by the simulations such as iron or neon as they can generally give insight into the enrichment history from SNe. In light of future X-ray missions, it is important to understand the effects a real observation would have on the results and whether the same conclusions can be drawn. The full treatment of a mock observation includes not only the telescope response but also requires modeling of the fore- and background emission of various sources. In particular, we want to explore the capabilities of future X-ray microcalorimeter missions such as *HUBS* which are specifically targeted for the WHIM emission of the IGM. To achieve this goal, the photon lists generated by the PHOX algorithm will be reprocessed by making use of the SIXTE software package ([Dauser et al., 2019](#)), designed to accurately simulate the response of many specific telescopes, e.g. eROSITA or Athena ([Barret et al., 2018](#)).

Another important aspect to quantify further is the contribution of galaxies towards the signal of the Intra Cluster Medium (ICM). [Zhang et al. \(2024a\)](#) modeled galaxies according to empirical

scaling relations to clean their stacking procedure for filaments in eRASS:4. In our preliminary study, we attempted to highlight the effect of galaxies on the investigated correlations by explicitly masking the halos in the field of view. Nevertheless, we showed in Chap. 6 and 7 that our X-ray models of galaxies are in good agreement with real observations of galaxies. As such, we can self-consistently quantify galaxy contribution to the ICM instead of relying on semi-empirical modeling of e.g. XRBs.

## **Part IV**

# **Conclusions & Future Perspectives**



## 9 | Conclusion

In this work, we studied aspects of galaxy evolution and their large-scale environment using state-of-the-art hydrodynamic cosmological simulations. In particular, we focused our investigation on the X-ray properties of the hot plasma within and surrounding simulated galaxies in the *Magneticum* simulations. We derived X-ray properties by post-processing the simulation data using the virtual X-ray photon generator PHOX (Biffi et al., 2012, 2013). PHOX takes the simulation output and converts it into individual X-ray photons from idealized X-ray spectra in a Monte-Carlo-like sampling approach.

In Chap. 4, we introduced implementation details of physical models that were used to run the cosmological simulation *Magneticum*. We mainly focused on the numerical treatment of star formation and feedback from actively accreting supermassive black holes in the simulation. In Chap. 5, we presented the PHOX algorithm in more detail namely its three modules which can be executed independently of each other. Each submodule executes a unique step during a full X-ray mock observation conducted with PHOX where the first module is responsible for creating the initial photon distribution from the cosmological simulation, retaining a memory of the intrinsic properties of the X-ray emitting resolution element. The second module then performs the projection along a specified line of sight taking into account various redshift corrections to photon energies and positions. The third module completes the full mock observation and is responsible for simulating a real telescope response either by manually folding the created photon list with the corresponding response matrices or by utilizing dedicated software to simulate the telescope response such as SIXTE (Dauser et al., 2019).

For the PHOX algorithm we developed a new numerical model to include populations of both LMXB and HMXB using the stellar component of cosmological simulations which we presented in Chap. 6 (also in Vladutescu-Zopp et al., 2023). The model is calibrated to reproduce empirically derived X-ray luminosity functions of both LMXB and HMXB from the mass, age, and metallicity of a SSP. Since cosmological simulations represent the stellar component with instantaneously forming SSPs, the star formation history of a single SSP resembles a  $\delta$ -function which required estimating the number of HMXB per SSP through the SNII rate. This estimate is robust for highly star-forming galaxies but overestimates the number of HMXB for low star-formation rates. We performed various tests first confirming the correct spatial distribution for both HMXB and LMXB in simulated galaxies and their association to regions of predominantly young or old stars, respectively. Next, we verified that intrinsic luminosity functions of XRB are complete up to the flux limit of the mock observation. Scaling relations emerge self-consistently from our model where the total luminosity of HMXB scales linearly with SFR for star-forming

galaxies in the simulation and the total luminosity of LMXB scales linearly with the total stellar mass. We additionally tested a metallicity-dependent model for HMXB which also correctly reproduces the anti-correlation between metallicity and total HMXB X-ray luminosity expected from observations. We further analyzed the influence of XRB on the X-ray spectrum of simulated galaxies and found good agreement with models from the literature predicting the correct amount of XRB emission expected in various energy bands.

In a separate study, we analyzed the radial X-ray surface brightness distribution of simulated galaxies which we presented in Chap. 7 (also in [Vladutescu-Zopp et al., 2024](#)). Thanks to the modularity of the PHOX algorithm and the known properties of galaxies in the simulation, we could reliably distinguish the exact radial contribution of various sources to X-ray surface brightness profiles. As such, the contribution of XRB could be included directly in the mock observations for the first time, instead of deriving their local contribution from scaling relations. We found that XRBs mostly contribute to the radial scales of the ISM. At larger radii close to the virial radius of a galaxy, XRB nevertheless contributed about 10% of the X-ray signal on average. Furthermore, we constructed median surface brightness profiles for simulated galaxies binned by their X-ray temperature, stellar mass, and gas fraction revealing differences between SFG and QG. Focusing on the gaseous component of the simulated galaxies, we fitted  $\beta$ -profiles to the gas surface brightness revealing the underlying density structure. We found that the profile slope is steeper in simulated galaxies than in real galaxies by comparing directly with typical slopes found in the literature ([Babyk et al., 2018](#)). In addition, the slope is correlated to the simulated galaxies' overall gas fraction and the total gas luminosity. We found an additional positive correlation between the slope, gas fraction, and gas luminosity with the current accretion rate of the central SMBH indicating that the SMBH directly regulates the profile shape. We also calculated mean and median gas profiles for the MW stellar mass bin similar to the stacking results of eROSITA data in [Zhang et al. \(2024b\)](#). The median of our MW-like sample is in moderate agreement with the results in [Zhang et al. \(2024b\)](#) for the galaxy outskirts, however, our sample overestimates the central normalization and is again steeper than for the eROSITA results.

In Chap. 8 we showed a preliminary study on the X-ray emission of the ICM which was based on our work within the LEM collaboration, a future soft X-ray telescope employing microcalorimeter technology. In particular, we showed a cosmic filament connected to the second most massive clusters in *Box2/hr* of the *Magneticum* simulation. We showed that the oxygen line emission in  $O_{7(r)}$  and  $O_8$  traces the filament's underlying dark matter and galaxy distribution. We also demonstrated that the ratio of the two oxygen lines is a tracer for the temperature of the hot plasma in the filament and that a microcalorimeter would be able to distinguish between different emission models of the plasma. Our results still hold when explicitly masking the contribution from identified halos within the filament.

Overall, our proposed XRB model proved to reliably reproduce observed scaling relations of galaxies, opening a new avenue into realistic mock observations of galaxies.

# 10 | Outlook

## 10.1 Extensions of the XRB model

While the current implementation of the XRB module in PHOX already delivers promising results, a few improvements regarding the overall structure of the code can be made. In particular, the current design relies on pre-determined values for the spectral shape and empirical luminosity functions. Thus, while our model has flexibility in the choice of empirical model, the shape of the luminosity function is not a prediction of our model. Ideally, the starting point of the model would be a statistical representation of binary interaction in the SSPs of the cosmological simulations, e.g. using semi-analytic modeling of orbits and mass ratios in binary distributions (Moe & Di Stefano, 2017). However, as discussed in Chap. 3, depicting the complexity of binary interactions is rather complicated, needing a lot of additional effort for comparatively little gain given the uncertainties. A statistical approach to enhance the variety of depicted XRB sources would yield more merit following the compilation of HMXB sources in Sazonov & Khabibullin (2017b). Here, they differentiated between three different classes of luminous HMXB objects, namely hard, soft, and supersoft sources, depending on the spectral shape. A similar differentiation can be applied to our model enhancing the realism of individual HMXB systems by having more variable spectral shapes. This includes potential for line emission from the ionized plasma in and around the accretion flow of the binary of which oxygen and iron produce the most prominent lines, i.e. the Fe  $K\alpha$  line (6.4 keV).

Expanding upon the aspect of realism, a desirable feature for the projection phase in PHOX Unit 2 would be a lightweight ray tracer such that absorption or scattering in cold gas clumps local to the source could be included. Indeed, proper ray tracing of X-ray photons leads to enhanced emissivity in resonant lines (Nelson et al., 2023). The current concept behind PHOX does not allow for a direct ray tracing implementation since most of the original simulation output is discarded for the projection phase in favor of performance. Similarly, the amount of scattering expected for each source photon is difficult to estimate. Depending on the gas conditions behind the source, forward scattering or reflection of photons towards the line of sight can become more relevant. In contrast, to estimate the absorption along the line of sight, one could construct column density maps of the cold gas between the observer and the potential source externally and feed the results as an absorption column to Unit 2. While this approach would be slightly more expensive computationally, it directly reflects environmental conditions around the source.

## 10.2 Redshift evolution of XRB emission

At redshifts  $z \sim 6 - 7$  the universe entered the epoch of reionization where powerful electromagnetic radiation from the first stars and growing SMBH heated the neutral baryonic matter created after decoupling. However, the role of XRB during this epoch is unclear and it is suggested that ultra-luminous HMXB might have significantly contributed to recombination since they should have been more abundant in the highly star-forming and low-metallicity environments of the early cosmos (Sazonov & Khabibullin, 2017a; Saxena et al., 2021; Lehmer et al., 2021). Indeed, semi-analytic models showed that the total XRB emissivity varies with redshift due to the star formation and enrichment history of the universe (Fragos et al., 2013a,b; Wiktorowicz et al., 2017, 2021). Our numerical XRB model would be able to provide additional insights into the redshift dependence of their total emissivity.

Our model would place further constraints on the total XRB emissivity at high redshift in conjunction with different cosmological simulations. The modularity of our model allows for easy exchange of various stellar lifetime functions, stellar initial mass functions, and XRB luminosity functions to test out the possible parameter space. Furthermore, estimates place the contribution of XRB towards the CXB at about 10% (Dijkstra et al., 2012; Gilfanov & Merloni, 2014). Since cosmological simulations are also suited for the creation of X-ray lightcones (see e.g. Muñoz Rodríguez et al., 2023; Marini et al., 2024; Shreeram et al., 2024), a further possible application of our model is the direct estimation of the CXB from the simulations using all components currently implemented in `PHOX`. This would not only determine directly the relative contribution of the hot gas, XRB, and AGN components, but would also enable a study on the contribution of galaxies, clusters, and IGM to the soft CXB (Cappelluti et al., 2017).

## 10.3 Age dating of XRB populations

LMXB and HMXB follow the spatial distribution of old and young stars respectively. In Sec. 6.4 we demonstrated that our XRB model reflects this behavior by construction. Nevertheless, the direct association of the two XRB subclasses with the corresponding stellar age is ambiguous in observations of nearby galaxies mostly due to the limited spatial resolution of the instruments. Previous studies investigating the sub-galactic modeling of XRB emission as a function of the underlying stellar age or star formation history showed that the combined X-ray luminosity function declines with increasing stellar age and is quickly dominated by the old stellar populations (Lehmer et al., 2017; Kouroumpatzakis et al., 2020; Gilbertson et al., 2022). However, they based their analysis on population synthesis SED fitting using limited amounts of far infrared to far UV wavebands which could potentially bias the results. In light of the immense spectral and spatial resolution of the James-Webb Space Telescope (JWST), reinvestigation of these sub-galactic scales could refine and improve upon previously obtained results (Khabibullin et al., in prep.).

Our XRB model can be useful to provide a better understanding of the systematics following the underlying XRB distribution from a simulation standpoint. High-resolution zoom-in simulations of MW-like galaxies (Valentini et al., 2019) are a perfect testbed for an interdisciplinary study combining the mock X-ray and JWST-like observations. Leveraging additional examples

from the previously investigated cosmological volume would mitigate most of the uncertainties from a theoretical standpoint.

## 10.4 The X-ray bright Future of astronomy

With the age-driven decline of the currently running X-ray satellites such as *Chandra*, *XMM-Newton*, *NUSTAR*, and the shut-down of the SRG/eROSITA spacecraft, the X-ray community is waiting for the next flagship missions targeting the X-ray sky. The European Space Agency (ESA) is currently preparing for its largest X-ray facility ever to be built namely *Athena* (Barret et al., 2018) with a predicted launch window in 2037. The main science goals of *Athena* concern the assembly of structures in the universe with a particular focus on the inflow and outflow of hot gas around galaxies, groups, and clusters. A similar focus is placed on the formation and evolution of SMBH and the flow of matter in their vicinity. To reach its science goals, *Athena* will be equipped with two instruments complementing each other.

The X-ray Integral Field Unit (X-IFU) over a field of view of  $5'$  with  $5''$  pixels, achieving high spectral resolution of  $\sim 2.5$  eV in the  $0.2$ – $12$  keV energy range using microcalorimeter technology and an effective area of almost  $1\text{ m}^2$  at 1 keV (Barret et al., 2018). The Wide Field Imager (WFI) sports a large field of view of  $40' \times 40'$  and pixel size close to the on-axis angular resolution of  $5''$  and moderate spectral resolution of  $\leq 170$  eV in the  $0.2$ – $15$  keV energy range (Meidinger et al., 2020). The combined high spectral and spatial resolution of the X-IFU instrument and its large effective area will be ideal for studying individual objects, revealing the velocity structure of the CGM or the ICM. Its sensitivity also in the hard X-ray regime will be pivotal in understanding plasma properties in accretion discs around SMBH while improving our measurements of SMBH spin through reflection spectroscopy.

In the meantime, intermediate X-ray missions are scheduled to launch in the early 2030s bridging the large gap waiting for *Athena*. One such mission is the *HUBS* (Cui et al., 2020) mission which in essence shares many similarities with the LEM concept mission. The science goals are extremely similar and most studies conducted on LEM could be directly transferred to this instrument. As such, *HUBS* will be an important milestone in uncovering the processes within the hot low-density environments such as the CGM and cosmic filaments connecting galaxy clusters (Zhao et al., 2024).

Although LEM was not selected for the Phase A studies of NASA's APEX program, the Advanced X-ray Imaging Satellite (AXIS) is a still-running contender in the selection process planned to launch in the early 2030s (Reynolds et al., 2023). *AXIS* builds upon the successes of *Chandra* and improves upon many of its limitations. Compared to *Chandra* it has a much higher effective area, especially in the soft X-ray regime while retaining an almost constant high angular resolution of  $\sim 1.5''$  throughout its entire large field of view of  $24' \times 24'$ . It generally outperforms all current focusing instruments in various aspects by almost an order of magnitude, especially in grasp (field of view times effective area) and readout speed (Reynolds et al., 2023). Its enhanced sensitivity in the soft X-rays together with its high spatial resolution will be essential to discerning X-ray point sources from the diffuse plasma emission of a galaxy enabling more detailed studies of XRB populations and AGN in the center of galaxies. Especially faint XRB in

our Galaxy can be studied in much greater detail giving rise to in-depth analysis of the accretion geometry around compact stellar sources.

This thesis investigates various X-ray phenomena from a theoretical standpoint by using mock observations of cosmological simulations to explore the intrinsic X-ray properties of emerging phenomena. To this end, future X-ray missions will give new insights into unexplored physics and provide additional calibration for next-generation cosmological simulations for which our work lays the basis.

# Bibliography

- Abbott, B. P., Abbott, R., Abbott, T. D., et al. (2017a), *GW170817: Observation of Gravitational Waves from a Binary Neutron Star Inspiral*, Physical Review Letters, 119(16), 161101
- Abbott, B. P., Abbott, R., Abbott, T. D., et al. (2017b), *GW170817: Observation of Gravitational Waves from a Binary Neutron Star Inspiral*, Physical Review Letters, 119(16), 161101
- Aird, J., Coil, A. L., and Georgakakis, A. (2017), *X-rays across the galaxy population - I. Tracing the main sequence of star formation*, Monthly Notices of the RAS, 465(3), 3390
- Aird, J., Coil, A. L., Georgakakis, A., et al. (2015), *The evolution of the X-ray luminosity functions of unabsorbed and absorbed AGNs out to  $z \sim 5$* , Monthly Notices of the RAS, 451(2), 1892
- Aird, J., Nandra, K., Laird, E. S., et al. (2010), *The evolution of the hard X-ray luminosity function of AGN*, Monthly Notices of the RAS, 401(4), 2531
- Alexander, D. M., Bauer, F. E., Chapman, S. C., et al. (2005), *The X-Ray Spectral Properties of SCUBA Galaxies*, Astrophysical Journal, 632(2), 736
- Anders, E. and Grevesse, N. (1989), *Abundances of the elements: Meteoritic and solar*, Geochimica Cosmochimica Acta, 53(1), 197
- Anderson, M. E. and Bregman, J. N. (2011), *Detection of a Hot Gaseous Halo around the Giant Spiral Galaxy NGC 1961*, Astrophysical Journal, 737(1), 22
- Anderson, M. E., Bregman, J. N., and Dai, X. (2013), *Extended Hot Halos around Isolated Galaxies Observed in the ROSAT All-Sky Survey*, Astrophysical Journal, 762(2), 106
- Anderson, M. E., Gaspari, M., White, S. D. M., et al. (2015), *Unifying X-ray scaling relations from galaxies to clusters*, Monthly Notices of the RAS, 449(4), 3806
- Andrae, R., Schulze-Hartung, T., and Melchior, P. (2010), *Dos and don'ts of reduced chi-squared*, arXiv e-prints, arXiv:1012.3754
- Antoniou, V., Zezas, A., Drake, J. J., et al. (2019), *Deep Chandra Survey of the Small Magellanic Cloud. III. Formation Efficiency of High-mass X-Ray Binaries*, Astrophysical Journal, 887(1), 20

- Aragón-Calvo, M. A., van de Weygaert, R., and Jones, B. J. T. (2010), *Multiscale phenomenology of the cosmic web*, Monthly Notices of the RAS, 408(4), 2163
- Arbey, A. and Mahmoudi, F. (2021), *Dark matter and the early Universe: A review*, Progress in Particle and Nuclear Physics, 119, 103865
- Arnaud, K. A. (1996), *XSPEC: The First Ten Years*, in *Astronomical Data Analysis Software and Systems V*, edited by G. H. Jacoby, J. Barnes, volume 101 of *Astronomical Society of the Pacific Conference Series*, 17
- Arth, A., Dolag, K., Beck, A. M., et al. (2014), *Anisotropic thermal conduction in galaxy clusters with MHD in Gadget*, arXiv e-prints, arXiv:1412.6533
- Babyk, I. V., McNamara, B. R., Nulsen, P. E. J., et al. (2018), *X-Ray Scaling Relations of Early-type Galaxies*, Astrophysical Journal, 857(1), 32
- Balbus, S. A. and Hawley, J. F. (1991), *A Powerful Local Shear Instability in Weakly Magnetized Disks. I. Linear Analysis*, Astrophysical Journal, 376, 214
- Baraffe, I., Chabrier, G., Allard, F., and Hauschildt, P. H. (1998), *Evolutionary models for solar metallicity low-mass stars: mass-magnitude relationships and color-magnitude diagrams*, Astronomy and Astrophysics, 337, 403
- Barret, D., Lam Trong, T., den Herder, J.-W., et al. (2018), *The ATHENA X-ray Integral Field Unit (X-IFU)*, in *Space Telescopes and Instrumentation 2018: Ultraviolet to Gamma Ray*, edited by J.-W. A. den Herder, S. Nikzad, K. Nakazawa, volume 10699 of *Society of Photo-Optical Instrumentation Engineers (SPIE) Conference Series*, 106991G
- Beck, A. M., Murante, G., Arth, A., et al. (2016), *An improved SPH scheme for cosmological simulations*, Monthly Notices of the RAS, 455(2), 2110
- Becker, P. A. and Wolff, M. T. (2007), *Thermal and Bulk Comptonization in Accretion-powered X-Ray Pulsars*, Astrophysical Journal, 654(1), 435
- Biffi, V., Dolag, K., and Böhringer, H. (2013), *Investigating the velocity structure and X-ray observable properties of simulated galaxy clusters with PHOX*, Monthly Notices of the RAS, 428(2), 1395
- Biffi, V., Dolag, K., Böhringer, H., and Lemson, G. (2012), *Observing simulated galaxy clusters with PHOX: a novel X-ray photon simulator*, Monthly Notices of the RAS, 420(4), 3545
- Biffi, V., Dolag, K., and Merloni, A. (2018a), *AGN contamination of galaxy-cluster thermal X-ray emission: predictions for eRosita from cosmological simulations*, Monthly Notices of the RAS, 481(2), 2213
- Biffi, V., Dolag, K., Reiprich, T. H., et al. (2022), *The eROSITA view of the Abell 3391/95 field: Case study from the Magneticum cosmological simulation*, Astronomy and Astrophysics, 661, A17

- Biffi, V., Planelles, S., Borgani, S., et al. (2017), *The history of chemical enrichment in the intracluster medium from cosmological simulations*, Monthly Notices of the RAS, 468(1), 531
- Biffi, V., Planelles, S., Borgani, S., et al. (2018b), *The origin of ICM enrichment in the outskirts of present-day galaxy clusters from cosmological hydrodynamical simulations*, Monthly Notices of the RAS, 476(2), 2689
- Biffi, V., Sembolini, F., De Petris, M., et al. (2014), *The MUSIC of galaxy clusters - II. X-ray global properties and scaling relations*, Monthly Notices of the RAS, 439(1), 588
- Biffi, V. and Valdarnini, R. (2015), *The role of the artificial conductivity in SPH simulations of galaxy clusters: effects on the ICM properties*, Monthly Notices of the RAS, 446(3), 2802
- Binney, J. (1977), *The physics of dissipational galaxy formation.*, Astrophysical Journal, 215, 483
- Binney, J. and Tremaine, S. (2008), *Galactic Dynamics: Second Edition*, Princeton University Press
- Birnboim, Y. and Dekel, A. (2003), *Virial shocks in galactic haloes?*, Monthly Notices of the RAS, 345(1), 349
- Blanton, M. R., Schlegel, D. J., Strauss, M. A., et al. (2005), *New York University Value-Added Galaxy Catalog: A Galaxy Catalog Based on New Public Surveys*, Astronomical Journal, 129(6), 2562
- Bogdán, Á., Forman, W. R., Vogelsberger, M., et al. (2013), *Hot X-Ray Coronae around Massive Spiral Galaxies: A Unique Probe of Structure Formation Models*, Astrophysical Journal, 772(2), 97
- Bogdán, Á. and Gilfanov, M. (2011), *Unresolved and diffuse components of X-ray emission and X-ray-to-K-band luminosity ratios in nearby early-type and late-type galaxies*, Monthly Notices of the RAS, 418(3), 1901
- Bogdán, Á., Khabibullin, I., Kovács, O. E., et al. (2023), *Circumgalactic Medium on the Largest Scales: Detecting X-Ray Absorption Lines with Large-area Microcalorimeters*, Astrophysical Journal, 953(1), 42
- Bogdán, Á., Vogelsberger, M., Kraft, R. P., et al. (2015), *Hot Gaseous Coronae around Spiral Galaxies: Probing the Illustris Simulation*, Astrophysical Journal, 804(1), 72
- Bond, J. R., Kofman, L., and Pogosyan, D. (1996), *How filaments of galaxies are woven into the cosmic web*, Nature, 380(6575), 603
- Bondi, H. (1952), *On spherically symmetrical accretion*, Monthly Notices of the RAS, 112, 195
- Bondi, H. and Hoyle, F. (1944), *On the mechanism of accretion by stars*, Monthly Notices of the RAS, 104, 273

- Bonnor, W. B. (1956), *Boyle's Law and gravitational instability*, Monthly Notices of the RAS, 116, 351
- Booth, C. M. and Schaye, J. (2011), *Towards an understanding of the evolution of the scaling relations for supermassive black holes*, Monthly Notices of the RAS, 413(2), 1158
- Boroson, B., Kim, D.-W., and Fabbiano, G. (2011), *Revisiting with Chandra the Scaling Relations of the X-ray Emission Components (Binaries, Nuclei, and Hot Gas) of Early-type Galaxies*, Astrophysical Journal, 729(1), 12
- Bozzo, E., Falanga, M., and Stella, L. (2008), *Are There Magnetars in High-Mass X-Ray Binaries? The Case of Supergiant Fast X-Ray Transients*, Astrophysical Journal, 683(2), 1031
- Bregman, J., Cen, R., Chen, Y., et al. (2023), *Scientific objectives of the Hot Universe Baryon Surveyor (HUBS) mission*, Science China Physics, Mechanics, and Astronomy, 66(9), 299513
- Bressan, A., Marigo, P., Girardi, L., et al. (2012), *PARSEC: stellar tracks and isochrones with the PAdova and TRieste Stellar Evolution Code*, Monthly Notices of the RAS, 427(1), 127
- Brorby, M., Kaaret, P., Prestwich, A., and Mirabel, I. F. (2016), *Enhanced X-ray emission from Lyman break analogues and a possible  $L_X$ -SFR-metallicity plane*, Monthly Notices of the RAS, 457(4), 4081
- Brott, I., de Mink, S. E., Cantiello, M., et al. (2011), *Rotating massive main-sequence stars. I. Grids of evolutionary models and isochrones*, Astronomy and Astrophysics, 530, A115
- Brunner, H., Liu, T., Lamer, G., et al. (2022), *The eROSITA Final Equatorial Depth Survey (eFEDS). X-ray catalogue*, Astronomy and Astrophysics, 661, A1
- Buchner, J., Georgakakis, A., Nandra, K., et al. (2015), *Obscuration-dependent Evolution of Active Galactic Nuclei*, Astrophysical Journal, 802(2), 89
- Buchner, J., Georgakakis, A., Nandra, K., et al. (2014), *X-ray spectral modelling of the AGN obscuring region in the CDFS: Bayesian model selection and catalogue*, Astronomy and Astrophysics, 564, A125
- Buchner, J., Schulze, S., and Bauer, F. E. (2017), *Galaxy gas as obscurer - I. GRBs x-ray galaxies and find an  $N_H^3 \propto M_{\text{star}}$  relation*, Monthly Notices of the RAS, 464(4), 4545
- Bulbul, E., Randall, S. W., Bayliss, M., et al. (2016), *Probing the Outskirts of the Early-Stage Galaxy Cluster Merger A1750*, Astrophysical Journal, 818(2), 131
- Buote, D. A. (2017), *The Unusually High Halo Concentration of the Fossil Group NGC 6482: Evidence for Weak Adiabatic Contraction*, Astrophysical Journal, 834(2), 164
- Buote, D. A. and Barth, A. J. (2018), *The Luminous X-Ray Halos of Two Compact Elliptical Galaxies*, Astrophysical Journal, 854(2), 143

- Burchett, J. N., Tripp, T. M., Prochaska, J. X., et al. (2019), *The COS Absorption Survey of Baryon Harbors (CASBaH): Warm-Hot Circumgalactic Gas Reservoirs Traced by Ne VIII Absorption*, *Astrophysical Journal, Letters*, 877(2), L20
- Cappelluti, N., Li, Y., Ricarte, A., et al. (2017), *The Chandra COSMOS Legacy Survey: Energy Spectrum of the Cosmic X-Ray Background and Constraints on Undetected Populations*, *Astrophysical Journal*, 837(1), 19
- Cash, W. (1979), *Parameter estimation in astronomy through application of the likelihood ratio.*, *Astrophysical Journal*, 228, 939
- Cautun, M., van de Weygaert, R., Jones, B. J. T., and Frenk, C. S. (2014), *Evolution of the cosmic web*, *Monthly Notices of the RAS*, 441(4), 2923
- Cavaliere, A. and Fusco-Femiano, R. (1978), *The Distribution of Hot Gas in Clusters of Galaxies*, *Astronomy and Astrophysics*, 70, 677
- Cen, R. and Ostriker, J. P. (1999), *Cosmic Chemical Evolution*, *Astrophysical Journal, Letters*, 519(2), L109
- Chabrier, G. (2003), *Galactic Stellar and Substellar Initial Mass Function*, *Publications of the ASP*, 115(809), 763
- Chadayammuri, U., Bogdán, Á., Oppenheimer, B. D., et al. (2022), *Testing Galaxy Feedback Models with Resolved X-Ray Profiles of the Hot Circumgalactic Medium*, *Astrophysical Journal, Letters*, 936(1), L15
- Chatzikos, M., Bianchi, S., Camilloni, F., et al. (2023), *The 2023 Release of Cloudy*, *Revista Mexicana de Astronomía y Astrofísica*, 59, 327
- Cheng, Z., Li, Z., Xu, X., and Li, X. (2018), *A Chandra Survey of Milky Way Globular Clusters. I. Emissivity and Abundance of Weak X-Ray Sources*, *Astrophysical Journal*, 858(1), 33
- Churazov, E., Khabibullin, I., Bykov, A. M., et al. (2024), *North Polar Spur: gaseous plume(s) from star-forming regions at ~3-5 kpc from Galactic Center?*, arXiv e-prints, arXiv:2408.00752
- Churazov, E., Khabibullin, I. I., Dolag, K., et al. (2023), *Prospects of detecting soft X-ray emission from typical WHIM filaments around massive clusters and the coma cluster soft excess*, *Monthly Notices of the RAS*, 523(1), 1209
- Churazov, E., Sazonov, S., Sunyaev, R., et al. (2005), *Supermassive black holes in elliptical galaxies: switching from very bright to very dim*, *Monthly Notices of the RAS*, 363(1), L91
- Cimatti, A., Fraternali, F., and Nipoti, C. (2020), *Introduction to galaxy formation and evolution: from primordial gas to present-day galaxies*, Cambridge University Press

- Ciotti, L. and Ostriker, J. P. (2012), *AGN Feedback in Elliptical Galaxies: Numerical Simulations*, in *Astrophysics and Space Science Library*, edited by D.-W. Kim, S. Pellegrini, volume 378 of *Astrophysics and Space Science Library*, 83
- Comparat, J., Merloni, A., Salvato, M., et al. (2019), *Active galactic nuclei and their large-scale structure: an eROSITA mock catalogue*, *Monthly Notices of the RAS*, 487(2), 2005
- Comparat, J., Truong, N., Merloni, A., et al. (2022), *The eROSITA Final Equatorial Depth Survey (eFEDS). X-ray emission around star-forming and quiescent galaxies at  $0.05 < z < 0.3$* , *Astronomy and Astrophysics*, 666, A156
- Cui, W., Bregman, J. N., Bruijn, M. P., et al. (2020), *HUBS: a dedicated hot circumgalactic medium explorer*, in *Space Telescopes and Instrumentation 2020: Ultraviolet to Gamma Ray*, edited by J.-W. A. den Herder, S. Nikzad, K. Nakazawa, volume 11444 of *Society of Photo-Optical Instrumentation Engineers (SPIE) Conference Series*, 114442S
- Cui, W., Power, C., Biffi, V., et al. (2016), *How does our choice of observable influence our estimation of the centre of a galaxy cluster? Insights from cosmological simulations*, *Monthly Notices of the RAS*, 456(3), 2566
- Dage, K. C., Zepf, S. E., Peacock, M. B., et al. (2019), *X-ray spectral variability of ultraluminous X-ray sources in extragalactic globular clusters*, *Monthly Notices of the RAS*, 485(2), 1694
- Das, S., Mathur, S., and Gupta, A. (2020), *The Warm-Hot, Extended, Massive Circumgalactic Medium of NGC 3221: An XMM-Newton Discovery*, *Astrophysical Journal*, 897(1), 63
- Das, S., Mathur, S., Gupta, A., et al. (2019), *Evidence for a Massive Warm-Hot Circumgalactic Medium around NGC 3221*, *Astrophysical Journal*, 885(2), 108
- Dauser, T., Falkner, S., Lorenz, M., et al. (2019), *SIXTE: a generic X-ray instrument simulation toolkit*, *Astronomy and Astrophysics*, 630, A66
- Davé, R., Anglés-Alcázar, D., Narayanan, D., et al. (2019), *SIMBA: Cosmological simulations with black hole growth and feedback*, *Monthly Notices of the RAS*, 486(2), 2827
- Davé, R., Cen, R., Ostriker, J. P., et al. (2001), *Baryons in the Warm-Hot Intergalactic Medium*, *Astrophysical Journal*, 552(2), 473
- Davis, M., Efstathiou, G., Frenk, C. S., and White, S. D. M. (1985), *The evolution of large-scale structure in a universe dominated by cold dark matter*, *Astrophysical Journal*, 292, 371
- Di Matteo, T., Colberg, J., Springel, V., et al. (2008), *Direct Cosmological Simulations of the Growth of Black Holes and Galaxies*, *Astrophysical Journal*, 676(1), 33
- Di Matteo, T., Khandai, N., DeGraf, C., et al. (2012), *Cold Flows and the First Quasars*, *Astrophysical Journal, Letters*, 745(2), L29

- Di Matteo, T., Springel, V., and Hernquist, L. (2005), *Energy input from quasars regulates the growth and activity of black holes and their host galaxies*, *Nature*, 433(7026), 604
- Diehl, S. and Statler, T. S. (2007), *The Hot Interstellar Medium of Normal Elliptical Galaxies. I. A Chandra Gas Gallery and Comparison of X-Ray and Optical Morphology*, *Astrophysical Journal*, 668(1), 150
- Dietl, J., Pacaud, F., Reiprich, T. H., et al. (2024), *Discovery of a >13 Mpc long X-ray filament between two galaxy clusters beyond three times their virial radii*, arXiv e-prints, arXiv:2401.17281
- Dijkstra, M., Gilfanov, M., Loeb, A., and Sunyaev, R. (2012), *Constraints on the redshift evolution of the  $L_X$ -SFR relation from the cosmic X-ray backgrounds*, *Monthly Notices of the RAS*, 421(1), 213
- Dolag, K., Borgani, S., Murante, G., and Springel, V. (2009), *Substructures in hydrodynamical cluster simulations*, *Monthly Notices of the RAS*, 399(2), 497
- Dolag, K., Komatsu, E., and Sunyaev, R. (2016), *SZ effects in the Magneticum Pathfinder simulation: comparison with the Planck, SPT, and ACT results*, *Monthly Notices of the RAS*, 463(2), 1797
- Dolag, K., Mevius, E., and Remus, R.-S. (2017), *Distribution and Evolution of Metals in the Magneticum Simulations*, *Galaxies*, 5(3), 35
- Dolag, K., Vazza, F., Brunetti, G., and Tormen, G. (2005), *Turbulent gas motions in galaxy cluster simulations: the role of smoothed particle hydrodynamics viscosity*, *Monthly Notices of the RAS*, 364(3), 753
- Donahue, M. and Voit, G. M. (2022), *Baryon cycles in the biggest galaxies*, *Physics Reports*, 973, 1
- Done, C., Davis, S. W., Jin, C., et al. (2012), *Intrinsic disc emission and the soft X-ray excess in active galactic nuclei*, *Monthly Notices of the RAS*, 420(3), 1848
- Done, C., Gierliński, M., and Kubota, A. (2007), *Modelling the behaviour of accretion flows in X-ray binaries. Everything you always wanted to know about accretion but were afraid to ask*, *Astronomy and Astrophysics Reviews*, 15(1), 1
- Dopita, M. A. and Sutherland, R. S. (2003), *Astrophysics of the diffuse universe*, Springer
- Ebert, R. (1955), *Über die Verdichtung von H I-Gebieten. Mit 5 Textabbildungen*, *Zeitschrift fuer Astrophysik*, 37, 217
- Eckert, D., Gaspari, M., Gastaldello, F., et al. (2021), *Feedback from Active Galactic Nuclei in Galaxy Groups*, *Universe*, 7(5), 142
- Eckert, D., Jauzac, M., Shan, H., et al. (2015), *Warm-hot baryons comprise 5-10 per cent of filaments in the cosmic web*, *Nature*, 528(7580), 105

- Eggenberger, P., Ekström, S., Georgy, C., et al. (2021), *Grids of stellar models with rotation. VI. Models from 0.8 to 120  $M_{\odot}$  at a metallicity  $Z = 0.006$* , *Astronomy and Astrophysics*, 652, A137
- Eggleton, P. P. (1983), *Approximations to the radii of Roche lobes.*, *Astrophysical Journal*, 268, 368
- Eker, Z., Soyduğan, F., Soyduğan, E., et al. (2015), *Main-Sequence Effective Temperatures from a Revised Mass-Luminosity Relation Based on Accurate Properties*, *Astronomical Journal*, 149(4), 131
- Ekström, S., Georgy, C., Eggenberger, P., et al. (2012), *Grids of stellar models with rotation. I. Models from 0.8 to 120  $M_{\odot}$  at solar metallicity ( $Z = 0.014$ )*, *Astronomy and Astrophysics*, 537, A146
- Elbaz, D., Daddi, E., Le Borgne, D., et al. (2007), *The reversal of the star formation-density relation in the distant universe*, *Astronomy and Astrophysics*, 468(1), 33
- Fabbiano, G. (1989), *X-rays from normal galaxies.*, *Annual Review of Astron and Astrophys*, 27, 87
- Fabbiano, G. (2006), *Populations of X-Ray Sources in Galaxies*, *Annual Review of Astron and Astrophys*, 44(1), 323
- Fabbiano, G. (2019), *X-Rays from Galaxies*, in *The Chandra X-ray Observatory*, edited by B. Wilkes, W. Tucker, 7–1, IOP Publishing
- Fabian, A. C. (2012), *Observational Evidence of Active Galactic Nuclei Feedback*, *Annual Review of Astron and Astrophys*, 50, 455
- Fabian, A. C., Sanders, J. S., Taylor, G. B., and Allen, S. W. (2005), *A deep Chandra observation of the Centaurus cluster: bubbles, filaments and edges*, *Monthly Notices of the RAS*, 360(1), L20
- Fabjan, D., Borgani, S., Tornatore, L., et al. (2010), *Simulating the effect of active galactic nuclei feedback on the metal enrichment of galaxy clusters*, *Monthly Notices of the RAS*, 401(3), 1670
- Faerman, Y., Sternberg, A., and McKee, C. F. (2017), *Massive Warm/Hot Galaxy Coronae as Probed by UV/X-Ray Oxygen Absorption and Emission. I. Basic Model*, *Astrophysical Journal*, 835(1), 52
- Faerman, Y., Sternberg, A., and McKee, C. F. (2020), *Massive Warm/Hot Galaxy Coronae. II. Isentropic Model*, *Astrophysical Journal*, 893(1), 82
- Fall, S. M. and Efstathiou, G. (1980), *Formation and rotation of disc galaxies with haloes.*, *Monthly Notices of the RAS*, 193, 189

- Faucher-Giguère, C.-A. and Oh, S. P. (2023), *Key Physical Processes in the Circumgalactic Medium*, Annual Review of Astron and Astrophys, 61, 131
- Ferland, G. J., Chatzikos, M., Guzmán, F., et al. (2017), *The 2017 Release Cloudy*, Revista Mexicana de Astronomía y Astrofísica, 53, 385
- Ferland, G. J., Korista, K. T., Verner, D. A., et al. (1998), *CLOUDY 90: Numerical Simulation of Plasmas and Their Spectra*, Publications of the ASP, 110(749), 761
- Ferland, G. J., Porter, R. L., van Hoof, P. A. M., et al. (2013), *The 2013 Release of Cloudy*, Revista Mexicana de Astronomía y Astrofísica, 49, 137
- Forbes, D. A., Alabi, A., Romanowsky, A. J., et al. (2017), *The SLUGGS survey: revisiting the correlation between X-ray luminosity and total mass of massive early-type galaxies*, Monthly Notices of the RAS, 464(1), L26
- Foreman-Mackey, D., Hogg, D. W., Lang, D., and Goodman, J. (2013), *emcee: The MCMC Hammer*, Publications of the ASP, 125(925), 306
- Forman, W., Jones, C., Cominsky, L., et al. (1978), *The fourth Uhuru catalog of X-ray sources.*, Astrophysical Journal, Supplement, 38, 357
- Fornasini, F. M., Antoniou, V., and Dubus, G. (2023), *High-mass X-ray Binaries*, arXiv e-prints, arXiv:2308.02645
- Fornasini, F. M., Civano, F., and Suh, H. (2020), *Connecting the metallicity dependence and redshift evolution of high-mass X-ray binaries*, Monthly Notices of the RAS, 495(1), 771
- Fragos, T., Lehmer, B., Tremmel, M., et al. (2013a), *X-Ray Binary Evolution Across Cosmic Time*, Astrophysical Journal, 764(1), 41
- Fragos, T., Lehmer, B. D., Naoz, S., et al. (2013b), *Energy Feedback from X-Ray Binaries in the Early Universe*, Astrophysical Journal, Letters, 776(2), L31
- Frank, J., King, A., and Raine, D. J. (2002), *Accretion Power in Astrophysics: Third Edition*, Cambridge University Press
- Frenk, C. S., White, S. D. M., Davis, M., and Efstathiou, G. (1988), *The Formation of Dark Halos in a Universe Dominated by Cold Dark Matter*, Astrophysical Journal, 327, 507
- Frenk, C. S., White, S. D. M., Efstathiou, G., and Davis, M. (1985), *Cold dark matter, the structure of galactic haloes and the origin of the Hubble sequence*, Nature, 317(6038), 595
- Galárraga-Espinosa, D., Aghanim, N., Langer, M., et al. (2020), *Populations of filaments from the distribution of galaxies in numerical simulations*, Astronomy and Astrophysics, 641, A173

- Galárraga-Espinosa, D., Aghanim, N., Langer, M., and Tanimura, H. (2021), *Properties of gas phases around cosmic filaments at  $z = 0$  in the IllustrisTNG simulation*, *Astronomy and Astrophysics*, 649, A117
- Galárraga-Espinosa, D., Cadiou, C., Gouin, C., et al. (2024), *Evolution of cosmic filaments in the MTNG simulation*, *Astronomy and Astrophysics*, 684, A63
- Galárraga-Espinosa, D., Langer, M., and Aghanim, N. (2022), *Relative distribution of dark matter, gas, and stars around cosmic filaments in the IllustrisTNG simulation*, *Astronomy and Astrophysics*, 661, A115
- Gardini, A., Rasia, E., Mazzotta, P., et al. (2004), *Simulating Chandra observations of galaxy clusters*, *Monthly Notices of the RAS*, 351(2), 505
- Garofali, K., Lehmer, B. D., Basu-Zych, A., et al. (2020), *On the X-Ray Spectral Energy Distributions of Star-forming Galaxies: The 0.3-30 keV Spectrum of the Low-metallicity Starburst Galaxy VV 114*, *Astrophysical Journal*, 903(2), 79
- Garofali, K., Williams, B. F., Hillis, T., et al. (2018), *Formation time-scales for high-mass X-ray binaries in M33*, *Monthly Notices of the RAS*, 479(3), 3526
- Gaspari, M., Eckert, D., Etti, S., et al. (2019), *The X-Ray Halo Scaling Relations of Supermassive Black Holes*, *Astrophysical Journal*, 884(2), 169
- Georgakakis, A., Nandra, K., Laird, E. S., et al. (2008), *A new method for determining the sensitivity of X-ray imaging observations and the X-ray number counts*, *Monthly Notices of the RAS*, 388(3), 1205
- Giacconi, R., Branduardi, G., Briel, U., et al. (1979), *The Einstein (HEAO 2) X-ray Observatory.*, *Astrophysical Journal*, 230, 540
- Giacconi, R., Gursky, H., Paolini, F. R., and Rossi, B. B. (1962), *Evidence for x Rays From Sources Outside the Solar System*, *Physical Review Letters*, 9(11), 439
- Giacconi, R., Kellogg, E., Gorenstein, P., et al. (1971), *An X-Ray Scan of the Galactic Plane from UHURU*, *Astrophysical Journal, Letters*, 165, L27
- Gilbertson, W., Lehmer, B. D., Doore, K., et al. (2022), *The Stellar-age Dependence of X-Ray Emission from Normal Star-forming Galaxies in the GOODS Fields*, *Astrophysical Journal*, 926(1), 28
- Gilfanov, M. (2004), *Low-mass X-ray binaries as a stellar mass indicator for the host galaxy*, *Monthly Notices of the RAS*, 349(1), 146
- Gilfanov, M., Fabbiano, G., Lehmer, B., and Zezas, A. (2022), *X-Ray Binaries in External Galaxies*, in *Handbook of X-ray and Gamma-ray Astrophysics*, edited by C. Bambi, A. Sanganello, 105, Springer

- Gilfanov, M., Grimm, H. J., and Sunyaev, R. (2004a), *L<sub>X</sub>-SFR relation in star-forming galaxies*, Monthly Notices of the RAS, 347(3), L57
- Gilfanov, M., Grimm, H. J., and Sunyaev, R. (2004b), *Statistical properties of the combined emission of a population of discrete sources: astrophysical implications*, Monthly Notices of the RAS, 351(4), 1365
- Gilfanov, M. and Merloni, A. (2014), *Observational Appearance of Black Holes in X-Ray Binaries and AGN*, Space Science Reviews, 183(1-4), 121
- Gilli, R., Comastri, A., and Hasinger, G. (2007), *The synthesis of the cosmic X-ray background in the Chandra and XMM-Newton era*, Astronomy and Astrophysics, 463(1), 79
- Goulding, A. D., Greene, J. E., Ma, C.-P., et al. (2016), *The MASSIVE Survey. IV. The X-ray Halos of the Most Massive Early-type Galaxies in the Nearby Universe*, Astrophysical Journal, 826(2), 167
- Greco, J. P., Hill, J. C., Spergel, D. N., and Battaglia, N. (2015), *The Stacked Thermal Sunyaev-Zel'dovich Signal of Locally Brightest Galaxies in Planck Full Mission Data: Evidence for Galaxy Feedback?*, Astrophysical Journal, 808(2), 151
- Grimm, H. J., Gilfanov, M., and Sunyaev, R. (2003), *High-mass X-ray binaries as a star formation rate indicator in distant galaxies*, Monthly Notices of the RAS, 339(3), 793
- Grindlay, J. E., Hertz, P., Steiner, J. E., et al. (1984), *Determination of the mass of globular cluster X-ray sources.*, Astrophysical Journal, Letters, 282, L13
- Gunn, J. E., Siegmund, W. A., Mannery, E. J., et al. (2006), *The 2.5 m Telescope of the Sloan Digital Sky Survey*, Astronomical Journal, 131(4), 2332
- Günther, H. M., Schmitt, J. H. M. M., Robrade, J., and Liefke, C. (2007), *X-ray emission from classical T Tauri stars: accretion shocks and coronae?*, Astronomy and Astrophysics, 466(3), 1111
- Haardt, F. and Madau, P. (2001), *Modelling the UV/X-ray cosmic background with CUBA*, in *Clusters of Galaxies and the High Redshift Universe Observed in X-rays*, edited by D. M. Neumann, J. T. V. Tran, 64
- Haberl, F. and Sturm, R. (2016), *High-mass X-ray binaries in the Small Magellanic Cloud*, Astronomy and Astrophysics, 586, A81
- Harris, D. E. (1990), *The Einstein Observatory Catalog of IPC X-ray Sources*
- Harrison, F. A., Craig, W. W., Christensen, F. E., et al. (2013), *The Nuclear Spectroscopic Telescope Array (NuSTAR) High-energy X-Ray Mission*, Astrophysical Journal, 770(2), 103
- Hasinger, G. (2008), *Absorption properties and evolution of active galactic nuclei*, Astronomy and Astrophysics, 490(3), 905

- Hickox, R. C. and Alexander, D. M. (2018), *Obscured Active Galactic Nuclei*, Annual Review of Astron and Astrophys, 56, 625
- Hickox, R. C. and Markevitch, M. (2006), *Absolute Measurement of the Unresolved Cosmic X-Ray Background in the 0.5-8 keV Band with Chandra*, Astrophysical Journal, 645(1), 95
- Hirschmann, M., Dolag, K., Saro, A., et al. (2014), *Cosmological simulations of black hole growth: AGN luminosities and downsizing*, Monthly Notices of the RAS, 442(3), 2304
- Hopkins, P. F., Richards, G. T., and Hernquist, L. (2007), *An Observational Determination of the Bolometric Quasar Luminosity Function*, Astrophysical Journal, 654(2), 731
- Hou, M., He, L., Hu, Z., et al. (2024), *X-Ray Constraints on the Hot Gaseous Corona of Edge-on Late-type Galaxies in Virgo*, Astrophysical Journal, 961(2), 249
- Hoyle, F. and Lyttleton, R. A. (1939), *The effect of interstellar matter on climatic variation*, Proceedings of the Cambridge Philosophical Society, 35(3), 405
- Hubble, E. (1929), *A Relation between Distance and Radial Velocity among Extra-Galactic Nebulae*, Proceedings of the National Academy of Science, 15(3), 168
- Humphrey, P. J., Buote, D. A., Canizares, C. R., et al. (2011), *A Census of Baryons and Dark Matter in an Isolated, Milky Way Sized Elliptical Galaxy*, Astrophysical Journal, 729(1), 53
- Humphrey, P. J., Buote, D. A., O'Sullivan, E., and Ponman, T. J. (2012), *The ELIXr Galaxy Survey. II. Baryons and Dark Matter in an Isolated Elliptical Galaxy*, Astrophysical Journal, 755(2), 166
- Iben, Icko, J. (2013a), *Stellar Evolution Physics, Volume 1: Physical Processes in Stellar Interiors*, Cambridge University Press
- Iben, Icko, J. (2013b), *Stellar Evolution Physics, Volume 2: Advanced Evolution of Single Stars*, Cambridge University Press
- Ilc, S., Fabjan, D., Rasia, E., et al. (2024), *Properties of the diffuse gas component in filaments detected in the Dianoga cosmological simulations*, Astronomy and Astrophysics, 690, A32
- Inoue, Y., Yabe, K., and Ueda, Y. (2021), *A fundamental plane in X-ray binary activity of external galaxies*, Publications of the ASJ, 73(5), 1315
- Irwin, J. A. (2005), *The Birthplace of Low-Mass X-Ray Binaries: Field Versus Globular Cluster Populations*, Astrophysical Journal, 631(1), 511
- Jansen, F., Lumb, D., Altieri, B., et al. (2001), *XMM-Newton observatory. I. The spacecraft and operations*, Astronomy and Astrophysics, 365, L1
- Jubelgas, M., Springel, V., and Dolag, K. (2004), *Thermal conduction in cosmological SPH simulations*, Monthly Notices of the RAS, 351(2), 423

- Kaastra, J. S. and Mewe, R. (1993), *X-ray emission from thin plasmas. I - Multiple Auger ionisation and fluorescence processes for Be to Zn*, *Astronomy and Astrophysics, Supplement*, 97(2), 443
- Kataoka, J., Yamamoto, M., Nakamura, Y., et al. (2021), *Origin of Galactic Spurs: New Insight from Radio/X-Ray All-sky Maps*, *Astrophysical Journal*, 908(1), 14
- Katz, N. (1992), *Dissipational Galaxy Formation. II. Effects of Star Formation*, *Astrophysical Journal*, 391, 502
- Katz, N., Weinberg, D. H., and Hernquist, L. (1996), *Cosmological Simulations with TreeSPH*, *Astrophysical Journal, Supplement*, 105, 19
- Kaviraj, S., Laigle, C., Kimm, T., et al. (2017), *The Horizon-AGN simulation: evolution of galaxy properties over cosmic time*, *Monthly Notices of the RAS*, 467(4), 4739
- Kennicutt, Robert C., J. (1998), *The Global Schmidt Law in Star-forming Galaxies*, *Astrophysical Journal*, 498(2), 541
- Khabibullin, I. and Churazov, E. (2019), *X-ray emission from warm-hot intergalactic medium: the role of resonantly scattered cosmic X-ray background*, *Monthly Notices of the RAS*, 482(4), 4972
- Khabibullin, I., Galeazzi, M., Bogdan, A., et al. (2023), *LEM All-Sky Survey: Soft X-ray Sky at Microcalorimeter Resolution*, arXiv e-prints, arXiv:2310.16038
- Kim, D.-W. and Fabbiano, G. (2013), *X-Ray Scaling Relation in Early-type Galaxies: Dark Matter as a Primary Factor in Retaining Hot Gas*, *Astrophysical Journal*, 776(2), 116
- Kim, D.-W. and Fabbiano, G. (2015), *X-Ray Scaling Relations of 'Core' and 'Coreless' E and S0 Galaxies*, *Astrophysical Journal*, 812(2), 127
- Kim, D. W., Fabbiano, G., Brassington, N. J., et al. (2009), *Comparing GC and Field LMXBs in Elliptical Galaxies with Deep Chandra and Hubble Data*, *Astrophysical Journal*, 703(1), 829
- Kim, D. W., Fabbiano, G., Ivanova, N., et al. (2013), *Metallicity Effect on Low-mass X-Ray Binary Formation in Globular Clusters*, *Astrophysical Journal*, 764(1), 98
- Kim, D.-W., Traynor, L., Paggi, A., et al. (2020), *Temperature profiles of hot gas in early-type galaxies*, *Monthly Notices of the RAS*, 492(2), 2095
- Kimmig, L. C., Remus, R.-S., Seidel, B., et al. (2023), *Blowing out the Candle: How to Quench Galaxies at High Redshift – an Ensemble of Rapid Starbursts, AGN Feedback and Environment*, arXiv e-prints, arXiv:2310.16085
- Kippenhahn, R. and Weigert, A. (1967), *Entwicklung in engen Doppelsternsystemen I. Masse-naustausch vor und nach Beendigung des zentralen Wasserstoff-Brennens*, *Zeitschrift fuer Astrophysik*, 65, 251

- Kollmeier, J., Anderson, S. F., Blanc, G. A., et al. (2019), *SDSS-V Pioneering Panoptic Spectroscopy*, in *Bulletin of the American Astronomical Society*, volume 51, 274
- Komatsu, E., Smith, K. M., Dunkley, J., et al. (2011), *Seven-year Wilkinson Microwave Anisotropy Probe (WMAP) Observations: Cosmological Interpretation*, *Astrophysical Journal, Supplement*, 192(2), 18
- Kormendy, J. and Ho, L. C. (2013), *Coevolution (Or Not) of Supermassive Black Holes and Host Galaxies*, *Annual Review of Astron and Astrophys*, 51(1), 511
- Koulouridis, E., Faccioli, L., Le Brun, A. M. C., et al. (2018), *The XXL Survey. XIX. A realistic population of simulated X-ray AGN: Comparison of models with observations*, *Astronomy and Astrophysics*, 620, A4
- Kouroumpatzakis, K., Zezas, A., Sell, P., et al. (2020), *Sub-galactic scaling relations between X-ray luminosity, star formation rate, and stellar mass*, *Monthly Notices of the RAS*, 494(4), 5967
- Kraft, R., Markevitch, M., Kilbourne, C., et al. (2022), *Line Emission Mapper (LEM): Probing the physics of cosmic ecosystems*, arXiv e-prints, arXiv:2211.09827
- Kravtsov, A. V. and Borgani, S. (2012), *Formation of Galaxy Clusters*, *Annual Review of Astron and Astrophys*, 50, 353
- Kravtsov, A. V., Klypin, A. A., and Khokhlov, A. M. (1997), *Adaptive Refinement Tree: A New High-Resolution N-Body Code for Cosmological Simulations*, *Astrophysical Journal, Supplement*, 111(1), 73
- Kremer, K., Chatterjee, S., Rodriguez, C. L., and Rasio, F. A. (2018), *Accreting Black Hole Binaries in Globular Clusters*, *Astrophysical Journal*, 852(1), 29
- Kruckow, M. U., Tauris, T. M., Langer, N., et al. (2018), *Progenitors of gravitational wave mergers: binary evolution with the stellar grid-based code COMBINE*, *Monthly Notices of the RAS*, 481(2), 1908
- Kudritzki, R.-P. and Puls, J. (2000), *Winds from Hot Stars*, *Annual Review of Astron and Astrophys*, 38, 613
- Kudritzki, R.-P., Teklu, A. F., Schulze, F., et al. (2021), *Galaxy Look-back Evolution Models: A Comparison with Magneticum Cosmological Simulations and Observations*, *Astrophysical Journal*, 910(2), 87
- Kyritsis, E., Zezas, A., Haberl, F., et al. (2024), *The first all-sky survey of star-forming galaxies with eROSITA: Scaling relations and a population of X-ray luminous starbursts*, arXiv e-prints, arXiv:2402.12367

- Lehmer, B. D., Alexander, D. M., Bauer, F. E., et al. (2010), *A Chandra Perspective on Galaxy-wide X-ray Binary Emission and its Correlation with Star Formation Rate and Stellar Mass: New Results from Luminous Infrared Galaxies*, *Astrophysical Journal*, 724(1), 559
- Lehmer, B. D., Basu-Zych, A. R., Mineo, S., et al. (2016), *The Evolution of Normal Galaxy X-Ray Emission through Cosmic History: Constraints from the 6 MS Chandra Deep Field-South*, *Astrophysical Journal*, 825(1), 7
- Lehmer, B. D., Berkeley, M., Zezas, A., et al. (2014), *The X-Ray Luminosity Functions of Field Low-mass X-Ray Binaries in Early-type Galaxies: Evidence for a Stellar Age Dependence*, *Astrophysical Journal*, 789(1), 52
- Lehmer, B. D., Eufrasio, R. T., Basu-Zych, A., et al. (2021), *The Metallicity Dependence of the High-mass X-Ray Binary Luminosity Function*, *Astrophysical Journal*, 907(1), 17
- Lehmer, B. D., Eufrasio, R. T., Basu-Zych, A., et al. (2022), *Elevated Hot Gas and High-mass X-Ray Binary Emission in Low-metallicity Galaxies: Implications for Nebular Ionization and Intergalactic Medium Heating in the Early Universe*, *Astrophysical Journal*, 930(2), 135
- Lehmer, B. D., Eufrasio, R. T., Markwardt, L., et al. (2017), *On the Spatially Resolved Star Formation History in M51. II. X-Ray Binary Population Evolution*, *Astrophysical Journal*, 851(1), 11
- Lehmer, B. D., Eufrasio, R. T., Tzanavaris, P., et al. (2019), *X-Ray Binary Luminosity Function Scaling Relations for Local Galaxies Based on Subgalactic Modeling*, *Astrophysical Journal*, Supplement, 243(1), 3
- Lehmer, B. D., Ferrell, A. P., Doore, K., et al. (2020), *X-Ray Binary Luminosity Function Scaling Relations in Elliptical Galaxies: Evidence for Globular Cluster Seeding of Low-mass X-Ray Binaries in Galactic Fields*, *Astrophysical Journal*, Supplement, 248(2), 31
- Lehmer, B. D., Tyler, J. B., Hornschemeier, A. E., et al. (2015), *The 0.3-30 keV Spectra of Powerful Starburst Galaxies: NuSTAR and Chandra Observations of NGC 3256 and NGC 3310*, *Astrophysical Journal*, 806(1), 126
- Lemaître, G. (1931), *A homogeneous universe of constant mass and increasing radius accounting for the radial velocity of extra-galactic nebulae*, *Monthly Notices of the RAS*, 91, 483
- Lemaître, G. (1933), *L'Univers en expansion*, *Annales de la Société Scientifique de Bruxelles*, 53, 51
- Lewin, W. H. G. and van der Klis, M. (2006), *Compact Stellar X-ray Sources*, volume 39, Cambridge University Press
- Lewin, W. H. G., van Paradijs, J., and van den Heuvel, E. P. J., editors (1995), *X-ray binaries*

- Li, J.-T., Bregman, J. N., Wang, Q. D., et al. (2018), *Baryon Budget of the Hot Circumgalactic Medium of Massive Spiral Galaxies*, *Astrophysical Journal, Letters*, 855(2), L24
- Li, J.-T., Bregman, J. N., Wang, Q. D., et al. (2017), *The Circum-Galactic Medium of Massive Spirals. II. Probing the Nature of Hot Gaseous Halo around the Most Massive Isolated Spiral Galaxies*, *Astrophysical Journal, Supplement*, 233(2), 20
- Li, J.-T. and Wang, Q. D. (2013), *Chandra survey of nearby highly inclined disc galaxies - II. Correlation analysis of galactic coronal properties*, *Monthly Notices of the RAS*, 435(4), 3071
- Linden, T., Kalogera, V., Sepinsky, J. F., et al. (2010), *The Effect of Starburst Metallicity on Bright X-ray Binary Formation Pathways*, *Astrophysical Journal*, 725(2), 1984
- Liske, J., Baldry, I. K., Driver, S. P., et al. (2015), *Galaxy And Mass Assembly (GAMA): end of survey report and data release 2*, *Monthly Notices of the RAS*, 452(2), 2087
- Liu, A., Bulbul, E., Ghirardini, V., et al. (2022a), *The eROSITA Final Equatorial-Depth Survey (eFEDS). Catalog of galaxy clusters and groups*, *Astronomy and Astrophysics*, 661, A2
- Liu, T., Buchner, J., Nandra, K., et al. (2022b), *The eROSITA Final Equatorial-Depth Survey (eFEDS). The AGN catalog and its X-ray spectral properties*, *Astronomy and Astrophysics*, 661, A5
- Longair, M. S. (2011), *High Energy Astrophysics*, Cambridge University Press
- Lotz, M., Dolag, K., Remus, R.-S., and Burkert, A. (2021), *Rise and fall of post-starburst galaxies in Magneticum Pathfinder*, *Monthly Notices of the RAS*, 506(3), 4516
- Lotz, M., Remus, R.-S., Dolag, K., et al. (2019), *Gone after one orbit: How cluster environments quench galaxies*, *Monthly Notices of the RAS*, 488(4), 5370
- Lovisari, L., Etti, S., Gaspari, M., and Giles, P. A. (2021), *Scaling Properties of Galaxy Groups*, *Universe*, 7(5), 139
- Lovisari, L., Reiprich, T. H., and Schellenberger, G. (2015), *Scaling properties of a complete X-ray selected galaxy group sample*, *Astronomy and Astrophysics*, 573, A118
- Lynden-Bell, D. (1967), *Statistical mechanics of violent relaxation in stellar systems*, *Monthly Notices of the RAS*, 136, 101
- Madau, P. and Fragos, T. (2017), *Radiation Backgrounds at Cosmic Dawn: X-Rays from Compact Binaries*, *Astrophysical Journal*, 840(1), 39
- Maeder, A. and Meynet, G. (1989), *Grids of evolutionary models from 0.85 to 120M : observational tests and the mass limits.*, *Astronomy and Astrophysics*, 210, 155
- Magdziarz, P. and Zdziarski, A. A. (1995), *Angle-dependent Compton reflection of X-rays and gamma-rays*, *Monthly Notices of the RAS*, 273(3), 837

- Maio, U., Ciardi, B., Dolag, K., et al. (2010), *The transition from population III to population II-I star formation*, Monthly Notices of the RAS, 407(2), 1003
- Maio, U., Dolag, K., Ciardi, B., and Tornatore, L. (2007), *Metal and molecule cooling in simulations of structure formation*, Monthly Notices of the RAS, 379(3), 963
- Malavasi, N., Aghanim, N., Douspis, M., et al. (2020), *Characterising filaments in the SDSS volume from the galaxy distribution*, Astronomy and Astrophysics, 642, A19
- Mapelli, M., Colpi, M., and Zampieri, L. (2009), *Low metallicity and ultra-luminous X-ray sources in the Cartwheel galaxy*, Monthly Notices of the RAS, 395(1), L71
- Marchant, P. and Bodensteiner, J. (2024), *The Evolution of Massive Binary Stars*, Annual Review of Astron and Astrophys, 62(1), 21
- Marconi, A., Risaliti, G., Gilli, R., et al. (2004), *Local supermassive black holes, relics of active galactic nuclei and the X-ray background*, Monthly Notices of the RAS, 351(1), 169
- Marini, I., Popesso, P., Lamer, G., et al. (2024), *Detecting galaxy groups populating the local Universe in the eROSITA era*, Astronomy and Astrophysics, 689, A7
- Marsh, T. R. and Horne, K. (1990), *Emission-Line Mapping of the Dwarf Nova IP Pegasi in Outburst and Quiescence*, Astrophysical Journal, 349, 593
- Martínez-Núñez, S., Kretschmar, P., Bozzo, E., et al. (2017), *Towards a Unified View of Inhomogeneous Stellar Winds in Isolated Supergiant Stars and Supergiant High Mass X-Ray Binaries*, Space Science Reviews, 212(1-2), 59
- Martizzi, D., Vogelsberger, M., Artale, M. C., et al. (2019), *Baryons in the Cosmic Web of IllustrisTNG - I: gas in knots, filaments, sheets, and voids*, Monthly Notices of the RAS, 486(3), 3766
- Massey, R., Kitching, T., and Richard, J. (2010), *The dark matter of gravitational lensing*, Reports on Progress in Physics, 73(8), 086901
- Mathur, S., Gupta, A., Das, S., et al. (2021), *Probing the Hot Circumgalactic Medium with Broad O VI and X-Rays*, Astrophysical Journal, 908(1), 69
- McCammon, D., Almy, R., Apodaca, E., et al. (2002), *A High Spectral Resolution Observation of the Soft X-Ray Diffuse Background with Thermal Detectors*, Astrophysical Journal, 576(1), 188
- McConnell, N. J. and Ma, C.-P. (2013), *Revisiting the Scaling Relations of Black Hole Masses and Host Galaxy Properties*, Astrophysical Journal, 764(2), 184
- McIntosh, A. (2016), *The Jackknife Estimation Method*, arXiv e-prints, arXiv:1606.00497

- Meidinger, N., Albrecht, S., Beitler, C., et al. (2020), *Development status of the wide field imager instrument for Athena*, in *Space Telescopes and Instrumentation 2020: Ultraviolet to Gamma Ray*, edited by J.-W. A. den Herder, S. Nikzad, K. Nakazawa, volume 11444 of *Society of Photo-Optical Instrumentation Engineers (SPIE) Conference Series*, 114440T
- Merloni, A., Bongiorno, A., Brusa, M., et al. (2014), *The incidence of obscuration in active galactic nuclei*, *Monthly Notices of the RAS*, 437(4), 3550
- Merloni, A., Lamer, G., Liu, T., et al. (2024), *The SRG/eROSITA all-sky survey. First X-ray catalogues and data release of the western Galactic hemisphere*, *Astronomy and Astrophysics*, 682, A34
- Mernier, F., Biffi, V., Yamaguchi, H., et al. (2018), *Enrichment of the Hot Intracluster Medium: Observations*, *Space Science Reviews*, 214(8), 129
- Mernier, F., Su, Y., Markevitch, M., et al. (2023), *Exploring chemical enrichment of the intra-cluster medium with the Line Emission Mapper*, arXiv e-prints, arXiv:2310.04499
- Miller, M. J. and Bregman, J. N. (2015), *Constraining the Milky Way's Hot Gas Halo with O VII and O VIII Emission Lines*, *Astrophysical Journal*, 800(1), 14
- Mineo, S., Fabbiano, G., D'Abrusco, R., et al. (2014a), *The Radial Distribution of X-Ray Binaries and Globular Clusters in NGC 4649 and their Relation with the Local Stellar Mass Density*, *Astrophysical Journal*, 780(2), 132
- Mineo, S., Gilfanov, M., Lehmer, B. D., et al. (2014b), *X-ray emission from star-forming galaxies - III. Calibration of the  $L_X$ -SFR relation up to redshift  $z \approx 1.3$* , *Monthly Notices of the RAS*, 437(2), 1698
- Mineo, S., Gilfanov, M., and Sunyaev, R. (2012a), *X-ray emission from star-forming galaxies - I. High-mass X-ray binaries*, *Monthly Notices of the RAS*, 419(3), 2095
- Mineo, S., Gilfanov, M., and Sunyaev, R. (2012b), *X-ray emission from star-forming galaxies - II. Hot interstellar medium*, *Monthly Notices of the RAS*, 426(3), 1870
- Mo, H., van den Bosch, F. C., and White, S. (2010), *Galaxy Formation and Evolution*, Cambridge University Press
- Moe, M. and Di Stefano, R. (2017), *Mind Your Ps and Qs: The Interrelation between Period (P) and Mass-ratio (Q) Distributions of Binary Stars*, *Astrophysical Journal, Supplement*, 230(2), 15
- Morrison, R. and McCammon, D. (1983), *Interstellar photoelectric absorption cross sections, 0.03-10 keV.*, *Astrophysical Journal*, 270, 119
- Muñoz Rodríguez, I., Georgakakis, A., Shankar, F., et al. (2023), *Cosmic evolution of the incidence of active galactic nuclei in massive clusters: simulations versus observations*, *Monthly Notices of the RAS*, 518(1), 1041

- Murante, G., Monaco, P., Borgani, S., et al. (2015), *Simulating realistic disc galaxies with a novel sub-resolution ISM model*, Monthly Notices of the RAS, 447(1), 178
- Mushtukov, A. and Tsygankov, S. (2022), *Accreting strongly magnetised neutron stars: X-ray Pulsars*, arXiv e-prints, arXiv:2204.14185
- Navarro, J. F., Frenk, C. S., and White, S. D. M. (1996), *The Structure of Cold Dark Matter Halos*, Astrophysical Journal, 462, 563
- Navarro, J. F. and White, S. D. M. (1993), *Simulations of Dissipative Galaxy Formation in Hierarchically Clustering Universes - Part One - Tests of the Code*, Monthly Notices of the RAS, 265, 271
- Nebot Gómez-Morán, A. and Oskinova, L. M. (2018), *The X-ray catalog of spectroscopically identified Galactic O stars. Investigating the dependence of X-ray luminosity on stellar and wind parameters*, Astronomy and Astrophysics, 620, A89
- Nelson, D., Byrohl, C., Ogorzalek, A., et al. (2023), *Resonant scattering of the O VII X-ray emission line in the circumgalactic medium of TNG50 galaxies*, Monthly Notices of the RAS, 522(3), 3665
- Nica, A., Oppenheimer, B. D., Crain, R. A., et al. (2022), *Predictions for the X-ray circumgalactic medium of edge-on discs and spheroids*, Monthly Notices of the RAS
- Nicastro, F., Kaastra, J., Krongold, Y., et al. (2018), *Observations of the missing baryons in the warm-hot intergalactic medium*, Nature, 558(7710), 406
- Nicastro, F., Krongold, Y., Fang, T., et al. (2023), *X-Ray Detection of the Galaxy's Missing Baryons in the Circumgalactic Medium of L\* Galaxies*, Astrophysical Journal, Letters, 955(1), L21
- Nicastro, F., Senatore, F., Krongold, Y., et al. (2016), *A Distant Echo of Milky Way Central Activity Closes the Galaxy's Baryon Census*, Astrophysical Journal, Letters, 828(1), L12
- Offner, S. S. R., Moe, M., Kratter, K. M., et al. (2023), *The Origin and Evolution of Multiple Star Systems*, in *Protostars and Planets VII*, edited by S. Inutsuka, Y. Aikawa, T. Muto, K. Tomida, M. Tamura, volume 534 of *Astronomical Society of the Pacific Conference Series*, 275
- Oppenheimer, B. D., Babul, A., Bahé, Y., et al. (2021), *Simulating Groups and the IntraGroup Medium: The Surprisingly Complex and Rich Middle Ground between Clusters and Galaxies*, Universe, 7(7), 209
- Oppenheimer, B. D., Bogdán, Á., Crain, R. A., et al. (2020), *EAGLE and Illustris-TNG Predictions for Resolved eROSITA X-Ray Observations of the Circumgalactic Medium around Normal Galaxies*, Astrophysical Journal, Letters, 893(1), L24

- O'Sullivan, E., Ponman, T. J., and Collins, R. S. (2003), *X-ray scaling properties of early-type galaxies*, Monthly Notices of the RAS, 340(4), 1375
- Padovani, P., Alexander, D. M., Assef, R. J., et al. (2017), *Active galactic nuclei: what's in a name?*, Astronomy and Astrophysics Reviews, 25(1), 2
- Padovani, P. and Matteucci, F. (1993), *Stellar Mass Loss in Elliptical Galaxies and the Fueling of Active Galactic Nuclei*, Astrophysical Journal, 416, 26
- Paerels, F., Kaastra, J., Ohashi, T., et al. (2008), *Future Instrumentation for the Study of the Warm-Hot Intergalactic Medium*, Space Science Reviews, 134(1-4), 405
- Pearson, W. J., Wang, L., Hurley, P. D., et al. (2018), *Main sequence of star forming galaxies beyond the Herschel confusion limit*, Astronomy and Astrophysics, 615, A146
- Peebles, P. J. E. (1969), *Origin of the Angular Momentum of Galaxies*, Astrophysical Journal, 155, 393
- Pellegrini, S. (2012), *Hot Gas Flows on Global and Nuclear Galactic Scales*, in *Astrophysics and Space Science Library*, edited by D.-W. Kim, S. Pellegrini, volume 378 of *Astrophysics and Space Science Library*, 21
- Penzias, A. A. and Wilson, R. W. (1965), *A Measurement of Excess Antenna Temperature at 4080 Mc/s.*, Astrophysical Journal, 142, 419
- Perlmutter, S., Aldering, G., Goldhaber, G., et al. (1999), *Measurements of  $\Omega$  and  $\Lambda$  from 42 High-Redshift Supernovae*, Astrophysical Journal, 517(2), 565
- Péroux, C. and Howk, J. C. (2020), *The Cosmic Baryon and Metal Cycles*, Annual Review of Astron and Astrophys, 58, 363
- Persic, M. and Rephaeli, Y. (2002), *X-ray spectral components of starburst galaxies*, Astronomy and Astrophysics, 382, 843
- Persic, M. and Rephaeli, Y. (2003), *Starburst galaxies and the X-ray background*, Astronomy and Astrophysics, 399, 9
- Petrucchi, P. O., Merloni, A., Fabian, A., et al. (2001), *The effects of a Comptonizing corona on the appearance of the reflection components in accreting black hole spectra*, Monthly Notices of the RAS, 328(2), 501
- Pillepich, A., Springel, V., Nelson, D., et al. (2018), *Simulating galaxy formation with the IllustrisTNG model*, Monthly Notices of the RAS, 473(3), 4077
- Pinto, C., Steiner, J. F., Bodaghee, A., et al. (2024), *Probing extreme black-hole outflows on short timescales via high spectral-resolution x-ray imagers*, Astronomische Nachrichten, 345, e20240027

- Planck Collaboration, Ade, P. A. R., Aghanim, N., et al. (2013), *Planck intermediate results. V. Pressure profiles of galaxy clusters from the Sunyaev-Zeldovich effect*, *Astronomy and Astrophysics*, 550, A131
- Planck Collaboration, Aghanim, N., Akrami, Y., et al. (2020), *Planck 2018 results. VI. Cosmological parameters*, *Astronomy and Astrophysics*, 641, A6
- Postnov, K. A. and Yungelson, L. R. (2014), *The Evolution of Compact Binary Star Systems*, *Living Reviews in Relativity*, 17(1), 3
- Pratt, G. W., Böhringer, H., Croston, J. H., et al. (2007), *Temperature profiles of a representative sample of nearby X-ray galaxy clusters*, *Astronomy and Astrophysics*, 461(1), 71
- Predehl, P., Andritschke, R., Arefiev, V., et al. (2021), *The eROSITA X-ray telescope on SRG*, *Astronomy and Astrophysics*, 647, A1
- Predehl, P., Sunyaev, R. A., Becker, W., et al. (2020), *Detection of large-scale X-ray bubbles in the Milky Way halo*, *Nature*, 588(7837), 227
- Preibisch, T. and Feigelson, E. D. (2005), *The Evolution of X-Ray Emission in Young Stars*, *Astrophysical Journal, Supplement*, 160(2), 390
- Preibisch, T., Kim, Y.-C., Favata, F., et al. (2005), *The Origin of T Tauri X-Ray Emission: New Insights from the Chandra Orion Ultradeep Project*, *Astrophysical Journal, Supplement*, 160(2), 401
- Price, D. J. (2012), *Smoothed particle hydrodynamics and magnetohydrodynamics*, *Journal of Computational Physics*, 231(3), 759
- Ranalli, P., Comastri, A., and Setti, G. (2003), *The 2-10 keV luminosity as a Star Formation Rate indicator*, *Astronomy and Astrophysics*, 399, 39
- Rappaport, S. A., Podsiadlowski, P., and Pfahl, E. (2005), *Stellar-mass black hole binaries as ultraluminous X-ray sources*, *Monthly Notices of the RAS*, 356(2), 401
- Rasia, E., Mazzotta, P., Bourdin, H., et al. (2008), *X-MAS2: Study Systematics on the ICM Metallicity Measurements*, *Astrophysical Journal*, 674(2), 728
- Rauw, G. (2022), *X-Ray Emission of Massive Stars and Their Winds*, in *Handbook of X-ray and Gamma-ray Astrophysics*, edited by C. Bambi, A. Sanganelo, 108, Springer
- Rees, M. J. and Ostriker, J. P. (1977), *Cooling, dynamics and fragmentation of massive gas clouds: clues to the masses and radii of galaxies and clusters.*, *Monthly Notices of the RAS*, 179, 541

- Reiprich, T. H., Veronica, A., Pacaud, F., et al. (2021), *The Abell 3391/95 galaxy cluster system. A 15 Mpc intergalactic medium emission filament, a warm gas bridge, infalling matter clumps, and (re-) accelerated plasma discovered by combining SRG/eROSITA data with ASKAP/EMU and DECam data*, *Astronomy and Astrophysics*, 647, A2
- Remillard, R. A. and McClintock, J. E. (2006), *X-Ray Properties of Black-Hole Binaries*, *Annual Review of Astron and Astrophys*, 44(1), 49
- Remus, R.-S., Dolag, K., Naab, T., et al. (2017), *The co-evolution of total density profiles and central dark matter fractions in simulated early-type galaxies*, *Monthly Notices of the RAS*, 464(3), 3742
- Revnivtsev, M., Postnov, K., Kuranov, A., and Ritter, H. (2011), *On the nature of the break in the X-ray luminosity function of low-mass X-ray binaries*, *Astronomy and Astrophysics*, 526, A94
- Revnivtsev, M., Sazonov, S., Churazov, E., et al. (2009), *Discrete sources as the origin of the Galactic X-ray ridge emission*, *Nature*, 458(7242), 1142
- Reynolds, C. S., Kara, E. A., Mushotzky, R. F., et al. (2023), *Overview of the advanced x-ray imaging satellite (AXIS)*, in *UV, X-Ray, and Gamma-Ray Space Instrumentation for Astronomy XXIII*, edited by O. H. Siegmund, K. Hoadley, volume 12678 of *Society of Photo-Optical Instrumentation Engineers (SPIE) Conference Series*, 126781E
- Ricci, C., Walter, R., Courvoisier, T. J. L., and Paltani, S. (2011), *Reflection in Seyfert galaxies and the unified model of AGN*, *Astronomy and Astrophysics*, 532, A102
- Riccio, G., Yang, G., Małek, et al. (2023), *X-ray luminosity-star formation rate scaling relation: Constraints from the eROSITA Final Equatorial Depth Survey (eFEDS)*, arXiv e-prints, arXiv:2309.03578
- Richter, P., Paerels, F. B. S., and Kaastra, J. S. (2008), *FUV and X-Ray Absorption in the Warm-Hot Intergalactic Medium*, *Space Science Reviews*, 134(1-4), 25
- Riess, A. G., Filippenko, A. V., Challis, P., et al. (1998), *Observational Evidence from Supernovae for an Accelerating Universe and a Cosmological Constant*, *Astronomical Journal*, 116(3), 1009
- Rihtaršič, G., Biffi, V., Fabjan, D., and Dolag, K. (2024), *Environmental dependence of AGN activity and star formation in galaxy clusters from Magneticum simulations*, *Astronomy and Astrophysics*, 683, A57
- Romanowsky, A. J. and Fall, S. M. (2012), *Angular Momentum and Galaxy Formation Revisited*, *Astrophysical Journal, Supplement*, 203(2), 17
- Rothschild, R., Boldt, E., Holt, S., et al. (1979), *The cosmic X-ray experiment aboard HEAO-1.*, *Space Science Instrumentation*, 4, 269

- Rubin, V. C., Ford, W. K., J., and Thonnard, N. (1980), *Rotational properties of 21 SC galaxies with a large range of luminosities and radii, from NGC 4605 ( $R=4\text{kpc}$ ) to UGC 2885 ( $R=122\text{kpc}$ )*, *Astrophysical Journal*, 238, 471
- Salpeter, E. E. (1955), *The Luminosity Function and Stellar Evolution.*, *Astrophysical Journal*, 121, 161
- Salvato, M., Wolf, J., Dwelly, T., et al. (2022), *The eROSITA Final Equatorial-Depth Survey (eFEDS). Identification and characterization of the counterparts to point-like sources*, *Astronomy and Astrophysics*, 661, A3
- Sarazin, C. L. (1988), *X-ray emission from clusters of galaxies*, Cambridge University Press
- Saxena, A., Ellis, R. S., Förster, P. U., et al. (2021), *The VANDELS Survey: new constraints on the high-mass X-ray binary populations in normal star-forming galaxies at  $3 < z < 5.5$* , *Monthly Notices of the RAS*, 505(4), 4798
- Sazonov, S. and Khabibullin, I. (2017a), *Bright end of the luminosity function of high-mass X-ray binaries: contributions of hard, soft and supersoft sources*, *Monthly Notices of the RAS*, 466(1), 1019
- Sazonov, S. and Khabibullin, I. (2017b), *The intrinsic collective X-ray spectrum of luminous high-mass X-ray binaries*, *Monthly Notices of the RAS*, 468(2), 2249
- Scannapieco, C., Tissera, P. B., White, S. D. M., and Springel, V. (2006), *Feedback and metal enrichment in cosmological SPH simulations - II. A multiphase model with supernova energy feedback*, *Monthly Notices of the RAS*, 371(3), 1125
- Schaye, J., Crain, R. A., Bower, R. G., et al. (2015), *The EAGLE project: simulating the evolution and assembly of galaxies and their environments*, *Monthly Notices of the RAS*, 446(1), 521
- Schellenberger, G., Bogdán, Á., ZuHone, J. A., et al. (2023), *Mapping the imprints of stellar and AGN feedback in the circumgalactic medium with X-ray microcalorimeters*, arXiv e-prints, arXiv:2307.01259
- Schellenberger, G., Bogdán, Á., ZuHone, J. A., et al. (2024), *Mapping the Imprints of Stellar and Active Galactic Nucleus Feedback in the Circumgalactic Medium with X-Ray Microcalorimeters*, *Astrophysical Journal*, 969(2), 85
- Schneider, F. R. N., Podsiadlowski, P., and Müller, B. (2021), *Pre-supernova evolution, compact-object masses, and explosion properties of stripped binary stars*, *Astronomy and Astrophysics*, 645, A5
- Schulze, F., Remus, R.-S., Dolag, K., et al. (2020), *Kinematics of simulated galaxies II: Probing the stellar kinematics of galaxies out to large radii*, *Monthly Notices of the RAS*, 493(3), 3778

- Schulze, F., Remus, R.-S., Dolag, K., et al. (2018), *Kinematics of simulated galaxies - I. Connecting dynamical and morphological properties of early-type galaxies at different redshifts*, Monthly Notices of the RAS, 480(4), 4636
- Shakura, N. I. and Sunyaev, R. A. (1973), *Black holes in binary systems. Observational appearance.*, Astronomy and Astrophysics, 24, 337
- Shreeram, S., Comparat, J., Merloni, A., et al. (2024), *Quantifying Observational Projection Effects with a Simulation-based hot CGM model*, arXiv e-prints, arXiv:2409.10397
- Shtykovski, P. and Gilfanov, M. (2005a), *High mass X-ray binaries in the LMC: Dependence on the stellar population age and the “propeller” effect*, Astronomy and Astrophysics, 431, 597
- Shtykovski, P. and Gilfanov, M. (2005b), *High-mass X-ray binaries in the Small Magellanic Cloud: the luminosity function*, Monthly Notices of the RAS, 362(3), 879
- Shtykovski, P. E. and Gilfanov, M. R. (2007), *High-mass X-ray binaries and recent star formation history of the Small Magellanic Cloud*, Astronomy Letters, 33(7), 437
- Sijacki, D. and Springel, V. (2006), *Hydrodynamical simulations of cluster formation with central AGN heating*, Monthly Notices of the RAS, 366(2), 397
- Sijacki, D., Springel, V., Di Matteo, T., and Hernquist, L. (2007), *A unified model for AGN feedback in cosmological simulations of structure formation*, Monthly Notices of the RAS, 380(3), 877
- Sijacki, D., Vogelsberger, M., Genel, S., et al. (2015), *The Illustris simulation: the evolving population of black holes across cosmic time*, Monthly Notices of the RAS, 452(1), 575
- Silk, J. (1977), *On the fragmentation of cosmic gas clouds. I. The formation of galaxies and the first generation of stars.*, Astrophysical Journal, 211, 638
- Sivakoff, G. R., Jordán, A., Sarazin, C. L., et al. (2007), *The Low-Mass X-Ray Binary and Globular Cluster Connection in Virgo Cluster Early-Type Galaxies: Optical Properties*, Astrophysical Journal, 660(2), 1246
- Smith, B., Sigurdsson, S., and Abel, T. (2008), *Metal cooling in simulations of cosmic structure formation*, Monthly Notices of the RAS, 385(3), 1443
- Smith, R. K., Brickhouse, N. S., Liedahl, D. A., and Raymond, J. C. (2001), *Collisional Plasma Models with APEC/APED: Emission-Line Diagnostics of Hydrogen-like and Helium-like Ions*, Astrophysical Journal, Letters, 556(2), L91
- Soria, R., Kolehmainen, M., Graham, A. W., et al. (2022), *A Chandra Virgo cluster survey of spiral galaxies - I. Introduction to the survey and a new ULX sample*, Monthly Notices of the RAS, 512(3), 3284

- Sousbie, T. (2011), *The persistent cosmic web and its filamentary structure - I. Theory and implementation*, Monthly Notices of the RAS, 414(1), 350
- Sousbie, T., Pichon, C., and Kawahara, H. (2011), *The persistent cosmic web and its filamentary structure - II. Illustrations*, Monthly Notices of the RAS, 414(1), 384
- Springel, V. (2005), *The cosmological simulation code GADGET-2*, Monthly Notices of the RAS, 364(4), 1105
- Springel, V., Di Matteo, T., and Hernquist, L. (2005), *Modelling feedback from stars and black holes in galaxy mergers*, Monthly Notices of the RAS, 361(3), 776
- Springel, V. and Hernquist, L. (2003), *Cosmological smoothed particle hydrodynamics simulations: a hybrid multiphase model for star formation*, Monthly Notices of the RAS, 339(2), 289
- Springel, V., White, S. D. M., Tormen, G., and Kauffmann, G. (2001), *Populating a cluster of galaxies - I. Results at  $z=0$* , Monthly Notices of the RAS, 328(3), 726
- Staubert, R., Trümper, J., Kendziorra, E., et al. (2019), *Cyclotron lines in highly magnetized neutron stars*, Astronomy and Astrophysics, 622, A61
- Steinborn, L. K., Dolag, K., Comerford, J. M., et al. (2016), *Origin and properties of dual and offset active galactic nuclei in a cosmological simulation at  $z=2$* , Monthly Notices of the RAS, 458(1), 1013
- Steinborn, L. K., Dolag, K., Hirschmann, M., et al. (2015), *A refined sub-grid model for black hole accretion and AGN feedback in large cosmological simulations*, Monthly Notices of the RAS, 448(2), 1504
- Stern, J., Fielding, D., Faucher-Giguère, C.-A., and Quataert, E. (2020), *The maximum accretion rate of hot gas in dark matter haloes*, Monthly Notices of the RAS, 492(4), 6042
- Stern, J., Fielding, D., Hafen, Z., et al. (2023), *Accretion onto disk galaxies via hot and rotating CGM inflows*, arXiv e-prints, arXiv:2306.00092
- Stocke, J. T., Keeney, B. A., Danforth, C. W., et al. (2013), *Characterizing the Circumgalactic Medium of Nearby Galaxies with HST/COS and HST/STIS Absorption-line Spectroscopy*, Astrophysical Journal, 763(2), 148
- Strickland, D. K. and Heckman, T. M. (2009), *Supernova Feedback Efficiency and Mass Loading in the Starburst and Galactic Superwind Exemplar M82*, Astrophysical Journal, 697(2), 2030
- Strickland, D. K., Heckman, T. M., Colbert, E. J. M., et al. (2004), *A High Spatial Resolution X-Ray and H $\alpha$  Study of Hot Gas in the Halos of Star-forming Disk Galaxies. I. Spatial and Spectral Properties of the Diffuse X-Ray Emission*, Astrophysical Journal, Supplement, 151(2), 193

- Strickland, D. K. and Stevens, I. R. (2000), *Starburst-driven galactic winds - I. Energetics and intrinsic X-ray emission*, Monthly Notices of the RAS, 314(3), 511
- Strohmayer, T. and Bildsten, L. (2006), *New views of thermonuclear bursts*, in *Compact stellar X-ray sources*, edited by W. H. G. Lewin, M. van der Klis, volume 39, 113–156, Cambridge University Press
- Su, M., Slatyer, T. R., and Finkbeiner, D. P. (2010), *Giant Gamma-ray Bubbles from Fermi-LAT: Active Galactic Nucleus Activity or Bipolar Galactic Wind?*, Astrophysical Journal, 724(2), 1044
- Sunyaev, R., Arefiev, V., Babushkin, V., et al. (2021), *SRG X-ray orbital observatory. Its telescopes and first scientific results*, Astronomy and Astrophysics, 656, A132
- Sutherland, R. S. and Dopita, M. A. (1993), *Cooling Functions for Low-Density Astrophysical Plasmas*, Astrophysical Journal, Supplement, 88, 253
- Szczygieł, D. M., Socrates, A., Paczyński, B., et al. (2008), *Coronal Activity from the ASAS Eclipsing Binaries*, Acta Astronomica, 58, 405
- Takahashi, T., Kokubun, M., Mitsuda, K., et al. (2016), *The ASTRO-H (Hitomi) x-ray astronomy satellite*, in *Space Telescopes and Instrumentation 2016: Ultraviolet to Gamma Ray*, edited by J.-W. A. den Herder, T. Takahashi, M. Bautz, volume 9905 of *Society of Photo-Optical Instrumentation Engineers (SPIE) Conference Series*, 99050U
- Tanimura, H., Aghanim, N., Douspis, M., and Malavasi, N. (2022), *X-ray emission from cosmic web filaments in SRG/eROSITA data*, Astronomy and Astrophysics, 667, A161
- Tanimura, H., Aghanim, N., Kolodzig, A., et al. (2020), *First detection of stacked X-ray emission from cosmic web filaments*, Astronomy and Astrophysics, 643, L2
- Tashiro, M., Maejima, H., Toda, K., et al. (2020), *Status of x-ray imaging and spectroscopy mission (XRISM)*, in *Space Telescopes and Instrumentation 2020: Ultraviolet to Gamma Ray*, edited by J.-W. A. den Herder, S. Nikzad, K. Nakazawa, volume 11444 of *Society of Photo-Optical Instrumentation Engineers (SPIE) Conference Series*, 1144422
- Tauris, T. M., Kramer, M., Freire, P. C. C., et al. (2017), *Formation of Double Neutron Star Systems*, Astrophysical Journal, 846(2), 170
- Tauris, T. M. and van den Heuvel, E. P. J. (2006), *Formation and evolution of compact stellar X-ray sources*, volume 39, 623–665, Cambridge University Press
- Tauris, T. M. and van den Heuvel, E. P. J. (2023), *Physics of Binary Star Evolution. From Stars to X-ray Binaries and Gravitational Wave Sources*, Princeton University Press
- Teklu, A. F., Remus, R.-S., Dolag, K., et al. (2015), *Connecting Angular Momentum and Galactic Dynamics: The Complex Interplay between Spin, Mass, and Morphology*, Astrophysical Journal, 812(1), 29

- Teklu, A. F., Remus, R.-S., Dolag, K., and Burkert, A. (2017), *The morphology-density relation: impact on the satellite fraction*, Monthly Notices of the RAS, 472(4), 4769
- Tempel, E., Stoica, R. S., Martínez, V. J., et al. (2014), *Detecting filamentary pattern in the cosmic web: a catalogue of filaments for the SDSS*, Monthly Notices of the RAS, 438(4), 3465
- Teyssier, R., Moore, B., Martizzi, D., et al. (2011), *Mass distribution in galaxy clusters: the role of Active Galactic Nuclei feedback*, Monthly Notices of the RAS, 414(1), 195
- Tornatore, L., Borgani, S., Dolag, K., and Matteucci, F. (2007), *Chemical enrichment of galaxy clusters from hydrodynamical simulations*, Monthly Notices of the RAS, 382(3), 1050
- Tornatore, L., Borgani, S., Matteucci, F., et al. (2004), *Simulating the metal enrichment of the intracluster medium*, Monthly Notices of the RAS, 349(1), L19
- Torres, G., Andersen, J., and Giménez, A. (2010), *Accurate masses and radii of normal stars: modern results and applications*, Astronomy and Astrophysics Reviews, 18(1-2), 67
- Truemper, J. (1982), *The ROSAT mission*, Advances in Space Research, 2(4), 241
- Truong, N., Pillepich, A., Nelson, D., et al. (2023), *X-ray metal line emission from the hot circumgalactic medium: probing the effects of supermassive black hole feedback*, Monthly Notices of the RAS, 525(2), 1976
- Truong, N., Pillepich, A., Nelson, D., et al. (2021a), *Predictions for anisotropic X-ray signatures in the circumgalactic medium: imprints of supermassive black hole driven outflows*, Monthly Notices of the RAS, 508(2), 1563
- Truong, N., Pillepich, A., and Werner, N. (2021b), *Correlations between supermassive black holes and hot gas atmospheres in IllustrisTNG and X-ray observations*, Monthly Notices of the RAS, 501(2), 2210
- Truong, N., Pillepich, A., Werner, N., et al. (2020), *X-ray signatures of black hole feedback: hot galactic atmospheres in IllustrisTNG and X-ray observations*, Monthly Notices of the RAS, 494(1), 549
- Tumlinson, J., Peeples, M. S., and Werk, J. K. (2017), *The Circumgalactic Medium*, Annual Review of Astron and Astrophys, 55(1), 389
- Tumlinson, J., Thom, C., Werk, J. K., et al. (2013), *The COS-Halos Survey: Rationale, Design, and a Census of Circumgalactic Neutral Hydrogen*, Astrophysical Journal, 777(1), 59
- Tuominen, T., Nevalainen, J., Tempel, E., et al. (2021), *An EAGLE view of the missing baryons*, Astronomy and Astrophysics, 646, A156
- Tyler, K., Quillen, A. C., LaPage, A., and Rieke, G. H. (2004), *Diffuse X-Ray Emission in Spiral Galaxies*, Astrophysical Journal, 610(1), 213

- Ueda, Y., Akiyama, M., Hasinger, G., et al. (2014), *Toward the Standard Population Synthesis Model of the X-Ray Background: Evolution of X-Ray Luminosity and Absorption Functions of Active Galactic Nuclei Including Compton-thick Populations*, *Astrophysical Journal*, 786(2), 104
- Ursino, E., Galeazzi, M., and Roncarelli, M. (2010), *Effect of Metallicity on X-ray Emission from the Warm-hot Intergalactic Medium*, *Astrophysical Journal*, 721(1), 46
- Valentini, M., Borgani, S., Bressan, A., et al. (2019), *Chemical evolution of disc galaxies from cosmological simulations*, *Monthly Notices of the RAS*, 485(1), 1384
- Valenzuela, L. M. and Remus, R.-S. (2024), *A stream come true: Connecting tidal tails, shells, streams, and planes with galaxy kinematics and formation history*, *Astronomy and Astrophysics*, 686, A182
- Valenzuela, L. M., Remus, R.-S., Dolag, K., and Seidel, B. A. (2024), *Galaxy shapes in Magneticum. I. Connecting stellar and dark matter shapes to dynamical and morphological galaxy properties and the large-scale structure*, arXiv e-prints, arXiv:2404.01368
- Virtanen, P., Gommers, R., Oliphant, T. E., et al. (2020), *SciPy 1.0: Fundamental Algorithms for Scientific Computing in Python*, *Nature Methods*, 17, 261
- Vladutescu-Zopp, S., Biffi, V., and Dolag, K. (2023), *Decomposition of galactic X-ray emission with PHOX. Contributions from hot gas and X-ray binaries*, *Astronomy and Astrophysics*, 669, A34
- Vladutescu-Zopp, S., Biffi, V., and Dolag, K. (2024), *Radial X-ray profiles of simulated galaxies: Contributions from hot gas and XRBs*, arXiv e-prints, arXiv:2406.02686
- Vogelsberger, M., Genel, S., Springel, V., et al. (2014), *Introducing the Illustris Project: simulating the coevolution of dark and visible matter in the Universe*, *Monthly Notices of the RAS*, 444(2), 1518
- Voit, G. M., Donahue, M., O'Shea, B. W., et al. (2015a), *Supernova Sweeping and Black Hole Feedback in Elliptical Galaxies*, *Astrophysical Journal, Letters*, 803(2), L21
- Voit, G. M., Donahue, M., O'Shea, B. W., et al. (2015b), *Supernova Sweeping and Black Hole Feedback in Elliptical Galaxies*, *Astrophysical Journal, Letters*, 803(2), L21
- Voss, R., Gilfanov, M., Sivakoff, G. R., et al. (2009), *Luminosity Functions of LMXBs in Centaurus a: Globular Clusters Versus the Field*, *Astrophysical Journal*, 701(1), 471
- Vulic, N., Hornschemeier, A. E., Haberl, F., et al. (2022), *The eROSITA Final Equatorial-Depth Survey (eFEDS). Presenting the demographics of X-ray emission from normal galaxies*, *Astronomy and Astrophysics*, 661, A16
- Warner, B. (1995), *Cataclysmic variable stars*, volume 28, Cambridge University Press

- Weinberg, S. (1972), *Gravitation and Cosmology: Principles and Applications of the General Theory of Relativity*, Wiley-VCH
- Weinmann, S. M., Kauffmann, G., von der Linden, A., and De Lucia, G. (2010), *Cluster galaxies die hard*, Monthly Notices of the RAS, 406(4), 2249
- Weisskopf, M. C., Tananbaum, H. D., Van Speybroeck, L. P., and O'Dell, S. L. (2000), *Chandra X-ray Observatory (CXO): overview*, in *X-Ray Optics, Instruments, and Missions III*, edited by J. E. Truemper, B. Aschenbach, volume 4012 of *Society of Photo-Optical Instrumentation Engineers (SPIE) Conference Series*, 2–16
- Werk, J. K., Prochaska, J. X., Cantalupo, S., et al. (2016), *The COS-Halos Survey: Origins of the Highly Ionized Circumgalactic Medium of Star-Forming Galaxies*, Astrophysical Journal, 833(1), 54
- Werk, J. K., Prochaska, J. X., Tumlinson, J., et al. (2014), *The COS-Halos Survey: Physical Conditions and Baryonic Mass in the Low-redshift Circumgalactic Medium*, Astrophysical Journal, 792(1), 8
- Werner, N., Finoguenov, A., Kaastra, J. S., et al. (2008), *Detection of hot gas in the filament connecting the clusters of galaxies Abell 222 and Abell 223*, Astronomy and Astrophysics, 482(3), L29
- White, S. D. M. and Frenk, C. S. (1991), *Galaxy Formation through Hierarchical Clustering*, Astrophysical Journal, 379, 52
- White, S. D. M., Frenk, C. S., Davis, M., and Efstathiou, G. (1987), *Clusters, Filaments, and Voids in a Universe Dominated by Cold Dark Matter*, Astrophysical Journal, 313, 505
- White, S. D. M. and Rees, M. J. (1978), *Core condensation in heavy halos: a two-stage theory for galaxy formation and clustering.*, Monthly Notices of the RAS, 183, 341
- Wiersma, R. P. C., Schaye, J., and Smith, B. D. (2009), *The effect of photoionization on the cooling rates of enriched, astrophysical plasmas*, Monthly Notices of the RAS, 393(1), 99
- Wijers, N. A. and Schaye, J. (2022), *The warm-hot circumgalactic medium around EAGLE-simulation galaxies and its detection prospects with X-ray-line emission*, Monthly Notices of the RAS, 514(4), 5214
- Wik, D. R., Lehmer, B. D., Hornschemeier, A. E., et al. (2014), *Spatially Resolving a Starburst Galaxy at Hard X-Ray Energies: NuSTAR, Chandra, and VLBA Observations of NGC 253*, Astrophysical Journal, 797(2), 79
- Wiktorowicz, G., Lasota, J.-P., Belczynski, K., et al. (2021), *Wind-powered Ultraluminous X-ray Sources*, Astrophysical Journal, 918(2), 60

- Wiktorowicz, G., Sobolewska, M., Lasota, J.-P., and Belczynski, K. (2017), *The Origin of the Ultraluminous X-Ray Sources*, *Astrophysical Journal*, 846(1), 17
- Wilms, J., Allen, A., and McCray, R. (2000), *On the Absorption of X-Rays in the Interstellar Medium*, *Astrophysical Journal*, 542(2), 914
- Winston, E., Megeath, S. T., Wolk, S. J., et al. (2007), *A Combined Spitzer and Chandra Survey of Young Stellar Objects in the Serpens Cloud Core*, *Astrophysical Journal*, 669(1), 493
- Wong, K.-W., Irwin, J. A., Shcherbakov, R. V., et al. (2014), *The Megasecond Chandra X-Ray Visionary Project Observation of NGC 3115: Witnessing the Flow of Hot Gas within the Bondi Radius*, *Astrophysical Journal*, 780(1), 9
- Wood, K. S., Meekins, J. F., Yentis, D. J., et al. (1984), *The HEAO A-1 X-ray source catalog.*, *Astrophysical Journal*, Supplement, 56, 507
- Woosley, S. E. (2019), *The Evolution of Massive Helium Stars, Including Mass Loss*, *Astrophysical Journal*, 878(1), 49
- Woosley, S. E., Heger, A., and Weaver, T. A. (2002), *The evolution and explosion of massive stars*, *Reviews of Modern Physics*, 74(4), 1015
- Xue, Y. Q., Luo, B., Brandt, W. N., et al. (2011), *The Chandra Deep Field-South Survey: 4 Ms Source Catalogs*, *Astrophysical Journal*, Supplement, 195(1), 10
- Yoshida, N., Abel, T., Hernquist, L., and Sugiyama, N. (2003), *Simulations of Early Structure Formation: Primordial Gas Clouds*, *Astrophysical Journal*, 592(2), 645
- Yukita, M., Hornschemeier, A. E., Lehmer, B. D., et al. (2016), *A Hard X-Ray Study of the Normal Star-forming Galaxy M83 with NuSTAR*, *Astrophysical Journal*, 824(2), 107
- Zahid, H. J., Geller, M. J., Fabricant, D. G., and Hwang, H. S. (2016), *The Scaling of Stellar Mass and Central Stellar Velocity Dispersion for Quiescent Galaxies at  $z < 0.7$* , *Astrophysical Journal*, 832(2), 203
- Zahid, H. J., Kudritzki, R.-P., Conroy, C., et al. (2017), *Stellar Absorption Line Analysis of Local Star-forming Galaxies: The Relation between Stellar Mass, Metallicity, Dust Attenuation, and Star Formation Rate*, *Astrophysical Journal*, 847(1), 18
- Zdziarski, A. A., Dziełak, M. A., De Marco, B., et al. (2021), *Accretion Geometry in the Hard State of the Black Hole X-Ray Binary MAXI J1820+070*, *Astrophysical Journal*, Letters, 909(1), L9
- Zhang, X., Bulbul, E., Malavasi, N., et al. (2024a), *The SRG/eROSITA all-sky survey. X-ray emission from the warm-hot phase gas in long cosmic filaments*, arXiv e-prints, arXiv:2406.00105
- Zhang, Y., Comparat, J., Ponti, G., et al. (2024b), *The Hot Circum-Galactic Medium in the eROSITA All Sky Survey I. X-ray Surface Brightness Profiles*, arXiv e-prints, arXiv:2401.17308

- Zhang, Y., Comparat, J., Ponti, G., et al. (2024c), *The Hot Circum-Galactic Medium in the eROSITA All Sky Survey II. Scaling Relations between X-ray Luminosity and Galaxies' Mass*, arXiv e-prints, arXiv:2401.17309
- Zhang, Z., Gilfanov, M., and Bogdán, Á. (2012), *Dependence of the low-mass X-ray binary population on stellar age*, *Astronomy and Astrophysics*, 546, A36
- Zhang, Z., Gilfanov, M., and Bogdán, Á. (2013), *Low-mass X-ray binary populations in galaxy outskirts: Globular clusters and supernova kicks*, *Astronomy and Astrophysics*, 556, A9
- Zhang, Z., Gilfanov, M., Voss, R., et al. (2011), *Luminosity functions of LMXBs in different stellar environments*, *Astronomy and Astrophysics*, 533, A33
- Zhao, Y., Xu, H., Liu, A., et al. (2024), *The warm-hot intergalactic medium (WHIM) in inter-cluster filaments – A forecast for HUBS observations based on eRASS1 superclusters*, arXiv e-prints, arXiv:2410.06836
- ZuHone, J. A., Schellenberger, G., Ogorzałek, A., et al. (2024), *Properties of the Line-of-sight Velocity Field in the Hot and X-Ray-emitting Circumgalactic Medium of Nearby Simulated Disk Galaxies*, *Astrophysical Journal*, 967(1), 49
- Zwicky, F. (1933), *Die Rotverschiebung von extragalaktischen Nebeln*, *Helvetica Physica Acta*, 6, 110



# Acknowledgements

First and foremost, I want to thank my supervisors Klaus Dolag and Veronica Biffi for their great supervision, patience, and mentorship and for always being available when I had questions or doubts about my work. I also want to thank you for providing me with a great and friendly environment to pursue my scientific endeavors.

I also want to thank Ildar Khabibullin for the in-depth discussions, for his advice on various topics, and for sharing his profound knowledge about high-energy astrophysical phenomena.

I want to thank all my colleagues at the institute and all members of the CAST group for all the fun discussions in the office, during coffee meetings, and lunch. Thank you all for the discussion, the great fun, and the support.

I want to thank my colleagues Freddy, Luca, Tirso, Elena, Laura, Ilaria, and Ludwig for all the experiences we shared during our travels.

In particular, I want to thank Frederick Groth for his undisputed ability to navigate the horrors of administrative duties and travel requests. I also want to thank Freddy for his support and help during the write-up of the thesis and for sharing our concerns during our simultaneous writing.

I want to thank Veronica Biffi, Ildar Khabibullin, Daniel Karner, Luca Sala, Lucas Valenzuela, Silvio Fortuné, Benjamin Seidl, and Frederick Groth for proofreading my thesis and providing me with helpful comments.

I want to thank the LEM collaboration for giving me the opportunity to work on an exciting proposal and future-directed science enabling the preliminary study presented in this thesis.

Finally, I want to thank my parents Ionel and Rosemarie, my brothers Niki and Dani, and my friends for their unconditional support and for giving me the opportunity to pursue my dreams. Without you, all of this would not have been possible and I can not express in words all the gratitude I feel.

*Danke für eure uneingeschränkte Unterstützung und Zuneigung. Ohne euch hätte ich diesen Traum nie in Erfüllung bringen können und ich kann meine Dankbarkeit nicht in Worte fassen.*